NASA/CR—2011-217237

Inlet Flow Control and Prediction Technologies for Embedded Propulsion Systems

Program Summary Report

Michelle L. McMillan
SynGenics Corporation, Delaware, Ohio

Scott A. Mackie
The Boeing Company, St. Louis, Missouri

Abe Gissen and Bojan Vukasinovic
Georgia Institute of Technology, Atlanta, Georgia

Matthew T. Lakebrink
The Boeing Company, St. Louis, Missouri

Ari Glezer
Georgia Institute of Technology, Atlanta, Georgia

Mori Mani and James L. Mace
The Boeing Company, St. Louis, Missouri

December 2011

NASA STI Program . . . in Profile

Since its founding, NASA has been dedicated to the advancement of aeronautics and space science. The NASA Scientific and Technical Information (STI) program plays a key part in helping NASA maintain this important role.

The NASA STI Program operates under the auspices of the Agency Chief Information Officer. It collects, organizes, provides for archiving, and disseminates NASA's STI. The NASA STI program provides access to the NASA Aeronautics and Space Database and its public interface, the NASA Technical Reports Server, thus providing one of the largest collections of aeronautical and space science STI in the world. Results are published in both non-NASA channels and by NASA in the NASA STI Report Series, which includes the following report types:

- TECHNICAL PUBLICATION. Reports of completed research or a major significant phase of research that present the results of NASA programs and include extensive data or theoretical analysis. Includes compilations of significant scientific and technical data and information deemed to be of continuing reference value. NASA counterpart of peer-reviewed formal professional papers but has less stringent limitations on manuscript length and extent of graphic presentations.

- TECHNICAL MEMORANDUM. Scientific and technical findings that are preliminary or of specialized interest, e.g., quick release reports, working papers, and bibliographies that contain minimal annotation. Does not contain extensive analysis.

- CONTRACTOR REPORT. Scientific and technical findings by NASA-sponsored contractors and grantees.

- CONFERENCE PUBLICATION. Collected papers from scientific and technical conferences, symposia, seminars, or other meetings sponsored or cosponsored by NASA.

- SPECIAL PUBLICATION. Scientific, technical, or historical information from NASA programs, projects, and missions, often concerned with subjects having substantial public interest.

- TECHNICAL TRANSLATION. English-language translations of foreign scientific and technical material pertinent to NASA's mission.

Specialized services also include creating custom thesauri, building customized databases, organizing and publishing research results.

For more information about the NASA STI program, see the following:

- Access the NASA STI program home page at *http://www.sti.nasa.gov*

- E-mail your question via the Internet to *help@sti.nasa.gov*

- Fax your question to the NASA STI Help Desk at 443–757–5803

- Telephone the NASA STI Help Desk at 443–757–5802

- Write to:
  NASA Center for AeroSpace Information (CASI)
  7115 Standard Drive
  Hanover, MD 21076–1320

NASA/CR—2011-217237

Inlet Flow Control and Prediction Technologies for Embedded Propulsion Systems

Program Summary Report

Michelle L. McMillan
SynGenics Corporation, Delaware, Ohio

Scott A. Mackie
The Boeing Company, St. Louis, Missouri

Abe Gissen and Bojan Vukasinovic
Georgia Institute of Technology, Atlanta, Georgia

Matthew T. Lakebrink
The Boeing Company, St. Louis, Missouri

Ari Glezer
Georgia Institute of Technology, Atlanta, Georgia

Mori Mani and James L. Mace
The Boeing Company, St. Louis, Missouri

Prepared under Contract NNC07CB76C

National Aeronautics and
Space Administration

Glenn Research Center
Cleveland, Ohio 44135

December 2011

This work was sponsored by the Fundamental Aeronautics Program
at the NASA Glenn Research Center.

Level of Review: This material has been technically reviewed by NASA expert reviewer(s).

Available from

NASA Center for Aerospace Information
7115 Standard Drive
Hanover, MD 21076–1320

National Technical Information Service
5301 Shawnee Road
Alexandria, VA 22312

Available electronically at http://www.sti.nasa.gov

Preface

This report documents the fundamental aeronautics research performed by The Boeing Company under NASA Contract No. NNC07CB76C during Fiscal Years 2008, 2009, and 2010. Subcontractors supporting The Boeing Company in this Contract were SynGenics Corporation and Georgia Institute of Technology. Ms Julianne C. Dudek of NASA served as the Contract Officer's Technical Representative.

Contents

List of Figures

List of Tables

Nomenclature

AIP	Aerodynamic Interface Plane
AFLR	Advancing-Front/Local-Reconnection
BCFD	Boeing Computational Fluid Dynamics
BLI	Boundary Layer Ingesting
BWB	Blended Wing Body
CCW	Counter-Clockwise
CD	CD
CFD	Computational Fluid Dynamics
CRSV	Counter-Rotating Streamwise Vortices
CW	Clockwise
D_{eng}	Engine Face Diameter
DES	Detached Eddy Simulation
$DPCP_{ave}$	Average SAE Circumferential Total-pressure distortion
$DPCP_H$	Hub Average SAE Circumferential Total-pressure distortion
$DPCP_i$	Ring Circumferential Distortion
$DPCP_T$	Tip Average SAE Circumferential Total-pressure distortion
$DPRP_H$	Hub Average SAE Radial Total-pressure distortion
$DPRP_T$	Tip Average SAE Radial Total-pressure distortion
δ	Boundary Layer Thickness
δ_{apex}	Boundary layer thickness at the Wind-Tunnel-Test-Section Apex
Theta, θ	Spacial Distortion Extent Angle
f	Synthetic Jet Actuator Driving Frequency
FMRL	Fluid Mechanics Research Laboratory
GaTech	Georgia Institute of Technology
GRC	NASA Glenn Research Center
GRS1	Coarse Computational Grid
GRS2	Refined Grid 1
GRS3	Refined Grid 2
GRS4	Refined Grid 3
h	Shape Factor
h_0	Baseline Shape Factor
HFC	Hybrid Flow Control
HLLE	Harten-Lax-van Leer-Einfeldt
HWB	Hybrid Wing / Body
P_{Ti}	Instantaneous Total Pressure Recovery
IFCPT	Inlet Flow Control and Prediction Technologies
L_{duct}	Diffuser Axial Length
LaRC	Langley Research Center
LES	Large Eddy Simulation
M	Mach Number
M2	AIP Mach Number
MADCAP	Modular Aerodynamic Design Computational Analysis Process
MPR	Multiple per Revolution (Number of Equivalent Low-Pressure Regions)
N2	Tunnel Compressor Speed [rpm]
OEW	Operating Empty Weight
P_0	Ambient Pressure
P_{ref}	Reference Pressure

P_T	Total Pressure
P_{T0}	Tunnel Total Pressure
P_{T2}	AIP Face-Average Total Pressure
$PT_{2\ i\ rms}$	rms of an Individual Dynamic Pressure Signal
P_{Tss}	Steady-state Total Pressure
PAV	Equivalent Low-Pressure Region
PIV	Particle Image Velocimetry
PK	Peak
RANS	Reynolds Averaged Navier-Stokes
RSM	Response Surface Model
SA	Spalart-Allmaras
SARC	Spalart-Allmaras with rotation correction
SFC	Specific Fuel Consumption
SLA	Stereolithography
SS	Steady State
SST	Shear-Stress-Transport
St	Strouhal Number ($=f\ \zeta\ /\ U_j$)
T_T	Total Temperature
TRL	Technology Readiness Level
$TURB_i$	Turbulence (per Probe)
U	Streamwise Velocity
U*	Time-Averaged Streamwise Velocity
ΔU	Streamwise Velocity Difference Relative to the Baseline
Uj	Average Synthetic Jet Velocity During Expulsion Cycle
U_0	Freestream Velocity
V	Vertical Velocity Component
V*	Time-Averaged Vertical Velocity
W2	AIP Mass Flow Rate [pps]
W2c	Corrected AIP Mass Flow Rate [pps]
x	Streamwise Direction
y	Vertical Direction
z	Spanwise Direction
ζ	Disk Displacement Amplitude

Inlet Flow Control and Prediction Technologies for Embedded Propulsion Systems (IFCPT) Program Final Report

Summary

Fail-safe, hybrid flow control (HFC) may be an enabling technology for meeting high-speed cruise efficiency, low noise signature, and reduced fuel burn goals for future HWB aircraft with embedded engines. The objectives of the Boeing IFCPT program were to develop flow-control technologies for highly integrated, offset inlets, as well as, to develop and improve novel test methods and validated tools for predicting active HFC effectiveness in managing inlet pressure distortion. The approach to accomplish the objectives encompasses experimental investigations of flow-control devices conducted in combination with numerical simulations incorporating robust flow-control-device modeling and advanced Computational Fluid Dynamics (CFD) tools.

In support of the program objective to develop flow-control technologies, flow-control devices, including 2nd Generation, hybrid, flow-control devices that produce favorable mean-flow structures, which lower steady-state distortion in BLI inlets without adversely influencing total-pressure recovery were developed. The 2nd Gen HFC system implemented here produced only a small reduction in dynamic distortion over the steady-state value due to the operating frequency. However, results indicated that operating the synthetic jets with a cycle time of approximately 1/revolution of the engine fan would reduce dynamic distortion. In addition, vehicle-level performance benefits of a 2nd generation, HFC system, which uses synthetic jets in lieu of microjets, and therefore, requires no bleed-air extractions, were quantified.

In support of the program objective to improve and validate tools and test methods for predicting active, hybrid flow-control performance, new test techniques for evaluating BLI-inlet flow-control technologies were developed through this program. The ability to generate a BLI-like inlet-entrance flow in a direct-connect, wind-tunnel facility was developed and successfully demonstrated. In addition, the use of D-optimal, statistically designed experiments was successfully demonstrated, which enabled interpretation and implementation of the test results. The use of response surface methodology allowed geometric and aerodynamic factors to be identified which had statistical significance in influencing the AIP aerodynamic performance, and subsequently allowed design guidelines to be formulated.

In addition to advances in experimental test techniques, numerical analysis tools and methods were also improved and validated. Reynolds-Averaged Navier-Stokes CFD, as implemented here using BCFD, was successful in simulating the steady-state flow physics, including the basic flow in the diffuser, as well as, that created by the flow-control devices. A mathematical model representing the flow exiting a synthetic-jet was formulated using experimental data obtained through statistically designed experiments. The model was implemented as a wall boundary condition for CFD. Finally, numerical methods were employed in a ground-breaking attempt to directly simulate dynamic distortion. However, shortfalls were found with the ability of Direct-Eddy Simulation CFD to simulate the turbulent flow structure responsible for producing dynamic distortion.

This program had two key objectives. The first was to develop fail-safe, flow-control technologies for highly-integrated offset inlets to move towards “N+2” project goals. The second was to develop and improve novel test methods and validate tools for predicting active hybrid flow-control effectiveness in managing inlet pressure distortion. Through results from this

program, a 2nd-generation HFC technology was developed that could enable improved inlet performance in future HWB vehicles with highly integrated inlets and embedded engines without adversely affecting vehicle performance. In addition, validated computational tools were developed to improve system trades for advanced inlet concepts. These prediction capabilities are applicable to a range of subsonic, fixed-wing aircraft, and validated for advanced HWB vehicles. The tools enable improved accuracy in predicting active hybrid flow-control-system effectiveness in controlling BLI-inlet total-pressure distortion at flight conditions. The advances in inlet technologies and prediction tools accomplished in this program will help to obtain high-speed cruise efficiency and low-noise signature and fuel burn while reducing field lengths for future HWB aircraft.

Introduction

This document reports on the goals, objectives, and results of the Inlet Flow Control and Prediction Technologies (IFCPT) program, which was conducted during Fiscal Years 2008, 2009, and 2010 for an element of the NASA AMRD Fundamental Aeronautics program effort, Appendix A.2, Topic A.2.4.2 – Integrated Embedded Propulsion Systems. This work focuses on developing prediction tools for innovative aeronautical technologies for Hybrid Wing / Body (HWB) aircraft configurations.

Background

Major advancements beyond current technologies are needed to obtain high-speed cruise efficiency and low noise while reducing field lengths for HWB aircraft. The use of embedded turbofan engines in this HWB aircraft, Figure 1, is being studied as a means to attain both high-speed cruise efficiency and low-noise signature and fuel burn. Boeing is advancing both inlet technologies and prediction tools specifically focused at lowering and managing flow distortion using fail-safe, hybrid flow-control technologies. The investigations are to advance prediction methods for inlet flows by applying designed experiments using integrated Computational Fluid Dynamics (CFD) and tests to establish a database in a relevant environment and validate the methods.

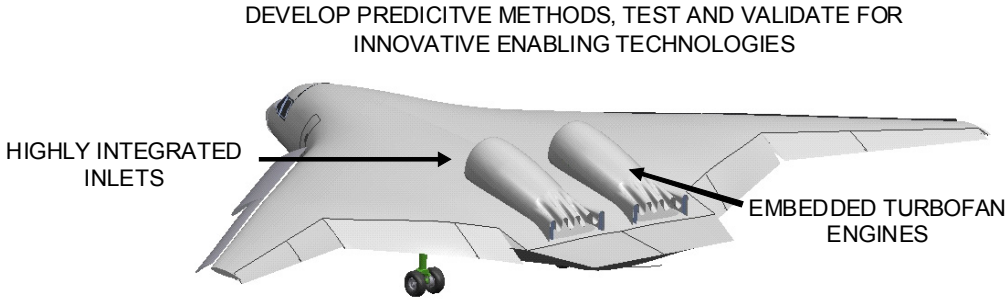

Figure 1. "N+2" Next Generation HWB Aircraft

This program supported the NASA Fundamental Aeronautics Program goal to pursue long-term, cutting-edge research in all flight regimes to produce data, knowledge, and design tools that are applicable across a broad range of vehicles by applying fail-safe hybrid flow-control technologies to manage flow distortion, thereby attaining both high-speed cruise efficiency and low-noise signature. Furthermore, The Boeing Company worked in collaboration with NASA Glenn Research Center (GRC), Georgia Institute of Technology (GaTech), and SynGenics Corporation to extend the current state-of-the-art in active, hybrid flow control analytical design tools. Hybrid flow control analytical design tools have been validated through component-level testing, in an environment relative to embedded inlets of future-generation, HWB aircraft designs. This not only supported the aforementioned strategic goal, but led directly to the strategic outcome of developing multidisciplinary design, analysis, and optimization capabilities.

Although the use of highly integrated, aft, surface-mounted inlets with embedded engines in HWB aircraft provides a means to meet future efficiency, performance, and noise goals, it presents significant challenges in meeting inlet performance goals. For instance, surface-mounting inlets, in the aft section of the vehicle places the inlets in a transonic-flow region where the approach boundary layer thickness approximates one-third of the aperture height,

which is ingested by the inlet, resulting in low total-pressure recovery, Figure 2. In addition, embedded engine designs require the integration of compact diffusers with L_{duct}/D_{eng} on the order of 1.7 and offsets of approximately a full engine diameter. These compact, highly offset diffusers produce internal flows with adverse pressure gradients that can cause flow separation, as well as, secondary flows that adversely affect flow angles and create large regions of low-pressure flow at the AIP, both of which contribute to engine operability challenges in terms of total-pressure distortion and swirl distortion.

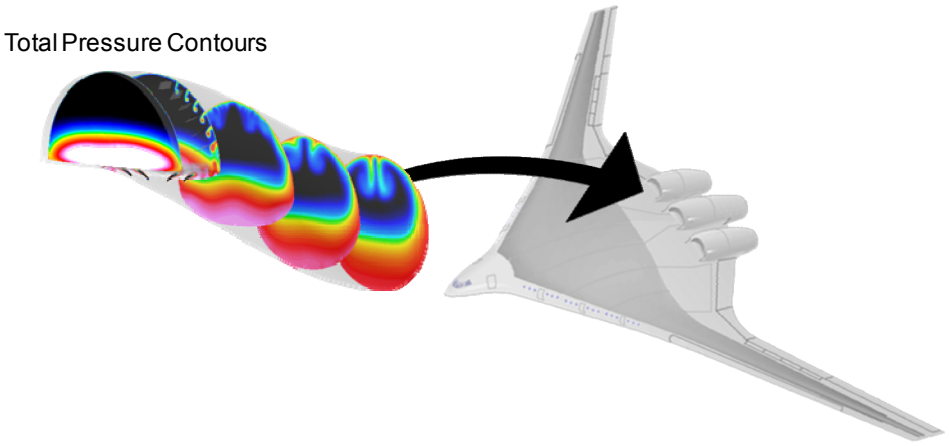

Figure 2. BLI Inlet Diffuser Total Pressure Contours

Flow-control devices have been employed to mitigate inlet operability challenges. To mitigate the operability challenges of a BLI-inlet duct, flow-control devices have been used to create vortical flow in offset diffusers, which induces secondary flow motion that helps to distribute concentrated regions of low-pressure flow by pulling it toward the duct sides, Figure 3. Specifically, discrete votices from individual microvanes coalesce to form large-scale, counter-rotating vortices, which can redistribute the low-pressure flow around the duct.

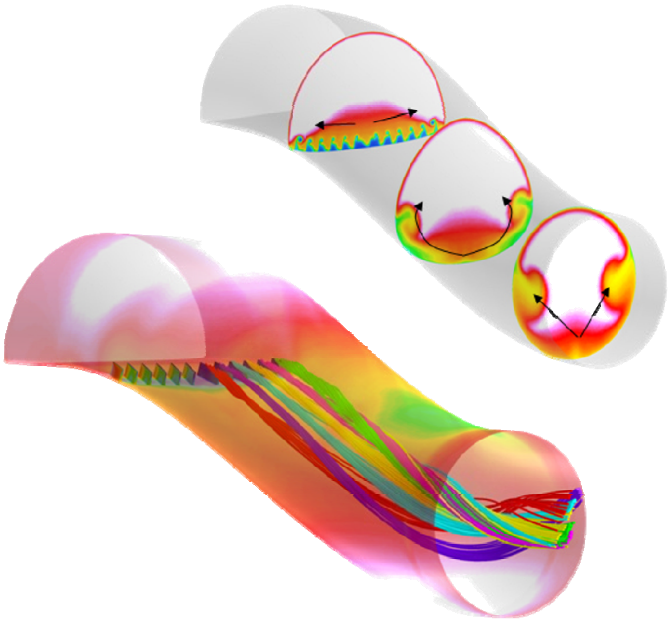

Figure 3. Flow Physics of Microvane Flow Control in an Offset Duct

Scope

The Boeing program, as depicted in Figure 4, combined technological advances made at NASA GRC in robust modeling of flow-control systems with advances in flow-control device modeling and testing at Boeing and GaTech. The combination of testing and numerical simulation, integrated with robust design methods from SynGenics, made it possible to improve and validate current, state-of-the-art prediction tools necessary to quantify the benefits and optimize the design of flow-control systems in advanced inlets. In collaboration with GRC, the Boeing-led team designed experiments where data from test and CFD were used to produce response surfaces representing performance of inlet flow-control-system-design features to arrive at a proof of concept and demonstrate the physics of a hybrid system in a laboratory environment, Technology Readiness Level (TRL) of 3-4, at the completion of the 3-year program. This technology base formed the foundation on which a hybrid system was designed.

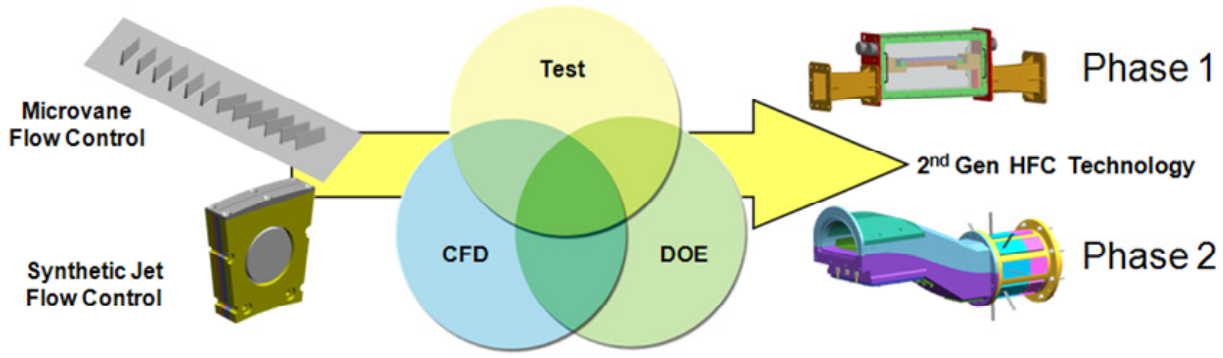

Figure 4. Approach to Improve and Validate Numerical Analysis Tools and Develop Advanced Hybrid Active Flow-control system for Improved Performance, Reduced Weight, and Reduced Emissions

Boeing has been conducting research on an earlier variation of a hybrid flow-control system for an inlet. This earlier system combines passive microvanes and active microjets into an integrated hybrid system. The passive microvanes ensure flight-critical engine operability, while the active microjets provide flight-mission operability. With this earlier hybrid flow-control technology, a failure in the active flow control elements of the system places no operability demands on the engine's compression system because of the presence of the passive flow control element. Hence, the risk of compromising a mission or a vehicle would be substantially reduced using a hybrid flow-control system in comparison to relying on an active, inlet-flow-control system with microjets alone. As a result, the development time and risk for introducing this new technology into an operational vehicle would be significantly reduced compared to that of a system relying solely on active flow control to provide flight-critical operation.

Hybrid flow control has been demonstrated to be a more effective tool in reducing BLI inlet total-pressure distortion than steady jet or vane flow control alone (Owens, Allan, & Gorton, 2006). Various steady-jet configurations and a fixed vane configuration were investigated independently and as a 1st generation hybrid system. The use of steady jets resulted in significant distortion reductions but with the penalty of requiring up to 2.5% of the inlet mass flow in bleed-air extractions. Vanes were also proven effective at reducing distortion at high mass flows but ineffective at low mass flows. However, a hybrid system, comprising inlet vanes and steady jets, was shown to be a more effective and efficient system in that it maintained low circumferential distortion levels across the full range of inlet operating mass-flow rates, with

reduced jet mass flow requirements. Nevertheless, even the hybrid system required up to 0.5% inlet mass flow to provide the desired distortion reduction.

The 2nd generation hybrid flow-control system under development in this program extends substantially beyond previous systems. Here the hybrid system is composed of microvanes and synthetic jets integrated into the inlet offset diffuser, Figure 5. Microvanes were selected for this study based on their proven effectiveness in controlling secondary flows in offset diffuser designs required for HWB aircraft with embedded engines. Furthermore, the use of synthetic jets, in lieu of microjets, results in less fuel burn, because no bleed-air extractions are used with synthetic jets. The fact that bleed air ducting and control systems are not needed in this approach facilitates system level benefits.

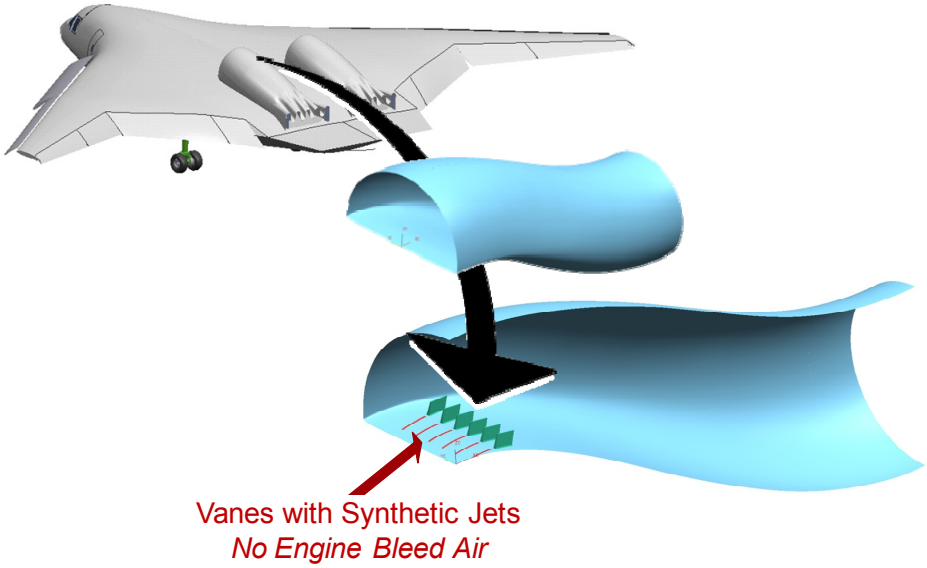

Figure 5. Integrated Microvane/Synthetic Jet Inlet Hybrid Flow-control system

Objectives

This program had two key objectives. The first was to develop fail-safe, flow-control technologies for highly-integrated offset inlets to move towards "N+2" project goals. The second was to develop and improve novel test methods and validate tools for predicting active hybrid flow-control effectiveness in managing inlet pressure distortion. Through results from this program, validated computational tools are available to improve system trades for advanced inlet concepts. The prediction capabilities are applicable to a range of subsonic, fixed-wing aircraft, and validated for advanced HWB vehicles. The tools enable accurate prediction of active hybrid flow-control-system effectiveness in controlling inlet total-pressure distortion at conditions relevant to flight.

The objectives were accomplished in two phases. In Phase 1, passive, active, and hybrid flow-control devices were used to alter boundary-layer characteristics for improved resistance to separation in the presence of an adverse pressure gradient. CFD was employed in combination with experimental testing to characterize the flow physics of flow-control devices. CFD-based analysis tools for the simulation of active hybrid flow-control devices were developed and validated against test data. The Phase 1 work was completed in Fiscal Year 2008.

The Phase 2 program was conducted during Fiscal Years 2009 and 2010. During Phase 2, the flow physics that govern the interaction between passive and active components of hybrid flow-

control devices was investigated. The influence of flow control on inlet performance in an offset duct was quantified, and a system-level assessment of the benefits of inlet hybrid flow control in a HWB configuration was conducted. CFD-based tools developed in Phase 1 were expanded to simulate active, hybrid flow control in an offset duct and validated against test data, and progress was made toward accurately predicting dynamic distortion in an offset, BLI diffuser.

Procedures

Experimental investigations, robust modeling, and numerical simulations comprise the approach employed to accomplish the program objectives. During Phase 1, experimental investigations were conducted in a 2-D test section of a wind tunnel where the contoured surface was designed to mimic the adverse pressure gradient in an offset diffuser of an advanced HWB vehicle. Flow-control hardware was integrated into the duct wall and used to develop test techniques and evaluate the effectiveness of passive, active, and hybrid flow-control devices in improving boundary-layer characteristics. Detailed flow diagnostics, including high-magnification particle image velocimetry (PIV), were employed to develop an understanding of the flow physics associated with the flow-control actuators. These measurements were used to identify flow control configurations that would be effective for controlling secondary flows and flow separation in an offset diffuser, as well as, to validate advanced, numerical modeling tools. Response surface model (RSM) approaches were applied, in conjunction with CFD methods, to simulate the local flow properties of synthetic-jet actuators.

Phase 2 built on the accomplishments of Phase 1 by characterizing the interaction between passive and active flow-control devices, demonstrating performance benefits of hybrid flow-control devices in an offset diffuser, and developing and validating CFD-based analysis tools for the simulation of hybrid flow-control devices. Benefits of hybrid-inlet-flow control were assessed in terms of both inlet performance improvements and vehicle system integration. Response surfaces derived from the flow-control performance database were used to develop design guidelines for flow-control actuators. In addition, the experimental database provides details to understand the complex physics of flow control and supports development of numerical modeling techniques.

In addition, experimental techniques were developed and applied to characterize the flow resulting from flow-control actuators. Results of the experiments were used to validate and improve CFD capabilities. Validated CFD tools were employed to assess the baseline and actuated flow in a Boundary-Layer-Ingesting (BLI) inlet diffuser. In addition, CFD simulations of an offset BLI-inlet diffuser were conducted in order to assess the capability of using Hybrid-RANS / LES-CFD for predicting dynamic pressure distortion. The design and fabrication of an offset diffuser was completed. The diffuser was used to measure the effects of flow-control technologies on inlet distortion and recovery in a BLI-inlet diffuser at the GaTech Fluid Mechanics Research Laboratory (FMRL) transonic facility.

Experimental Procedures

The experimental approach to this investigation comprises the design and testing of various passive, active, and hybrid flow-control approaches in laboratory environments designed to simulate the flowfield in a BLI-inlet. Quantitative and qualitative measurement techniques were applied to evaluate the performance of devices. A 2-D, converging-diverging test-section was used to assess local interactions of surface-mounted devices with the cross flow, and a 5%-scale, offset diffuser model was employed to test multiple devices and assess their impact on BLI-inlet performance.

Wind Tunnel Facility

The experimental investigations conducted under this program were performed in the GaTech FMRL transonic facility, shown schematically in Figure 6a. This facility is an open-return, pull-

down wind tunnel. The tunnel uses a 150 hp inverter duty motor capable of pulling 215.9 cm (85 in) of water (gage) to reach test section speeds of M = 0.73. The motor speed is controllable to within 0.005% of maximum speed, and a 60-ton, air-cooled hermetic scroll, liquid chiller, coupled with an ultra low-pressure drop heat exchanger maintains ambient room temperature.

The test section has a 5in x 5in (12.7cm × 12.7cm) cross-section with a length of 2 ft (60.96cm), shown in Figure 6b. The normally flat, upper wall of the test section was contoured for the present study to create a pressure gradient consistent with that in a HWB vehicle inlet. Specifically, the flat, upper wall was replaced with a converging-diverging (C-D) profile, shown in Figure 6*c*. The profiled wall was designed to produce an adverse pressure gradient of d(ps/pinf)/dx ≈ 0.38, which is consistent with pressure gradients in diffusers of HWB vehicles.

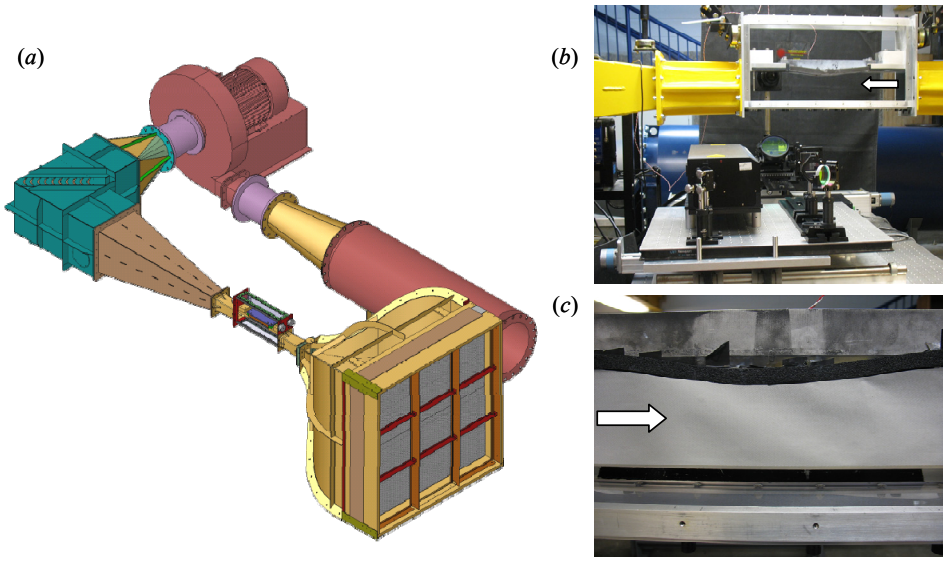

Figure 6. (a) The Transonic Wind Tunnel, Test Section and (b) PIV Optical Setup, and (c) Profiled Upper Wall of the Test Section.

Diagnostics employed to assess flow-control performance in the 2-D duct included qualitative and quantitative techniques. Qualitative assessments of flow structures resulting from flow-control actuation were obtained through the use of oil surface-flow visualization. The visualization oil was a mixture of linseed oil and titanium dioxide paint. Quantitative measurements included high-resolution, high-speed PIV measurements at multiple cross-stream planes of the flowfield. The PIV optical setup, Figure 6b, included synchronized, computer-controlled, motorized motion of all the optics and the laser, along the test section axial direction and additional motorized motion of the PIV camera in the cross-stream direction. The PIV field of view measured 0.67in (17mm) on the side and the magnification was 6.7×10^{-4} in/pixel (17 μm/pixel). The PIV measurement stations are shown in Figure 7. Near-field measurements were taken at centerspan, where the PIV view is comprised of four, partially overlapping streamwise fields. Far-field measurements were taken at x/δ_{apex}= 42 downstream of the aft edge of the microramp, at cross-stream planes 0.039in (1mm) apart.

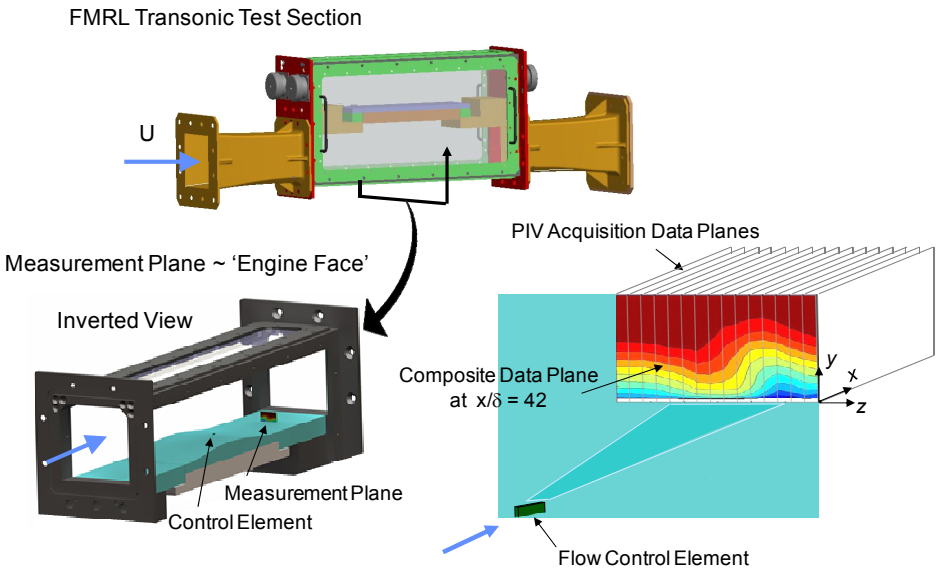

Figure 7. FMRL Tunnel 2-D Test Section Data Measurement Planes

Offset Diffuser

In addition to the 2-D test section, flow control device testing was conducted in an offset duct consistent with future HWB vehicles. The 5%-scale duct model, Figure 8, replaced the 2-D test section in the GaTech FMRL and utilized the existing upstream contraction and down stream diffuser. The FMRL transonic wind tunnel provided airflow requirements for the duct. In order to account for the diffuser offset and slightly longer overall length of the assembly, the contraction was moved approximately 2.5in downstream and approximately 5.2in to one side. This, along with the adjustability of the support struts suspending the tunnel, was sufficient to mate the new hardware to the existing hardware.

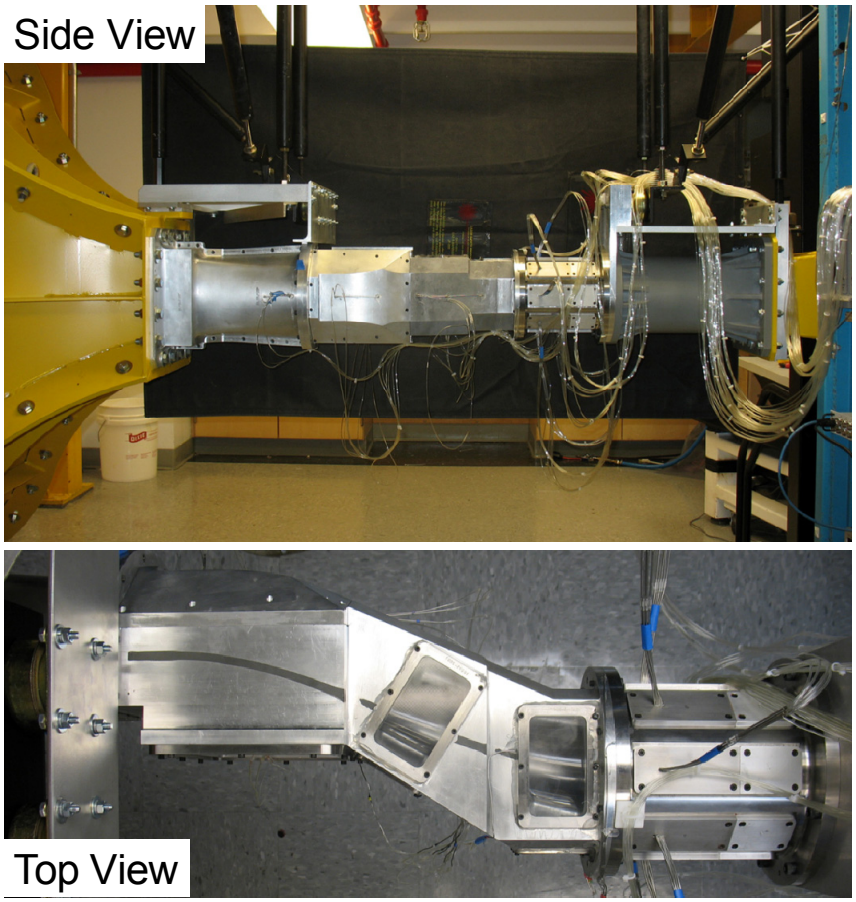

Figure 8. Offset Duct 5%-Scale Model

The offset duct model consisted of a forward adapter, S-duct, AIP total pressure rake assembly, and aft adapter, Figure 9. The diffuser-assembly moldline was defined based on the BWB diffuser moldline at 5% scale. The forward adapter served as the transition between the existing facility contraction and the offset duct. It contained the mounting assembly for a boundary-layer fence, Figure 10. The duct model was designed with a removable insert in the lower surface for installing flow-control devices. Two sets of contoured windows were incorporated into the design to facilitate the acquisition of PIV data. Three hot-wire installation locations were also included near the duct throat. The duct assembly terminated with the aft adapter, which served to mate the AIP to the existing facility expansion section.

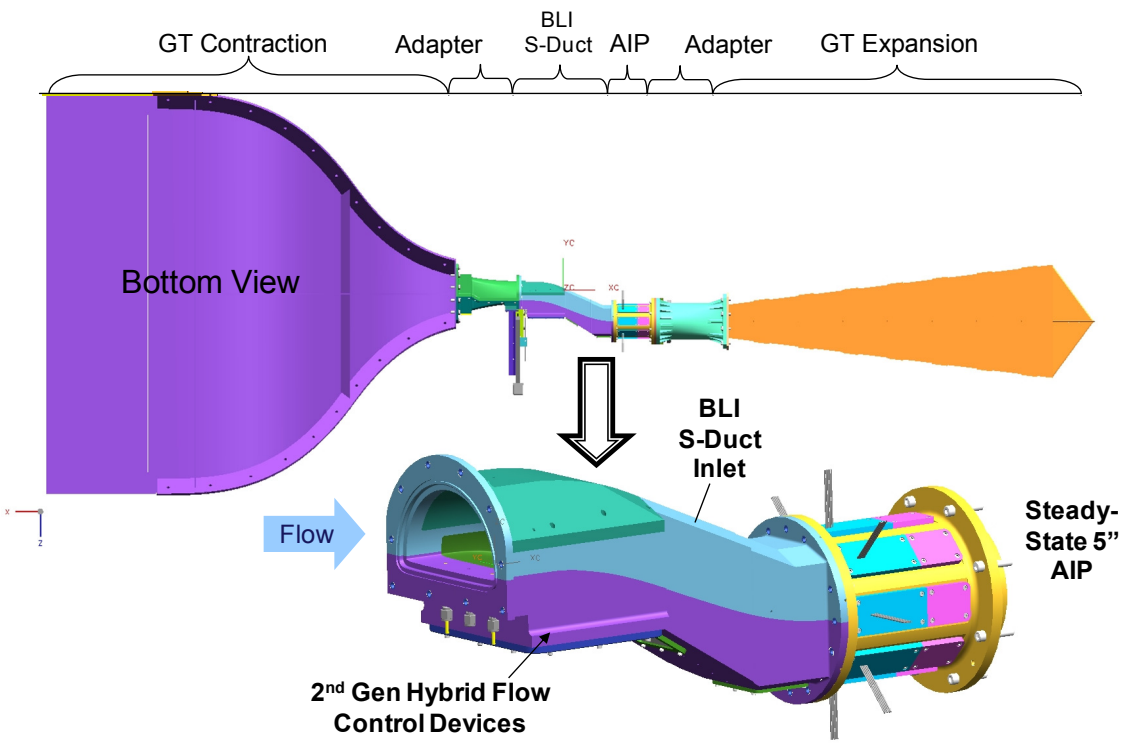

Figure 9. BLI Offset Diffuser Model

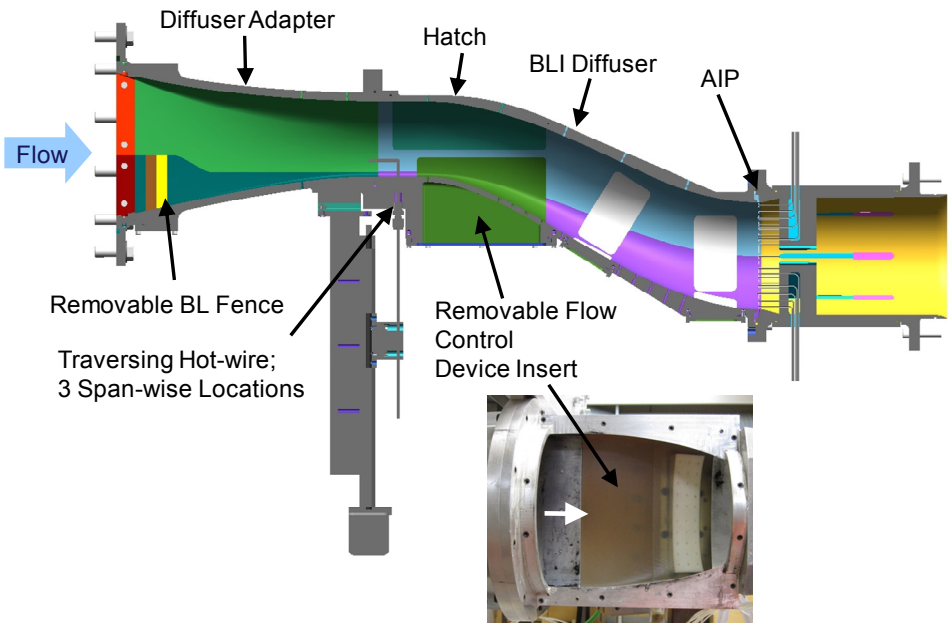

Figure 10. Offset Diffuser Model Details

Instrumentation on the model included twenty-one static-pressure taps distributed about the inner-moldline surface. In addition to the static taps, the model included a steady-state, total-pressure rake assembly, Figure 11, which consisted of eight equiangularly spaced rakes around the circumference of the AIP. Each rake contained five total pressure probes located at the

centers of equal areas. The rake assembly was designed such that the eight rakes would be interchangeable with dynamic-total-pressure rakes for the acquisition of dynamic distortion data. The model mass flow was computed based on the Mach number computed at the AIP using the static and total pressure instrumentation. Flow through the offset duct was controlled using the facility compressor. Model drawings and tap locations are located in Appendix A and dynamic data reduction equations are located in Appendix B.

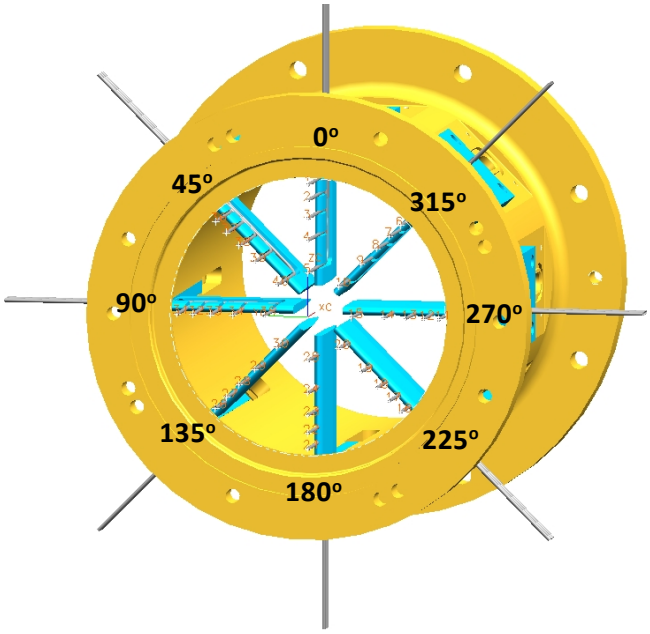

Figure 11. AIP Total-Pressure Rake Assembly

Boundary-Layer Fence

A representative BLI-inlet approach flowfield was established in the offset diffuser by installing a honeycomb fence in the model. The multilayer, 2.5in tall fence was placed upstream of the diffuser throat to generate a momentum deficit in the lower region of the duct. The composite, honeycomb boundary-layer fence, Figure 12, employed toe-in turning and mesh-induced momentum deficit generation to simulate a BLI inlet diffuser flowfield. The momentum deficit was realized by a gradual decrease in size of the cells toward the wall, combined with the profiled extension in length of the cells. Both of which produced a representative boundary-layer profile with a continuously increasing deficit from the freestream to the wall. The toe-in was varied across the span such that there was more aggressive flow turning at the side boundaries that weakened toward the central plane. This was done to be consistent with an integrated BLI inlet (Owens, Allan, & Gorton, 2006), where the flow turning is most pronounced near the corner where the cowl intersects the airframe. The offset duct with the fence installed was adopted as the baseline duct configuration for experiments within this study. The offset diffuser in the absence of the boundary layer fence was denoted as the clean duct.

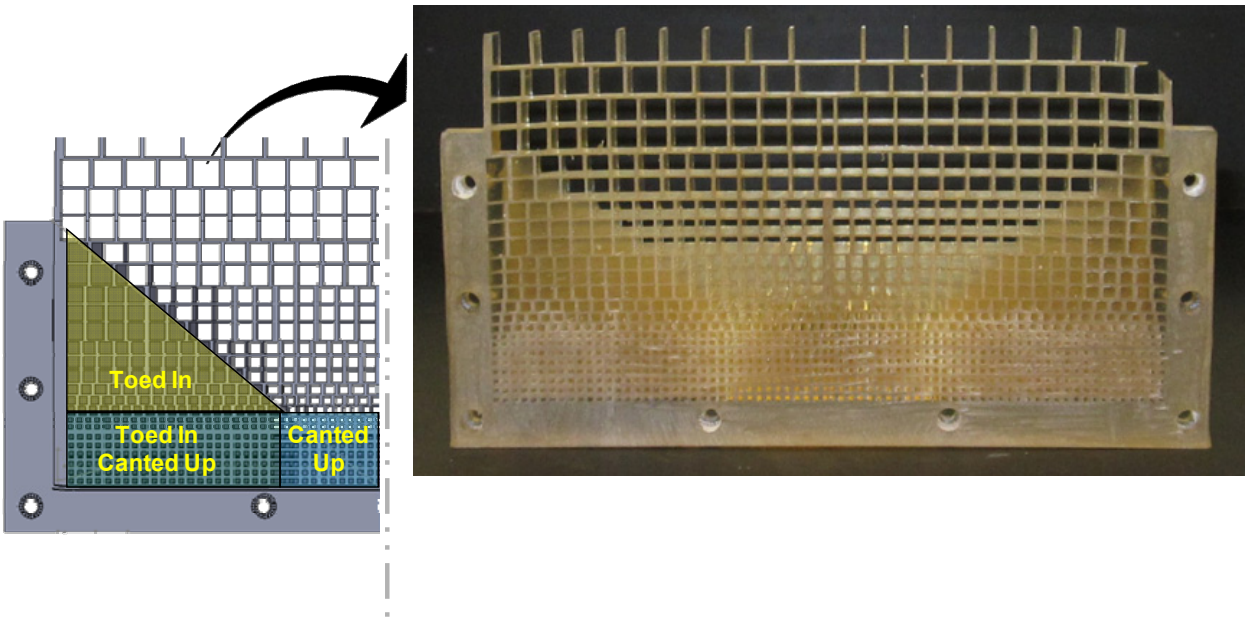

Figure 12. A honeycomb fence designed for boundary layer manipulation.

Flow-control devices

Passive, active, and hybrid flow-control devices were employed in this study. The passive devices included both microramps and microvanes. The active devices included steady-jet, piezoelectric synthetic-jet, and piston-driven synthetic jet. Hybrid devices were comprised of coupled passive and active synthetic flow-control device.

The sizing guidelines used to design the passive devices tested in the 2-D test secton were based on design guidelines presented in the statistically designed studies by Anderson et al. (2004, 2006). The characteristic scaling of the passive devices was defined in terms of local boundary layer thickness, δ. The microramp, Figure 13, measured 0.51 δ high, 3 δ wide, and 3.4 δ long, and had a half angle of 24°. The microvane, Figure 14, was designed with a rectangular planform measuring 0.25 δ in height and 2.56 δ in the length. It was oriented at an angle of 8°, relative to the duct centerline.

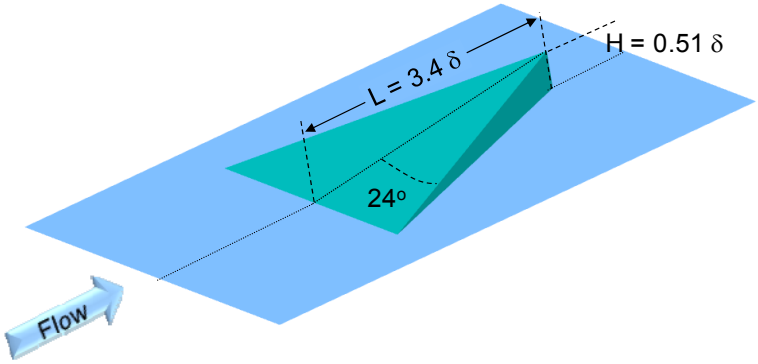

Figure 13. Microramp Definition for Testing in the 2-D Tunnel

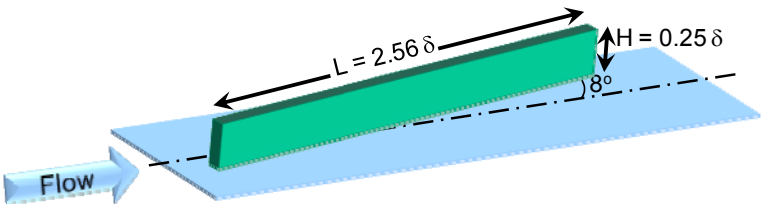

Figure 14. Microvane Definition for Testing in the 2-D Tunnel

In addition to passive devices, active devices were employed in this study. The piezoelectric synthetic-jet actuator used for active boundary layer control in the 2-D test section was developed and built at Georgia Tech, along with the necessary driving electronics. The synthetic-jet orifice, shown in Figure 15 measured 0.98in (25mm) long by 0.02in (0.5mm) wide and operated within the range of 1 to 2.5 kHz.

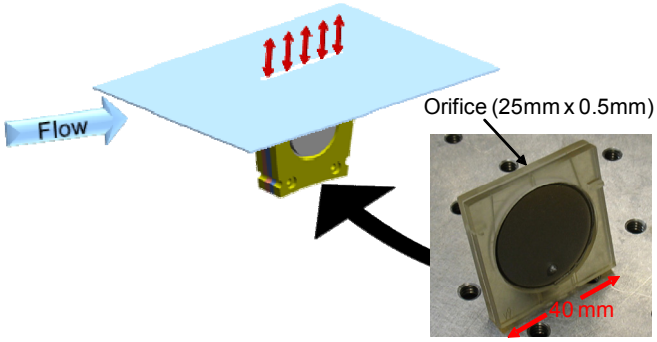

Figure 15. GT Synthetic-jet actuator

Passive (microvane or microramp) and active (synthetic-jet) flow-control elements tested in the 2-D test section were surface mounted near the apex (the maximum height of the convergent-divergent wall) of the C-D test-section. Schematic descriptions of devices are shown in Figure 16, where the streamwise position was measured relative to the wall apex.

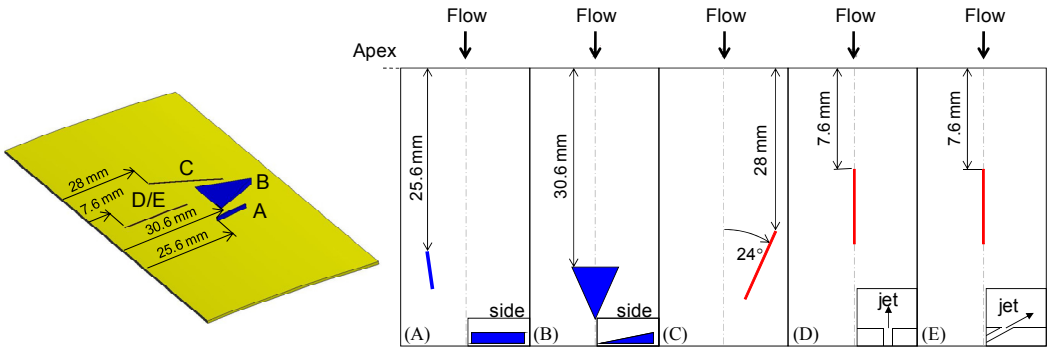

Figure 16. Flow-Control Element Configurations: a) Microvane, b) Microramp, c) Slanted Synthetic Jet, d) Streamwise Synthetic Jet, e)Skewed Synthetic Jet

Hybrid flow-control actuators were also tested in the 2-D test section. The hybrid flow-control configurations included a passive microramp or microvane with an active, synthetic jet. In the

microramp hybrid devices, the microramp was located such that its leading edge was aligned in the spanwise direction and was 1.2in (30.6mm) downstream from the location of the wall apex. The leading edge of the streamwise-oriented, synthetic jet orifice was 0.3in (7.6mm) downstream from the wall apex. The streamwise-aligned jet was located along the microramp centerline, 0.31in (8mm) upstream of the microramp, Figure 17. In the microvane hybrid configurations, the synthetic jet was slanted at the same angle as the microvane and skewed to blow at 45° in the spanwise direction, Figure 18.

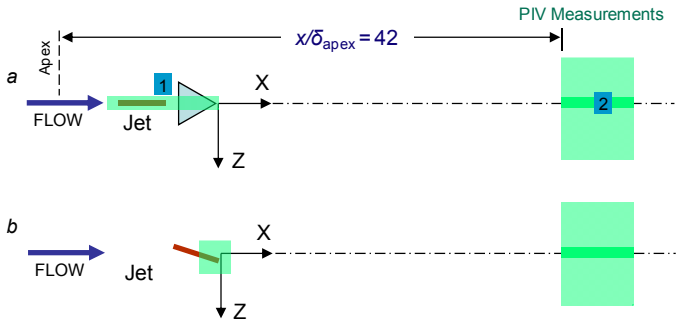

Figure 17. Schematics of the Three PIV Measurement Domains for the (a) Hybrid Flow Control, (b) Slanted-Jet Active Flow Control

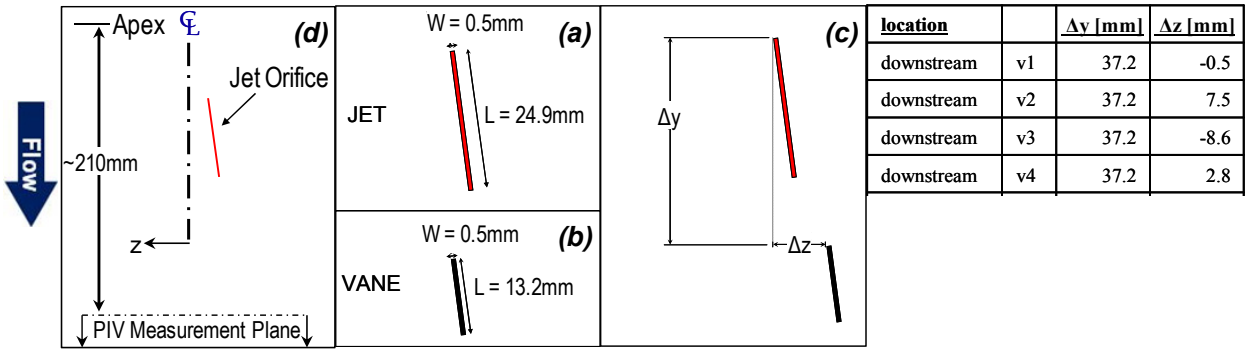

location		Δy [mm]	Δz [mm]
downstream	v1	37.2	-0.5
downstream	v2	37.2	7.5
downstream	v3	37.2	-8.6
downstream	v4	37.2	2.8

Figure 18. (a) Synthetic Jet and (b) Microvane Dimensions and (c) Relative Spacing. (d) Location and Orientation of PIV Measuring Station. (Flow from top to bottom of page.)

Passive, active, and hybrid devices were also tested in the offset duct, Figure 19. Passive devices included a number of microvane array configurations. Design parameters for the microvanes were derived from previous work on BLI inlet ducts (Owens, Allan, & Gorton, 2006). The microvanes in the arrays were all oriented at a fixed angle of 12.9° relative to the duct centerline. All microvanes had a thickness of 0.075in (1.9mm) at the hub that tapered to 0.025in (0.6mm) at the tip. Various microvane heights, as well as, axial locations and spanwise densities were tested as defined through a statistically designed experiment, discussed later.

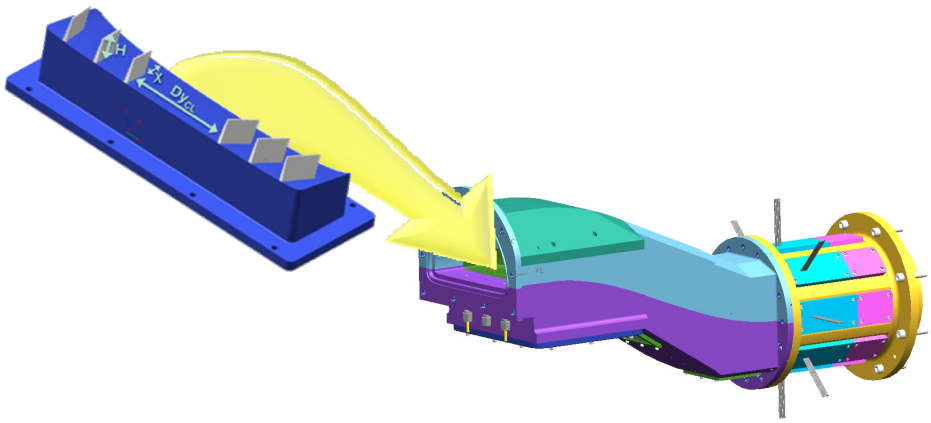

Figure 19. Microvane Definition for Testing in the Offset Duct

Active flow actuation was applied in the offset duct through the use of piston-driven, synthetic-jet actuators, Figure 20, developed under this study. The actuator was comprised of three pistons, synchronously driven, to generate expulsion and suction cycles through skewed-jet orifices, which symmetrically pointed outward of the central plane. The synthetic jets were operated harmonically, at variable frequencies of up to 133 Hz. The flow control insert was manufactured using Stereolithography (SLA) prototyping, and was split into two components so that the upstream part could be replaced independently of the rest of the structure, Figure 21.

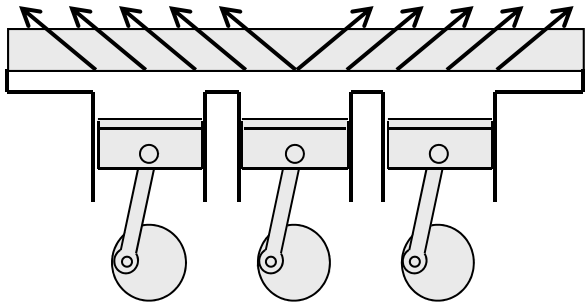

Figure 20. Schematics of the Synthetic Jet Modules.

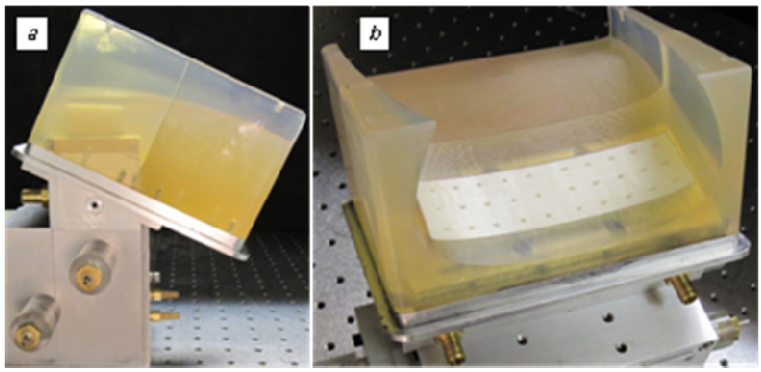

Figure 21. Power synthetic jet modules integrated into the control insert (a) and jet orifice plate (b)

The flow control insert body and actuator module mated at an aluminum module cover plate. The orifice plate was mounted onto the aluminum cover plate, Figure 21a. The orifice plate was made out of SLA to match the moldline of the s-duct. The model allowed for different jet

configurations to be integrated by replacing the jet orifice plates. The model allowed for passive flow-control devices to be installed in the upstream insert in any location or pattern, independent of the downstream, jet-populated insert. Thereby, configurations utilizing only active or hybrid control could be installed by mounting either a solid or a vane-populated upstream insert, respectively.

Two types of hybrid devices were tested in the offset duct, one in which the active component was steady jets, and one in which it was piston-driven synthetic jets. The passive component in all the hybrid configurations tested in the offset duct was the microvane array selected from the microvane DOE study. The selected array contained 6 microvanes oriented at an angle of 12.9° with respect to the duct centerline. The height of the microvanes was 25% of the boundary-layer height. The length to height ratio of the microvanes was approximately 10. The steady-jets employed in the hybrid configurations were circular, 0.06in (1.5mm) in diameter, and skewed at 45°. Multiple rows of jets were integrated into a control insert with the microvane array, Figure 22. The jet orifices shown in Figure 22 could be individually activated in any pattern, which enabled testing of various actuation configurations.

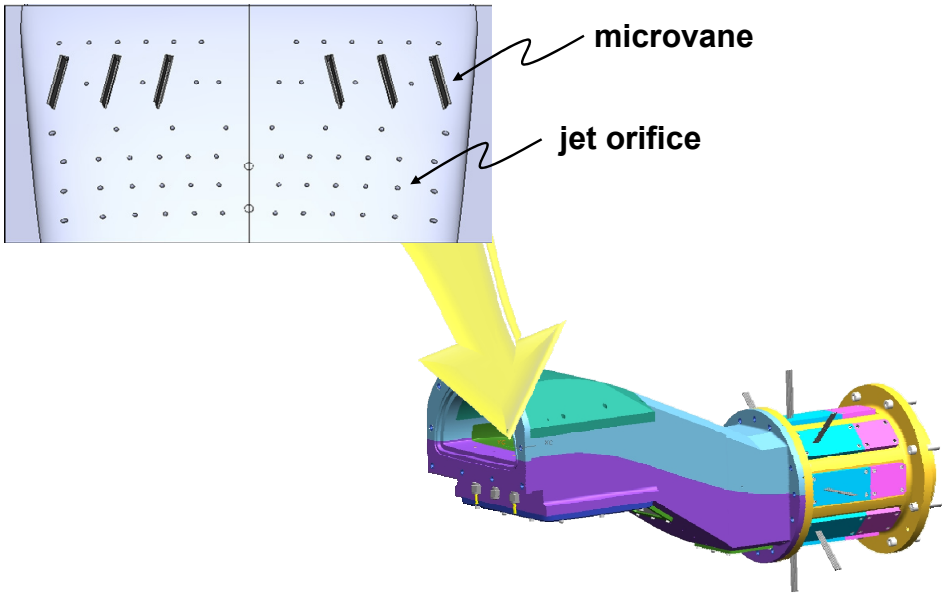

Figure 22. Steady Jet / Microvane Model Insert

The microvane/synthetic jet configuration, Figure 23, included the microvane array selected from the passive DOE study combined with 3 rows of synthetic jets. The piston-driven synthetic jets had hole diameters of 4% to 6% of the boundary layer thickness. The jets were skewed outboard at an angle of 90° to the centerline and slanted upward at an angle of 45° from the surface.

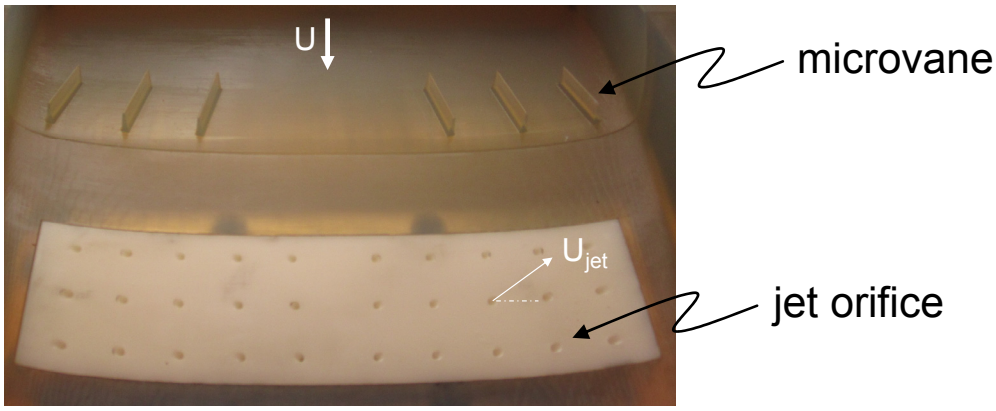

Figure 23. Hybrid Flow Control Configuration Tested in Offset Duct

Simulation Procedures

Code Details, Turbulence Models, BC's and Flow Conditions

The numerical simulations in this study were conducted using the Boeing-developed flow solver, BCFD. BCFD is a derivative of the WIND CFD code, the NPARC Alliance code (Mani, Cary, Ramakrishnan, 2000). BCFD is a Navier-Stokes and Euler flow solver capable of performing steady-state and time-dependent simulations of geometries represented by structured, unstructured, or hybrid grids. BCFD provides several options for turbulence modeling. For the steady-state simulations, both Spalart-Allmaras (SA) (Spalart, Allmaras,1992) and Shear-Stress-Transport (SST) turbulence models were used to close the Reynolds Averaged Navier-Stokes (RANS) equations. For the vast majority of configurations in the present study, the SA turbulence model produced simulations, which exhibited flow-field characteristics more closely matching those measured experimentally. Time-dependent phenomena was simulated using the SA turbulence model with Detached Eddy Simulation (DES) (Travin, Shur, Strelets, Spalart, 2000). In this study, the RANS algorithms used were 2nd order accurate in space, while the DES algorithms were 2nd order accurate in time and space.

In the present study, the no-slip, adiabatic, boundary condition was used to model walls. At inflow boundaries, Mach number, total temperature, total pressure, and flow angularity were prescribed. Constant back pressure was prescribed on outflow boundaries to achieve a desired flow rate.

In order to model synthetic jets, a time-varying boundary velocity component was developed and applied. A response surface model, detailed in Appendix E, based on experimental results was used to create the synthetic-jet boundary condition which, based on input voltage and operating frequency, determined a peak jet velocity. This peak velocity was applied to a modified sine wave to arrive at the instantaneous velocity prescribed at the boundary.

The incoming boundary layer of a BLI inlet was initially simulated in the offset duct by prescribing a total-pressure profile on the inflow boundary. This condition was used for several simulations of the S-duct diffuser, with and without vane flow control. However, with the development of the boundary-layer fence employed in the experimental investigations, a more detailed boundary condition was developed and applied to simulate the BLI-inlet flow generated in the offset duct. Two boundary conditions were required to simulate the fence employed in the experimental test setup. The first boundary condition prescribed a velocity profile representative of a BLI-inlet. The boundary-layer profile shown in Figure 24 was imposed as a boundary

condition in a structured grid, upstream of the duct, in the computational domain. This block was coupled to an unstructured-grid representation of the S-duct to complete the computational mesh.

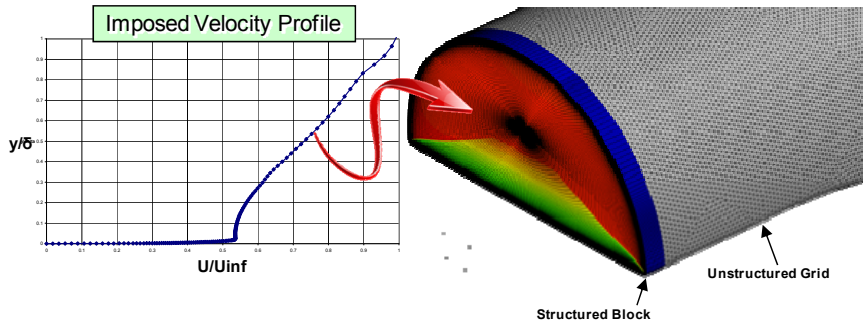

Figure 24. BLI Inlet Simulation Velocity Profile Boundary Condition

The second boundary condition used to enable simulation of the boundary-layer fence consisted of a collection of surfaces bearing a screen boundary condition. This boundary condition models a screen by prescribing the appropriate jump in flow conditions across the discontinuous screen boundary according to Cornell (1958). The fence used in the experiment contained several different sections, which made direct application of the screen boundary condition insufficient to appropriately model the effects of the experimental fence. The separate regions of the fence (Toed In, Toed In Canted Up, and Canted Up) combined with the variable solidity distribution in the streamwise and wall normal directions made it necessary to use several boundaries with different conditions in the computational model. Figure 25 shows the computational boundary modeling the geometry of the downstream side of the boundary-layer fence used in the experiments. The screen boundary is color coded according to the solidity prescribed on that portion of the boundary in the simulation. Additionally, flow angularity of 3° upward canting was prescribed on regions corresponding to the canted up regions in and 32° toe in angularity was prescribed on regions denoted Toed In. In total, 17 surfaces with unique screen boundary specifications were used to model the experimental fence.

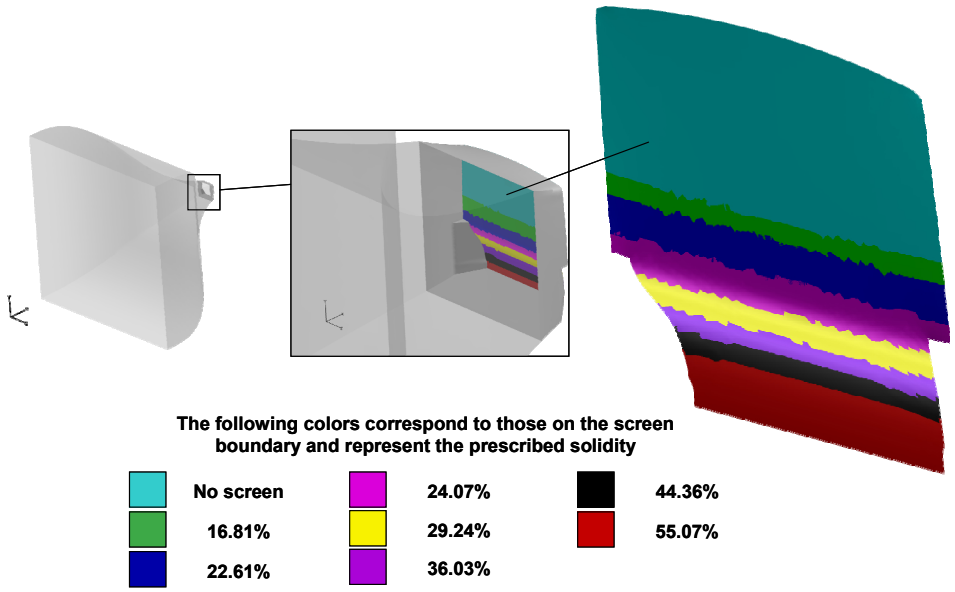

Figure 25. Computational screen boundary colored by solidity

Results and Discussion

This document reports on the results of experimental flow-control technology development studies and improvements in novel test methods and validation tools for predicting flow-control effectiveness in managing inlet total-pressure distortion. Experimentally obtained results showing the local interaction of surface-mounted, passive, active, and hybrid flow-control devices with the cross flow in a 2-D converging-diverging test section in Mach 0.5 flow are presented. Active, passive, and hybrid flow control effectiveness in managing BLI-inlet performance assessed at the AIP of an isolated, offset diffuser in terms of experimentally obtained steady-state and dynamic total-pressure recovery and distortion is also reported. In addition to experimental investigations, numerical tools for predicting flow-control performance in BLI-inlets were improved and validated. Results of numerical simulations of isolated devices in a 2-D, CD tunnel are reported and validated against experimental data, with a focus on the sensitivity of the accuracy of the results to the applied simulation methodology. Results from steady-state and time-accurate simulations of multiple devices in a BLI-inlet diffuser are also reported and compared with experimental data in order to assess and improve steady-state and dynamic distortion prediction capabilities. Finally, results of a system-level assessment of hybrid flow control in HWB vehicles are reported. Specifically, the system-level payoffs and penalties of steady and synthetic jet hybrid flow-control systems were evaluated for an N+2 HWB configuration. Sensitivities to vehicle range were assessed in terms of weight, performance, power extraction, and engine bleed.

Flow Control Technology Development

In the present study, flow-control technologies were designed to enhance the performance of complex, three-dimensional, offset, BLI-inlet ducts in embedded propulsion systems for HWB-aircraft configurations. The actuators investigated ranged from simple, passive devices to more complex, hybrid devices. Hybrid devices comprise passive and active devices combined such that flight-critical operability would be maintained even if the active element of the flow-control system failed. It is anticipated that this actuation approach will lead to highly effective performance enhancements of embedded propulsion systems with minimal system-level penalties in terms of weight, power consumption, robustness and maintenance. Furthermore, unlike conventional fluidic flow control approaches, synthetic-jet actuation does not rely on a supply of bleed air (e.g., from the engine) or on suction and thereby, obviates the need for complex fluidic plumbing and integration.

In the present study, flow-control devices were evaluated in terms of how they altered local boundary-layer characteristics and flow features, as well as, their effectiveness in managing BLI-inlet total-pressure distortion. Integrated experimental and numerical investigations were conducted using statistically designed experiments and response-surface analyses not only to advance flow-control technology development, but to improve and validate numerical methods as well, including the prediction of dynamic distortion in a BLI offset duct, for the design and assessment of flow control in future HWB vehicles.

Characterization of Flow-Control-Device Physics

In support of the program objective to develop flow-control technologies, the local interaction of surface-mounted, passive, active, and hybrid flow-control devices with the cross flow was examined. The evolution of streamwise vortices induced by flow control was investigated in an adverse pressure gradient that mimiced the pressure gradient within a diffuser compatible with future HWB vehicles. Counter-rotating vortex pairs and single-sense vortices were formed and

characterized using passive microramps and microvanes, respectively. Similar streamwise vortices were also generated using synthetic-jet actuators. The jets had rectangular orifices that were slanted and/or skewed to produce single-sense vortices or streamwise aligned to produce vortex pairs. Finally, flow-control characteristics of hybrid actuation approaches were investigated by combining a passive microvane and synthetic jet in a tandem arrangement.

Passive Flow Control

The influences of microvanes and microramps on boundary layers in an adverse pressure gradient were investigated in the 2-D, C-D test section where the freestream Mach number was 0.5 and the boundary layer measured 0.20in (5mm) in thickness at the wall apex. The single-sense and counter-rotating, streamwise vortices induced by microvanes and microramps were characterized in the adverse pressure gradient domain downstream of the test-section-wall apex, Figure 6c. The initial vortex formation from the passive elements was investigated through surface oil visualization using a mixture of linseed oil and titanium-dioxide paint. The oil traces around the microvane, Figure 26*a*, indicated stagnation points upstream and downstream of the microvane leading and trailing edges, respectively. The pressure differential across the microvane surfaces resulted in the rollup of a "tip vortex", which formed a single-sense, streamwise vortex. The oil-streak accumulation downstream from the trailing edge of the microvane indicated an upwash region across the boundary layer. Figure 26*b* shows the near-wall topology of the flow over the microramp and initial vortex formation. A symmetric split of the oncoming flow over the microramp was visible, and the footprint of the initial streamwise vortex was evident from the wall traces on each side of the microramp. As more fluid rolled into each streamwise vortex that formed along the microramp edge, its footprint on the microramp sidewall intensified. The vortices pair was contiguous at the end of the microramp and then advected downstream. This was evident from the two narrow traces about the microramp axis. These traces were not a normal projection of the vortex cores. They delineated the upwash due to the vortex-induced, spanwise flow. The vortex pair self-advected away from the surface as was evidenced by the streamwise thinning of the upwash traces. Nevertheless, the streamwise flow clearly dominated the way in which the vortex pair was convected downstream.

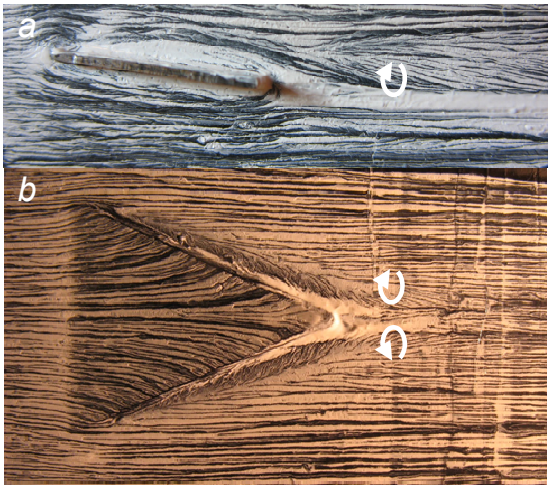

Figure 26. Surface oil-flow visualization of the streamwise single-sign (a) and vortex pair (b) formation.

The far-field effect of the microramp on the boundary layer at x/δ_{apex}=42 was elucidated from a sequence of planar PIV measurements. Contours of time-averaged, streamwise and vertical velocity distributions in the *y*-*z* plane are shown in Figure 27*a* and Figure 27b, respectively. In

addition, contours of the streamwise velocity difference, in the presence and absence of the microvane, are shown in Figure 27c. All velocities are normalized by the freesteam velocity. The crossstream (z-y) plane in the raster plots was viewed in the upstream direction. Note that at x/δ_{apex}=42, the curvature of the tunnel wall produced a negative V-velocity component even in the baseline, non-actuated, case. The distributions in Figure 27 indicate a upwash at center span (the centerline of the microramp) which was accompanied by downwash with peaks at z/δ_{apex}=+1 and -1 on both sides. These were a direct consequence of the counter-rotating vortex pair induced by the microramp. To isolate the effect of the streamwise vortex, the streamwise velocity increment and decrement relative to the non-actuated flow, ΔU is shown in Figure 27*c*. Inspection of Figure 27*c* indicates a streamwise velocity deficit was caused by the upwash of the vortices along with higher speed flow in the near wall region. The bias in the PIV measurements, in which the boundary layer appears slightly inclined in the absence of the microramp, was caused by a misalignment between the PIV camera horizon and the wall contour.

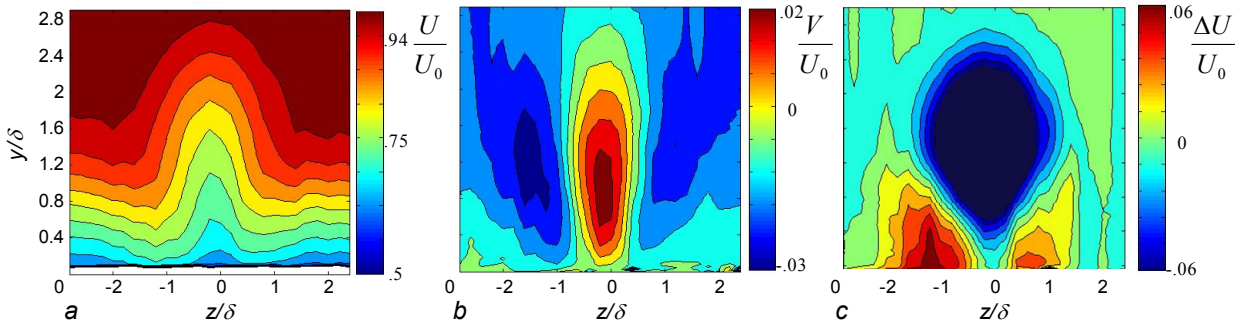

Figure 27. Color, raster, composite, time-averaged contour plots at x/δapex=42 downstream of the microramp of (a) streamwise velocity, U, (b) vertical velocity, V, and (c) streamwise velocity difference from baseline

A cross-stream integral effect of the microramp on the boundary layer flow was assessed from the relative spanwise changes in the shape factor, *h,* of the cross-stream velocity distribution in the absence and presence of the microramp, Figure 28. These data show that the spanwise extent of the microramp was almost $5\delta_{apex}$, while the microramp width was about $3\delta_{apex}$. The most prominent feature of the boundary-layer shape factor was that the induced, streamwise vortices lower the shape factor through most of the influenced, spanwise domain. Even though the upwash along the centerline of the microramp increased the boundary-layer-velocity deficit, Figure 27, the vortex pair was sufficiently far from its source, such that its lift off the wall actually led to a decrease of the velocity deficit near the wall. In the downwash region, the transport of high-momentum fluid towards the surface led to an increase in the velocity deficit near the wall. The combination of displaced upwash bounded on both sides by downwash regions was what made the microramp attractive (when properly scaled) for boundary layer separation delay (Lin, 2002).

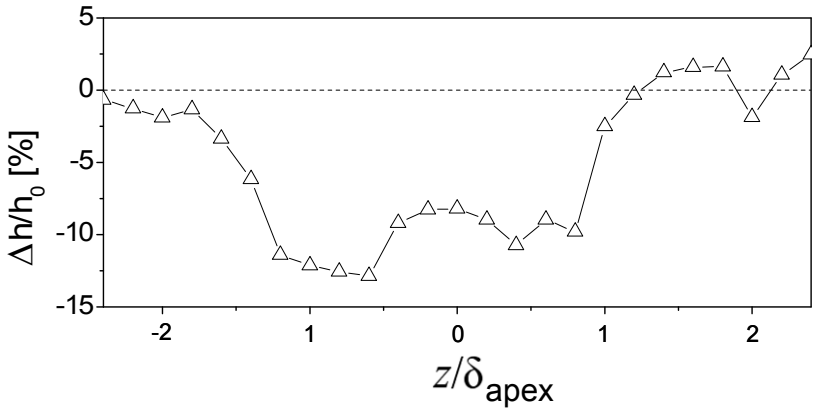

Figure 28. Spanwise distribution of the boundary-layer shape factor, h, downstream of the microramp at x/δapex=42 normalized by the baseline shape factor, h0

Similar to Figure 27, the changes in the flowfield caused by a microvane were measured at x/δ_{apex}=42 and are shown in color raster plots, Figure 29. The time-averaged distribution of the streamwise velocity *U*, Figure 29*a,* shows the upwash ($0.5<z/\delta_{apex}<2$) and downwash ($2<z/\delta_{apex}<3$) domains, indicating the presence of a streamwise vortex. This was further supported by the distribution of the vertical velocity, Figure 29*b*, that includes adjacent zones of fluid motion in opposing directions. As might be expected, owing to the presence of the wall, the vertical elevations of the peaks (positive and negative) of Δ*U,* Figure 29*c,* were different.

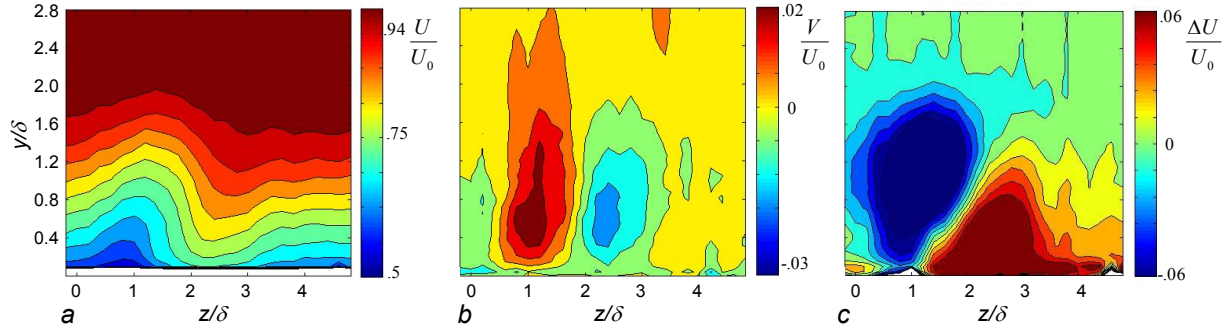

Figure 29. Color, raster, composite, time-averaged contour plots at x/δapex=42 downstream of the microvane of (a) streamwise velocity, U, (b) vertical velocity, V, and (c) streamwise velocity difference

The deficit owing to the upward advection of low-momentum fluid at $y/\delta_{apex}\approx1.2$ was farther away from the surface than the high-momentum fluid at $y/\delta_{apex}\approx0.4$. In fact, the transported high-momentum appeared to spread in the spanwise direction along the surface. It is noteworthy that the flow upwash, in absence of an opposite-sense vortex, was not sufficient to displace the low momentum fluid away from the surface indicating that the effectiveness of the microvane in terms of overcoming flow separation may be lower than that of the microramp. This was further confirmed by the distribution of the shape factor, *h* across the span, Figure 30. In comparison to the corresponding distribution for the microramp, the domain in which *h* increased was considerably broader. However, considering that the spanwise projection of the microvane was approximately $0.4\delta_{apex}$, compared to $3\delta_{apex}$for the microramp, perhaps comparable effects could be achieved by increasing the density of the microvanes.

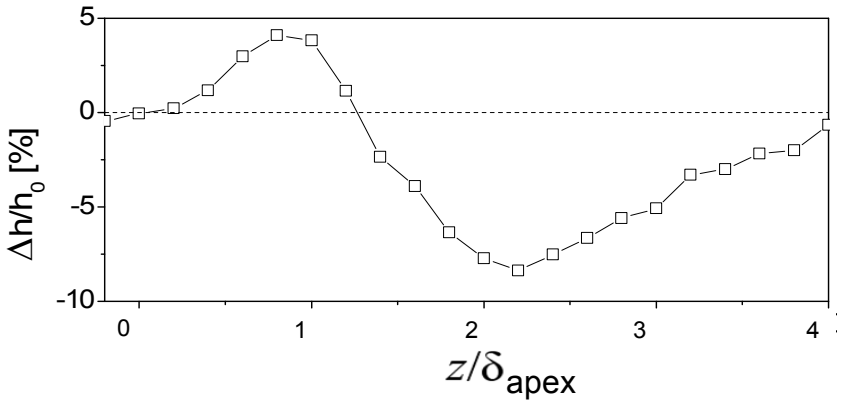

Figure 30. Spanwise distribution of the boundary-layer shape factor, h, downstream of the microvane x/δapex=42 normalized by the baseline shape factor, h_0

Active Flow Control

In addition to passive devices, active, synthetic-jet, flow-control devices were tested to investigate the formation of controlled, counter-rotating or single-sense, streamwise-vorticity concentrations resulting from active, flow actuation. Figure 31*a* and Figure 31*b* show phase-averaged vorticity, just after the onset and at the end of expulsion period, respectively. A pair of counter-rotating vortices issued during the expulsion cycle is clearly visible near the orifice (x = y = 0). In addition, the diffused and weakened pair of vortices injected during the previous expulsion cycle is also visible at the upper edge of the image. Following the expulsion cycle, in Figure 31*b*, the vortex pair maintains its trajectory while spreading and weakening. Although the instantaneous flow is comprised of a train of vortex pairs, the mean flow field in Figure 31*c* illustrates another important feature of synthetic jets; namely, that they develop as any other turbulent jet, having the same statistical properties (Smith & Glezer, 1998). The key difference between synthetic and jets formed by mass injection is that the former is fully synthesized out of the surroundings, as also seen in Figure 31*c*, where the mean flow along the wall is induced towards the jet orifice. This layer is a dominant source for the jet formation.

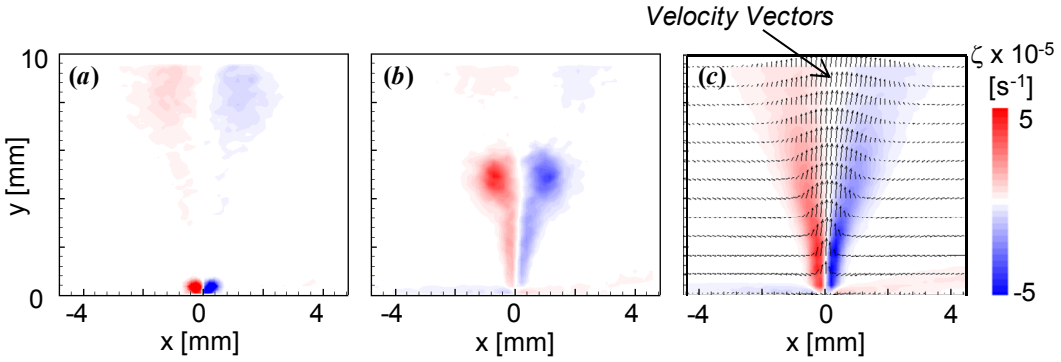

Figure 31. Vorticity Concentrations in a Synthetic Jet Operating in Still Air at the Beginning (a) and End (b) of the Jet Expulsion Cycle, and the Time-Averaged Jet Velocity and Vorticity Fields c)

A comprehensive calibration of the actuators was performed in a calibration stand, where simultaneous dynamic measurements of the exit jet velocity, the displacement at the center of the piezoceramic driver, and cavity pressure and temperature were recorded. Figure 32*a* shows the calibration actuator while the calibration data are shown in Figure 32*b* in terms of the

jet Strouhal number ($St = f \cdot \zeta / U_j$, where f is the driving frequency, ζ is the disk displacement amplitude, and U_j is the jet average velocity during the expulsion part of the cycle). Two regimes of operation can be seen in Figure 32b: first, at the low operating voltage and a given frequency, the jet exit velocity approximately scales with $f \cdot \zeta$, i.e., it is a direct function of the disk displacement. As the applied voltage is increased, St dependence on pressure approaches a second limit state in which p/U_j^2 is approximately constant, which implies that the jet velocity is directly proportional to the cavity pressure. It should be noted that the constant p/U_j^2 is not a universal constant, but rather a complex function of the inner geometry and disk displacement.

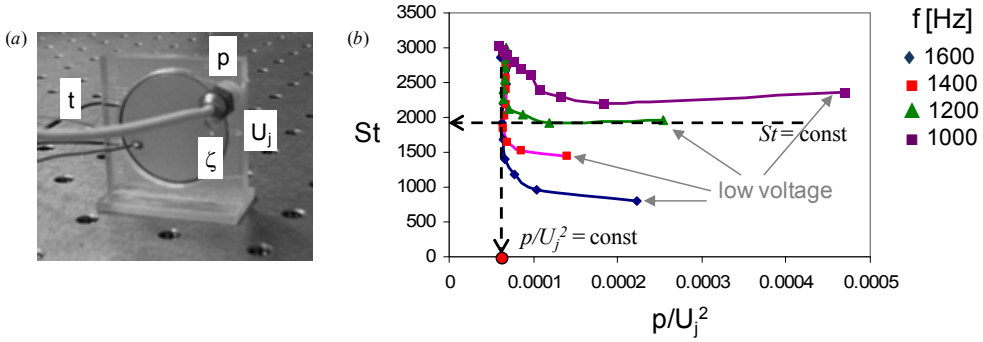

Figure 32. a) Synthetic-Jet Actuator Multi-Parameter Calibration and b) Calibration Results

The synthetic-jet actuator that would provide the active component of a hybrid flow control was tested in a stand-alone configuration. The study was aimed at isolating the effect of a synthetic jet on the boundary layer flow, in the absence of a passive device. In an attempt to mimic the effect of the microramp, the synthetic jet orifice was slanted relative to the freestream direction. The jet axis formed a 24° angle relative to the freestream, the same as the microramp examined previously, such that it would generate predominantly single-sign vorticity, comparable to that emanating from a single side of a microramp. The jet was installed such that the orifice leading edge was 0.5in (12.7 mm) downstream from the wall apex. The resulting boundary layer flows, with and without the active control by slanted synthetic jet, were measured using PIV in the farfield; Figure 17.

A contour map of the non-dimensional streamwise velocity difference between the active flow control and the baseline flow is shown in Figure 33*a*. The dominant downwash was near the wall in a region from 4 mm to 8 mm outboard of the centerline. The presence of this downwash was indicated by an increase in the streamwise velocity within this region. The influence that active flow control has on the streamwise and vertical boundary layer velocity profiles are provided in Figure 33 *b* and *c*, respectively. A significant downwash was measured at that location (z = 5 mm). It should be noted that the flow control was placed on the upper wall of the tunnel and thus inverted. This means that positive components of vertical velocity, V, infers downwash towards the upper wall of the tunnel.

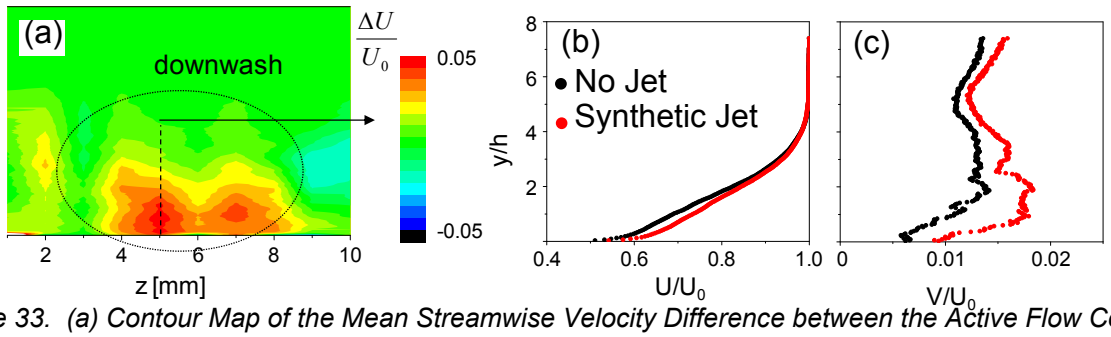

Figure 33. (a) Contour Map of the Mean Streamwise Velocity Difference between the Active Flow Control and the Baseline Flow, and (b) the Corresponding Mean Streamwise (c) and Vertical Velocity Profiles at z = 5 mm

The resulting distribution of a boundary layer shape factor is shown in Figure 34, where the shape factor was reduced with active flow control actuation, particularly between z = 4 mm to 8 mm. Overall results of the active flow control using the slanted jet indicated that there may be an opportunity for expanding the hybrid, spanwise domain of influence in the formation of streamwise vortices.

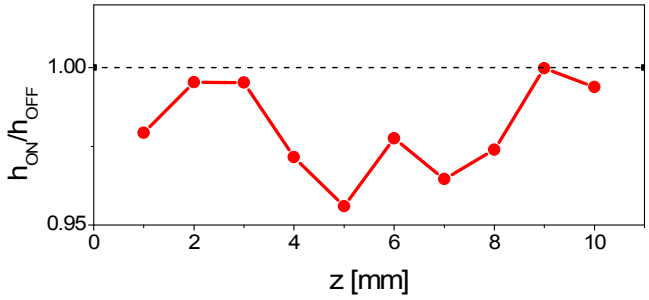

Figure 34. Distribution of the Boundary Layer Shape Factor Ratio (Active Flow Control (h_{ON}) and in the Baseline Flow (h_{OFF})) across the Span

Aligning the major axis of the rectangular jet orifice with the direction of the freestream, as illustrated in Figure 16, produced a pair of counter-rotating, streamwise vortices. In still air, the counter-rotating vortices were generated along the orifice at each actuation cycle. In the presence of a cross flow, the vortices were augmented by the tilting and rollup, predominantly in the spanwise direction, of boundary-layer vorticity and often loosely connected at their downstream end, similar to a lambda vortex. The vortices, which were advected with the local cross flow, were interrupted and vanished during the suction stroke. Because the strength of the streamwise vortices is modulated, the time-averaged vortex strength can be considerably weaker than the instantaneous strength. A streamwise, vortex pair induces an upwash along its common axis and a downwash elsewhere. The resulting changes in the time-averaged streamwise and vertical velocity components are shown in Figure 35. As expected, when the streamwise jet was active, Figure 35*a*, there was a noticeable upwash near the centerline peak in boundary layer thickness. The peak is flanked on either side by weaker downwash where the high-speed flow was drawn closer to the wall. Analogous to Figure 27*c*, the distributions of the streamwise velocity differences relative to the unforced flow, ΔU are shown in Figure 35*c*. These data indicate that the time-averaged flow induced by the synthetic jet was qualitatively similar to the far-field structure of the flow induced by the microramp. The corresponding shape

factor, Figure 36, indicates that the synthetic jet led to an overall decrease in the shape factor, but the magnitude of the decrease was smaller than that induced by the microramp. Since the jet-orifice orientation is fixed, the jet momentum, or impulse per stroke, controlled the strength of the induced streamwise vortices. However, in this case, for a fixed jet velocity, the characteristic, spanwise scale of the jet also impacted the strength of the ensuing streamwise vortices. In the present configuration, the spanwise domain of influence of the jet was approximately $5\delta_{apex}$, which was similar to that of the microramp. However, the spanwise width of the jet was about 30 times smaller than that of the microramp or $0.1\delta_{apex}$ compared to $3\delta_{apex}$.

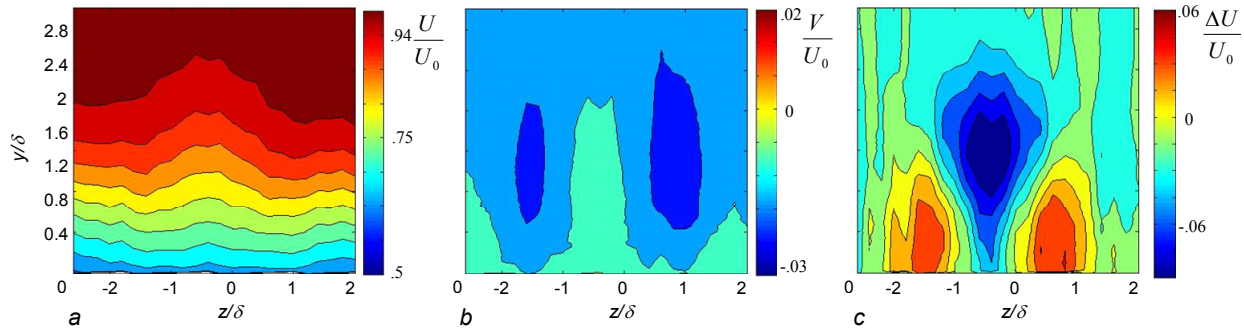

Figure 35. Time-averaged contour plots at x/δapex=42 downstream of the streamwise synthetic jet of (a) streamwise velocity, U, (b) vertical velocity, V, and (c) streamwise velocity difference

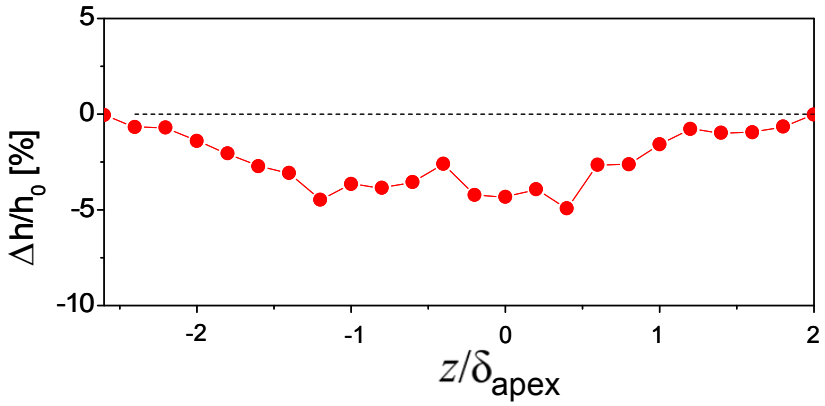

Figure 36. Spanwise distribution of the boundary-layer shape factor, Δh, downstream of the streamwise synthetic jet x/δapex=42 normalized by the baseline shape factor, h_0

Unlike the streamwise-aligned jet, slanting the orifice of the jet, relative to the freestream, in the orientation shown in Figure 16c produced a single, streamwise vortex. The jet-slant angle was the same as the half angle of the microramp. The resulting flow in the far field, Figure 37, indicates the presence of a counter clockwise vortex. Unlike the streamwise jet, the low-speed flow that was pushed out away from the wall, was not convected upward as strongly, which led to areas of both increased and decreased velocity deficits in the near-wall region, as also illustrated in Figure 37c. Although the synthetic jet was slanted at the same direction as the microvane they generated single, streamwise vortices of opposite sense. Specifically, the vortex formed by a microvane is similar to a tip vortex of a lifting surface. However, the vortex that is formed by the jet appears to form as a result of the bending of the jet by the cross flow, as shown by Peake et al (1999) for continuous, conventional jets. This result is also consistent with the measurements of Compton and Johnson (1992) for skewed jets.

The near-field formation of the vortex that was generated by the slanted jet was measured in 16 cross-stream (y-z) planes spaced 0.039in (1 mm) apart, where the field of view measured 0.669in x 0.669in (17 × 17 mm). The measurement region began at x/δ_{apex}=2 downstream of the upstream orifice edge, Figure 17. The resulting rendition of a 3D composite of near-field flow is shown in Figure 38. Figure 38*a* shows surfaces of the vertical velocity. The presence of the jet forces the oncoming flow up away from the surface along the jet orifice and induces a downward flow in a domain that is outboard and downstream from the jet orifice. The bending of the jet by the cross flow is evident in surfaces of the streamwise velocity difference, relative to the baseline flow, Figure 38b. This phenomenon is accompanied by an increase in the streamwise velocity on the right, downstream of the orifice, and a small decrease owing to the flow turning on the left. Clearly, the differences in the sense of the streamwise vortices that are formed by slanted, passive obstructions and by similar-slant, synthetic jets must be taken into consideration in the design of hybrid actuators that are comprised of both elements.

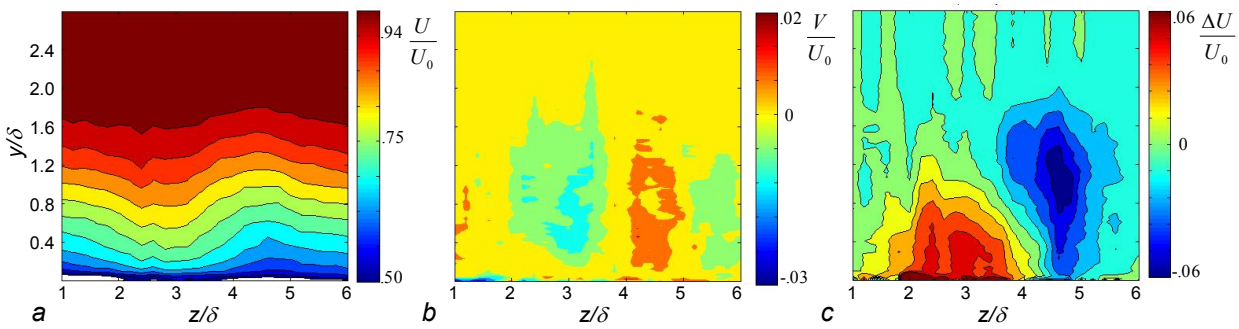

Figure 37. Time-averaged contour plots at x/δapex=42 downstream of the slanted, synthetic jet of (a) streamwise velocity, U, (b) vertical velocity, V, and (c) streamwise velocity difference

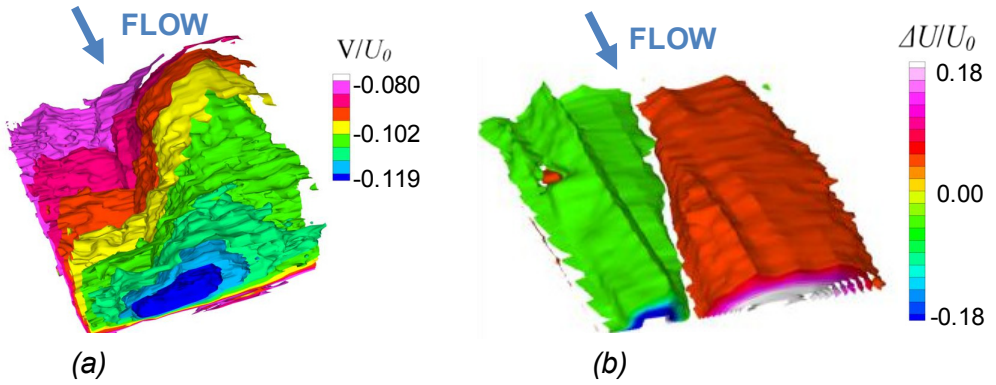

Figure 38. Composite, upstream view, 3D, time-averaged velocity field downstream of the slanted, synthetic jet showing surfaces of (a) V and (b) ΔU

The spanwise distributions of the changes in the shape factor affected by the slanted jet are shown in Figure 39. The spanwise extent of the changes in shape factor that are induced by the slanted jet and by the microvane, Figure 30 were quite similar at approximately $3\delta_{apex}$ in the far field. The streamwise projection of the microvane into the spanwise plane was $0.4\delta_{apex}$ and the streamwise projection of the jet into the spanwise plane was $2\delta_{apex}$. Furthermore, the magnitude of the effect of the jet was only about 15% lower based on the averaged change in shape factor.

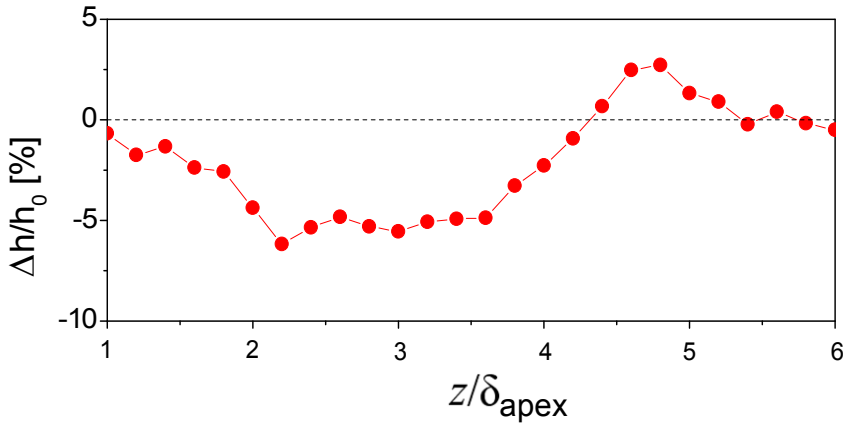

Figure 39. Spanwise distribution of the boundary-layer shape factor, Δh, downstream of the slanted, synthetic jet x/δapex=42 normalized by the baseline shape factor, h0

Hybrid flow control

The performance benefits attained by adding an active component to a passive flow-control approach was investigated. Hybrid devices were tested to characterize the interaction between closely-coupled, passive and active devices. Initially, a boundary layer microramp was selected as the passive component of the hybrid, flow-control system. Initial insight into the dynamics of simultaneous flow control by an active synthetic jet, upstream from the microramp was achieved using phase-averaged measurements over the measurement domain (2) as shown in Figure 17a. Measurements were locked to the signal applied to the actuator, and eight phase-averaged measurements were taken 45° apart. Three of the resulting flowfields are shown in Figure 40, at the beginning, Figure 40*a,* and end, Figure 40*b,* of the expulsion cycle, and at the peak of the suction cycle, Figure 40*c*. Significant vorticity manipulation of the baseline boundary layer is seen in each of the plots, as boundary layer vorticity in the central plane, induced by the synthetic jet vortex pair, becomes temporally and spatially manipulated. Besides the high vorticity levels associated with the boundary layer, a strong shear layer in the flow separating from the microramp was observed. At the beginning of the expulsion cycle, Figure 40*a*, a residual vorticity signature from the previous expulsion cycle was seen just over the microramp edge, interacting with the baseline microramp shear layer. At the end of the expulsion cycle, Figure 40*b*, the vorticity disturbance from the previous expulsion cycle was about to leave the field of view, when the induced vorticity created a strong temporal alteration of the boundary layer vorticity just upstream from the microramp. Note the comparable effects of the jet and microramp vortices. The vorticity manipulation was convected downstream onto the microramp, with further progression in phase, and at the peak of a suction cycle, Figure 40*c*, as the jet effect began to interact with the microramp shear layer. These measurements indicated that, in addition to the continuous flux of vorticity into the boundary layer from the microramp, a synthetic jet introduces a time-varying manipulation of the boundary-layer vorticity.

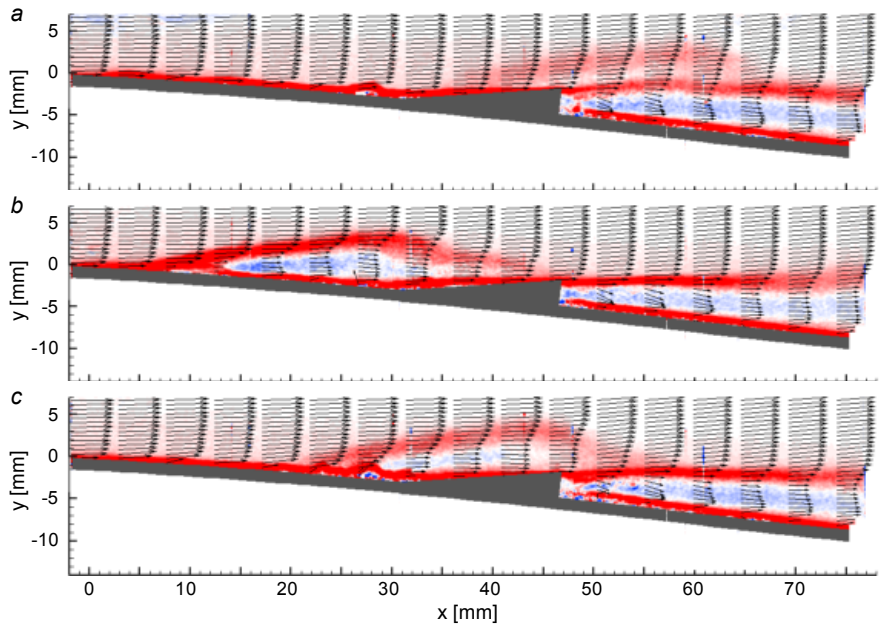

Figure 40. Contour Plots of the Phase-Averaged Vorticity with Overlaid Velocity Profiles at the Beginning of the Jet Expulsion Cycle (a), End of the Expulsion Cycle (b), and at the Peak of the Suction Cycle (c) of the Actuation Period

Compared to exclusively passive control, hybrid flow control introduces an additional dynamic component to boundary layer vorticity manipulation in the near field. The level of preservation of such dynamic effects in the far field was assessed by obtaining additional phase-averaged measurements at measurement location (3), as described in Figure 17. Eight phase-averaged measurements that were taken 45 deg apart in phase and six characteristic profiles are shown in Figure 41. Profiles are shown for the mean streamwise velocities in Figure 41*a,* vertical velocities in Figure 41*b,* and streamwise velocity fluctuations in Figure 41*c*. As a reference, the corresponding profiles of pure passive flow control (no active control) are also added to the plots. It is seen that the oscillatory nature of the flowfield is preserved in the farfield, and that flow parameters periodically vary in time at the actuation frequency. Substantial variation in the shape of the instantaneous velocity profiles induces both a temporary increase and decrease in the downwash of the flow. However, as evidenced by the predominant reduction in near-wall velocity deficit in the streamwise velocity component, Figure 41*a*, and accompanying increase in the vertical velocity component, Figure 41*b,* the overall effect of simultaneous active and passive flow control is expected to result in enhanced stability of the boundary layer.

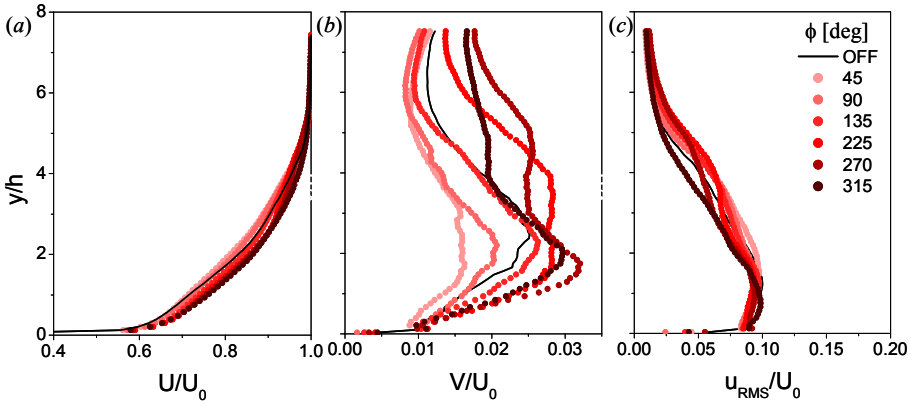

Figure 41. Mean Streamwise (a) and Vertical (b) Velocity Profiles and the Corresponding RMS Velocity Fluctuations (c) for the Baseline (—) and Actuated Flow at Six Phases of the Actuation Cycle, Measured at the PIV Domain (3)

The dynamic nature of the boundary layer manipulation is further characterized by calculation of instantaneous shape factors (h) based on the streamwise velocity profiles shown in Figure 41*a*. The corresponding shape factors are shown in Figure 42*a* as a function of the phase of the actuation cycle. Also, a schematic of one actuation cycle is shown in Figure 42*b* with the matching phase instances. Continuous variation of the boundary layer shape factor during one actuation period induces a net reduction in the shape factor, as it remains lower than in the baseline (passive flow control) for most of the actuation period. Overall reduction of the shape factor in hybrid flow control is estimated to be about 2% relative to exclusively passive flow control.

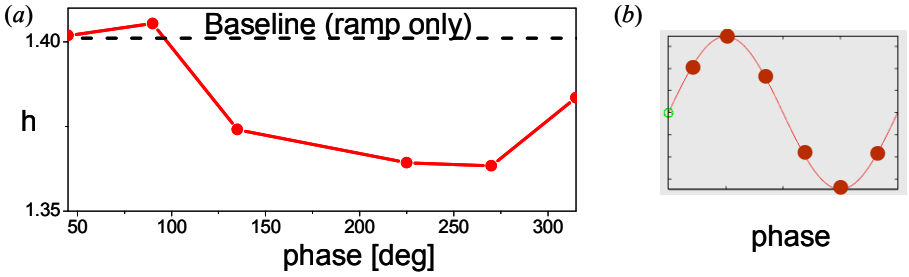

Figure 42. a) Phase (Time) Variation of the BL Shape Factor (●) of the Measured BL Profiles Shown in Figure 41a b) Illustration of the Corresponding Phase-Points of the Actuation Cycle

The key effects of passive and hybrid flow control on the boundary layer stability are illustrated in Figure 43. A main effect of the microramp passive control is illustrated in Figure 43*a*. A pair of streamwise, counter-rotating vortices, formed off the microramp, grow in size and spread in the spanwise direction. The vorticies produce an upwash motion of the fluid in the central domain (measurement station (2)) while a downwash motion is predominantly induced on either side of the vortex pair (e.g., measurement station (3)). Once the periodic jet is superimposed on the steady passive control, Figure 43*b,* the two counter-rotating vortices formed off the microramp become dynamically modulated. This increases their instability, generating more streamwise vorticity in the spanwise (z) direction, which then also undergoes the same instability and spreads further. This indicated that the major effect of the addition of synthetic jet control is to enhanced growth of secondary, streamwise vorticity and spanwise spreading of the favorable effect of the vortex pair generated by the microramp.

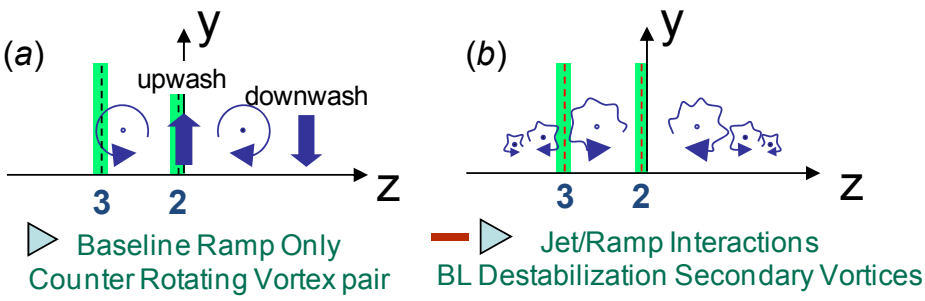

Figure 43. Illustration of the Main Flow Effect of Passive (a) and Hybrid (b) Flow Control Surrounding PIV Measurement Locations (2) and (3)

Velocity profiles taken at measurement locations (2) and (3) for the passive and hybrid flow control were compared to observe the enhanced effectiveness of hybrid flow control, Figure 44. This shows that hybrid, synthetic-jet actuation leads to an overall increase in downwash and thus resistance to separation by less upwash at the centerline location (2) and increased upwash at the off centerline location (3).

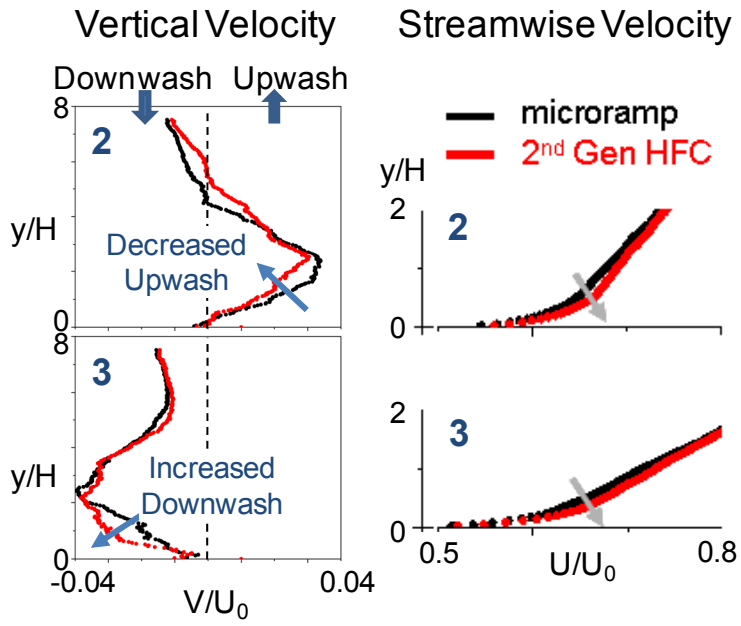

Figure 44. Measured Mean Vertical (a) and Streamwise (b) Velocity Profiles for the Passive and Hybrid Flow Control at PIV Measurement Locations, Centerline (2) and Outboard (3)

Finally, spatial distributions of the boundary layer shape factor for both passive and hybrid flow control are shown in Figure 45. Specifically, shape factors for both flow control techniques are provided in Figure 45*a*. For convenience, the ratio of shape factors resulting from hybrid and passive flow control techniques is shown in Figure 45*b*. The figure shows the integrated hybrid flow control reduces the boundary layer shape factor across the span.

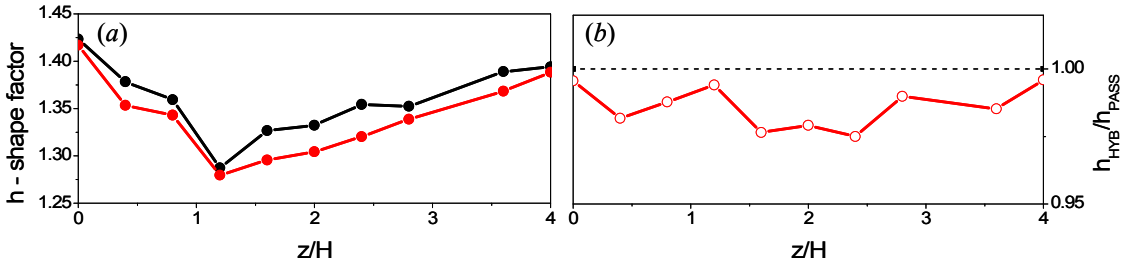

Figure 45. Shape Factor Distributions (a) and the Ratio (b) upon the Passive (●) and Hybrid (●) Flow Control across the Span between the Measurement Stations (2) and (3)

Performance enhancements due to the incorporation of a synthetic jet with a passive microvane were assessed by comparing distributions of the time-averaged, streamwise and vertical velocities downstream of the microramp, in the absence and presence of the jet, Figure 46. These data clearly show the central upwash domain and two downwash regions on either side. In addition, these data indicate that the time-averaged effect of the jet in this configuration was somewhat limited in that there was only a slight enhancement of both the upwash and downwash. The spanwise effect of the hybrid actuation was assessed based on spanwise distributions of the shape factor, Figure 47. This figure shows the additional changes in the shape factor with the synthetic jet are somewhat smaller than the percent changes induced by the jet alone.

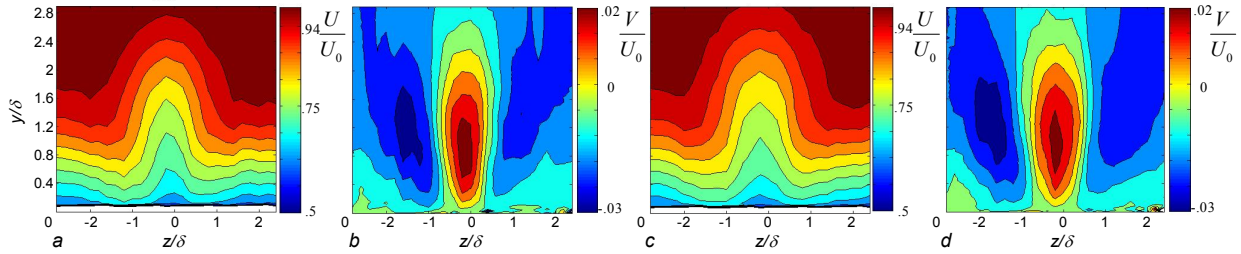

Figure 46. Color, raster, composite, time-averaged contour plots at x/δapex=42 downstream. (a) streamwise velocity of isolated microramp, (b) vertical velocity, V of isolated microramp, (c) streamwise velocity of hybrid microramp/synthetic jet, (d) vertical velocity, V of hybrid, microramp/synthetic jet

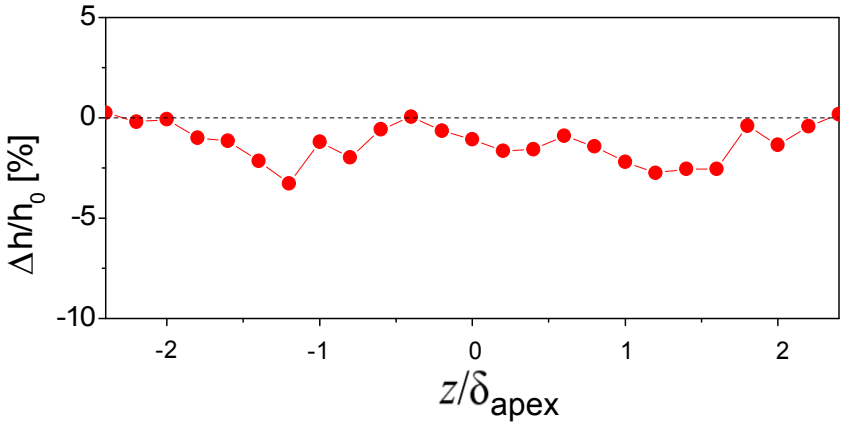

Figure 47. The shape-factor distribution for the hybrid control (h) relative to the passive (h0) control across the span in the far-field domain

In addition to hybrid devices comprised of synthetic jets and microramps, synthetic jet/microvane hybrid devices were examined. In the preceding section, it was illustrated that a synthetic jet emerging normal to a surface and slanted at the same direction as the microvane generates single, streamwise vortices of a sense opposite to the microvane, Figure 37. Therefore, in order to facilitate development of a fully integrated hybrid device, the jet orifice was modified such that the jet emanated at a 45° skew angle, meaning at an angle in the spanwise direction rather than normal to the surface. Various relative positions and orientations of the microvane and synthetic jet were tested to assess performance sensitivities to these parameters. Schematic descriptions of the various devices used in this study are shown in Figure 18, where the streamwise position was measured relative to the wall apex. A nominal microvane at an angle of 8°, Figure 18*a*, has a rectangular planform measuring 0.059in x 0.602in (1.5mm × 15.3mm) in the vertical and streamwise directions, respectively, relative to the freestream.

The slanted, skewed jet produced a single-sign vortex causing a disturbance in the streamwise component of the velocity, as seen in Figure 48. Coherent regions of upwash and downwash are visible in Figure 48*a* and Figure 48*b*, respectively. Such a disturbance induces a decrease in the velocity deficit near wall, as visible in Figure 48*c*, which shows the difference between the resulting flow and the baseline, uncontrolled flow. The effect of the skewed, slanted jet on the baseline flow was comparable to that of an isolated microvane in a cross flow, Figure 29. Determination that a skewed and slanted jet orifice can generate the same-sense, streamwise vorticity as a parallel microvane enables utilization of a synthetic jet to enhance the performance benefits of a microvane.

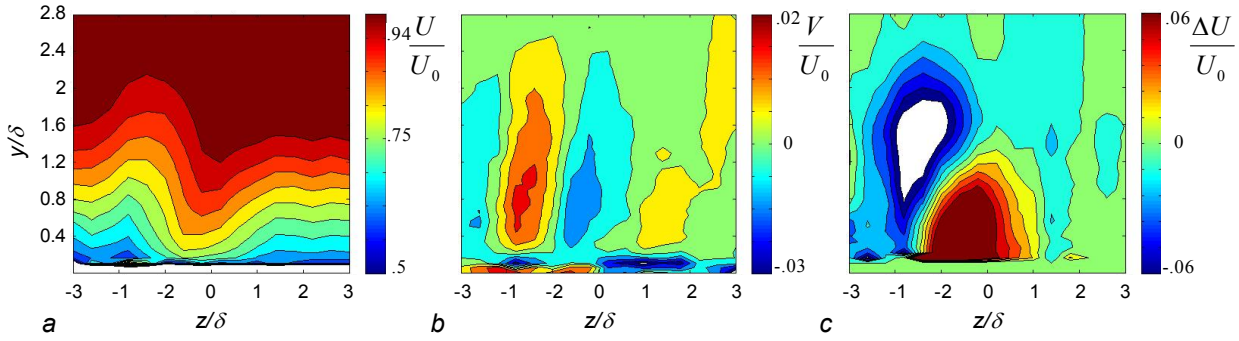

Figure 48. Color, raster, composite, time-averaged contour plots at x/δapex=42 downstream of the skewed, slanted, synthetic jet of (a) streamwise velocity, U, (b) vertical velocity, V, and (c) streamwise velocity difference

Through this investigation, it was found that although the sign of the single-sense vortices resulting from skewed and slanted-jet actuation is determined by the direction of the skew angle of the orifice, the strength of the vortices, for a constant skew angle, is determined by the jet slant angle, Figure 49. When the synthetic-jet orifice is aligned with the flow, Figure 49b, a single-sign vortex is formed. As the jet is slanted at a nonzero angle, the spanwise projection of the orifice increases, and the induced vorticity gives rise to its spanwise component. A small, positive slant angle slightly increases the farfield area of influence and somewhat enhances the decrease in velocity deficit, Figure 49a. As the orifice slant angle is increased in the opposite direction, a clear trend of increased area of influence and decreased effect magnitude will result, Figure 49c–e. Based on this study, the jet orifice, slanted at the same angle as the microvane,

was selected for further studies, due to the significant, far-field effect and convenience for any interlaced integration of the jets and the microvanes in a hybrid-control element.

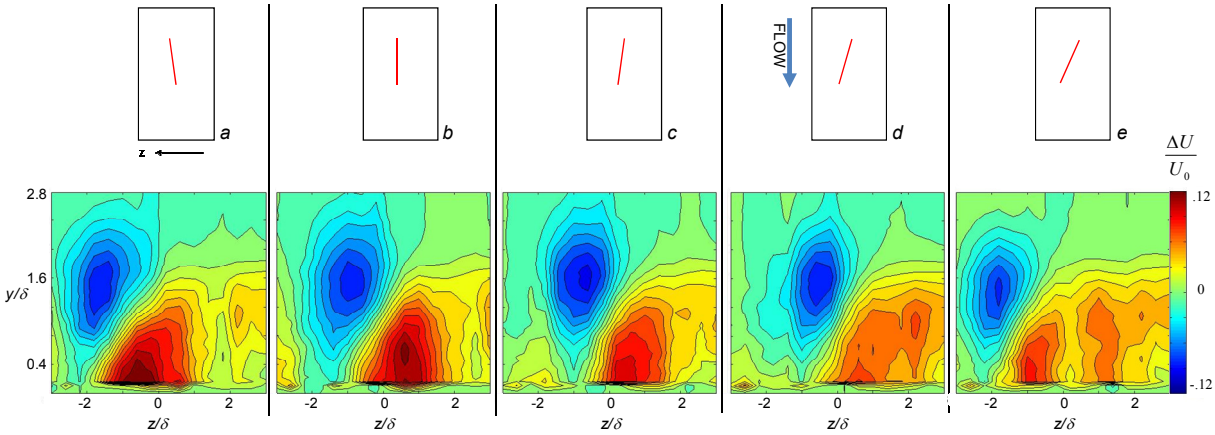

Figure 49. Contours of the streamwise velocity difference (in the presence and absence of the synthetic jet) are shown for slant angles of: (a) 8, (b) 0, (c) -8, (d) -16, (e) -24.

Following selection of the microvane hybrid device fluidic component configuration, the skewed, slanted, synthetic jet, the passive and active devices were installed in tandem, as a hybrid device, to examine the resulting flow physics in detail. Experiments were performed with the microvane located both upstream and downstream of the jet and in various, relative spanwise locations to provide insight into the nonlinear superposition of the two, distinct, resulting flowfields. Distributions of the time-averaged, streamwise and vertical velocities, U* and V*, downstream of the microvane, in the absence and presence of the jet, for various upstream spatial locations of the microvane, Figure 50, were used to assess the performance of the hybrid devices. As the microvane was moved in the positive spanwise direction, the resulting vortex that formed off the microvane shifted within the measured field of view, Figure 50. Analyses of the vortices induced by actuation from hybrid configurations at various spanwise spacing between the microvane and jet also showed that the maximum vortex strength was attained when the spanwise spacing was minimized, Figure 50a and c. Aligning the jet with the microvane resulted in slightly reduced vortex strength, Figure 50b. The least favorable configuration was one in which the spanwise distance between the microvane and jet was maximized, Figure 50d, where two weakly interacting but distinct vortices were seen under superposition of the jet and the microvane.

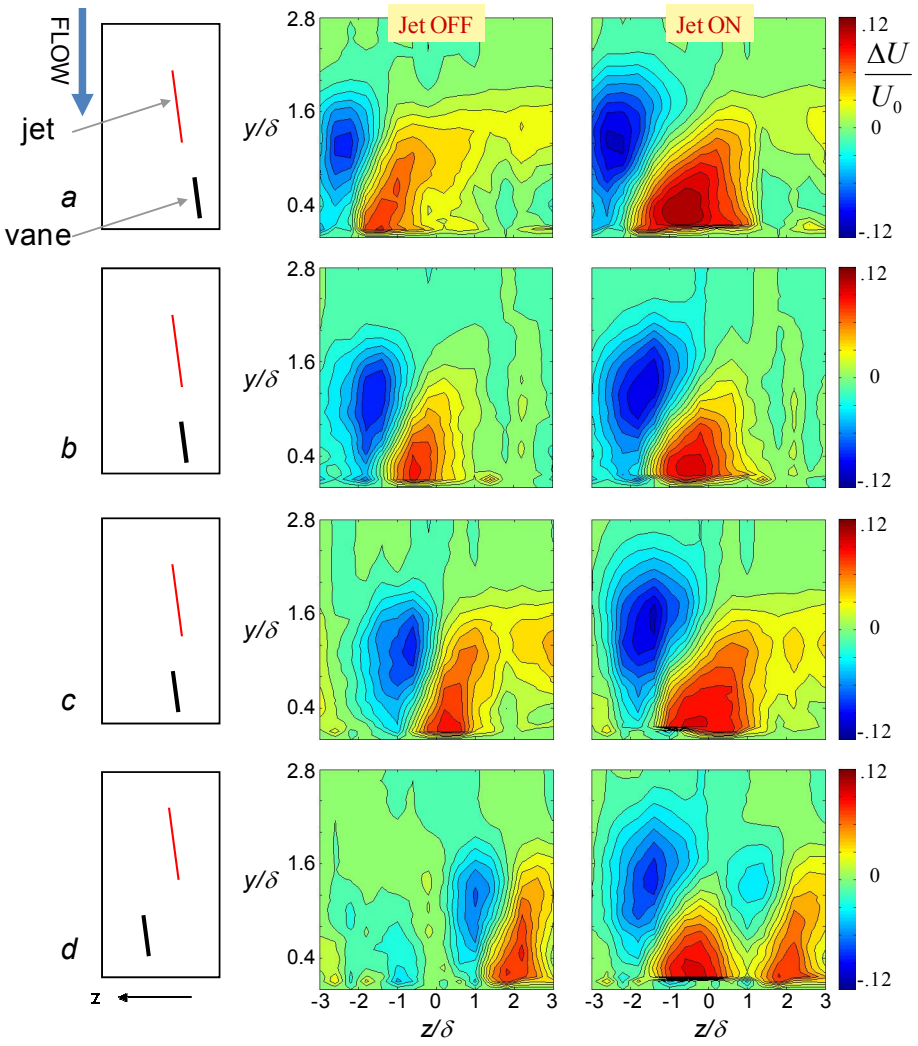

Figure 50. Contours of the streamwise velocity difference in the presence and absence of the synthetic-jet flow control for various relative spanwise locations of the synthetic jet and microvane

One strategy previously shown to counteract flow distortion resulting from significant boundary-layer ingestion is to apply flow control that redistributes the concentrated, low total pressure, boundary layer flow around the perimeter of the AIP, thus creating a distortion pattern to which engines are typically more tolerant. This result may be achieved by using flow control to generate two, large-scale, counter-rotating vortices that sweep the concentrated boundary layer flow up and around the outer perimeter of the duct. In previous studies (Anabtawi et al. 1999), it has been shown that an array of streamwise vortices must be generated such that they merge into a large-scale vortex downstream of the duct, which requires consideration of the vortex sources, sizes and spacing. It is this prerequisite that often dictates the packing density and number of devices. The use of a hybrid system, in place of a passive system offers the potential of reducing the required number of microvanes, thereby potentially reducing total-pressure losses, maintainability, and supportability issues. To this end, two microvanes were placed in the flow such that the pair of resulting vortices exhibited weak interaction at the downstream measuring plane, Figure 51a and c. This microvane pair was then mated with a synthetic jet, analogous to the configuration illustrated in Figure 48 and Figure 50a. When the jet was activated the microvane-generated vortices merged into one larger, coherent structure,

as indicated by the large domain of influence of diminished velocity deficit, Figure 51b, and by the vertical-velocity component, Figure 51d, which indicated only one zone of upwash and one zone of downwash.

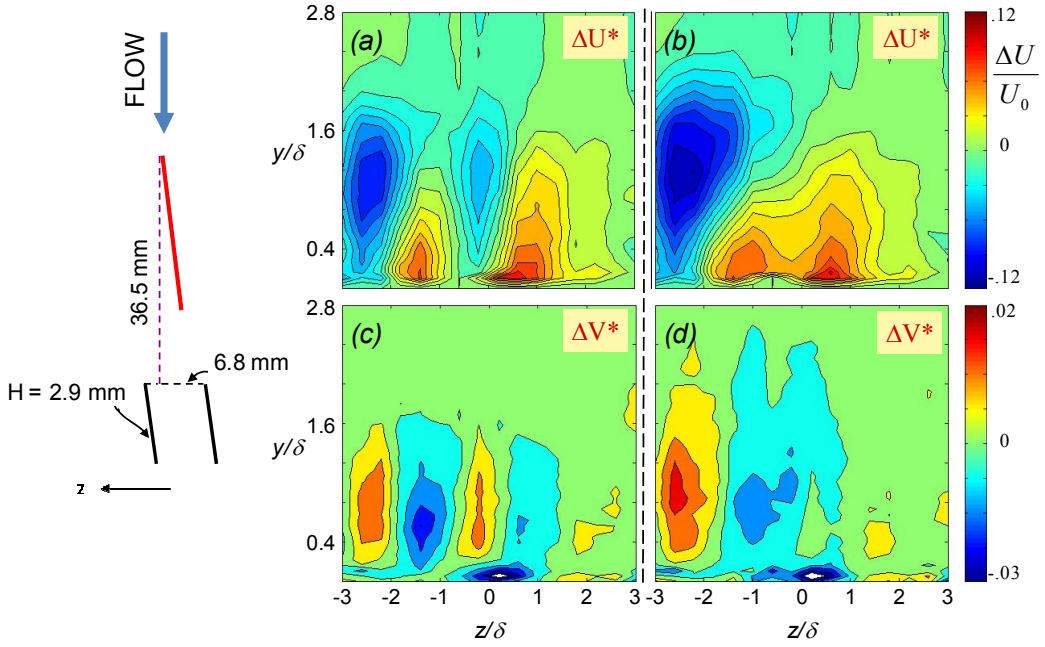

Figure 51. Contours of the streamwise (a, b) and vertical (c, d) velocity difference (in the presence and absence of the active flow-control device) are shown for the case where two microvanes are paired with inactive (a, c) and active (b, d) synthetic jet.

The integration of a synthetic jet with a pair of microvanes was proven to enhance the weakly-interacting vortices that resulted from passive, microvane actuation. Specifically, hybrid, synthetic-jet/microvane flow control resulted in vortices that merged into one large, coherent structure. After learning how the active control element can enhance an intentionally sub-optimized pair of vanes, further integration effort was made to examine a configuration that more closely resembled a subset of an array of microvanes. For that purpose, three vanes were set in tandem with two interlaced jets. This study included variation of the vane-to-vane spacing, such that the passive-control effects included both near-optimal and sub-optimal vane configurations. Three tested configurations are outlined in Figure 52, where the vane spacing is varied among 1.6δ, 2δ, and 2.4δ. The resulting flow fields are shown in Figure 52 in terms of both ΔU and V raster plots. The first column in Figure 52 also has projections of the passive vanes labeled along the x-axis of the plots. For the closest vane spacing, sole passive control shows that the initial three vortices begin to interact upstream from the measurement plane, but do not merge into a single vortex by that point. Rather, two interacting vortical structures are detected at the measurement plane. Upon activation of the jets, it appears that each dominant vortical structure becomes enhanced. As the vanes are spaced further apart by 2δ (middle row), all three vortices generated by the vanes become visible at the measurement plane, as their interaction becomes spatially delayed. Activation of the jets not only enhances these passive-generated vortices, but also promotes their merging, as only signatures of two vortices are measured at the PIV plane. Finally, as expected, further increase in the vane spacing (bottom row) separates initial vortices formed off the vanes even more, and three distinct vortices are detected for the passive control case. Activation of the jets at this vane spacing is

less effective in promoting merging of the vanes' vortices than in the previous configuration, although there is a strong enhancement of the streamwise vortices, but with a less coherent imprint due to their spacing.

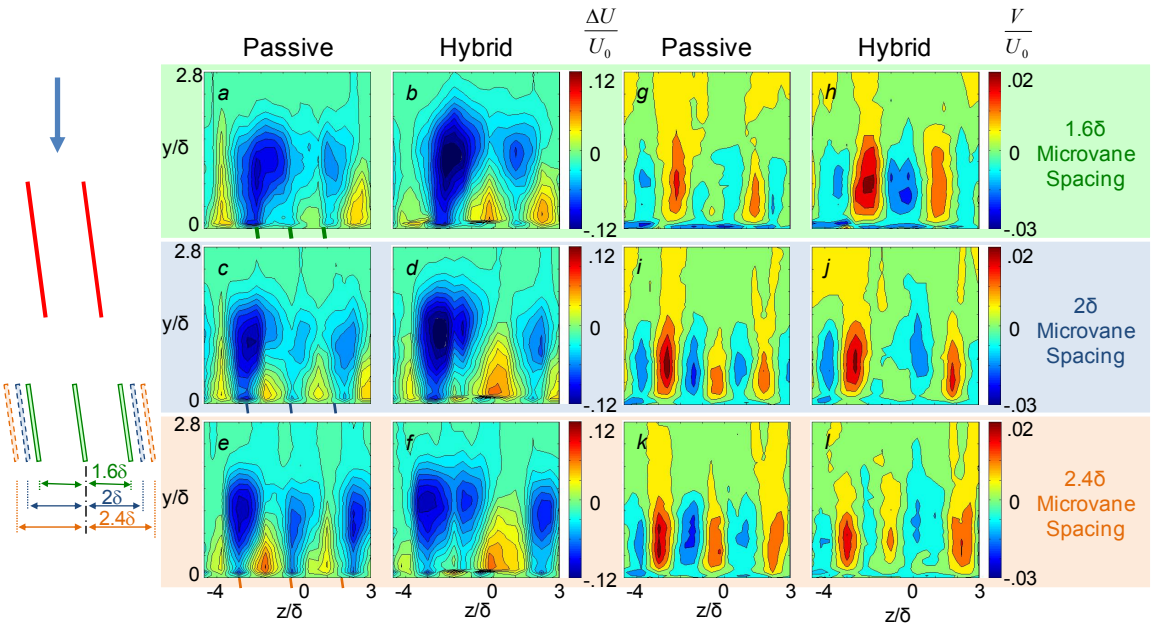

Figure 52. Streamwise Difference (a-f) and Vertical (g-l) Velocity Contours for Passive and Hybrid Control for Two Jets in Tandem with Three Microvanes Spaced at 1.6 δ, 2 δ, and 2.4δ

These results suggest that implementation of a row of synthetic jets followed by a row of microvanes could be made more efficient by implementing this concept of merging vortices. Furthermore, hybrid microvane/jet devices offer the benefit of reducing distortion with a reduced size and/or number of microvanes, thus offering potential improvements in inlet performance, as well as, system-level requirements such as supportability and maintainability.

BLI Offset Diffuser Performance Assessments

Active, passive, and hybrid flow-control effectiveness in managing BLI-inlet performance was assessed at the AIP of the isolated, offset diffuser in terms of recovery and steady-state and dynamic total-pressure distortion. Experimentally obtained, baseline BLI-inlet performance is reported and compared with performance resulting from flow-control actuation applied just downstream of the throat. Experimental results are reported for flow-control devices including passive microvane arrays, active steady and synthetic jets, and hybrid systems comprised of microvanes with steady jets or synthetic jets.

BLI inlet performance was evaluated in terms of total pressure recovery and distortion as measured with a 40-probe total-pressure rake located at the duct AIP. Additional details pertaining to the rake are provided in Appendix A. Total-pressure distortion was defined in terms of the SAE spatial distortion descriptor elements and indices (SAE ARP1420B, 2002). Specifically, circumferential distortion at the hub and tip, $DPCP_H$, Equation 1, and $DPCP_T$, Equation 2, respectively, were computed, as well as, radial distortion at the hub and tip, $DPRP_H$, Equation 3, and $DPRP_T$, Equation 4, respectively. Appendix B contains additional information regarding the computation of the distortion descriptors. The metrics were measured against limits consistent with current, high-bypass engines compatible with an "N+2" HWB-type vehicle. The circumferential distortion limits varied with mass flow ratio. At max airflow, the steady-state

limits were 0.025 and 0.040 for the hub and tip, respectively. The radial steady-state distortion limits were 0.000 and 0.030 for the hub and tip, respectively. An average circumferential distortion, $DPCP_{ave}$, Equation 5, was also computed; as well as, the total pressure recovery. Total pressure recovery was computed as the area-averaged AIP total pressure. A complete listing of the data reduction equations applied to assess diffuser performance are given in Appendix B of this report.

$$DPCP_H = (DPCP_1 + DPCP_2) / 2$$

Equation 1

$$DPCP_T = (DPCP_4 + DPCP_5) / 2$$

Equation 2

$$DPRP_H = DPRP_1$$

Equation 3

$$DPRP_T = DPRP_5$$

Equation 4

$$DPCPave = (DPCP_1 + DPCP_2 + DPCP_3 + DPCP_4 + DPCP_5) / 5$$

Equation 5

Baseline Duct Performance

The complex internal flowfield of a BLI inlet resulting from the ingestion of a thick boundary layer and the interaction of the boundary layer with inlet cowl was replicated in isolated diffuser tests through the use of a honeycomb fence installed upstream from the duct throat. The resulting approach flow to the tested diffuser was characterized by hot-wire measurements at three spanwise locations z/H = -0.5, 0, and 0.5 and an axial location of x/H = 1 upstream from the diffuser inlet. (H was the height of the diffuser aperture.) The resulting profiles of the mean velocity and RMS velocity fluctuations are shown in Figure 53, along with the corresponding profiles of the flow without the honeycomb fence, for a reference. Symmetry of the profiles about the central plane (z/H = 0) is noted in for both cases. A significant thickening of the boundary layer was achieved, as the thin boundary layer of the non-manipulated flow was thickened to more than a third of the diffuser inlet height. The difference in velocity deficit between the center plane and the outer profiles suggested a three-dimensionality of the oncoming flow that was consistent with an inlet flow in an integrated diffuser. Secondary peaks in the RMS velocity profile at the central plane were attributed to the shear layer that formed at the fence boundary and subsequently decayed in the downstream direction. It was therefore expected that these features would become further suppressed before the characterized flow reached the diffuser inlet plane (x/H = 0).

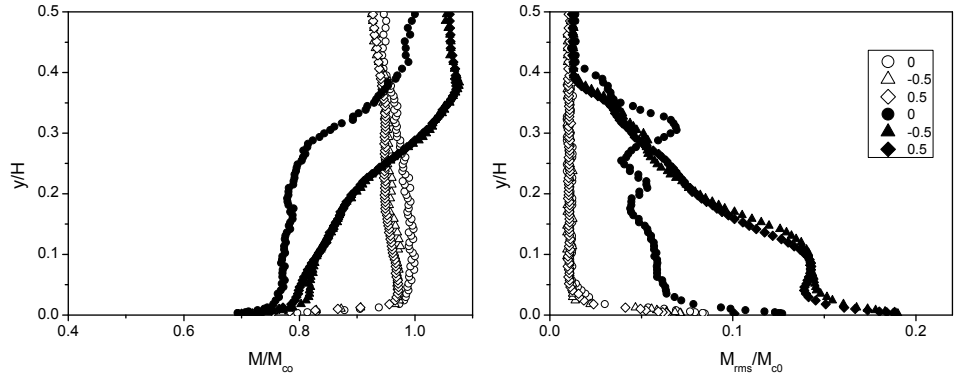

Figure 53. Velocity (a) and the RMS velocity fluctuation profiles (b) for the natural (open symbols) and the baseline flow manipulated by the honeycomb fence (solid symbols) at the centerline (circle), and 0.5H port (triangle), and starboard (diamond) hot-wire measurement location.

The baseline flow in the diffuser was further characterized by surface oil-flow visualization, and the resulting traces on part of the diffuser inner surface are shown in Figure 54. The main feature of this visualization was confirmation that the flow does not separate. The zoomed-in area of the flow around the flow-control inserts is emphasized in Figure 54b. The flow in this area will be assessed further in the controlled cases.

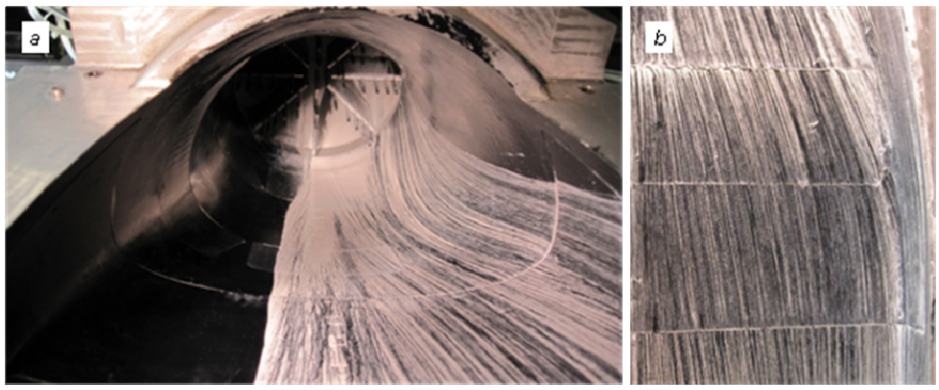

Figure 54. Surface oil-flow visualization of the baseline diffuser flow (a) and the zoomed-in control surface area (b) at M_{AIP} = 0.55.

Finally, the main characterization of the diffuser flow, from the standpoint of its interface to the engine was done using the forty-probe rake measurements and static pressure measurements at the base of each rake. In addition, the baseline flow was also characterized by the static pressure measurements along the upper and lower diffuser surfaces, from the diffuser inlet (x/H = 0) to the AIP (x/H = 3.4). The baseline results are shown in Figure 55. The AIP-contour map indicates that there is a low pressure region in the bottom center quadrant. The goal was to match the structures observed at the AIP during previous experiments that utilized a tunnel-mounted inlet that enabled the natural evolution of the inlet approach flowfield and its interaction with the inlet lip (Berrier 2004). Upon comparison, the global features observed at the AIP, Figure 55a, were similar in shape to those for the corresponding freestream Mach number and inlet capture ratios (Berrier 2004). The pressure profiles along the lower surface further confirm the lack of separation that was shown qualitatively in the flow visualization, and also served as a data base for the CFD validation of the diffuser flow.

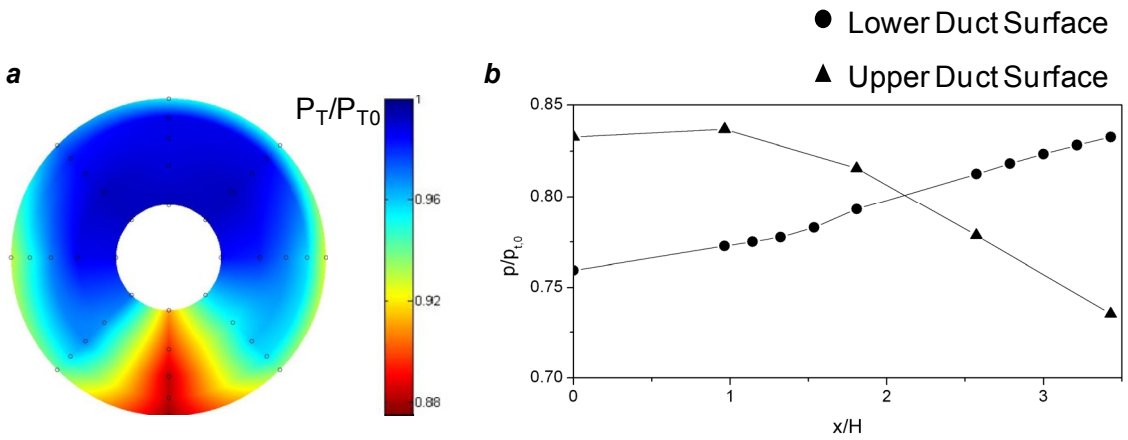

Figure 55. Total pressure contour plot measured at the AIP (a) and static pressure profiles along the upper and lower surfaces for the baseline flow at M_{AIP} = 0.55 ($DPCP_{ave}$ = 0.028).

As discussed previously, the key performance metrics in this study were recovery and total-pressure distortion measured at the AIP of the diffuser. The effects of the honeycomb fence on the steady-state, total-pressure recovery and the steady-state circumferential hub total-pressure distortion are shown in Figure 56. The plots provide a comparison of the recovery and distortion between the baseline configuration (with the upstream fence) and the clean duct (without an upstream fence) at various mass-flow rates. The upstream fence in the baseline configuration produced a decrease in recovery and an increase in the circumferential hub distortion when compared with the clean diffuser. At higher airflow rates, there was a larger decrease in recovery and increase in circumferential hub distortion, and the increase in diffuser airflow increased the circumferential hub distortion above the prescribed limits. The effects of the honeycomb fence on the AIP total pressure contours are shown in Figure 57. The effect of the upstream fence on the baseline configuration is visible near the bottom center of the AIP pattern as a decrease in total pressure that was representative of a BLI inlet. Furthermore, the resulting distortion levels were found to be above the prescribed limits indicating that flow control is required for this type of inlet.

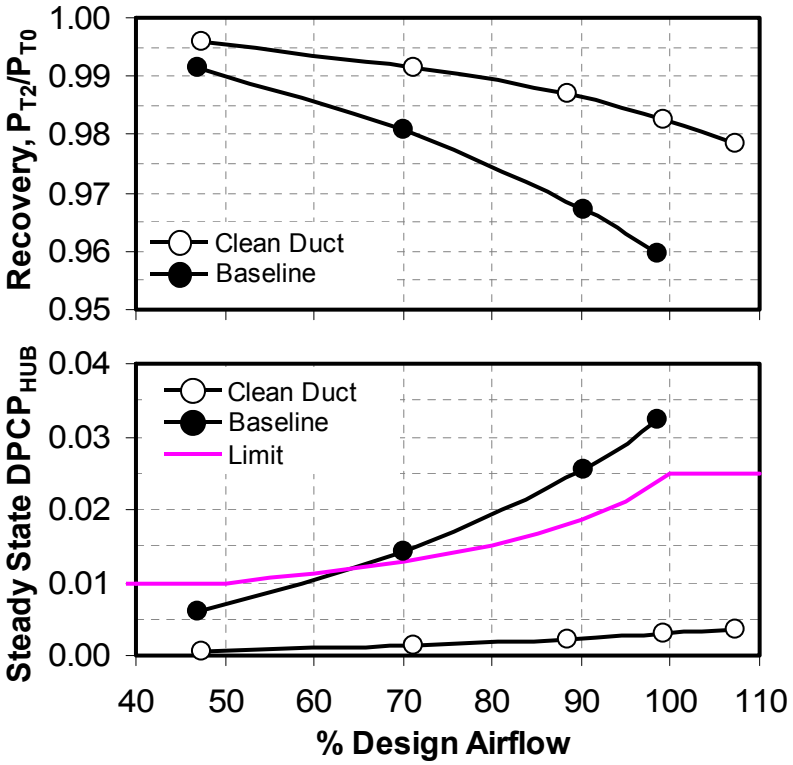

Figure 56. Comparisons of Time-Averaged AIP Total Pressure Recovery and Curcumferential Hub Total-pressure distortion at Various Mass-flow rates

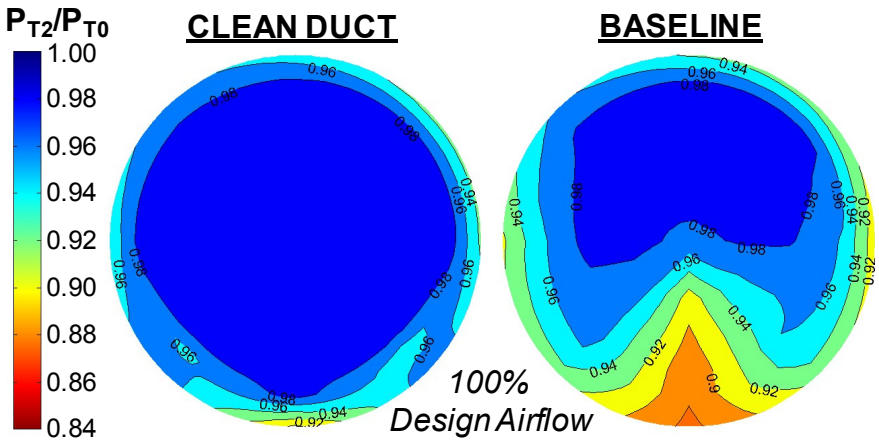

Figure 57. Comparisons of Time-Averaged AIP Total Pressure Contours

As discussed previously, dynamic total-pressure data was collected at the same probe locations as the time-average data. Dynamic distortion descriptors were computed and the largest value was defined as the "peak" value. The peak values of the circumferential hub total-pressure distortion at various diffuser airflows are shown in Figure 58. As was the case in the time-averaged data, as the airflow increased, the distortion increased beyond the limits. The AIP total-pressure pattern at the peak circumferential hub distortion is shown in Figure 59. The results show a larger decrease in total pressure near the bottom center of the AIP pattern.

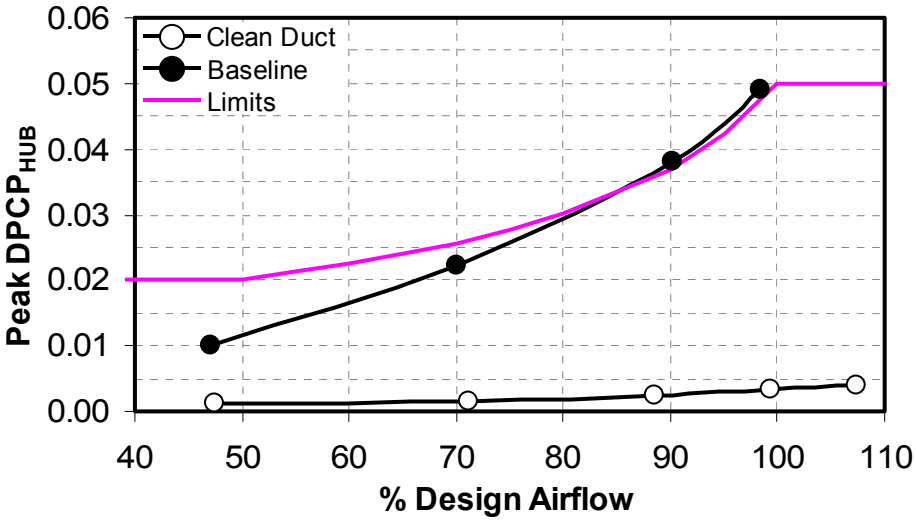

Figure 58. Comparisons of the Peak Circumferential Hub Total-pressure distortion at Various Mass-flow rates

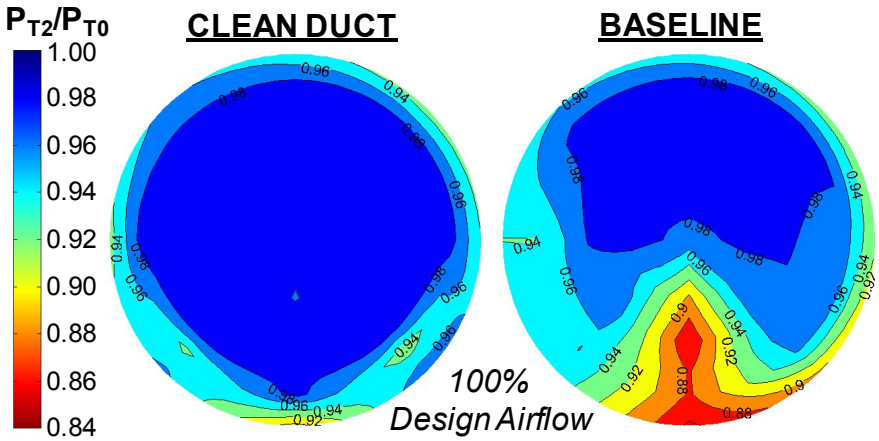

Figure 59. Comparisons of the Peak Circumferential Hub Total Pressure AIP Patterns

Passive Flow Control

As previously shown, the baseline, simulated BLI-inlet duct produced distortion levels that exceeded the limits of current, high-bypass engines consistent with future HWB vehicles. The effectiveness of applied passive flow control in reducing AIP total-pressure distortion was investigated. Statistically designed experiments were employed to evaluate the offset-duct-performance sensitivity to changes in microvane-array configurations. Microvane arrays were installed on the lower surface of the offset duct, downstream of the throat. The arrays were designed to enhance duct performance by counteracting secondary flows. The goal of this endeavor was not to optimize the microvane array, but to establish design guidelines to achieve fail-safe operability. Performance margin was not desired in this case, as that would be achieved through the addition of an active component to the flow-control system.

Four microvane-array design factors were investigated. They were microvane height (H), axial location of the array (X), spanwise distance between the centermost microvanes (Dy_{CL}), and the total number of microvanes (#), Figure 60. Factor limits were defined in both dimensional and non-dimensional parameters, Table 1. The microvane angle was fixed at 12.9° outboard

relative to the streamwise direction. All microvanes had a thickness of 0.075in at the base near the diffuser surface and tapered to 0.025in at the outer tip of the microvane. The factor limits and other design parameters were derived from previous work on BLI inlet ducts (Owens, Allan, & Gorton, 2006).

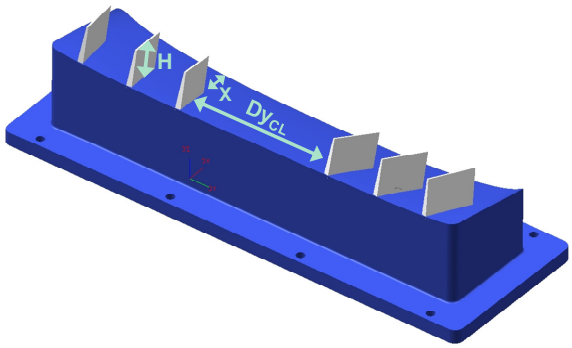

Figure 60. Microvane Array Design Factors

Table 1. Microvane DOE Factors and Limits

	Factor 1 A: Vane Height H [in]	Factor 2 B: Axial Distance from Throat X [in]	Factor 3 C: Spanwise Spacing of Centermost Microvanes Dy_{CL} [in]	Factor 4 D: Number of Microvanes [#]
min	0.25	1.25	0.59	6
max	0.49	1.75	2.28	*10*
	Factor 1 A: Vane Height [1/BL]	**Factor 2 B: Axial Distance from Throat [$1/D_{aip}$]**	**Factor 3 C: Spanwise Spacing of Centermost Microvanes [1/BL]**	**Factor 4 D: Number of Microvanes [#]**
min	0.20	0.25	0.48	6
max	0.40	0.35	1.85	10

The DOE factors were defined to address key issues in microvane-array design. Microvane height was investigated because taller microvanes would likely produce vortices with adequate strength to redistribute the low-pressure air at the AIP and thereby, reduce distortion. However, as the microvane height increased, so would losses in recovery. In the design of passive flow control, it is necessary to balance these effects, which can be accomplished using response surfaces. The axial distance of the array from the throat addressed the question of where to locate microvanes relative to the onset of flow separation, or secondary flow in this case, for maximum effectiveness. The distance between the centermost microvanes addressed the question of whether actuation could be limited to the outboard region of the duct surface, and when considered in conjunction with the number of vanes, the influence of vane-to-vane spacing could be investigated. It can be assumed that reducing the number of vanes would

result in minimizing recovery losses, as well as improve maintainability, manufacturability, and supportability, but the use of too few microvanes in an array would not provide the control required to adequately reduce distortion, so a balance between the metrics must be attained in a microvane array design.

The objective of this experiment was to only evaluate the main effects of the design factors on the performance metrics, with the idea that if a statistically acceptable model could not be defined for the data, additional runs would be conducted to capture the desired two-way interactions. A low-resolution, D-optimal design was employed for this study. D-optimal designs select design points in a way that minimizes the variance associated with the estimates of specified model coefficients. Since only the main effects of the design factors were sought, the D-optimal design was defined to estimate a linear model.

A minimum of five runs was required to solve the four-design-factor, linear problem. Five test configurations were defined based on the D-optimal design methodology. In addition, a center point in the design space, where each factor was set at the midpoint of the range, was added to asses the assumed linearity of the system. Flow control inserts were designed and fabricated such that the six microvane arrays configurations could be integrated into the offset duct model and tested, Figure 61.

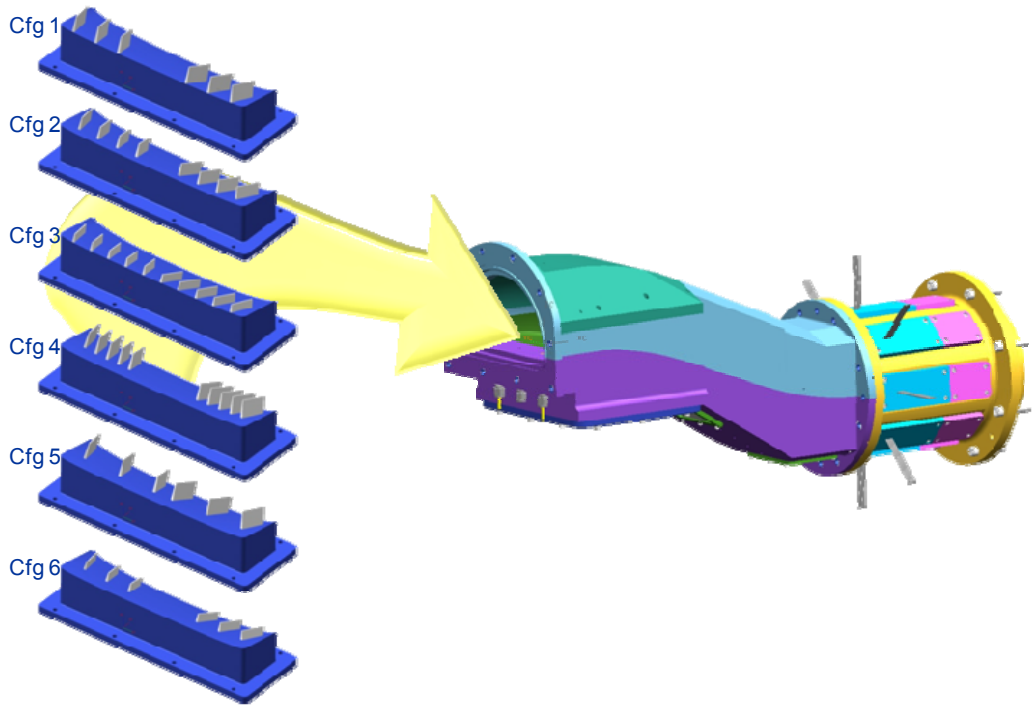

Figure 61. Microvane DOE Configurations

The complete dataset included the six configurations depicted in Figure 61 with repeats of configurations 5 and 6. Two runs from an additional configuration, cfg 0 were also included in the response-surface analysis. Cfg 0 was derived from the optimized results from a previous NASA BLI study (Owens, Allan, & Gorton, 2006). The additional configurations, the center point and cfg 0, were used to assess the model lack of fit, while the repeat runs provided an assessment of the pure error. In total, eleven runs or ten degrees of freedom were available to assess the influence of the four factors under consideration. Data for this study were obtained

experimentally in the GaTech FMRL wind tunnel using the offset duct and inflow fence. The baseline configuration, included only for reference, comprised the duct and fence without microvanes.

The key performance metrics were total pressure recovery and steady-state, total-pressure distortion, with emphasis being placed on the latter. Distortion was measured at the AIP and evaluated in terms of the SAE descriptors described previously. The variation in the measured recovery and distortion levels for the test configurations showed that the response variables were sensitive to the design factors examined in this study. The data showed that the use of microvanes decreased total pressure recovery in all cases, but that the greatest decrease was less than 1%, Figure 62. Generally, the use of passive devices does not improve recovery, and the design criterion is to optimize passive flow control for maximum distortion reduction with minimal reduction in recovery.

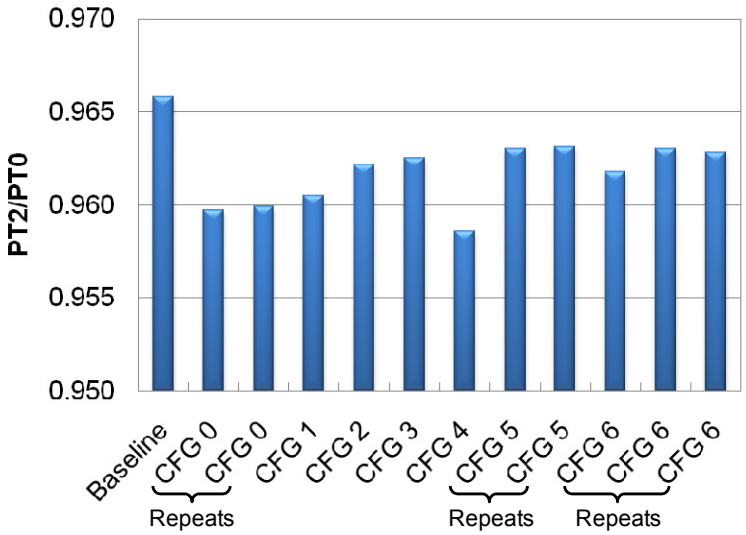

Figure 62. Total Pressure Recovery for DOE Microvane Array Configurations

In addition to recovery, the data showed that acceptable distortion levels could be achieved using microvane-array flow control. The tip circumferential distortion, $DPCP_T$, was below the limit of 0.04 for all configurations, including the baseline, Figure 63. The hub circumferential distortion, $DPCP_H$, exceeded the limit of 0.025 only in the baseline case, indicating that all microvane configurations effectively controlled $DPCP_H$, Figure 63. The radial distortion at the hub, $DPRP_H$ was found to be well below the limit of 0.0 for all configurations, including the uncontrolled baseline, Figure 64. However, all configurations met or exceeded the radial distortion limit at the tip, $DPRP_T$. Furthermore, many of the microvane configurations caused $DPRP_T$ to increase above the baseline value, Figure 64.

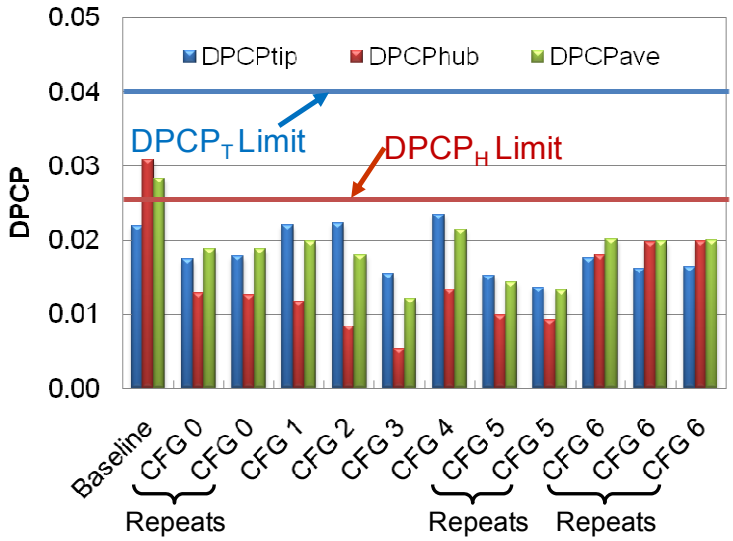

Figure 63. Circumferential Distortion for DOE Microvane Array Configurations

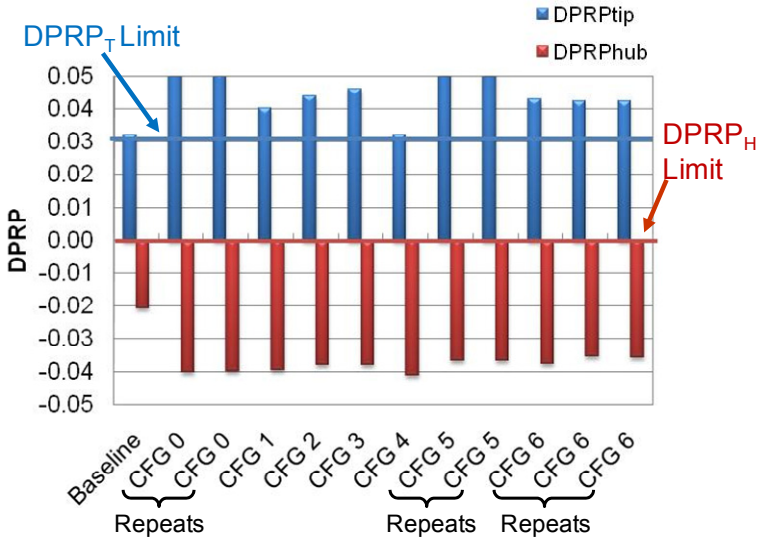

Figure 64. Radial Distortion for DOE Microvane Array Configurations

The effects of the microvanes on the baseline diffuser flow were characterized by the total-pressure measurements at the AIP and by the static-pressure measurements along the upper and lower diffuser surfaces. Figure 65 shows the total pressure contour plots for all the vane configurations. Qualitatively, it appears that the microvane configurations that did not have vanes distributed across the full span of the diffuser, configurations 1, 2, 4, and 6, were not as effective in distributing the low-pressure, baseline flow. Vortices emanating from individual vanes scaled with the vane characteristic dimension. As a result, their entrainment was limited in the spanwise direction. It is believed that once the discrete vortices from the microvanes merged into two large, counter-rotating vortices, they were already pushed towards the diffuser sides and could not significantly impact the mean central zone. Although all four vane configurations noted above had this common feature, there were differences among the resulting flow fields, due to particular characteristics of the microvanes. Thus, Configuration 6, which had three shorter vanes, located outboard on each side of the duct, distributed the baseline, center, low-pressure zone to the sides, without creating significant side lobes of low

pressure, and thereby, reduced the baseline $DPCP_{ave}$ by more than 35%. Configuration 2, which had four, larger vanes similarly distributed on either side of the duct generated a greater reduction in the central low-pressure zone, but also generated detached, stronger side lobes of low pressure that did not exist in the baseline flow. These two competing effects resulted in a reduction of the baseline $DPCP_{ave}$ by about 30%. The taller microvanes in Configuration 6 were even less effective in distributing the baseline, center, low-pressure region but produced equally strong side lobes of low pressure. The resulting reduction in $DPCP_{ave}$ compared to the baseline was just over 20%. Configuration 4, which included the maximum number of tall microvanes, densly packed outboard from the center of the duct was least effective in redistributing the baseline low-pressure flow and generated the strongest low-pressure lobes on the sides, resulting in only a 15% reduction in $DPCP_{ave}$ from the baseline. The two microvane configurations that appeared to be most effective in redistributing the low-pressure flow were Configurations 3 and 5. The six, tall vanes, evenly distributed across the duct with the greatest vane-to-vane spacing distributed most of the central, low-pressure flow found in the baseline case upward, along the walls, generating thicker layers of low-pressure along the sides than at the bottom,. The result was a reduction in the baseline $DPCP_{ave}$ by nearly 50%. However, the more uniform distribution of the low-pressure flow resulting from Configuration 3, which had more, shorter microvanes than Configuration 5 was most effective in reducing $DPCP_{ave}$ as proven by the nearly 60% reduction from the baseline.

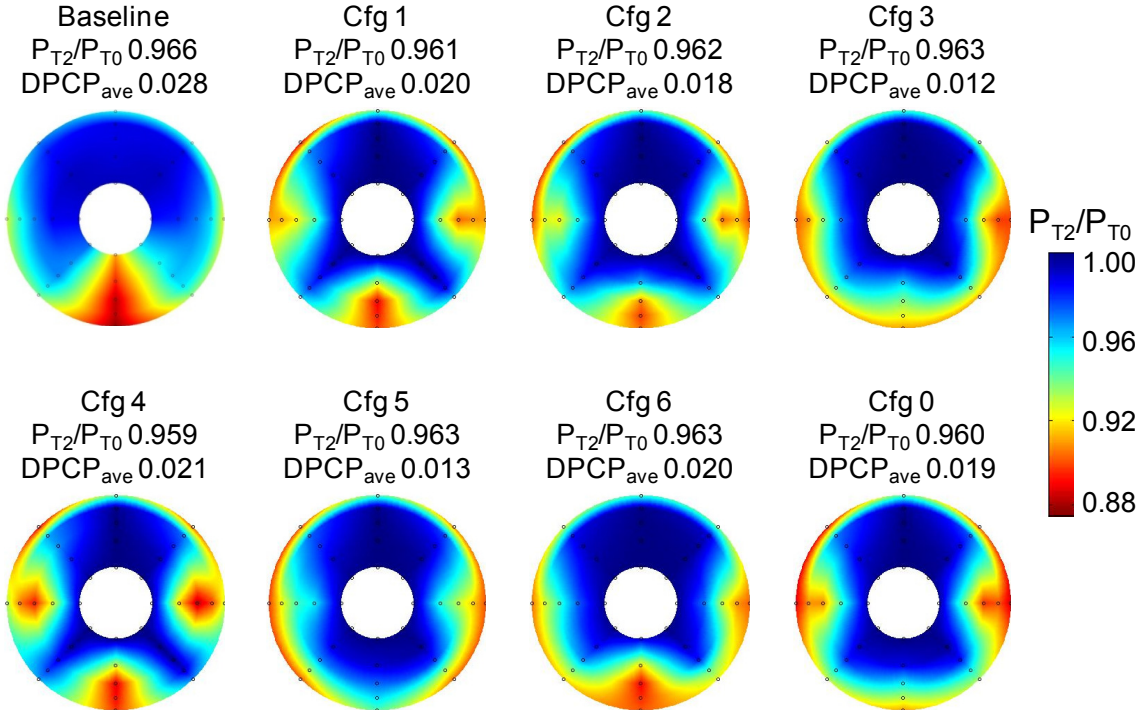

Figure 65. AIP Total pressure Contours for Passive Flow Control (M_{AIP} = 0.55)

Regression analyses of the dataset showed that there were nonlinearities in the responses that would not be accounted for by linear models. The eleven data points provided enough degrees of freedom to include non-linear terms, such as two-way interactions, in the analyses. However, since the design was defined with the objective of only predicting the main effects of the factors, several of the two-way interactions were confounded and could not be resolved. As a result, only the interactions between microvane height and microvane axial location and between

microvane spanwise location and microvane height could be evaluated in the response-surface analyses. It should be noted that interactions between factors other than those evaluated could have a significant influence on the response variables. For instance, the interaction between the number of microvanes and the spanwise spacing of the centermost vanes, which influences the vane-to-vane spacing, would likely affect the performance metrics, However, this interaction was confounded with the main effects and could therefore, not be isolated in the absence of additional data.

Response-surface models were generated for all of the performance metrics through backward regression analyses from a linear model plus the 2-way interactions between microvane height and microvane axial location and between microvane spanwise location and microvane height. Only statistically significant terms and those required to maintain the model hierarchy were retained in the final response-surface models.

The response surface analysis in terms of total pressure recovery showed that the factors of influence were microvane height, axial location, spanwise spacing of the centermost microvanes and the interactions between microvane height and microvane axial location and between microvane spanwise location and microvane height. The response surface equation, Equation 6, presented here in terms of actual (uncoded) factors, shows that the interaction between the spanwise location of the centermost vanes and the microvane height had the greatest influence on the recovery.

Recovery = 1.002 - 0.0622 * Vane Height - 0.0423 * Axial Location from Throat + 0.0339 * Spanwise Location of Centermost Vanes + 0.0785 * Vane Height * Axial Location from Throat - 0.0804 * Vane Height * Spanwise Location of Centermost Vanes

Equation 6

A surface plot of the response, as a function of spanwise microvane location and vane height shows that the highest recovery would be obtained by minimizing the microvane height and locating the microvanes outboard from the duct centerline, Figure 66. The response surface for recovery in terms of microvane height and axial location also shows that shorter vanes produce higher recovery, especially when located closer to the throat Figure 67.

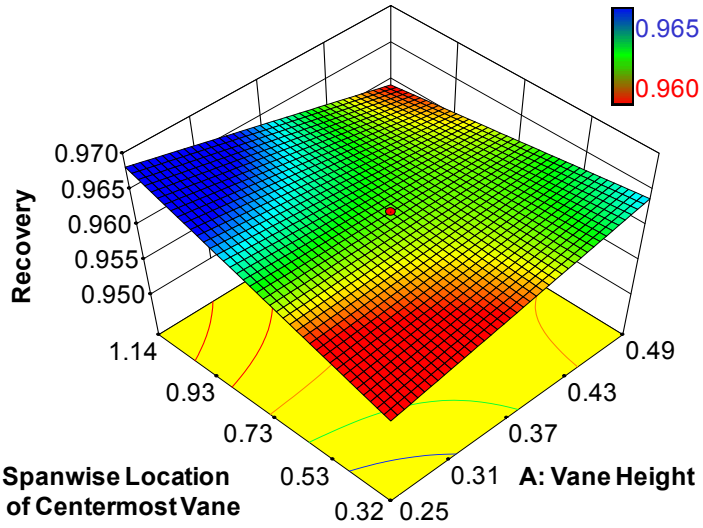

Figure 66. Influence of Microvane Spanwise Location and Microvane Height on Total Pressure Recovery

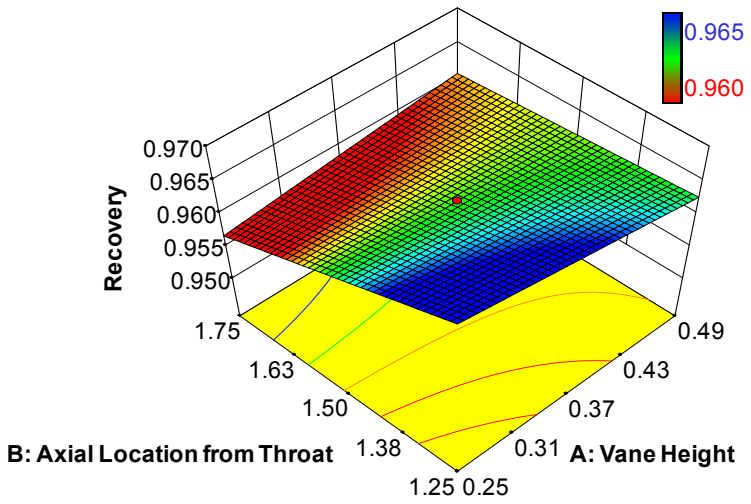

Figure 67. Influence of Microvane Height and Axial Location on Total Pressure Recovery

In addition to recovery, response surfaces were generated for circumferential total-pressure distortion at the hub. Through a backward regression analysis, the statistically significant terms in the hub distortion response surface equation, Equation 7, were found to be microvane height, axial location, spanwise spacing of centermost microvanes, number of microvanes, and the interactions between microvane height and microvane axial location and between microvane spanwise location and microvane height. The most influential terms were the axial location of the microvane array and the interaction between microvane spanwise location and height. Based on the model, hub circumferential distortion would be reduced by reducing the microvane height and locating the centermost microvanes outboard of the centerline, Figure 68. However, the taller microvanes combined with locating the center microvanes closer to the duct centerline was predicted to produce hub distortions nearly as low as the former combination, which fits well with the guideline derived from the microvane height/axial location interaction, Figure 69 that suggests designing taller microvanes located closer to the throat. Finally, the analysis predicted that the hub distortion would also be reduced by increasing the number of microvanes in the array, Figure 70.

$$DPCP_H = -0.190 + 0.332 * \text{Vane Height} + 0.246 * \text{Axial Location from Throat} - 0.184 * \text{Spanwise Location of Centermost Vane} - 3.08E\text{-}3 * \text{Number of Vanes} - 0.445 * \text{Vane Height} * \text{Axial Location from Throat} + 0.416 * \text{Vane Height} * \text{Spanwise Location of Centermost Vane}$$

Equation 7

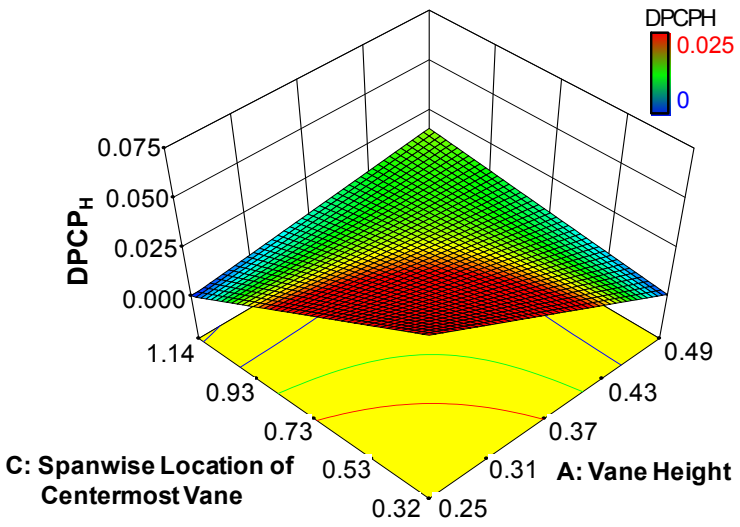

Figure 68. Influence of Microvane Spanwise Location and Microvane Height on Hub Circumferential Distortion

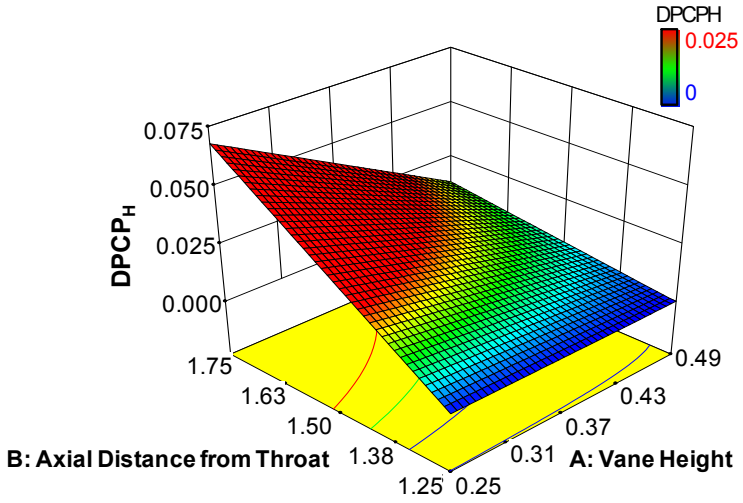

Figure 69. Influence of Microvane Axial Location and Microvane Height on Hub Circumferential Distortion

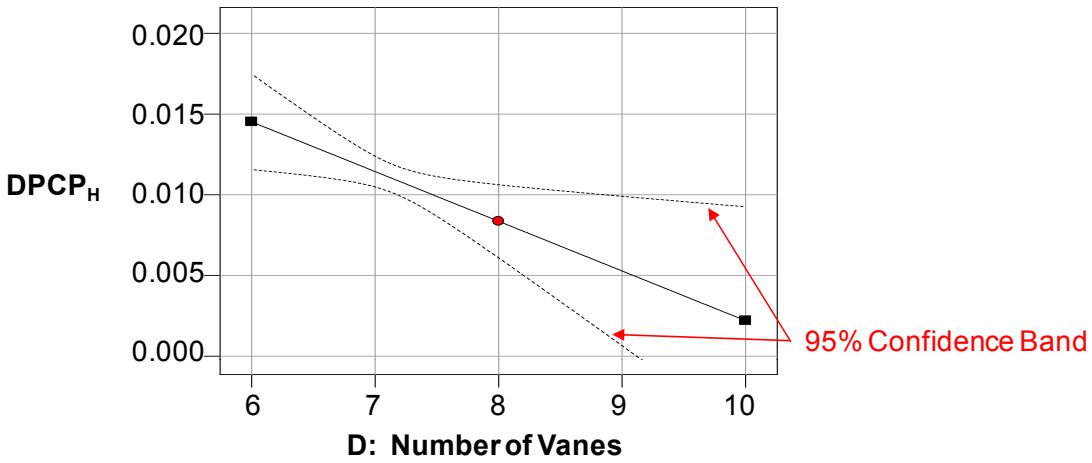

Figure 70. Effect of the Number of Microvanes on Hub Circumferential Distortion

In addition to hub circumferential distortion, design guidelines were developed for minimizing the tip circumferential distortion. As in the case of hub circumferential distortion, the statistically significant terms in the tip distortion response surface model, Equation 8, were microvane height, axial location, spanwise spacing of the centermost microvanes, number of microvanes, the interactions between microvane height and microvane axial location and between microvane spanwise location and microvane height. Again, the two most influential terms in the model were axial location of the microvane array and the interaction between microvane spanwise location and height, with the latter having a greater effect than the former. Based on the response surface, tip circumferential distortion would be lowered by reducing the microvane height and locating the centermost microvanes closer to the duct centerline, Figure 71. In addition, reduced $DPCP_T$ was predicted when shorter microvane arrays were located farther downstream of the throat, Figure 72. Finally, unlike $DPCP_H$, the tip circumferential distortion was predicted to decrease with a reduced number of microvanes in the array, Figure 73.

$DPCP_T$ = 0.144 - 0.181 * Vane Height - 0.238 * Axial Location from Throat + 0.239 * Spanwise Location of Centermost Vane + 0.005 * Number of Vanes + 0.407 * Vane Height * Axial Location from Throat - 0.518 * Vane Height * Spanwise Location of Centermost Vane

Equation 8

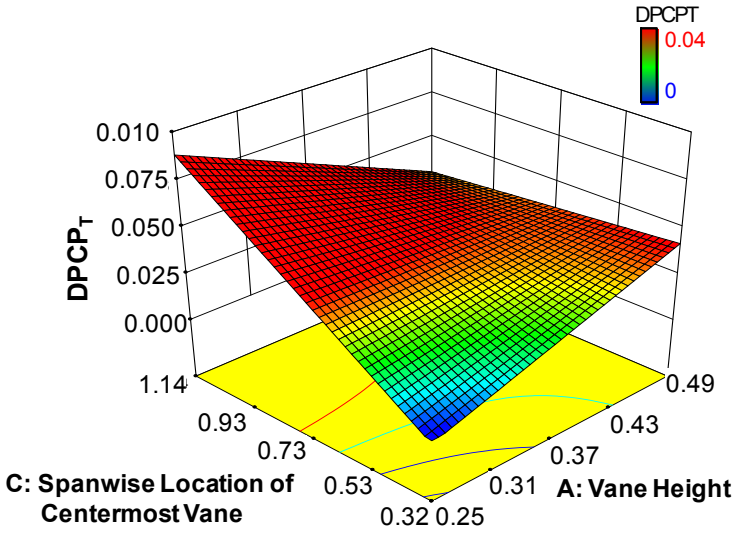

Figure 71. Influence of Microvane Spanwise Location and Microvane Height on Tip Circumferential Distortion

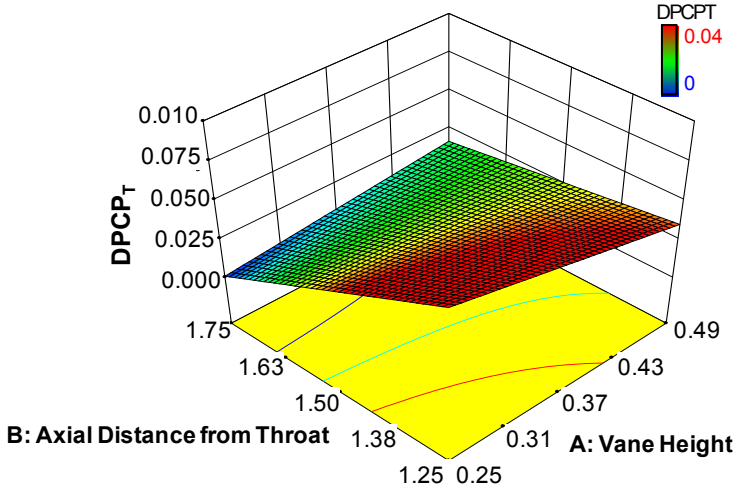

Figure 72. Influence of Microvane Axial Location and Microvane Height on Tip Circumferential Distortion

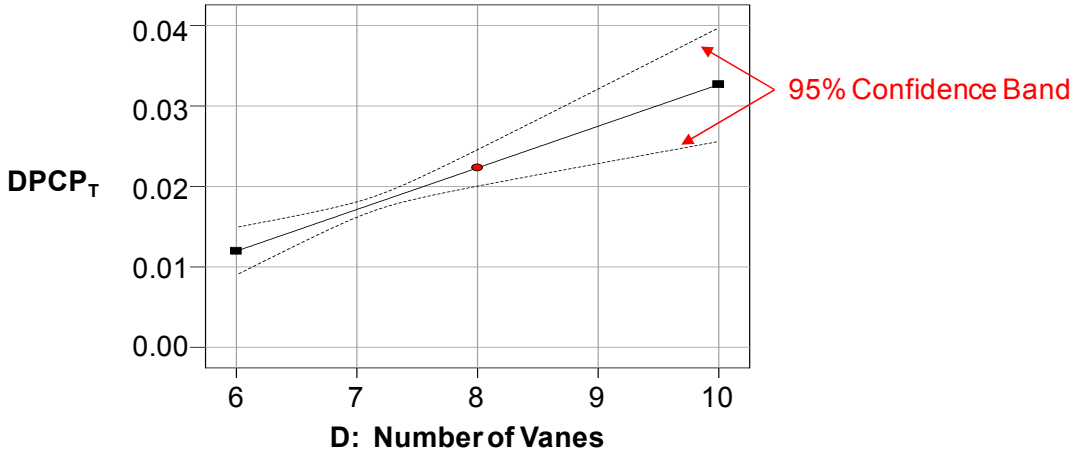

Figure 73. Effect of the Number of Microvanes on Tip Circumferential Distortion

Response surfaces were defined not only in terms of circumferential distortion parameters, but also in terms of radial distortion metrics. The response surface that resulted from a backward regression analysis of the design factors and two-way interactions in terms of radial distortion at the hub, Equation 9, was unique in that it was the only response variable that was accurately represented by a linear model. The design factors that were found to be statistically significant in the $DPRP_H$ model were the microvane height, spanwise spacing of the centermost microvanes, and the number of microvanes in the array. Axial location did not have a statistically significant impact on the radial distortion at the hub. The number of microvanes was found to be the largest contributor to the prediction of the hub radial distortion, followed closely by the microvane height. Based on the response surface, hub radial distortion would be reduced by increasing the number of microvanes and the microvane height, Figure 74 and Figure 75, respectively, and locating the centermost microvanes outboard from the duct centerline, Figure 76.

$$DPRP_H = -0.027 - 0.010 * \text{Vane Height} - 0.002 * \text{Spanwise Location of Centermost Vane} - 0.001 * \text{Number of Vanes}$$

Equation 9

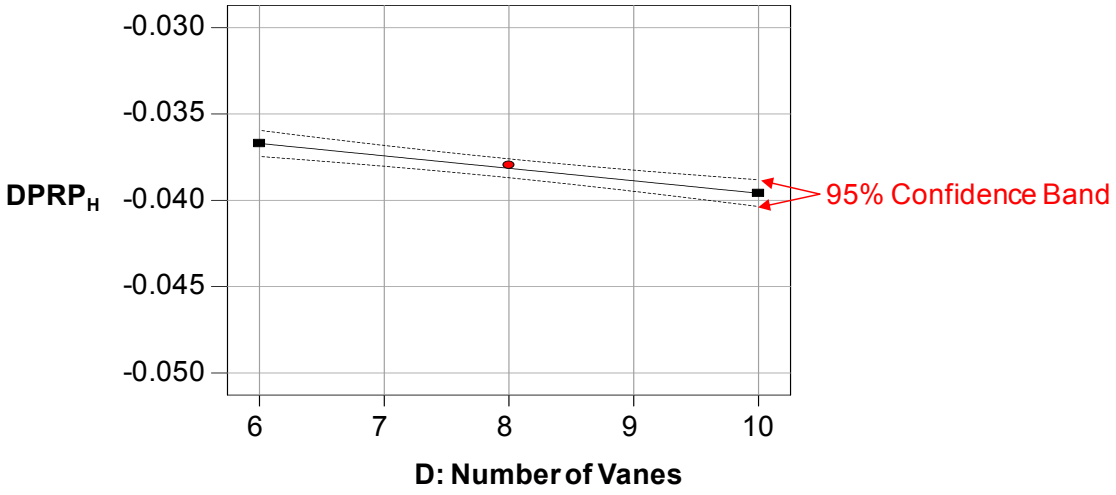

Figure 74. Effect of the Number of Microvanes on Hub Radial Distortion

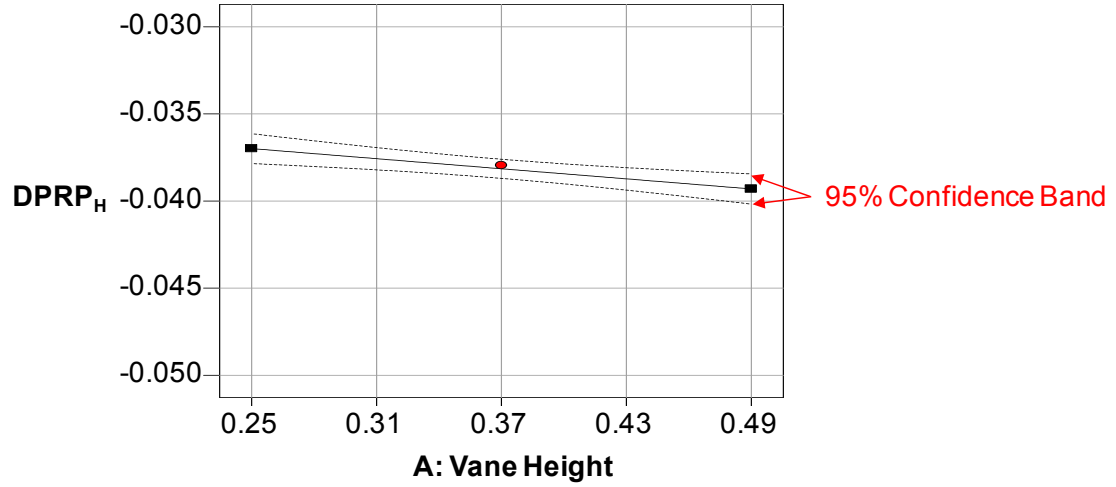

Figure 75. Effect of Microvane Height on Hub Radial Distortion

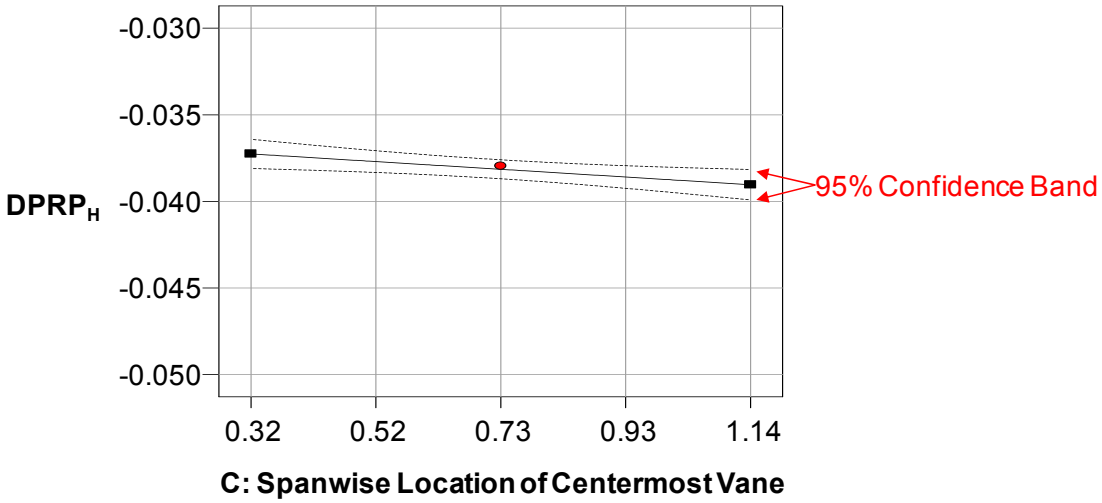

Figure 76. Effect of Microvane Spanwise Location on Hub Radial Distortion

The tip radial distortion response surface also contained a unique combination of terms. Specifically, the backward regression analysis of the design factors and two-way interactions showed that the tip radial distortion could be accurately represented by the microvane height, axial location of the microvanes from the throat, the spanwise spacing of the centermost microvanes, the number of microvanes in the array, and the interaction between the microvane height and the axial location of the microvanes, Equation 10. The spanwise spacing of the centermost vanes was found to have the largest effect on the tip radial distortion, followed by the interaction term and then the number of microvanes. The microvane height by itself was not found to be a statistically significant factor in predicting the tip radial distortion but was retained in the model to maintain the hierarchy. Unlike the hub radial distortion, identifying a microvane design within the design space of this investigation that would satisfy the distortion limit of 0.03 was challenging. The lowest tip radial distortions were predicted to occur when the spanwise spacing of the centermost vanes was maximized, Figure 78, when both the microvane height and the axial distance of the array from the throat were minimized, Figure 78, and finally, when the number of microvanes in the array was maximized, Figure 79.

$$DPRP_T = -0.0093 + 0.1835 * \text{Vane Height} + 0.0505 * \text{Axial Location from Throat} - 0.0210 * \text{Spanwise Location of Centermost Vane} - 0.0009 * \text{Number of Vanes} - 0.1215 * \text{Vane Height} * \text{Axial Location from Throat}$$

Equation 10

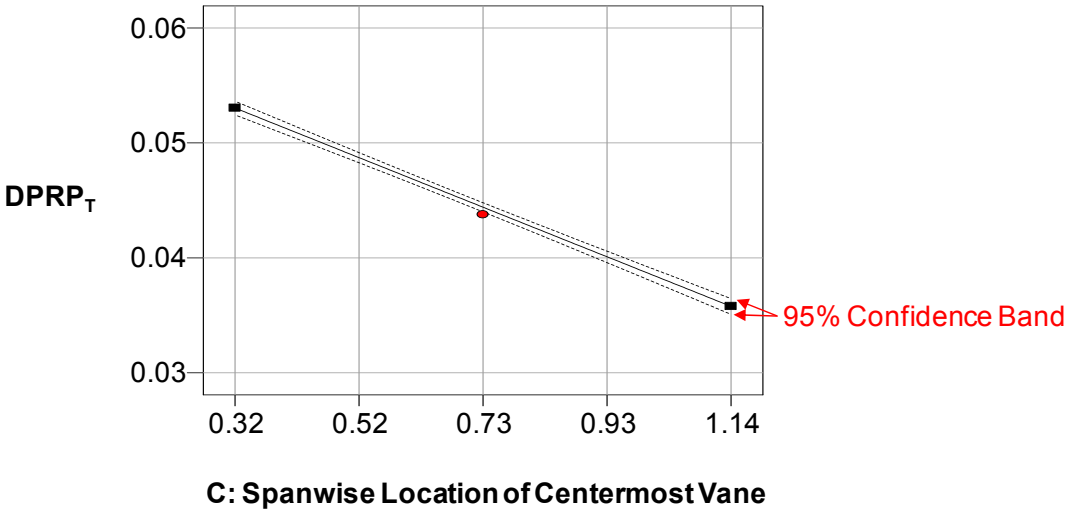

Figure 77. Effect of Microvane Spanwise Location on Tip Radial Distortion

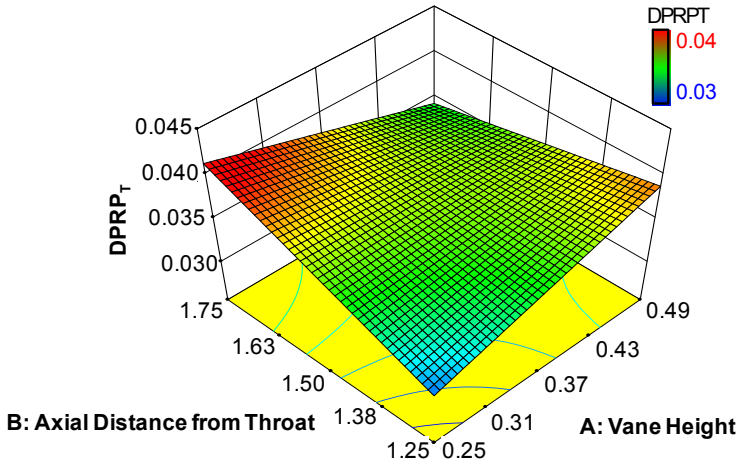

Figure 78. Influence of Microvane Axial Location and Height on Tip Radial Distortion

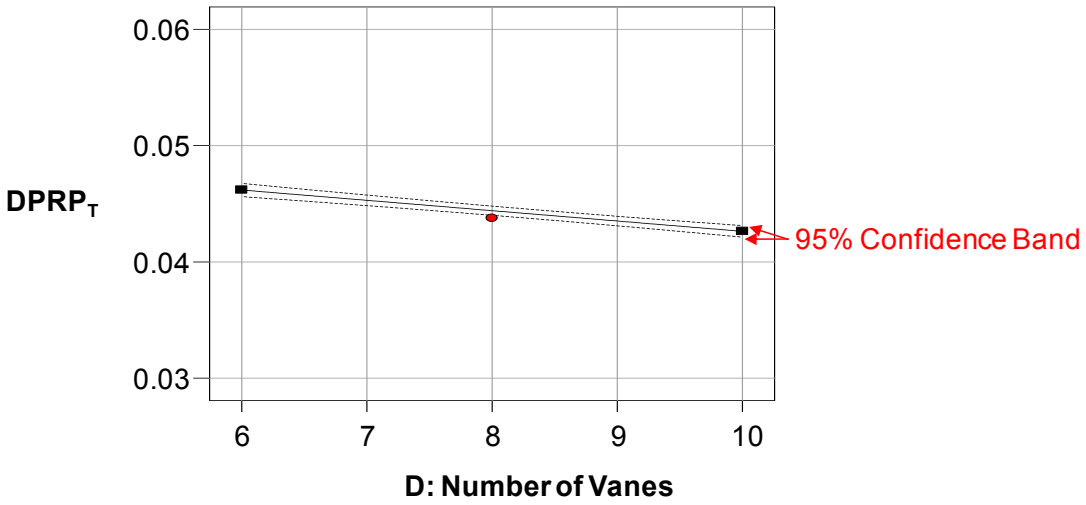

Figure 79. Effect of Number of Microvanes on Tip Radial Distortion

Design guidelines were developed in terms of microvane height, axial location, spanwise spacing of the centermost microvanes, and the number of microvanes in the array for improved total pressure recovery, circumferential hub and tip distortion and radial hub and tip distortion. The resulting design guidelines for maximizing recovery and minimizing total-pressure distortion are summarized in Table 2, where yellow cells and blue cells indicate minimum and maximum values of the design factors, respectively. Specifically, increased recovery was predicted to be obtained with shorter microvanes, axially located closer to the throat, with larger spanwise spacing between the centermost microvanes. Optimal hub circumferential distortion was predicted to result from designing arrays with more, taller microvanes that were evenly distributed across the span of the duct and located closer to the throat. However, tip circumferential distortion would be more likely optimized by employing arrays with fewer, shorter microvanes located downstream from the throat, but still equally spaced across the span of the duct. Finally, based on the results of the response surface analyses, radial distortion at the hub and tip would be optimized through the use of arrays with more, shorter microvanes, spaced outboard from the centerline and axially located closer to the throat.

Table 2. Microvane Design Guidelines

	Recovery	$DPCP_H$	$DPCP_T$	$DPRP_H$	$DPRP_T$	
Microvane Height	Shorter	Taller	Shorter	Shorter	Shorter	
Axial Location from Throat	Upstream	Upstream	Downstream		Upstream	Minimum
Spanwise Location of Centermost Microvane	Outboard	Inboard	Inboard	Outboard	Outboard	Maximum
Number of Microvanes		More	Fewer	More	More	

The response surface results were applied in designing the microvane configuration to use as the passive component of the hybrid flow-control system. Shorter microvanes were selected, because they tended to improve recovery, DPCPT, DPRPH, and DPRPT. In addition, shorter vanes offered benefits in terms of other metrics such as robustness, maintainability, and supportability. Generally, locating the microvanes upstream from the throat produced better performance for most metrics. However, it was not an influential factor in the hub radial

distortion. Furthermore, model hardware limitations resulted in a very small range for this factor, and the fact that the effects of axial location were confounded with some potentially influential two-way interactions would perhaps call for additional trials to verify that predicted changes in the response variable were actually due to changes in the axial location. Design guidelines in terms of the spanwise spacing between the centermost vanes for the response variables were conflicting. Radial distortion and recovery both favored increased center-microvane spacing. Finally, favorable responses for all the performance metrics, excluding the tip circumferential distortion were obtained by increasing the number of microvanes. However, the combination of more microvanes and increasing the gap between the centermost vanes resulted in a configuration with little space for installing active devices between the microvanes. For this reason, a configuration with fewer microvanes was selected for further study and integration with active devices. Microvane Configuration 6 possessed all of the selected design attributes and was therefore chosen as the passive-device configuration for the hybrid studies.

Figure 80 shows the time-averaged total pressure recovery and distortion resulting from the use of microvane flow control compared with the baseline at various mass-flow rates. The results show the passive flow control has little effect on recovery compared with baseline through a range of mass-flow rates. However, the passive flow control was shown to reduce the steady-state circumferential hub distortion. The distortion was reduced to near the limits. This indicates that the passive devices can effectively reduce distortion without adversely affecting the recovery of the inlet system. However, the results indicate that additional flow control is required to push the distortion below the limits into an operable range for this type of engine.

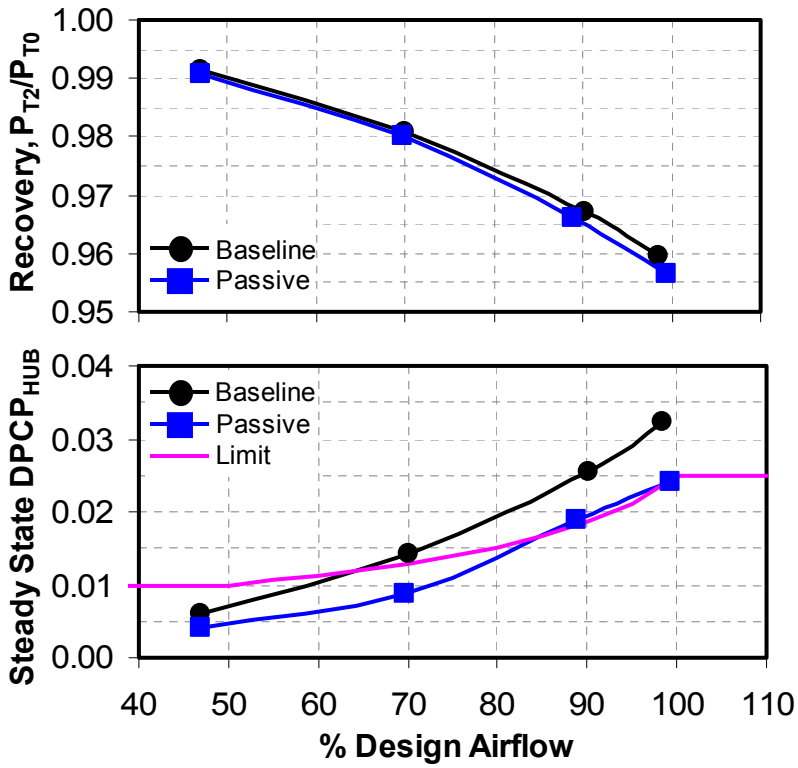

Figure 80. Passive Flow Control Comparisons of Time-Averaged AIP Total Pressure Recovery and Circumferential Hub Total-pressure distortion at Various Mass-flow rates

The time-average AIP total pressure contours are shown in Figure 81. This compares the AIP pattern from the baseline configuration and the passive configuration. The baseline pattern shows the total pressure losses are located at the lower centerline of the AIP pattern. The pattern for the passive array indicate that the microvanes are able to spread the losses occurring to three smaller areas of losses around the outer edge of the pattern. Spreading the one large area of loss into three smaller regions indicates the reasons the distortion was reduced and the recovery was unaffected.

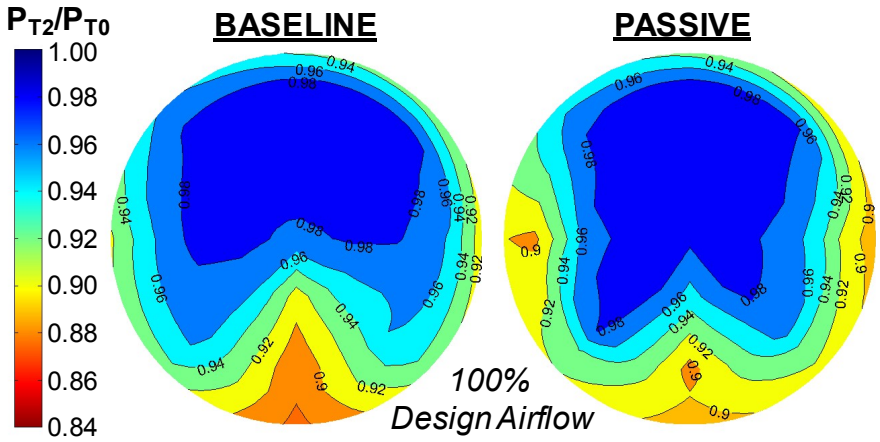

Figure 81. Passive Flow Control Comparisons of Time-Averaged AIP Total Pressure Contours

In addition to steady-state total-pressure measurements, dynamic data was collected with the passive flow-control devices as described previously for the baseline configuration. The dynamic data was collected at the AIP in the same probe locations as the time-averaged data. The peak data for each distortion descriptor was computed for each passive configuration that was tested. The peak circumferential hub total-pressure distortion is shown in Figure 82 for the passive configuration and is compared with the baseline data at various mass-flow rates. The results show the passive flow control is able to reduce the peak distortion just below the prescribed limit at the higher mass-flow rates. These results show the passive flow control is able to reduce the distortion below the limits, but further flow control could be utilized to gain additional margin for the peak distortion. The AIP peak total pressure contours are shown in Figure 83. The total pressure contours show similar results as the time averaged results. The passive flow control is able to spread the total pressure losses for the peak pattern and hence reduce the peak distortion value.

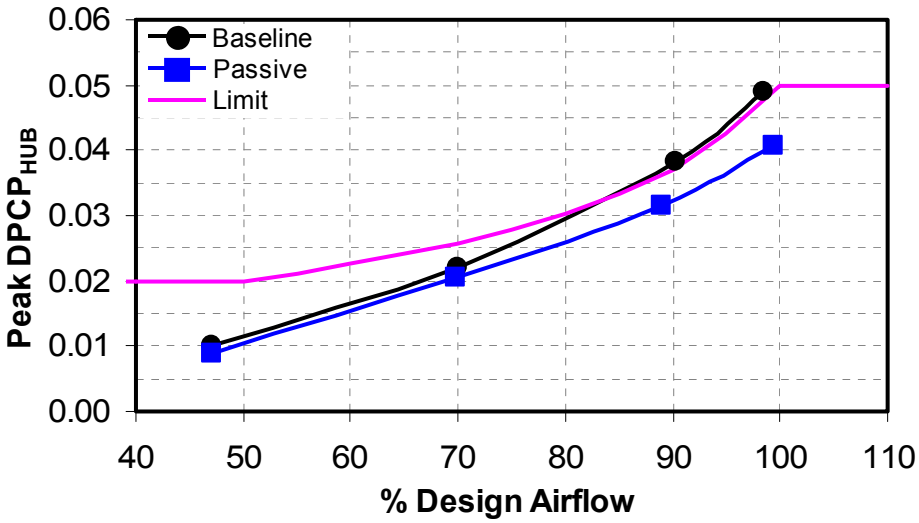

Figure 82. Passive Flow Control Comparisons of the Peak Circumferential Hub Total-pressure distortion at Various Mass-flow rates

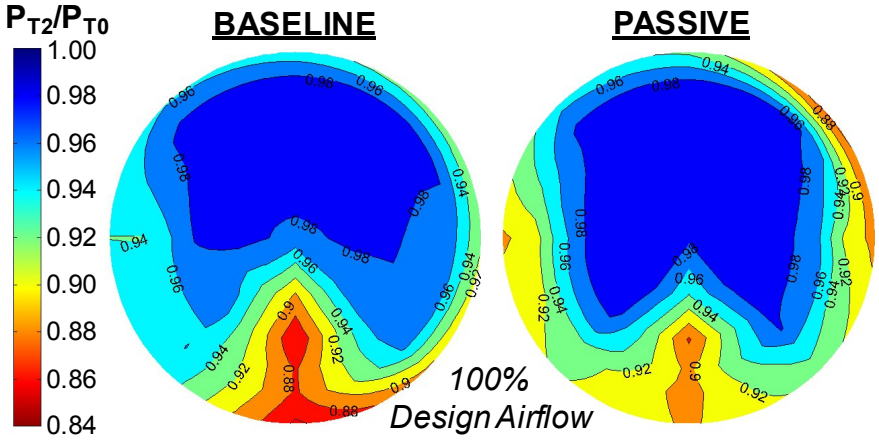

Figure 83. Passive Flow Control Comparisons of the Peak Circumferential Hub Total Pressure AIP Patterns

Active Flow Control

It was determined with initial testing that the flow control in the diffuser would required the development of more powerful synthetic jets than the ones that can be built as the current state-of-art piezoelectric-driven synthetic jets, which were used in preliminary studies in the square duct. As further development of the piezoelectric-based synthetic jets is an ongoing process in the engineering community, the initial study of the present project also serves as guidance for the necessary performance level of such synthetic-jet actuators, if they are to be used for high subsonic duct-flow applications. For the task at hand, however, an alternative piston-driven synthetic-jet actuator module was developed and utilized. Schematics of the actuator module are shown in Figure 20. Three pistons were synchronously driven to generate expulsion and suction cycles through the skewed jet orifices, which symmetrically point outward the central plane. The synthetic jets are operated harmonically, at variable frequencies up to 133 Hz in the present design. Nominally, for the hybrid control tests the upstream insert was populated with

passive flow control vanes in a pattern and location that was designated for the hybrid control integration, labeled as CFG 6 in the passive-control study.

Figure 84 shows the time-averaged total pressure recovery and circumferential hub total-pressure distortion at various diffuser mass-flow rates. The results show the active flow control had no effect on the time-average recovery, but was able to reduce the time-averaged distortion compared with the baseline results. The active flow control also has near constant effect across the airflow range giving more effectiveness at lower airflows than compared with the passive device. The comparison of the AIP total pressure patterns for the active flow control configuration and the baseline configuration are shown in Figure 85. The results show that the active flow control was able spread the total pressure losses around the outer portion of the AIP. This is similar to the results for the passive flow control, but slightly less effective. The passive and active flow control results were both effective at reducing the distortion without a negative effect on recovery. These results indicate the possibility of a hybrid system that can combine both the passive and active devices for additional reduction in distortion.

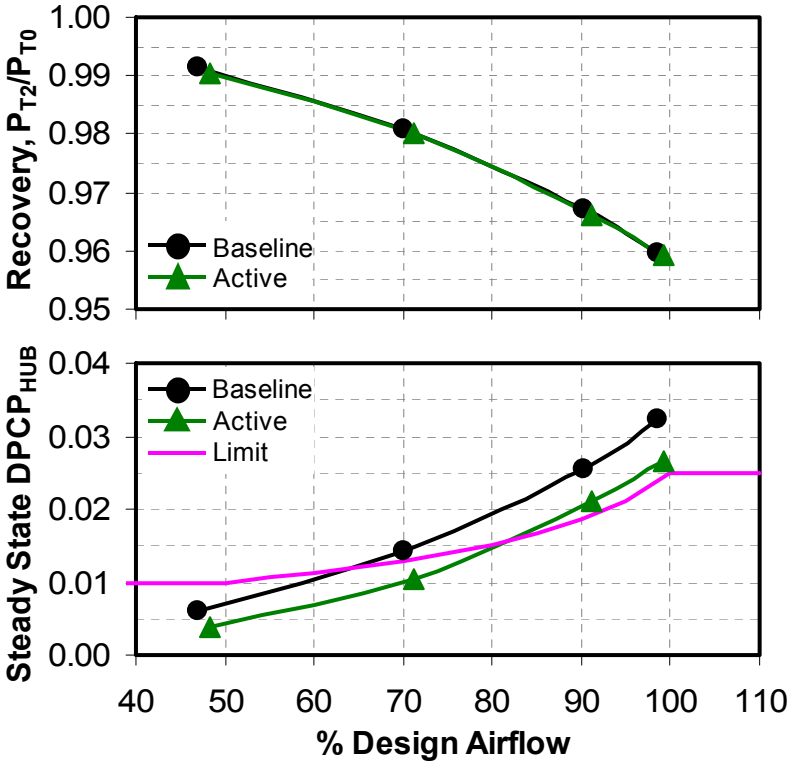

Figure 84. Active Flow Control Comparisons of Time-Averaged AIP Total Pressure Recovery and Circumferential Hub Total-pressure distortion at Various Mass-flow rates

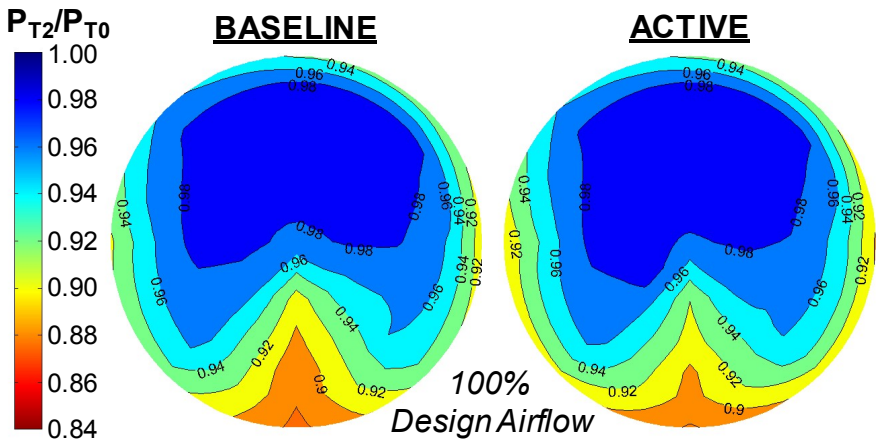

Figure 85. Active Flow Control Comparisons of Time-Averaged AIP Total Pressure Contours

Dynamic data was also computed for the active flow-control devices. Comparison of the peak circumferential hub total-pressure distortion for the active flow control with the baseline configuration is shown in Figure 86. The active flow control configuration slightly reduces the peak circumferential hub distortion, but is able to reduce it below the dynamic limits. The synthetic jets have less effectiveness than the passive devices on reducing peak distortion. This may be due to the frequency of the synthetic jet and further study is needed to adjust the frequency to increase the effectiveness on dynamic distortion. Figure 87 shows the AIP total pressure patterns at the peak circumferential for the active flow control and baseline configurations. The patterns show the active flow control is able to reduce the total pressure loss at the lower centerline location of the AIP by spreading the losses around the edges of the AIP.

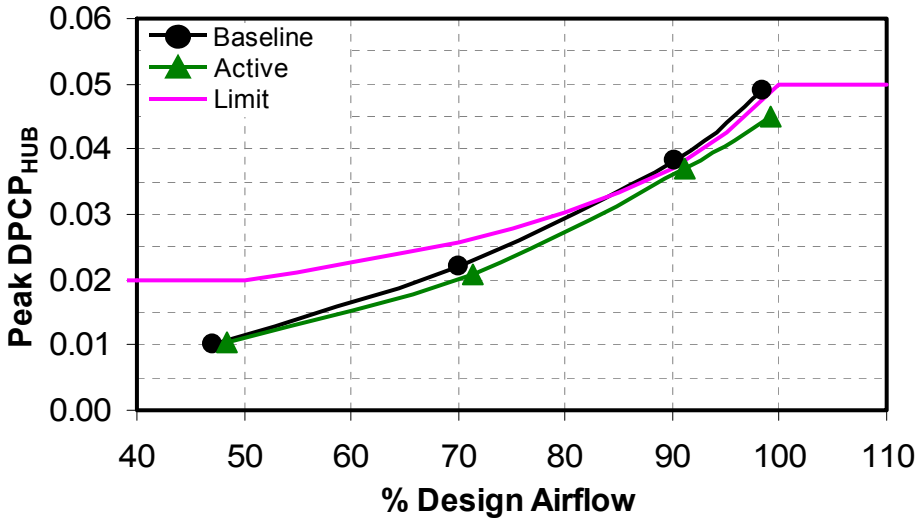

Figure 86. Active Flow Control Comparisons of the Peak Circumferential Hub Total-pressure distortion at Various Mass-flow rates

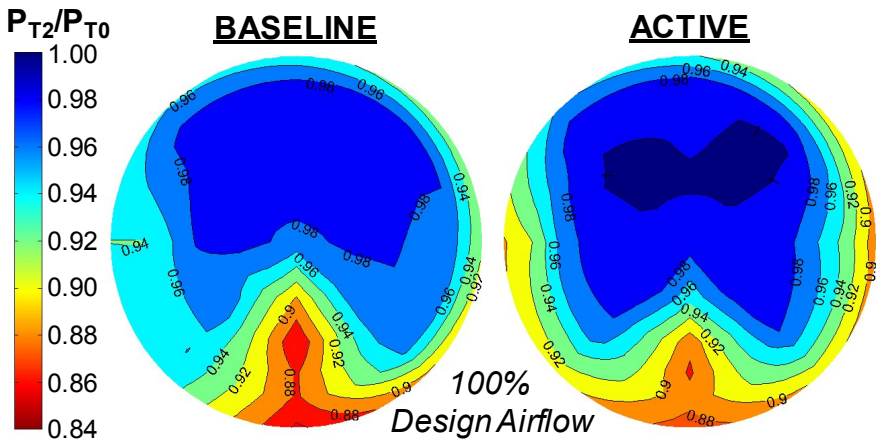

Figure 87. Active Flow Control Comparisons of the Peak Circumferential Hub Total Pressure AIP Patterns

Hybrid Flow Control

The spatial distributions of the hybrid flow-control devices that would impose the most favorable changes on the baseline flow and the jet momentum required to achieve such changes was examined in the offset diffuser. The preliminary study was conducted by utilizing steady jets in place of synthetic jets, as it was expected that the underlying dynamics were similar and the conclusions would therefore be transferable. In addition, use of steady jets significantly reduced the overall test time and required resources.

To investigate the efficacy of steady jets in the offset diffuser, arrays of jet orifices were distributed on the control surface such that the orifices were skewed off normal to the wall surface and were pointed laterally away from the center plane of symmetry, as schematically shown in Figure 88. Figure 88 shows two control inserts with integrated slotted rectangular jet orifices, Figure 88a, and round, circular orifices, Figure 88c. The exit area of the slotted jets was approximately twice that of the round jets. As a result, the mass flow rate of the slotted jets was set at approximately twice that of the round jets in order to produce approximately the same jet exit velocity in both types of jet. However, it should be noted that the slotted jets delivered twice the momentum to the flow.

As expected, individual same-sense vortices generated on each side of the duct merged into two, large-scale vortices, as reflected in the changes in the AIP pressure distributions shown for each control configuration. In both cases, a pair of counter-rotating vortices with opposite sense acted upon the secondary flow in the baseline diffuser. The vortices reduced the extents of the distortion pattern in the central, lower region and redistributed it circumferentially along the wall. The skewed, slot jets move the low-pressure region up, along the wall away from the plane of symmetry, Figure 88b, diffusing the concentration of low pressure and thereby, reduced the overall distortion ($DPCP_{ave}$) by 47%. The skewed circular jets had a similar impact on the flow, which was reflected in the movement of the low-pressure zone away from the centerline of the AIP, Figure 88d, resulting in a decrease in the $DPCP_{ave}$ of 32%, when compared to the baseline tunnel flow. Although the overall reduction in pressure distortion was lower for the circular jet pattern, it was also achieved at half the jet momentum, relative to the slotted jets.

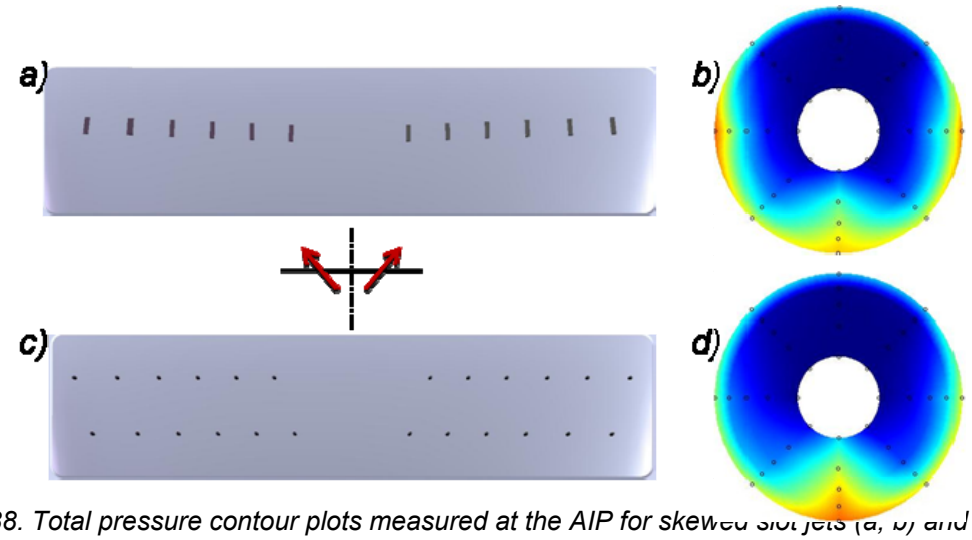

Figure 88. Total pressure contour plots measured at the AIP for skewed slot jets (a, b) and skewed circular jets (c, d) at MAIP = 0.49 (Q_{jet} = 600 lpm, $DPCP_{ave}$ = 0.0143), and MAIP = 0.51 (Q_{jet} = 300 lpm, $DPCP_{ave}$ = 0.0186) respectively. The Pressure contour levels are the same as in Figure 55

As previously documented in this report, a DOE analysis was conducted to identify the microvane configuration for the hybrid system. AIP total-pressure contours resulting from that microvane configuration (CFG 6), Figure 89a, revealed the addition of two counter-rotating vortices, which effectively distributed some of the low-pressure region, concentrated at the center, lower portion of the baseline flow, up, along the walls, away from the plane of symmetry. The three-lobed structure with a low-pressure remnant near the bottom, center of the AIP indicated that the two counter-rotating structures formed by the opposing microvane arrays were spaced too far apart to fully redistribute the pressure deficit. Consequently, only an 18% reduction in $DPCP_{ave}$ was achieved by exclusively passive control. However, pairing steady jets with CFG 6 in a passive/active-hybrid configuration would likely improve the performance the flow-control effectiveness.

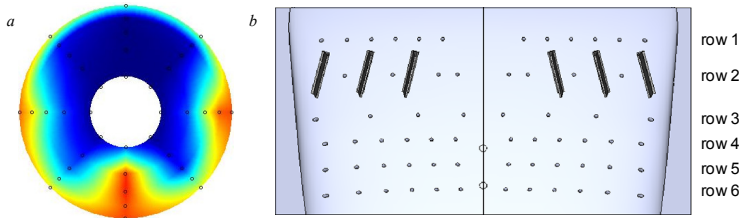

Figure 89. a) Total pressure contour plot measured at the AIP for the passive CFG6 control at MAIP = 0.56 ($DPCP_{ave}$ = 0.0222) and b) Schematics of the control insert illustrating relative position of the CFG6 microvanes and six rows of skewed circular jets. Pressure contour levels are the same as in Figure 55

The performance sensitivity to the relative location of the active and passive components of a hybrid system was enabled using the control insert depicted in Figure 89b. Besides the six passive vanes in CFG 6 configuration, the insert had six rows of skewed circular orifices analogous to those in Figure 88c. Circular exit orifices have previously been shown to be effective in active flow-control applications. The spatially-distributed orifices shown in Figure 89b could be individually activated in any desired pattern, which enabled testing of various actuation schemes at the fast pace.

A number of steady blowing patterns were tested in a hybrid configuration with the CFG 6 microvanes by using combinations of jet rows and various patterns of jet orifices at various flow rates. It is noteworthy that some configurations resulted in detrimental effect of the hybrid control relative to the passive control, in spite of the favorable effect of each of the hybrid components alone, which places a further emphasis on importance of the proper integration of passive and active control elements.

Although statistically designed experiments were not employed for this task, a response surface was generated following the completion of the experiment. Existing data was used to form the response surfaces that aided in evaluating the performance sensitivities to jet hole placement and mass flow. The response surface was defined in terms of three design factors and one performance metric. The design factors were the "first row number", which indicated the axial location of the row of jets farthest upstream, the "total number of rows" of jets, and the "mass flow per jet", Table 3. The response variable employed for this investigation was $DPCP_{ave}$.

Table 3. Steady Jet Response Surface Design Factors

	Factor 1 A: 1st Row #	Factor 2 B: Total # of Rows	Factor 3 C: Mass Flow per Jet [kg/s]
min	1	1	5.50E-05
max	6	3	4.95E-04

The resulting response surfaces were derived based on data from 24 runs. The response surface model developed for this database was derived from a linear model plus the 2-way interactions. Using backward elimination, the following terms were found to be statistically significant: A-First Row #, B-# of Rows, C-Jet Mass Flow, and the interactions of factors AC and BC. The final equation for the response surface, given in terms of the actual factors (as opposed to coded variables) is given in Equation 11.

DPCPave = 2.12E-02 + 6.45E-04 * First Row # + 4.91E-04 * # of Rows 1.36E+01 * Jet Mass Flow - 2.89E+00 * First Row # * Jet Mass Flow - 1.34E+01 * # of Rows * Jet Mass Flow

Equation 11

3-D contour plots of the response surfaces show that the lowest distortion, $DPCP_{ave}$, occurs when the blowing region is located further downstream from the throat and the jet mass flow is maximized, Figure 90. In addition, $DPCP_{ave}$ appears to be minimized through the combination of higher jet mass flows and more rows of jets, Figure 91. It should be noted that these results were not obtained through a statistical design and that the goal of this analysis was simply to obtain an initial understanding of the performance sensitivities to changes in relative microvane/jet placement. Future studies, preferably based on a statistically designed experiment, would be required to optimize jet locations and mass flow. However, for the purposes of this study, the results presented herein provided the fundamental guidance to design a hybrid system that would improve total-pressure distortion by employing multiple rows of jets, located as far downstream as the model would allow, operating at maximum effective strength.

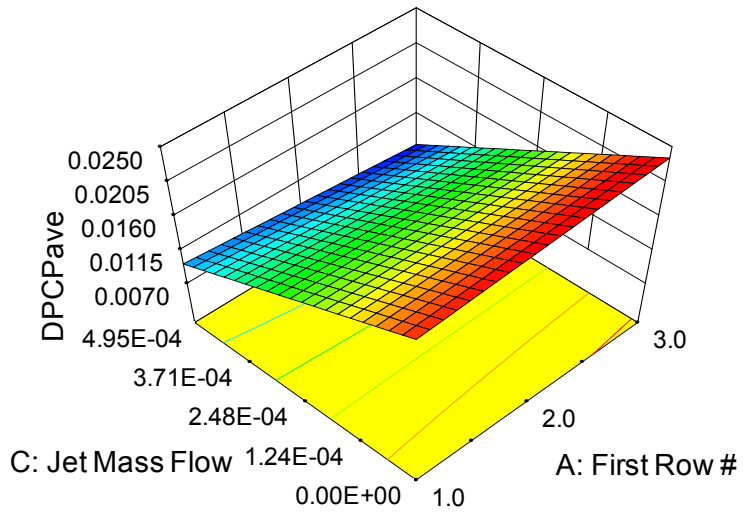

Figure 90. First Row Number / Jet Mass Flow Response Surface

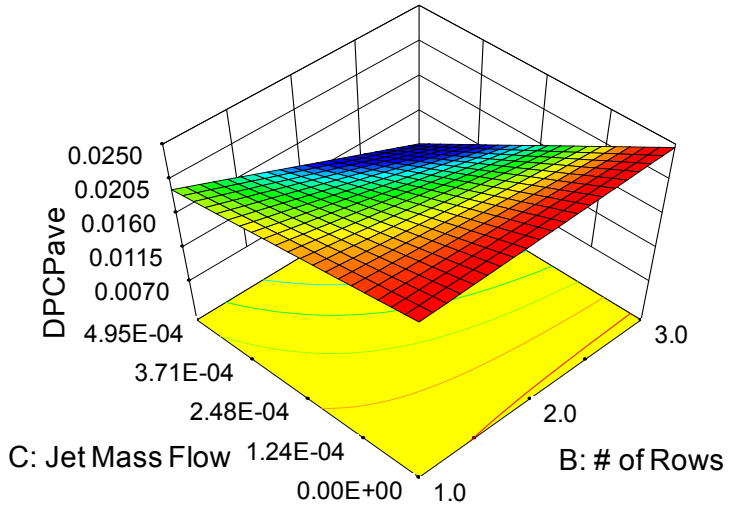

Figure 91. Total Number of Jet Rows / Jet Mass Flow Response Surface

Out of the five top performing configurations, all but one of them involved some combination or subset of rows 4, 5 and 6, which were the most downstream rows from the passive vanes. The two most effective configurations were rows 4, 5, and 6, and rows 2, 5 and 6, which reduced the DPCPave in excess of 40%. These results indicated two basic approaches in hybrid integration of active and passive devices. One approach being where active jets are interlaced with the passive vanes and act more as vane substitutes (row 2), or an alternative approach where passive and active vortices are spatially delayed but interact before reaching the AIP (rows 4, 5, and 6).

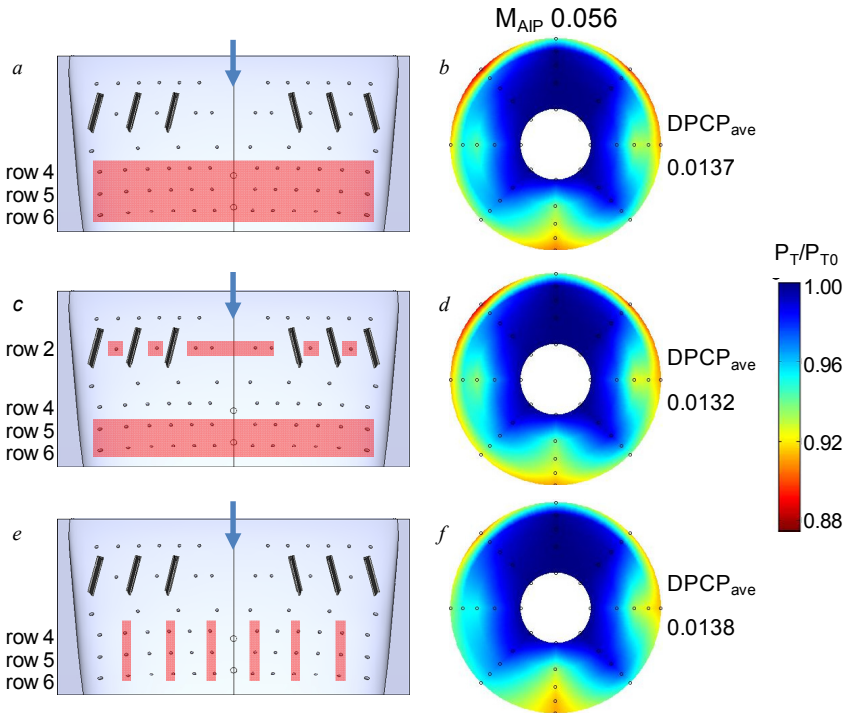

Figure 92. Total pressure contour plots (b, d, f) measured at the AIP for skewed circular jets: rows 4, 5, and 6 (a, b), 2, 5, and 6 (c, d), and every other row 4, 5, and 6 (e, f)

Three configurations that resulted in maximization of the sensitivity parameters were further characterized in Figure 92. The active jets are highlighted in each of the configuration schematics: rows 4, 5, and 6, Figure 92a, rows 2, 5, and 6, Figure 92c, and every other column in rows 4, 5, and 6, Figure 92e. Activation of the jets in all cases predominantly suppressed the three low-pressure lobes when compared to the passive control only, Figure 89a. When rows 4, 5 and 6 were activated, Figure 92b, a decrease in $DPCP_{ave}$ of 38% was induced when compared to the passive control. The activation of rows 2, 5 and 6 created a somewhat larger percent decrease in the DPCPave (41%). Interestingly, activation of every other column of jets within rows 4, 5 and 6 resulted in almost the same change in DPCPave as having all rows active, indicating that improvements in efficiency of the active component could be realized with a decreased number of jets. Overall, it was concluded that a single, compact synthetic-jet module could be designed to encompass rows 4, 5, and 6, as tested in this continuous jet study. Incorporation of the interlaced row 2 in the synthetic-jet actuation would have required additional, separate synthetic jet module, which was seen as a disadvantage in practical applications and not pursued in the present work. Furthermore, incorporation of complete rows of synthetic jets in the control module allowed for flexibility in the activation of jet patterns for future tests.

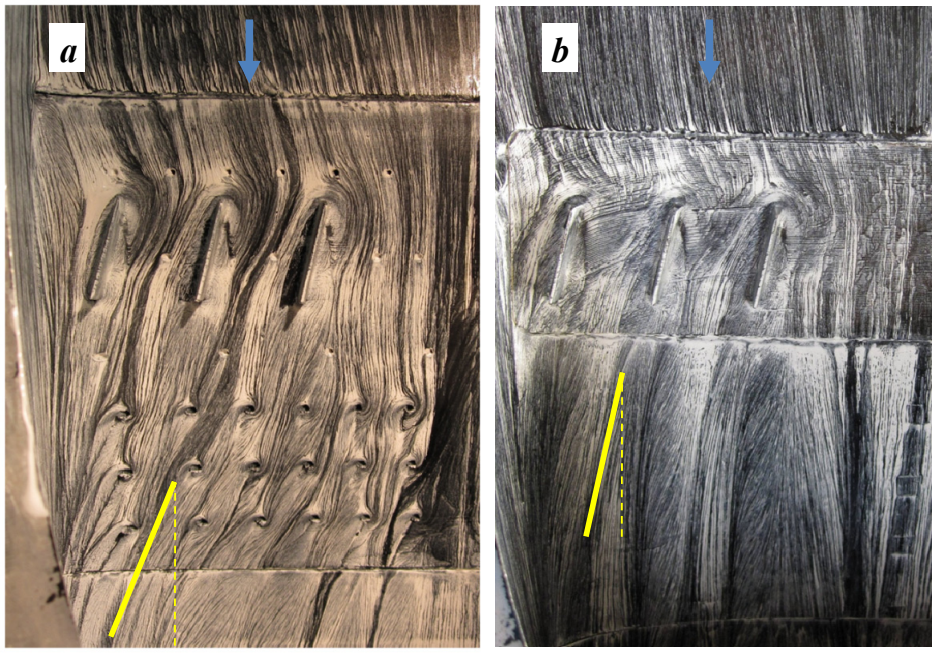

Figure 93. Surface oil-flow visualization of the control surface area for the and hybrid control shown in Figure 92a and by its passive component CFG6 vanes (b).

The interaction between vortices generated by the selected three rows of active jets (4, 5, and 6) and the passive vane array (CFG 6) was examined further through surface oil-flow visualization, which is shown over the control surface in Figure 93. The oncoming flow formed a streamwise vortex on the downstream side of each of the passive vanes, which was then advected downstream. The imprint of each vortex on one side of the diffuser can be clearly seen in Figure 93b. Activation of the jets in rows 4, 5, and 6, Figure 93a, induced individual streamwise vortices at each of the orifices, much like the ones generated by the vanes. However, many vortex imprints at the orifices did not persist far downstream in the duct. Instead, the jet-induced vortices readily merged with the larger, vane-induced vortices. As a result, the interaction and merging of these vortices assisted in displacing the low-pressure region at the AIP up along the wall, away from the symmetry plane. This was indicated by the increased angle of the flow, away from the center plane in Figure 93a in comparison to Figure 93b. The corresponding visualization of the pattern on the full lower surface of the diffuser is shown in Figure 94, with an overlaid contour plot of the AIP total pressure. The merging vortices can be seen as the traces of the structures that move up, away from the centerline and form one large structure in the right quadrant of the AIP (as shown by the dotted lines). The mostly undisturbed centerline oil traces in the duct show that the low-pressure lobe at the bottom, center of the AIP was due to low-speed flow traversing directly through the hybrid control effectors.

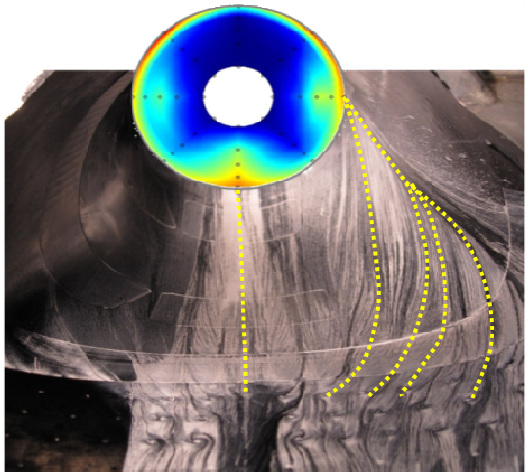

Figure 94. Surface oil-flow visualization for the hybrid control shown in Figure 92a. The corresponding total pressure plot is overlaid at the AIP. Dotted lines emphasize the flow direction.

Analysis of the Time-Dependent Component of a Hybrid Flow Control Device

Synthetic jets as active flow control components of hybrid control devices have two, distinct differences from continuous jets: they do not require any air supply (hence, they are also called 'zero-net-mass-flux' devices) and they are operated harmonically, introducing a time-dependent component into the flow control. A previous section discussed the overall, steady-state effects of the hybrid flow control using the synthetic-jet actuators, and here some aspects of the underlying dynamics of the flow control are uncovered by analysis of its time-dependent characteristics.

During the data acquisition, all the time-resolved high-bandwidth pressure data was acquired along with the reference signal from the synthetic-jet actuation. In order to elucidate time dependent features of the flow, the forty time traces from the dynamic pressure sensors are averaged with respect to the phase of the actuation cycle, thus forming the phase-averaged ensembles $\hat{p}(\phi)$, where ϕ = 0 to 2π. It should be noted that there was an arbitrarily (but constant) phase delay between the start of the expulsion cycle of the synthetic jet and its effect at the AIP, so that the onset of dynamic change in $DPCP_{avg}$ does not coincide with ϕ = 0. These phase-averaged ensembles of pressure fields are then used to compute the phase-averaged $DPCP_{avg}$ indices $DPCP_{avg}(\phi)$ that show the pressure field dynamics at the AIP relative to the actuation cycle.

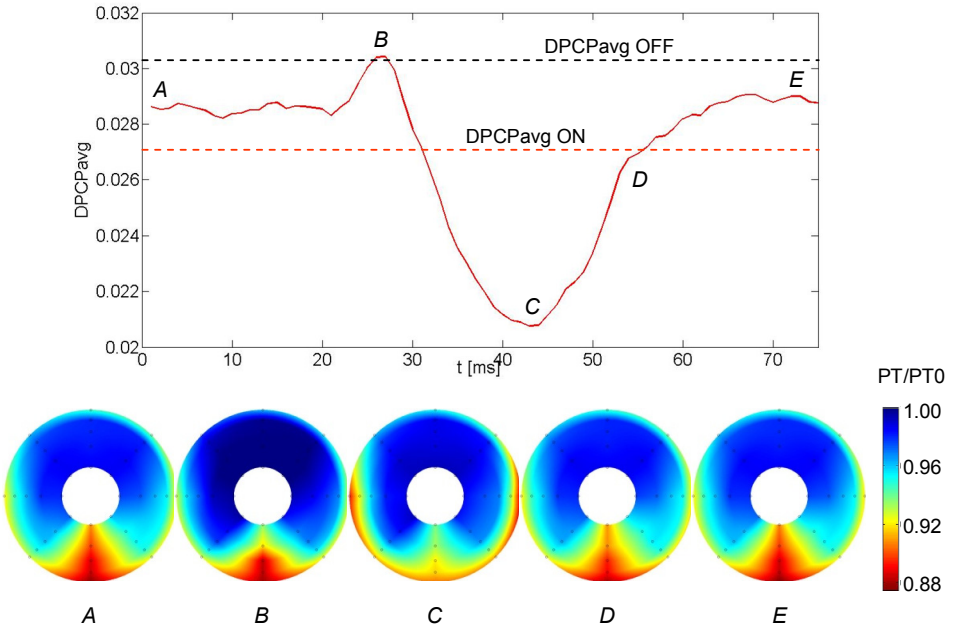

Figure 95. Time trace of the phase-averaged DPCPavg with contour plots of AIP pressure distribution at characteristic time (phase) points A through E, for the case of active flow control by synthetic-jets component of the hybrid flow control.

Prior to analysis of the hybrid control case, it was informative to examine the time-dependent aspect of the flow control by active control component only, i.e., without the passive vanes. The phase-averaged $DPCP_{avg}$ as a function of time is shown in Figure 95, where t = 0 to 75 ms corresponds to a phase (ϕ) of 0 to 2π. This dynamic change in the $DPCP_{avg}$ is accompanied by the corresponding dynamic changes in the $DPCP_{avg}$ in each of the five rings (1 through 5) of the forty-probe dynamic pressure rake, which are shown in Figure 96. First, the time-dependent nature of the flow control is marked by the dynamic change in to $DPCP_{avg}$ over about 60% of the actuation cycle (22 ms < t < 65 ms). At the onset of the dynamic change, there is a short increase in the $DPCP_{avg}$, which is followed by a favorable reduction of the $DPCP_{avg}$ over a larger portion of the actuation cycle. The peak reduction of about 35% in $DPCP_{avg}$ is measured at $t \approx$ 43 ms. To better illustrate dynamic nature of the $DPCP_{avg}$ change during the actuation cycle, several characteristic phase locations are selected and marked as A – E in Figure 95.

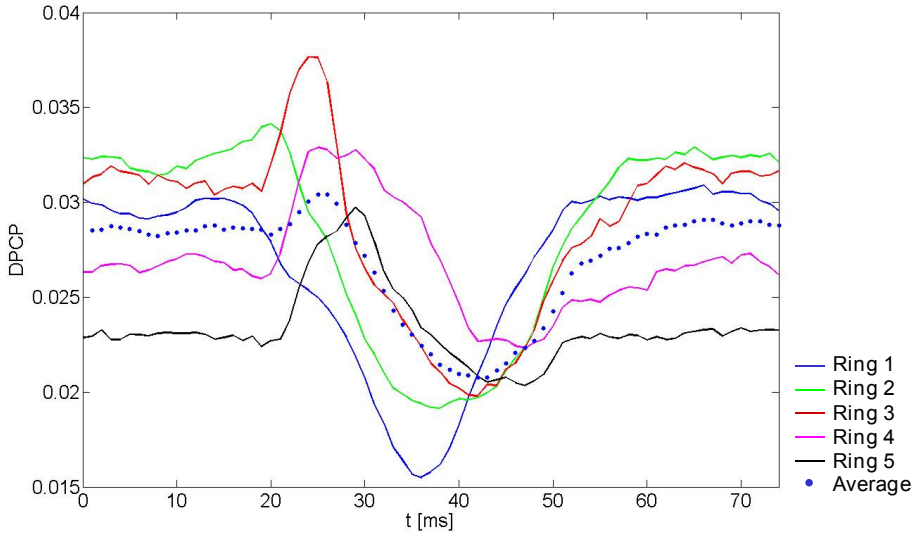

Figure 96. Time trace of the phase averaged DPCP indices, for the case of active flow control by synthetic-jets component of the hybrid flow control.

The corresponding contour plots of the total AIP pressure at the selected phase angles are shown in the bottom row of Figure 95. At 0 seconds (point A), the flow is very similar to the baseline flow both in the pressure contour plot structure, and in the magnitude of the $DPCP_{avg}$. At the point that the actuated flow starts to alter the $DPCP_{avg}$ ($t \approx 22$ ms), there is an initial increase in the $DPCP_{avg}$ (Figure 95). This is attributed to the following dynamics seen in Figure 96: as the low speed flow begins to move down toward the bottom surface away from the centerline of the duct, the two inner rings measure an increase in pressure as well as less circumferential change. Therefore, there is a lower DPCP in those two rings as is indicated in the decrease in ring one and two in Figure 96. At this point in the cycle, the low-pressure region is concentrated at the bottom of the AIP, specifically along the outer three rings, which is seen in the corresponding contour plot (Figure 95, point B). The resulting increase in the DPCP in rings three, four and five as the low pressure continues to move toward the bottom of the AIP is also seen in individual distributions in Figure 96. Further progression of the control impact at the AIP forces the low pressure flow along the wall and to the sides, away from the line of symmetry, and consequently the circumferential distortion decreases to Point C (Figure 95). After the peak effect of the jet's vortices passed, the following reduction in the jet momentum induces relaxation in the favorable effect in the $DPCP_{avg}$ reduction, and the flow also relaxes back to the baseline flow structure (Point E), where the transitional phase Point D is also shown.

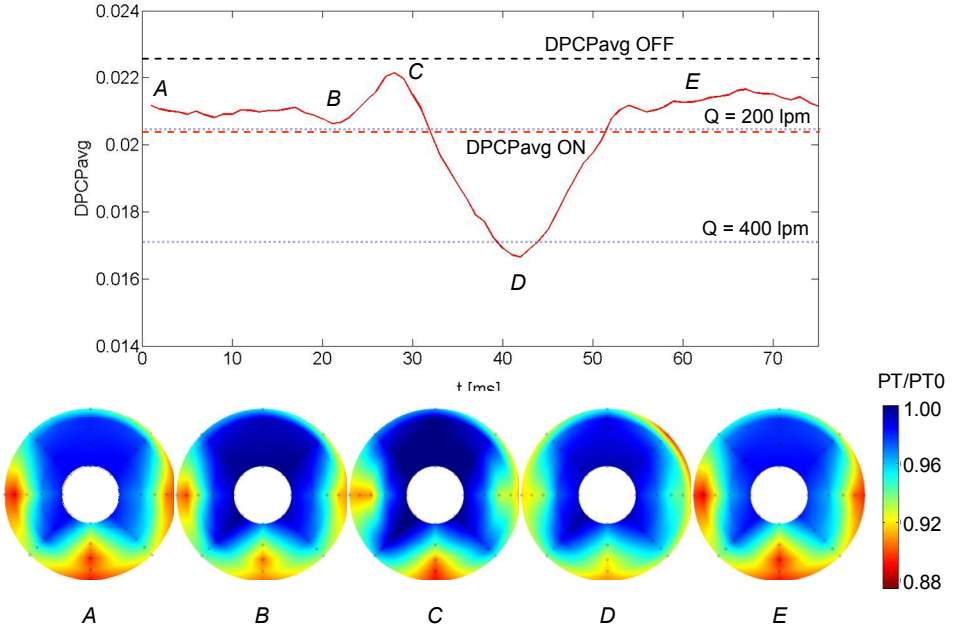

Figure 97. Time trace of the phase-averaged DPCPavg with contour plots of AIP pressure distribution at characteristic time (phase) points A through E, for the case of active flow control by the hybrid flow control. The DPCPavg results for the hybrid control with continuous jets at Q = 200 and 400 lpm (liters per minute) in place of synthetic jets are shows as a reference.

The characterization of the active flow control time-dependent effects was also applied to the hybrid control case, where the same active component – synthetic jets was paired with the selected passive component – a CFG 6 vane configuration. The phase-averaged $DPCP_{avg}$ for the hybrid case is shown in Figure 97, along with the AIP contour pressure plots for the characteristic phases marked as A through E. Similarly to the active control analysis, dynamics of each of the individual five pressure rings is further characterized in the accompanying Figure 98. Comparison between Figures Figure 95 and Figure 97 shows that the overall dynamics of the hybrid flow control is dominated by its active component, as expected, and comparable dynamics is observed. The main difference stems form the underlying passive control that alters the baseline flow even before the active component of the hybrid control is activated. Thus, all the AIP contour plots for the hybrid flow control exhibit three-lobed structure that was not present in the active control case discussed in Figure 95 and Figure 96. Some minor modifications in the observed dynamic of the active control are seen in a slight drop in the $DPCP_{avg}$ at Point B (Figure 97) which is due to the decrease in the low pressure intensity in rings one and two, as also seen in the individual time traces of DPCP (Figure 98).

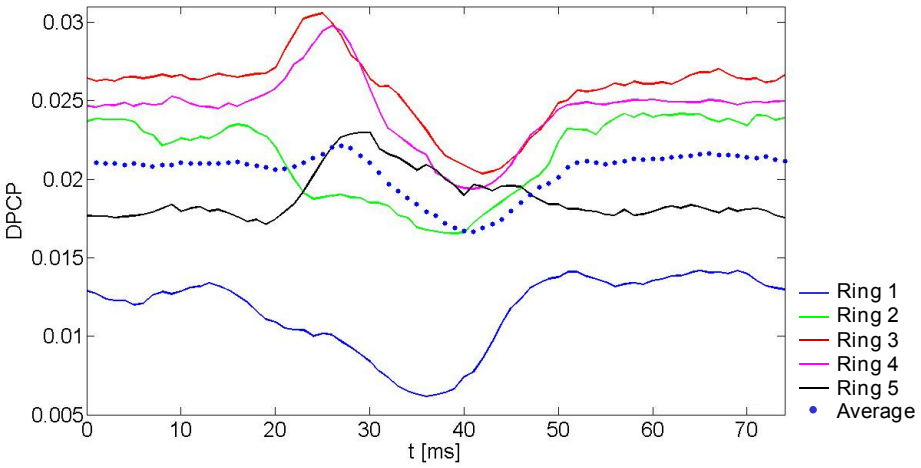

Figure 98. Time trace of the phase-averaged DPCP indices, for the case of the hybrid flow control.

As in the case of active flow control, the $DPCP_{avg}$ then increases, due to a combination of two factors. First, there is an increase in the pressure intensity at the bottom center of the duct, especially concentrating in rings four and five (see their time traces in Figure 98). Second, there is a decrease in intensity at other points around the circumference of the same rings which contributes to the steeper circumferential pressure change. Immediately following the $DPCP_{avg}$ peak (Figure 97, point C) the $DPCP_{avg}$ decreases as the pressure magnitudes in all three lobes become suppressed (Figure 97, point D), which is where the distortion levels reach their lowest point. As the jet momentum diminishes afterwards, the pressure contour map relaxes back to the baseline pattern and level (Figure 97, point E). It is of interest to note that ring five is relatively constant throughout the cycle (Figure 98). As the three lobes spread low pressure along the outer walls in a similar fashion during the entire cycle, except at point C where there is a spike in the distortion in ring five due to the initial movement of the low-pressure fluid towards the central bottom wall. Figure 97 also has two different levels for the reduction in $DPCP_{avg}$ added to the plot as a reference, when continuous jets are used in place of the synthetic jets as the active component of the hybrid control device. They point that, with respect to the $DPCP_{avg}$, the hybrid control with synthetic jets is equivalent to the control their continuous-jets replacement at Q = 200 lpm. Also, to achieve the peak effect of the synthetic jets, continuous jets need to run at the flow rate in excess of 400 lpm. It is expected that any following utilization of the synthetic jets in future would utilize the phase-offset operation of individual jets that could extend or eliminate a portion of the actuation cycle when there is a minimal impact at the $DPCP_{avg}$.

The results of isolated passive and active flow control shown in the previous sections prove that flow control may be employed to reduce time-averaged distortion with minimal effects on total pressure recovery. Passive and active flow control was shown to reduce the distortion levels to near or below the prescribed limits. However, the simultaneous application of passive and active flow control in a hybrid configuration was shown to further reduce the distortion and provide greater operating margin below the limits. The hybrid configuration tested in the present study comprised a microvane array followed by a synthetic-jet array. As in all the previous cases, flow control was applied downstream of the throat.

Time-averaged results for the passive, active, and hybrid configurations show no effect on the total-pressure recovery for the controlled configurations compared with the baseline

configuration, Figure 99. The results also show that passive and active flow control resulted in an equivalent reduction in circumferential hub distortion when compared to the baseline. At airflow rates above 85% of the design airflow, the passively and actively controlled hub distortion met or only slightly exceeded distortion limits. At airflow rates below 85% of the design airflow, passive and active flow control configurations reduced the baseline, time-averaged, hub, circumferential distortion to levels that were below the limits. The hybrid flow control provided the greatest reduction in hub circumferential distortion, especially at higher airflows, providing increased performance margin when compared to passive and active control.

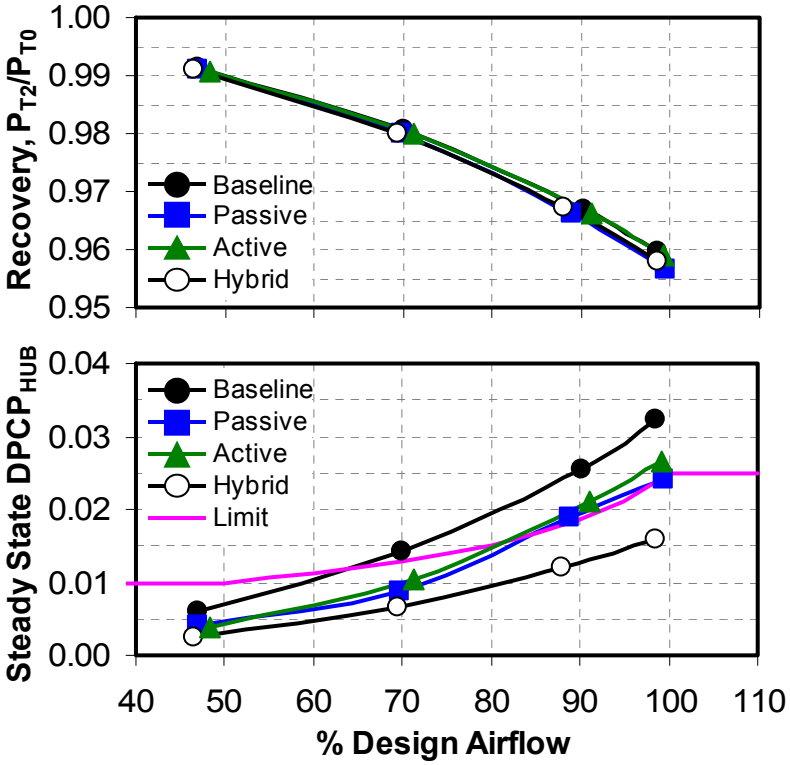

Figure 99. Hybrid Flow Control Comparisons of Time-Averaged AIP Total Pressure Recovery and Circumferential Hub Total-pressure distortion at Various Mass-flow rates

Figure 100 shows the AIP total pressure patterns comparing the baseline configuration with the hybrid flow-control configuration. The AIP patterns show the hybrid configuration was able to distribute the total-pressure losses, thus reducing the distortion. This result was similar to that with passive and active control. However, hybrid flow control distributed the low-pressure regions more effectively, resulting in more favorable distortion patterns.

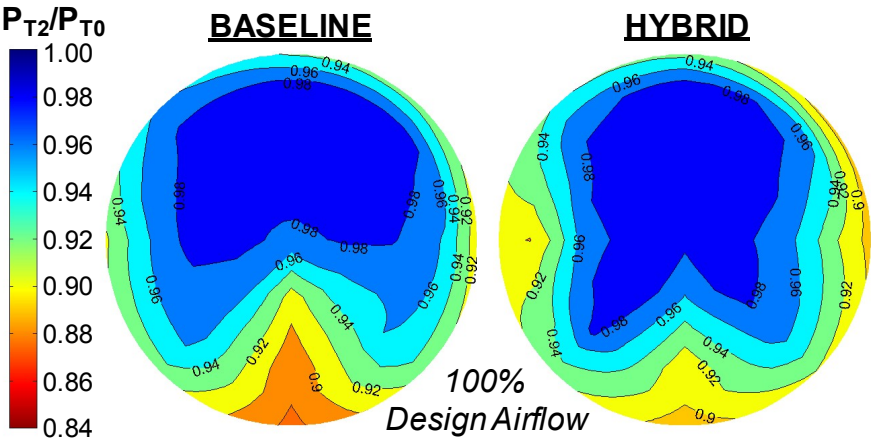

Figure 100. Hybrid Flow Control Comparisons of Time-Averaged AIP Total Pressure Contours

Dynamic data was also measured for the hybrid flow-control devices. Comparison of the peak circumferential hub total-pressure distortion for the passive, active and hybrid flow control with the baseline configuration is shown in Figure 101. The passive and the active flow control configurations both slightly reduced the peak circumferential hub distortion. The hybrid flow-control configuration further reduced the distortion below the limits. Figure 102 shows the AIP total-pressure patterns at the peak circumferential for the hybrid flow control and baseline configurations. The patterns show the hybrid flow control reduces the total pressure loss at the lower centerline location of the AIP by distributing the losses around the edges of the AIP.

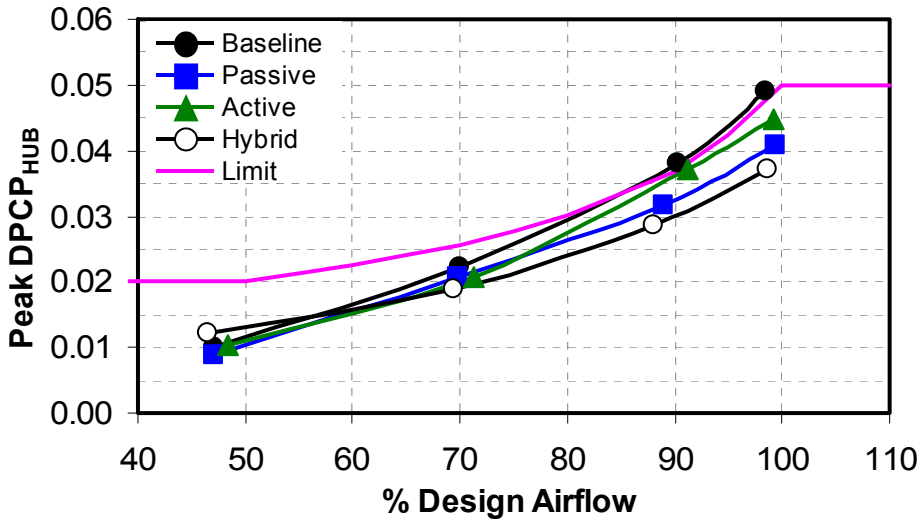

Figure 101. Flow Control Comparisons of the Peak Circumferential Hub Total-pressure distortion at Various Mass-flow rates

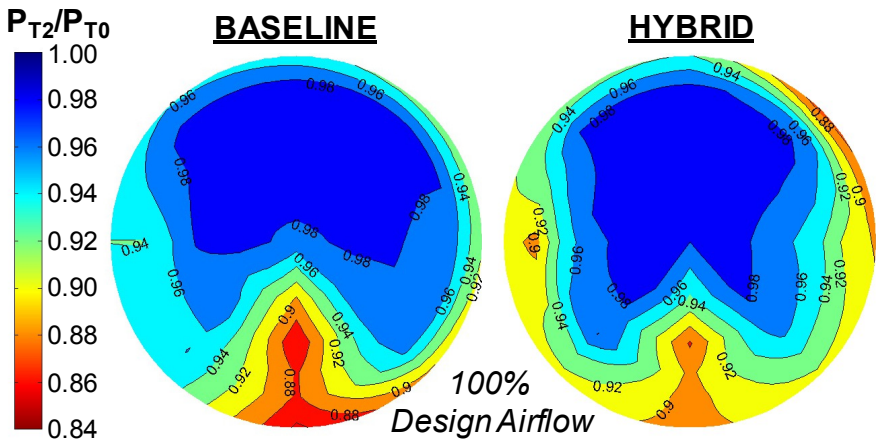

Figure 102. Hybrid Flow Control Comparisons of the Peak Circumferential Hub Total Pressure AIP Patterns

Flow Control Performance Prediction Capability Development and Validation

In addition to experimental investigations, numerical simulations were conducted under this program to develop prediction tools and capabilities for evaluating the effects of flow control on BLI-inlet performance. Results are presented and validated against experimental data for numerical simulations of isolated flow-control devices in a 2-D, CD wind-tunnel test section, as well as, multiple devices in an offset, BLI-inlet diffuser. A number of grid densities and simulation methodologies were investigated in order to evaluate the sensitivity of the results to the applied numerical approach. Qualitative and quantitative results are reported in terms of flow visualization, total-pressure contour plots, and total-pressure recovery and distortion. Steady-state and time-accurate simulations were conducted and compared with experimental results.

Simulated Flow Control Device Physics

A primary objective of this program was to improve and validate tools for predicting the aerodynamic effects induced using flow-control devices. In this section, numerical simulations of the passive device were conducted in the Georgia Institute of Technology FMRL tunnel test section with a profiled wall (Figure 103). Results of the numerical simulations were validated against experimental data. Several factors were varied to explore the sensitivity of numeric results to simulation methodology. These factors included grid resolution, turbulence model, and viscous-flux-calculation technique.

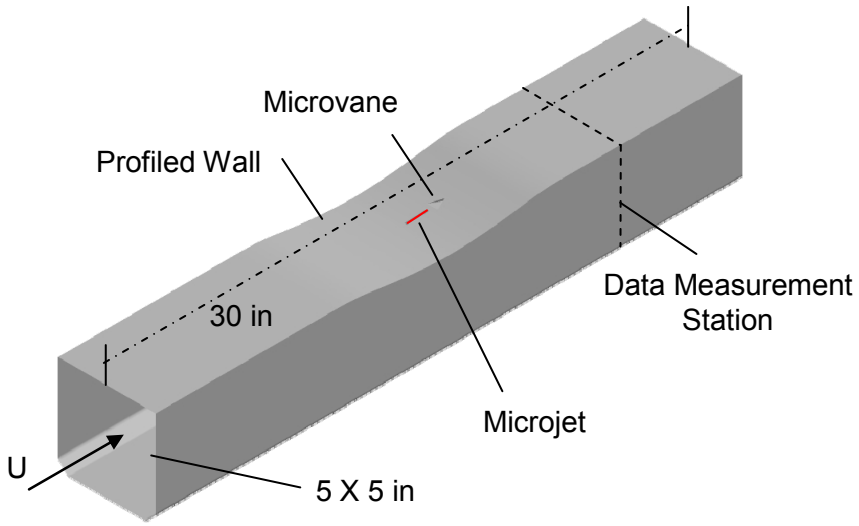

Figure 103. Computational domain with microvane / microjet, and data measurement plane

Empty Tunnel (Baseline)

The accuracy of numerical simulations of the baseline wind tunnel flow, in the absence of flow-control devices, was assessed. Specifically, measured and predicted boundary-layer velocity profiles on the profiled wall at the measurement plane in Figure 103 were compared (Figure 104). For the following figures containing boundary layer profiles, Y_{max} was ~0.69 in and U_{max} was ~550 ft/s. For the following figures containing velocity contours, U_0 was ~550 ft/s. The flow approaching the converging/diverging section was at Mach 0.5 with a total pressure of 14.23 psia and total temperature of 537 degree R . The measured profiles are denoted “GT” in the legend and are plotted at spanwise locations from 0.04 in (1mm) to 0.43 in (11mm) offset from the centerline. Based on the experimental profiles, the velocity deficit increased monotonically

with increasing spanwise offset. This was due to secondary flow, resulting from the sharp corners in the duct imposing an upwash on the otherwise uniform boundary layer.

The numerical simulations were conducted with both SA and SST turbulence models. Both models compared very closely with one another, but the SA model predicted the centerline experimental results slightly better. Away from the centerline, however, the numeric results did not exhibit the same upwash or velocity deficit effects that were measured in the experiment. In fact, the simulated profiles at 1mm, 5mm, and 11mm offset fell on top of one another. It is thought that flow interactions from the tunnel entrance contraction and corners were not resolved sufficiently resulting in omission of secondary flow features responsible for the upwash depicted in Figure 104.

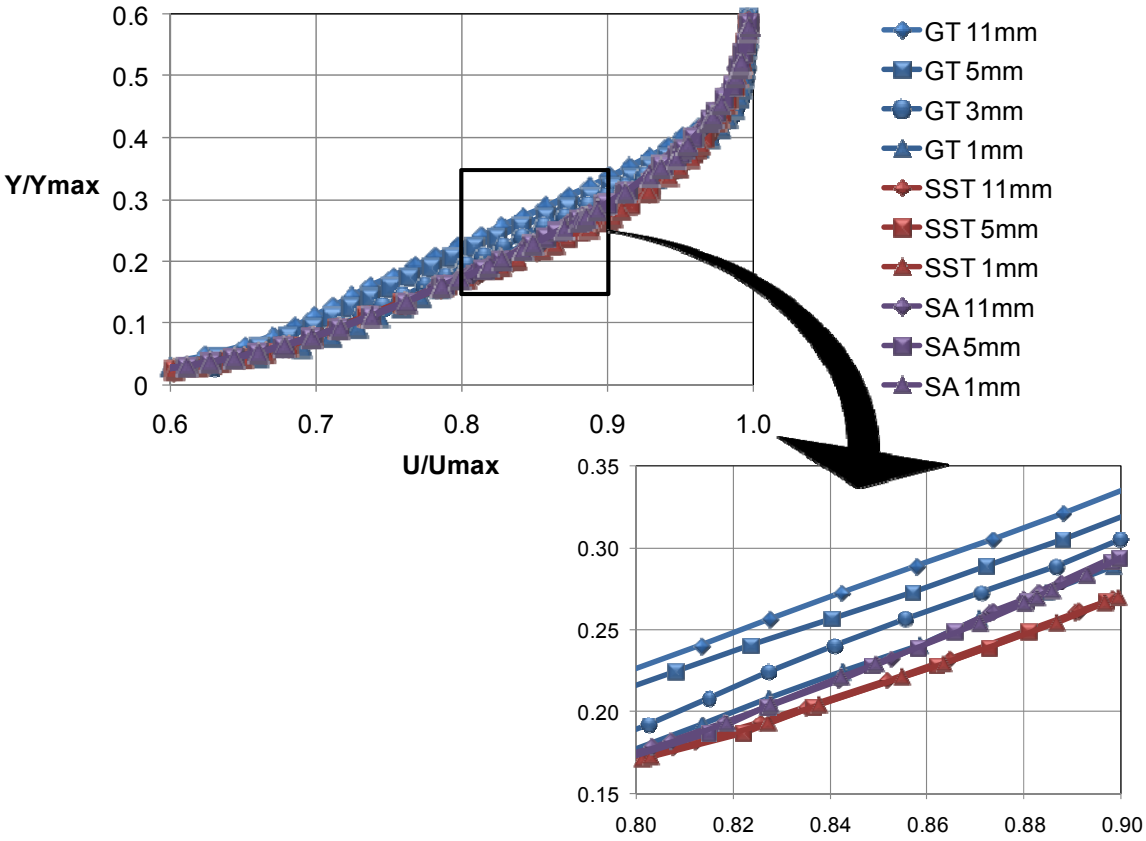

Figure 104. Baseline comparison of experimental and numerical results

Passive Device

Simulations of the microvane mounted near the throat of the FMRL tunnel were generated and validated against experimental data. Layout of the microvane is provided in Figure 105.

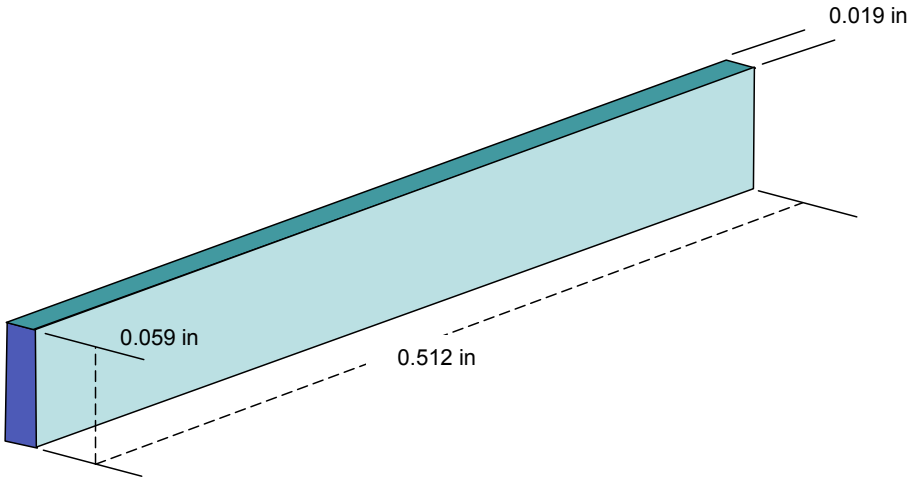

Figure 105. Microvane dimensions

Prior to making comparisons with experimental data, a grid resolution study was conducted to ensure that the grid was sufficiently refined to capture the flow physics. Specifically, the goal was to verify that the simulation accurately predicted the vortex shed by a microvane in an adverse pressure gradient. For each grid refinement level, boundary layer profiles and velocity contours were taken at a station downstream of the throat, Figure 103. These profiles were then compared between refinement levels to determine if the solution was grid independent. A coarse grid, GRS1, consisting of 4.3 million cells and a characteristic surface element size of 0.1 inch served as the starting grid. The method for refinement was to decrease the element size in the wake (Figure 106) downstream of the microvane in order to preserve the vortex strength as it convected downstream.

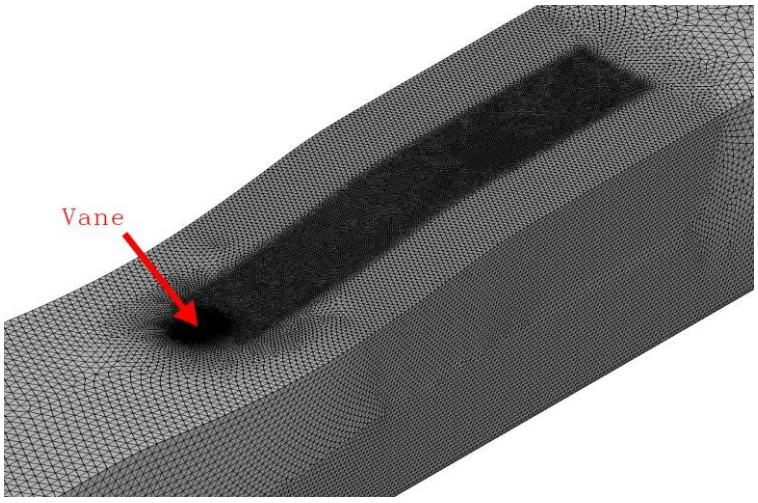

Figure 106. Wake refinement downstream of the microvane

Three levels of grid density were examined in the grid-convergence study. The first level of refinement, GRS2, produced a grid containing 5.2 million cells with an element size of 0.05in. Refining to the second level, GRS3, resulted in a grid with 7.4 million cells and an element size of 0.023in. The final refinement, GRS4, resulted in a 21.8 million cell grid with an element size of 0.01in. Normalized velocity contours are shown in Figure 107 through Figure 110 for the four grids. The black lines on the images represent the spanwise locations at which boundary layer

profiles, Figure 111, were extracted. The change in the vortex shape due to grid density variation was most noticeable between the coarse, Figure 107 and level 1, Figure 108 grids. A slight sharpening of the blue upwash peak can be seen from refinement level 1 to refinement level 2, Figure 109. Finally, there was negligible difference in the vortex shape between refinement levels 2 and 3, Figure 110. From these velocity contours, it is clear that the solution is grid independent at refinement level 2. The distance indicator (-3mm, 0mm, 3mm, and 5mm) represents how far offset from the duct centerline the profile was taken. As an example, the velocity profiles at 0 mm, Figure 111, show that the biggest shift in the profiles occurs between GRS1 and GRS2. There is a slight change from GRS2 to GRS3, but further refinement to GRS4 shows very little change in the velocity profiles.

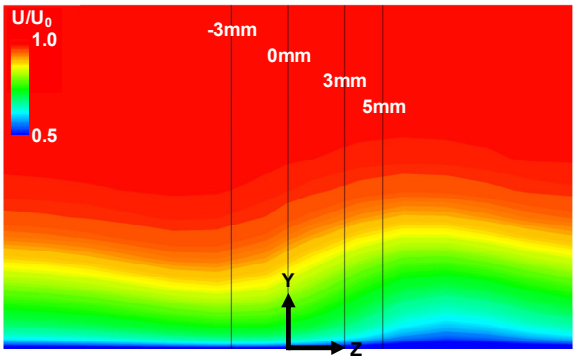

Figure 107. Velocity contours depicting vortex for coarse grid

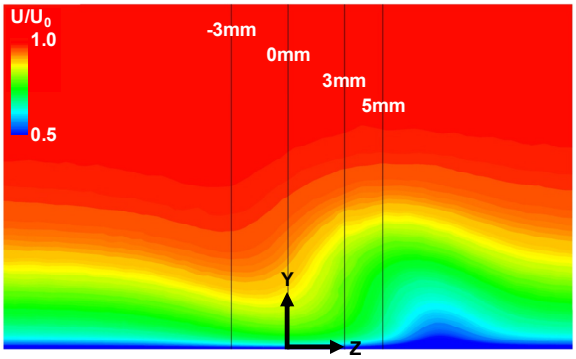

Figure 108. Velocity contours depicting vortex for level 1 refined grid

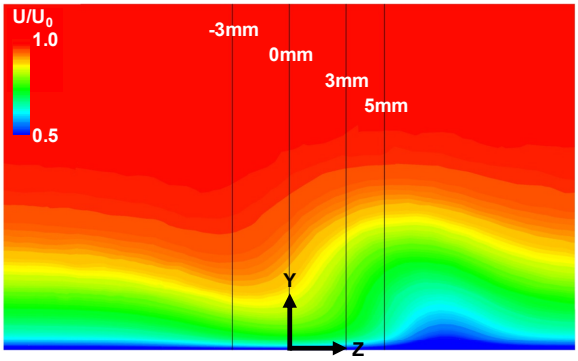

Figure 109. Velocity contours depicting vortex for level 2 refined grid

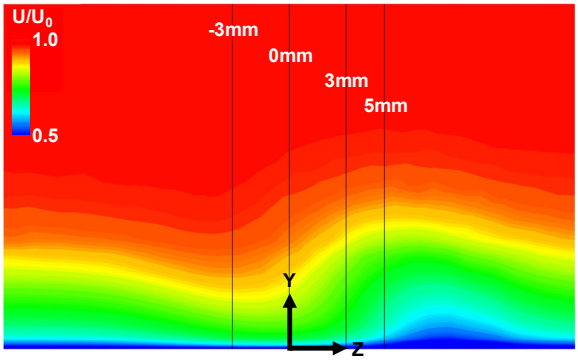

Figure 110. Velocity contours depicting vortex for level 3 refined grid

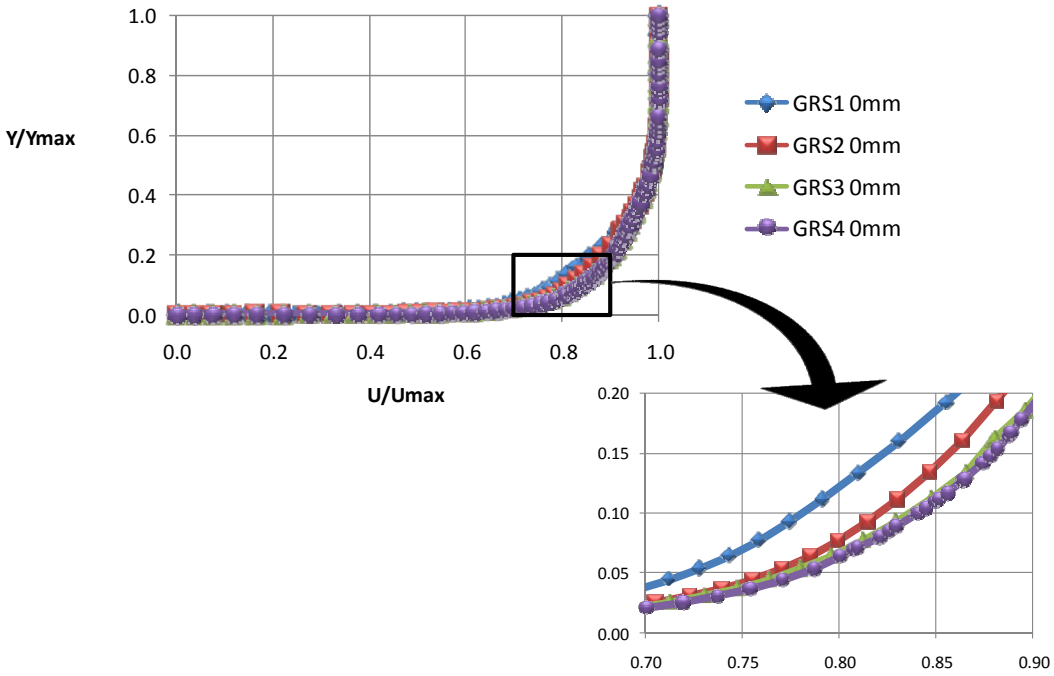

Figure 111. Velocity profiles depicting grid convergence

Comparison of simulated and measured velocity profiles downstream of the microvane showed that the SA turbulence model captured the induced vorticity. Here the grid spacing in the microvane wake was 0.023 inch. In general, the simulations over-predicted the strength of the vortex, especially the downwash component. However, the simulation captured the qualitative shape of the vortex and overall effects. Figure 112 shows velocity contours indicating that the height and width of the vortex from both simulation and experiment. The black line indicates the duct centerline location. The difference between the measured and predicted spanwise vortex location was a due to larger simulated vortex strength than measured; this enabled the simulated vortex to move closer to the centerline as it propagated downstream. The larger vortex strength was attributed to the fact that the simulations did not adequately capture the secondary flow motion produced the bell contraction and tunnel corners.

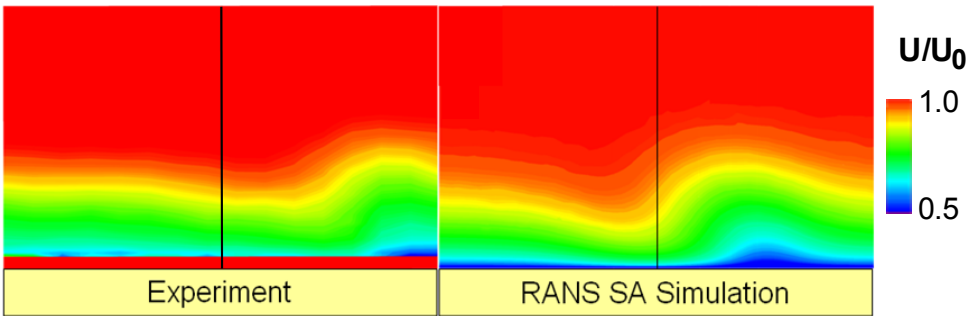

Figure 112. Measured and simulated vortex downstream of a microvane

Turbulence Model Sensitivity

The sensitivity of the predicted boundary-layer profiles and induced vorticity to turbulence models was assessed. SA, SA with rotation correction (SARC), and SST turbulence models were used with RANS and time-averaged RANS/LES algorithms. Comparisons were made with experimental results to determine which model best approximates the flow physics. Figure 113 illustrates these sensitivities in the boundary layer profiles at several spanwise locations. Data for the largest upwash and downwash profiles is presented. For example, the far left (7mm) profile for the SST RANS/LES group can be compared to the far right (-3mm) profile for the same group. The band enclosed by these two extremes represents the magnitude of the upwash and downwash effects, or strength of the vortex. A wider band would correspond to a stronger vortex, while a thinner band would correspond to a weaker vortex.

The experimental results, labeled “GT”, depict the measured vortex strength. The difference between these data (GT-13mm and GT-3mm) is less than those from the simulations. Less difference would indicate a weaker vortex. The time-averaged RANS/LES simulations using both SA and SST models appear to predict similar but higher vortex strengths than other models. The RANS SST and RANS SARC models predicted the next strongest vortices. Both of these models produce very similar results. The RANS SA model predicted the weakest of the vortices. This model agrees reasonably well with experiment in the upwash region.

It is believed that the difference in strength between the measured and predicted vortices is due to mot adequately simulating the secondary flow motion in the tunnel. The differences exist near the wall on a very small scale. It will be shown, in the next section, that these differences do not adversely affect the AIP flow properties in an S-duct diffuser.

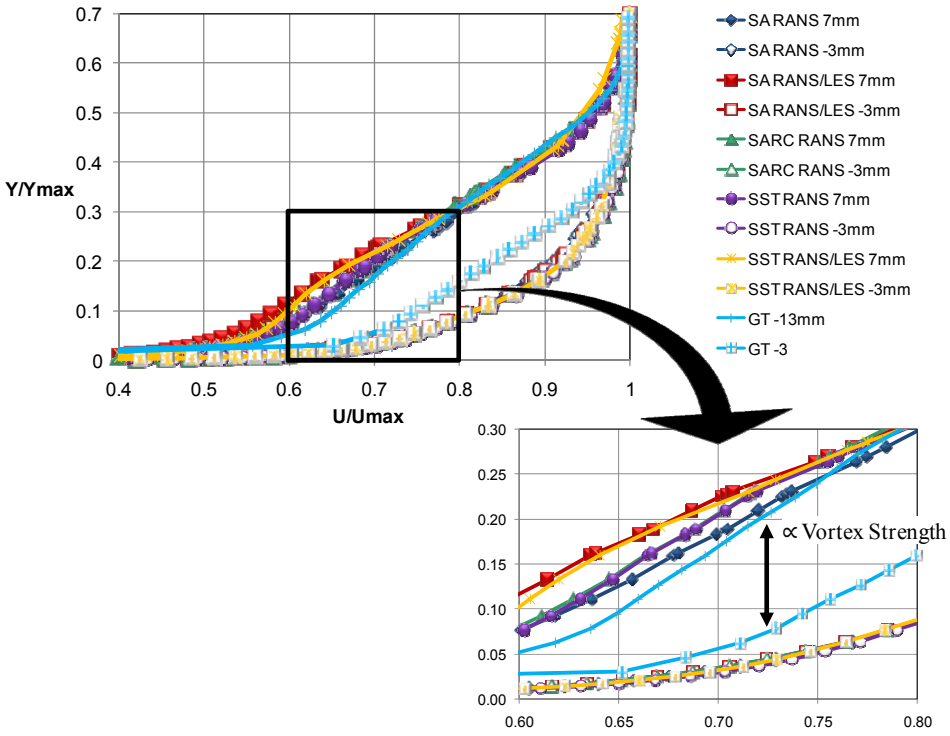

Figure 113. Boundary Layer Profile Sensitivity to Turbulence Model Variation

Simulated Flow Control Performance in a BLI Inlet S-Diffuser

To validate the numerical technique for simulating the effects of flow-control devices in an S-duct diffuser, a baseline diffuser without microvanes along with six vane configurations from the experimental DOE were modeled numerically and compared to experimental results. To improve the simulation, the boundary-layer fence used in the experiment was modeled as well. The two approaches used to model the effects of this fence were outlined in a previous section entitled "BLI-Inlet Fence Simulation Technique." These fence modeling techniques predict the same qualitative features as the experiment.

Preceding the simulations, grid resolution and turbulence model sensitivity studies were performed. It was determined that the SA turbulence model, with the rotation correction, best captured the flow physics. The solution was grid independent (based on AIP flow properties) with a cell size in the S-duct of 0.06 inch.

Baseline S-Duct Diffuser Simulations

Prior to simulating the S-duct with fence models and flow control, a baseline comparison was conducted to ensure that the simulation was adequately modeling the flow field through the diffuser. All the simulations in this section, except those using a prescribed boundary-layer inflow condition, made use of the geometry in Figure 114. The simulations in which the inflow boundary layer was prescribed did not model the AIP rake fairing, and so had a circular duct extending downstream of the AIP.

Pressure distributions along the centerline of the S-duct from the throat to the AIP were compared for both the upper and lower surfaces. The locations of the pressure instrumentation (grey dots) in Figure 114 represent the comparison region for the lower surface, and similarly for the upper surface. The silhouettes of the simulated AIP rakes are seen in Figure 114.

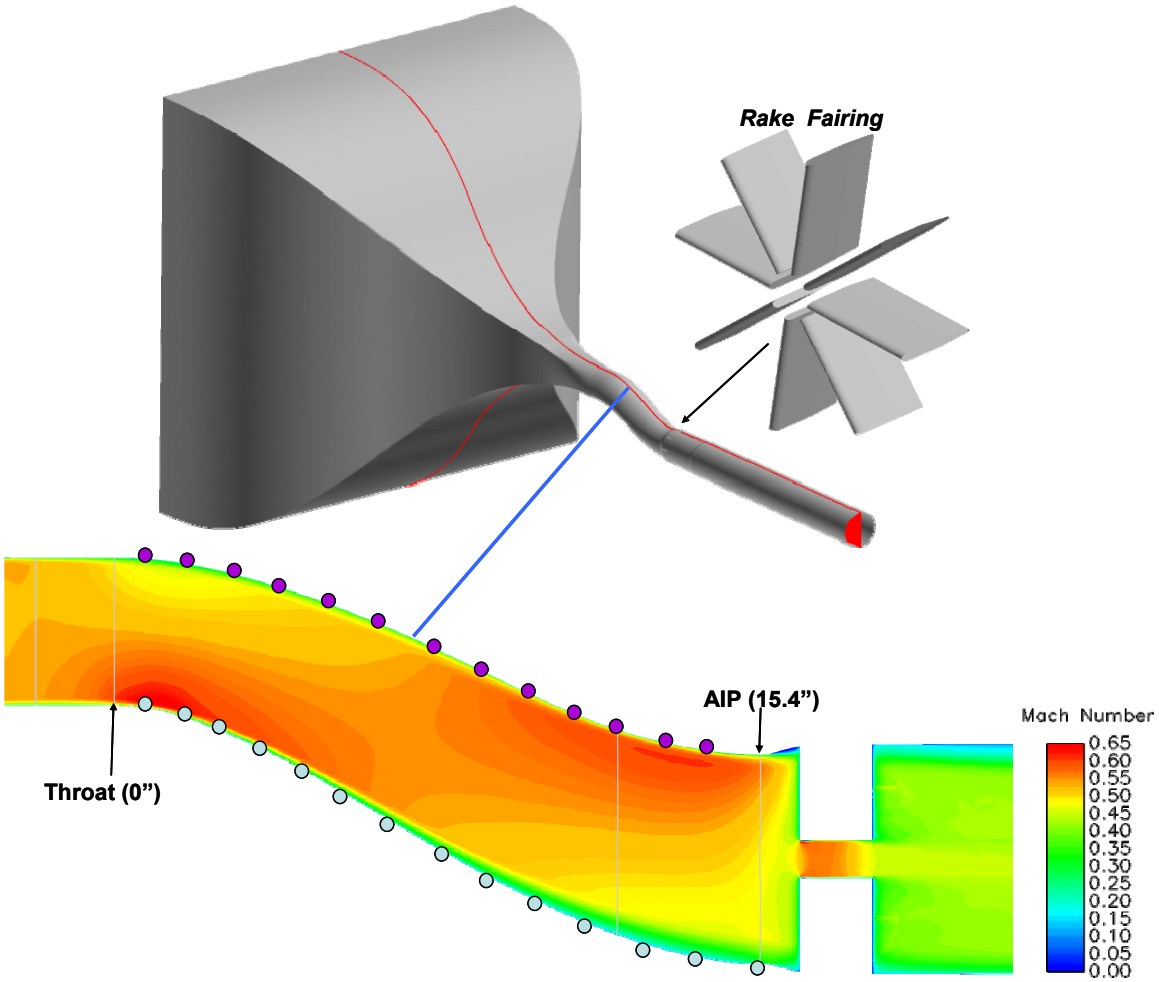

Figure 114. Geometry of the S-duct model with Mach number contours on centerline plane

Wall pressures on both the upper, Figure 115, and lower, Figure 116, surfaces were in good agreement between the simulation and experiment. The largest difference, about 1.8%, occurred at the second turn on the upper wall surface. At this location (x = 12 inch) the experiment predicts a stronger acceleration or suction region. Despite this difference, the pressure recovers to approximately the same level at the AIP in both the simulation and experiment.

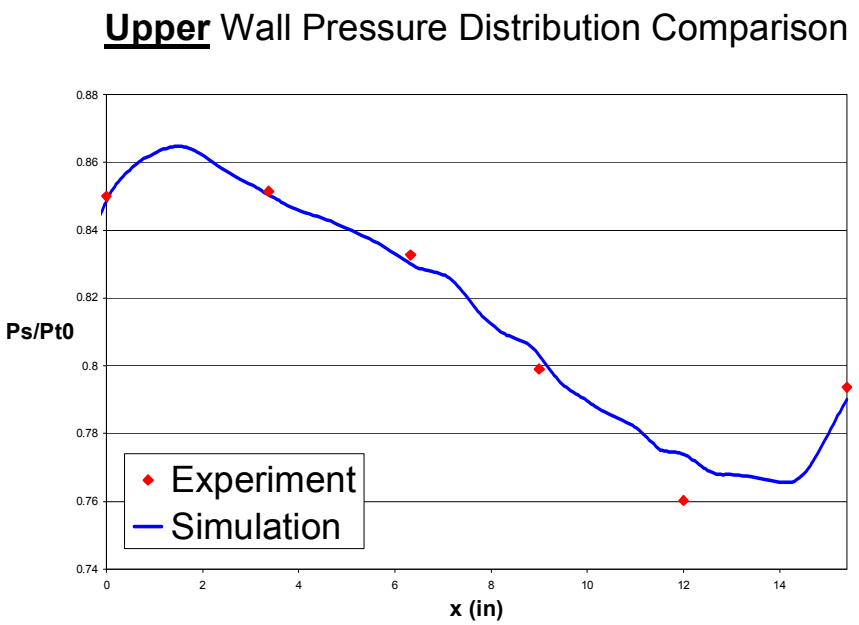

Figure 115. Pressure distribution on the upper surface of the baseline S-duct

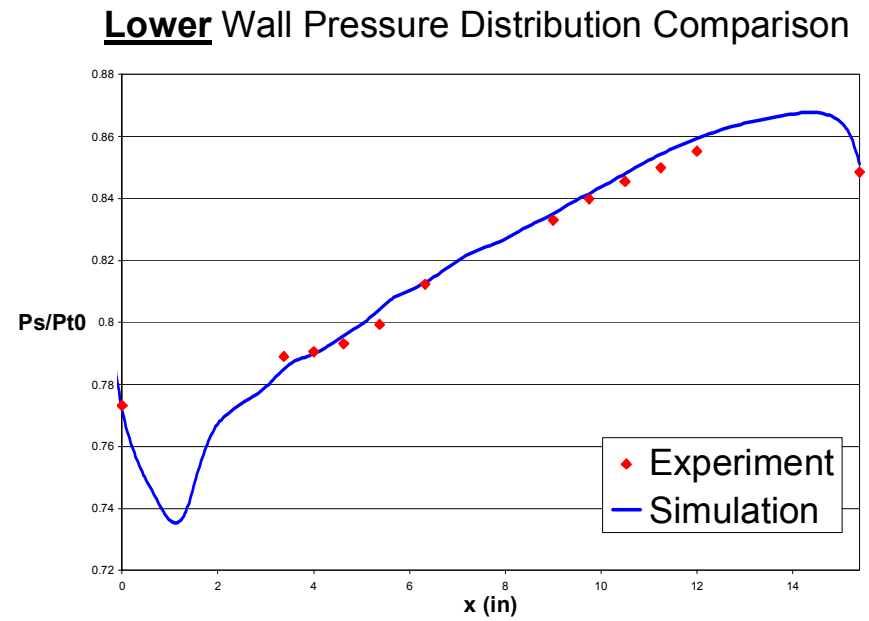

Figure 116. Pressure distribution on the lower surface of the baseline S-duct

In addition to the streamwise pressure distribution, comparisons of steady-state AIP total-pressure contours were made for the baseline S-duct. Figure 117 shows a comparison of the contours. Here the numerical data were interpolated to represent the 40-probe rake. Overall, the simulation contours agrees with the experiment. The largest deviation from the experimental contours exists where the secondary flow vortices are located. In this region, the simulation predicts a larger extent of total-pressure loss than the experiment. The simulation also predicts a larger total-pressure loss at the outermost ring around the entire AIP.

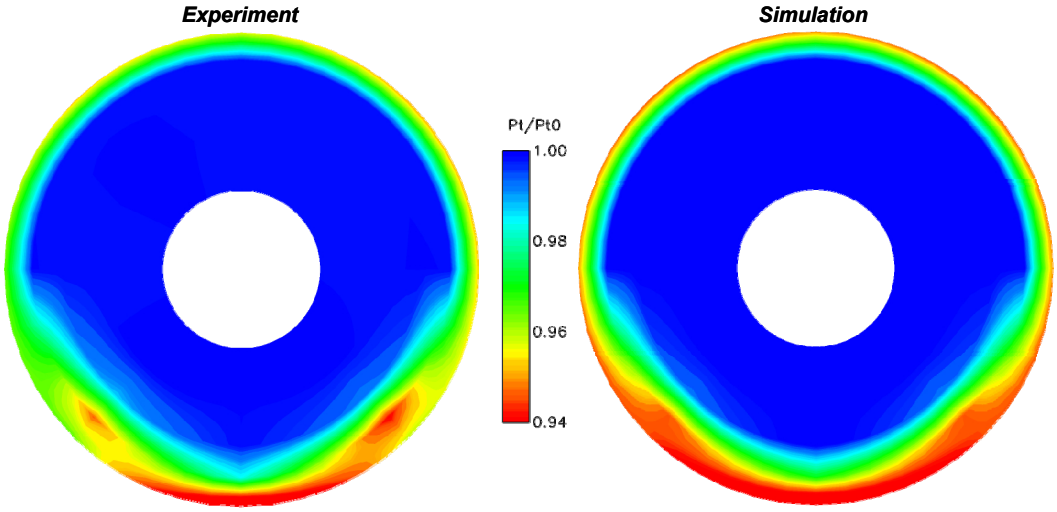

Figure 117. Comparison of AIP total-pressure contours for the baseline S-duct

A quantitative comparison of the recovery and steady-state distortion data at the AIP is given in Table 4. The predicted pressure recovery agrees well with that simulated. The circumferential distortion at the hub (DPCPh), tip (DPCPt), and ring-averaged ($DPCP_{ave}$) agree within 10% between simulation and experiment. Larger differences in radial distortion are seen, with the largest at the tip, DPRPt. This is not surprising based on recovery contours of the outermost ring in Figure 117.

Table 4. Recovery and distortion comparison for the baseline S-duct

	Recovery	DPCPave	DPCPh	DPCPt	DPRPh	DPRPt
Simulation	0.985	0.0073	0.0000	0.0169	-0.0152	0.0416
Experiment	0.986	0.0080	0.0000	0.0185	-0.0130	0.0338
% Diff	0.10	9.25	0.00	8.40	16.92	23.08

Simulations of the baseline S-duct with the boundary layer fence were also made and compared with test. Again, the fence was used in test to produce a BLI-like boundary layer at the entrance to the diffuser. The first comparison, Figure 118 and Table 5, focuses on the use of a screen boundary condition to model the fence. The low pressure region at 180° is the signature of a pair of streamwise counter-rotating vortices, with the upwash region located about 180°. In the simulation, this vortex pair is located farther from the wall than in the experiment. Furthermore, the extent of the losses induced by the fence model in the simulation are greater than those produced by the fence in test. As seen in Table 5, varying comparisons were found in recovery and distortion indices. The simulations generally had larger value of predicted distortion than found in test. On the other hand, the predicted recovery was 0.7% lower than test. Despite these differences, the flow features and quantitative data were sufficiently similar between the simulation and experiment to justify using this screen model throughout the remainder of the program.

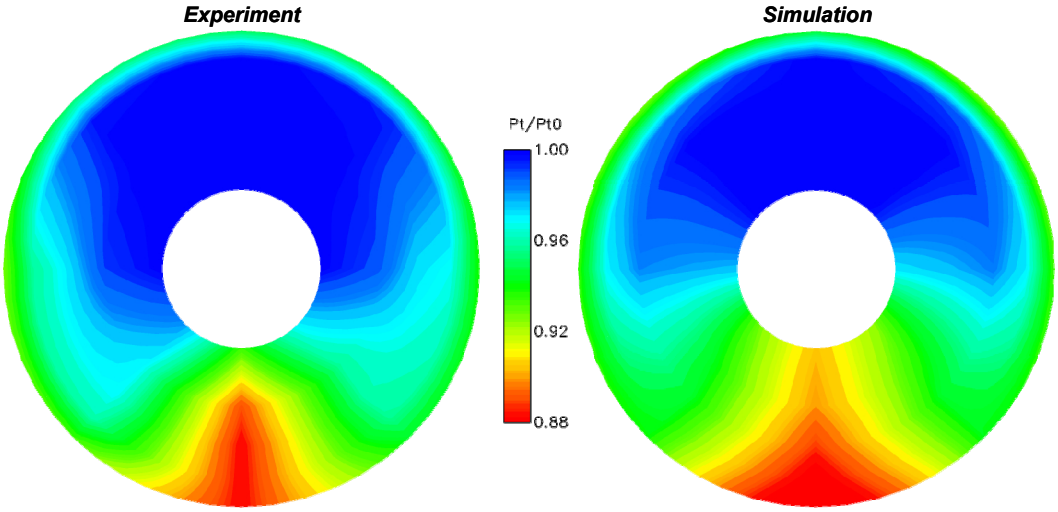

Figure 118. Comparison of AIP Recovery Contours for the Baseline S-Duct with Boundary Layer Fence

Table 5. Recovery and Distortion Comparison at AIP for Baseline S-duct with Fence

Experiment	
DPCPave	0.028
DPCPh	0.031
DPCPt	0.022
DPRPh	-0.021
DPRPt	0.032
Recovery	0.966

Simulation	
DPCPave	0.035
DPCPh	0.035
DPCPt	0.035
DPRPh	-0.005
DPRPt	0.032
Recovery	0.959

The formation of the streamwise counter-rotating vortices by the fence may be seen in Figure 119. It also shows their evolution as they convect downstream. Notice that near the throat, the vortices have joined together and begin to lift away from the lower surface of the duct. The vortices in the experiment do not lift away from the wall as far as those in the simulation, Figure 118.

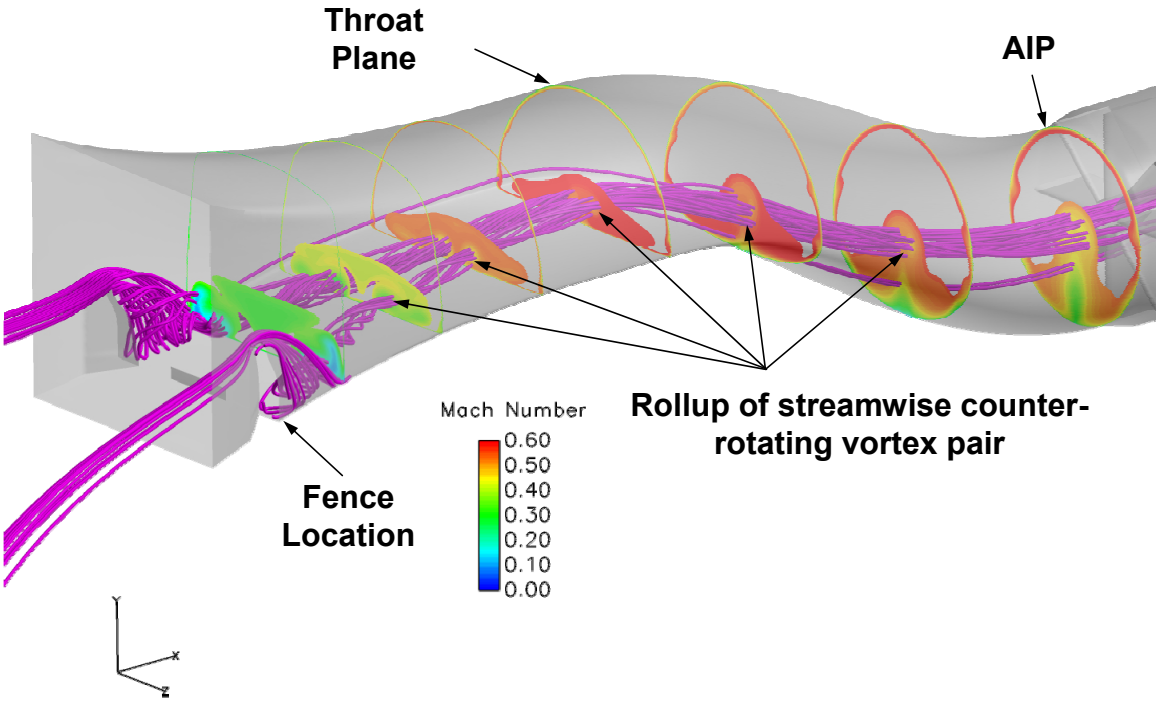

Figure 119. Formation and Evolution of Streamwise Oriented Counter Rotating Vortices Produced by the Fence

Prior to developing a numerical screen model for the fence, a simpler approach was attempted to produce a BLI-like entrance boundary layer. It is discussed here for completeness. In this approach, a tailored boundary-layer profile was prescribed as an inflow boundary condition. This profile was extracted from simulations of an integrated BLI inlet operating at flight conditions. The AIP recovery contours from this simulation, Figure 120, indicate the absence of the streamwise counter-rotating vortices as seen in experiment. Rather, this approach results in a large region of total pressure loss with little or no secondary flow content. Comparison of recovery and distortion, Table 6, show similar disagreement. These results suggested that this simpler approach was not appropriate for modeling a BLI-like inlet boundary layer.

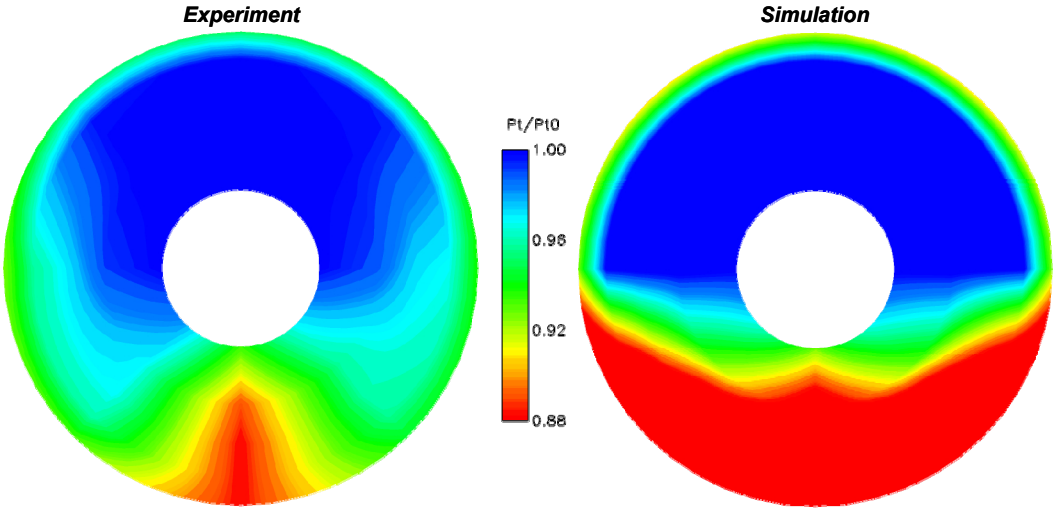

Figure 120. Comparison of AIP recovery Contours for the Baseline S-Duct with Prescribed Incoming Boundary Layer

Table 6. Recovery and Distortion Comparison for Baseline S-Duct with Prescribed Incoming Boundary Layer

Experiment		Simulation	
DPCPave	0.028	**DPCPave**	0.0727
DPCPh	0.031	**DPCPh**	0.0413
DPCPt	0.022	**DPCPt**	0.0968
DPRPh	-0.021	**DPRPh**	-0.0515
DPRPt	0.032	**DPRPt**	0.0748
Recovery	0.966	**Recovery**	0.935

Passive Flow Control in the S-Duct Diffuser

Of key importance to this program was the ability to simulate the impact of flow-control devices on the inlet flow. Towards that end, comparisons between experiment and simulation are presented here for the six microvane configurations used in the DOE. Given the findings from the previous section, all the simulations in this section made use of the screen boundary condition to model the boundary layer fence. The AIP recovery contours for microvane Configuration 1 are shown in Figure 121. As with the baseline, this simulation captures the presence and location of the key flow features, which consist of the secondary flow vortices at 180°, and the microvane vortices at both 90° and 270°. The main difference between the simulation and the test was the larger total pressure loss predicted in the simulation in the circulation region about the vortices.

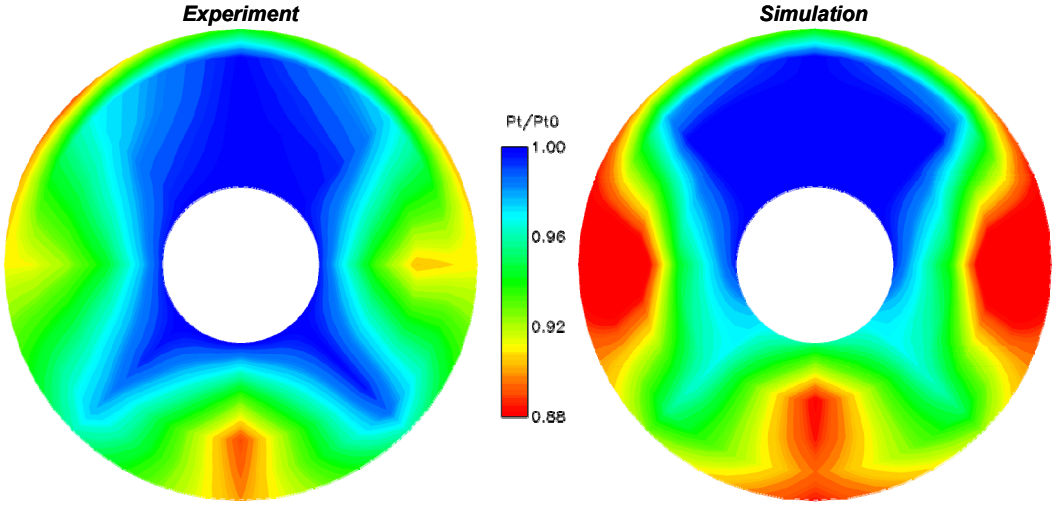

Figure 121. Comparison of AIP Recovery Contours for Microvane Configuration 1

A quantitative comparison of AIP recovery and distortion data for Configuration 1 is given in Table 7, and shows reasonable agreement between simulation and experiment. Circumferential hub distortion is predicted to be larger than found in experiment; this is consistent with the contour seen in Figure 121. The other distortion indices are in fair agreement. The predicted recovery is 1.5% lower than found in test.

Table 7. Recovery and Distortion Comparison for Microvane Configuration 1

Experiment		Simulation	
DPCPave	0.022	DPCPave	0.026
DPCPh	0.012	DPCPh	0.021
DPCPt	0.025	DPCPt	0.025
DPRPh	-0.040	DPRPh	-0.045
DPRPt	0.040	DPRPt	0.044
Recovery	0.960	Recovery	0.945

The comparisons for the remaining configurations used in the DOE indicate agreement between simulation and experiment is reasonably good. The data are given in Figure 122 through Figure 126 and Table 8 through Table 12.

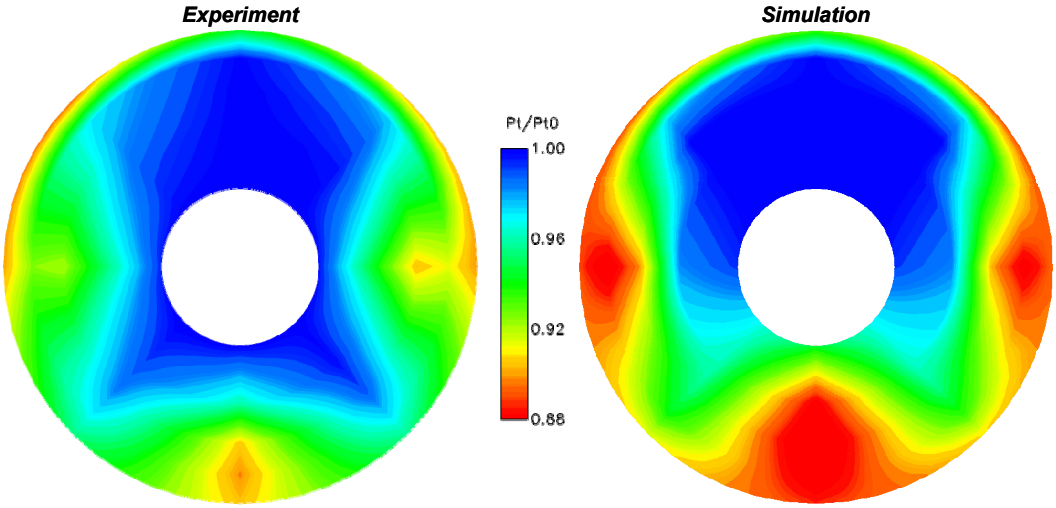

Figure 122. Comparison of AIP Recovery Contours for Microvane Configuration 2

Table 8. Recovery and Distortion Comparison for Microvane Configuration 2

Experiment		Simulation	
DPCPave	0.020	DPCPave	0.026
DPCPh	0.011	DPCPh	0.029
DPCPt	0.024	DPCPt	0.020
DPRPh	-0.038	DPRPh	-0.039
DPRPt	0.044	DPRPt	0.047
Recovery	0.962	Recovery	0.947

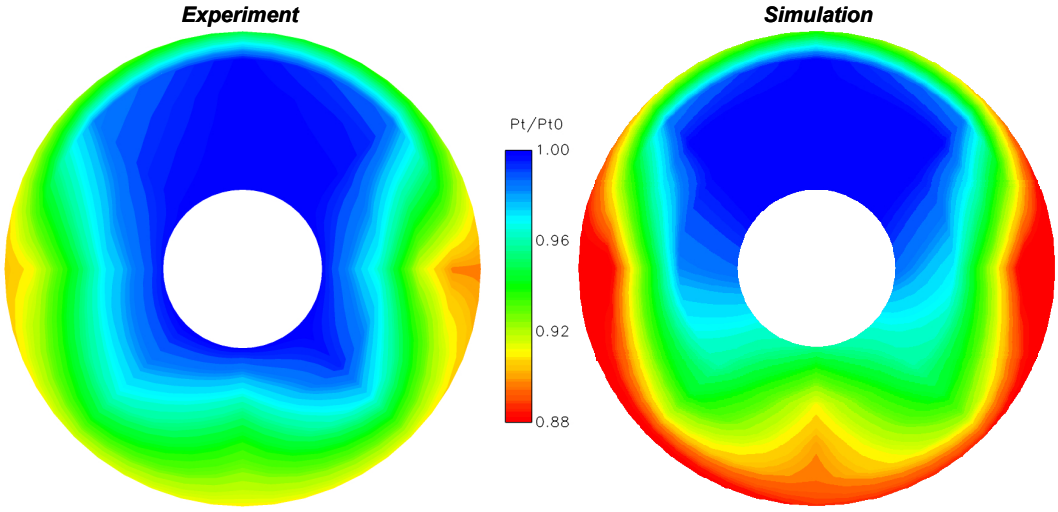

Figure 123. Comparison of AIP Recovery Contours for Microvane Configuration 3

Table 9. Recovery and Distortion Comparison for Microvane Configuration 3

Experiment		Simulation	
DPCPave	0.011	DPCPave	0.022
DPCPh	0.005	DPCPh	0.021
DPCPt	0.016	DPCPt	0.023
DPRPh	-0.038	DPRPh	-0.039
DPRPt	0.046	DPRPt	0.057
Recovery	0.963	Recovery	0.947

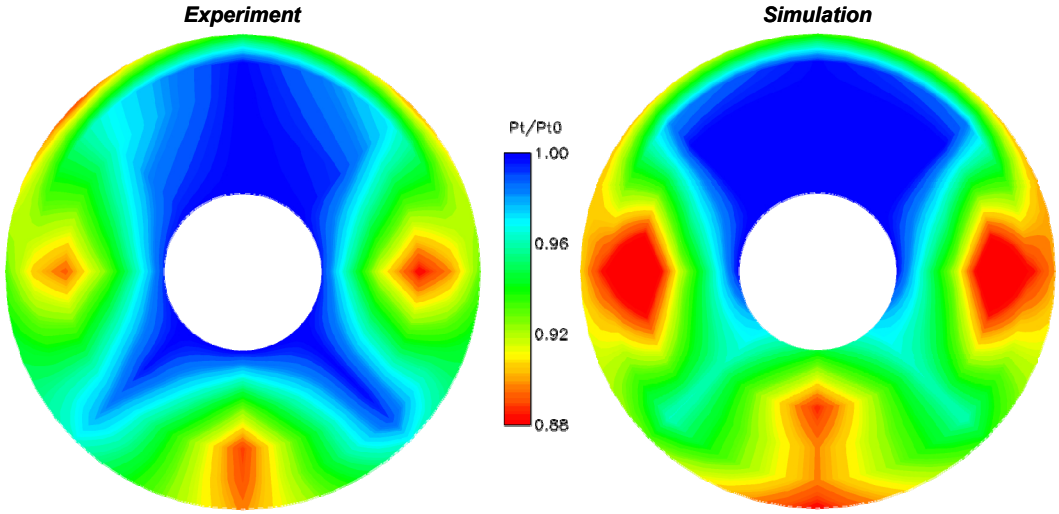

Figure 124. Comparison of AIP Recovery Contours for Microvane Configuration 4

Table 10. Recovery and Distortion Comparison for Microvane Configuration 4

Experiment		Simulation	
DPCPave	0.023	DPCPave	0.027
DPCPh	0.015	DPCPh	0.024
DPCPt	0.026	DPCPt	0.024
DPRPh	-0.041	DPRPh	-0.040
DPRPt	0.032	DPRPt	0.036
Recovery	0.959	Recovery	0.948

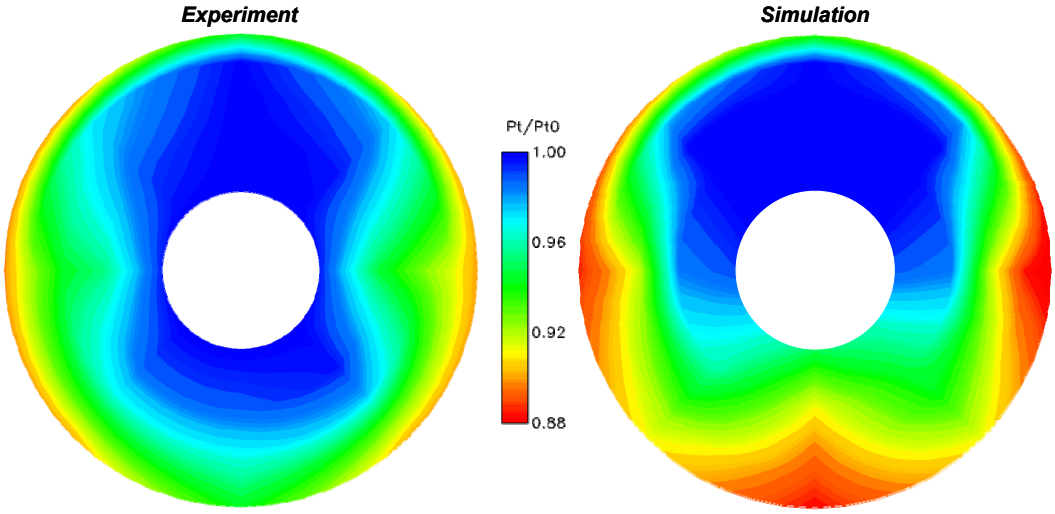

Figure 125. Comparison of AIP Recovery Contours for Microvane Configuration 5

Table 11. Recovery and Distortion Comparison for Microvane Configuration 5

Experiment		Simulation	
DPCPave	0.014	DPCPave	0.023
DPCPh	0.010	DPCPh	0.024
DPCPt	0.015	DPCPt	0.021
DPRPh	-0.037	DPRPh	-0.036
DPRPt	0.053	DPRPt	0.050
Recovery	0.963	Recovery	0.949

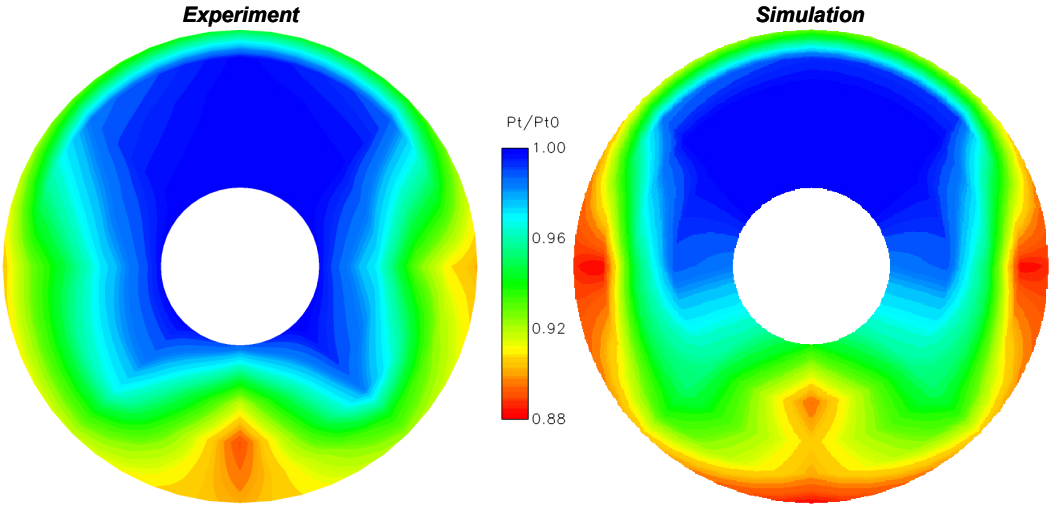

Figure 126. Comparison of AIP Recovery Contours for Microvane Configuration 6

Table 12. Recovery and Distortion Comparison for Microvane Configuration 6

Experiment		***Simulation***	
DPCPave	0.018	**DPCPave**	0.022
DPCPh	0.013	**DPCPh**	0.026
DPCPt	0.018	**DPCPt**	0.019
DPRPh	-0.038	**DPRPh**	-0.029
DPRPt	0.043	**DPRPt**	0.050
Recovery	0.962	**Recovery**	0.952

Review of this data indicates the circumferential hub distortion index, DPCPh, is predicted to be larger than found in test. This was consistent in all six configurations. It was also noted that the recovery was under predicted by 1 – 1.5% when compared to test.

It is apparent that the simulations techniques used here were able to reproduce the key features of the flow found in test. Secondary flows originating in the duct entrance were reproduced found to merge as they move downstream towards to AIP location. Vortices from the microvanes located in the throat region of the duct were reproduced. And the movement in the duct of the vortical flow from the microvanes was correctly modeled as evidenced by the total-pressure pattern found at the AIP. The simulations generally produced larger vortical extent and total-pressure losses than found in test. These were the key discrepancies found when comparing simulation results to those found in test. The differences in quantitative data (recovery and distortion) were largely driven by the larger vortical extent and total-pressure losses found in CFD.

Although it produced the correct qualitative flow structure, it is apparent that improvements to the screen model are needed to improve agreement with experiment for all microvane configurations. It is felt, however, that the use of a fence in test, and a screen model in simulations, shows promise. The degree to which quantitative agreement was found between test and simulation indicates these techniques can be used to provide design guidance. Of course, the fence used in the test and the screen model used in the CFD are surrogates used to produce a BLI-like entrance flow in a direct-connect test facility and simulation. Testing or

simulating a fully integrated boundary-layer ingesting inlet would preclude the need for either surrogate.

Dynamic Distortion Simulations

An integrated BLI inlet will be influenced by Reynolds number effects to a larger degree than a pylon-mounted inlet or a similar S-duct inlet with a boundary layer diverter. Correlation of wind-tunnel inlet data to flight conditions will be problematic for a BLI inlet because of Reynolds number effects. A strength of CFD methodologies is the ability to provide aerodynamic similarity. Inlet data of interest includes both steady-state data, like total-pressure recovery, as well as dynamic data like total-pressure distortion. The previous Section addressed prediction methodologies for steady-state data. This Section addresses the ability of CFD, as implemented here, to predict dynamic distortion. This capability is in its infancy, so that the information presented in this Section should be taken with realistic expectations.

The geometry used in the simulations was the S-duct diffuser using microvane Configuration 4. No boundary layer fence was used in either the experimental or computational geometry. The computational domain consisted of the tunnel contraction, diffuser, and extension as seen in Figure 127. The extension was used to prevent the computational outflow boundary from influencing the solution at the AIP. Microvanes were located on the bottom wall at the entrance to the diffuser. While the baseline duct offered a simpler geometry and flow structure, the ability of CFD to capture the dynamic content of vortical flow present with Configuration 4 was of interest. In total, the computational grid consisted of a mixture of prism, pyramid, and tetrahedral elements totaling approximately 46 million elements.

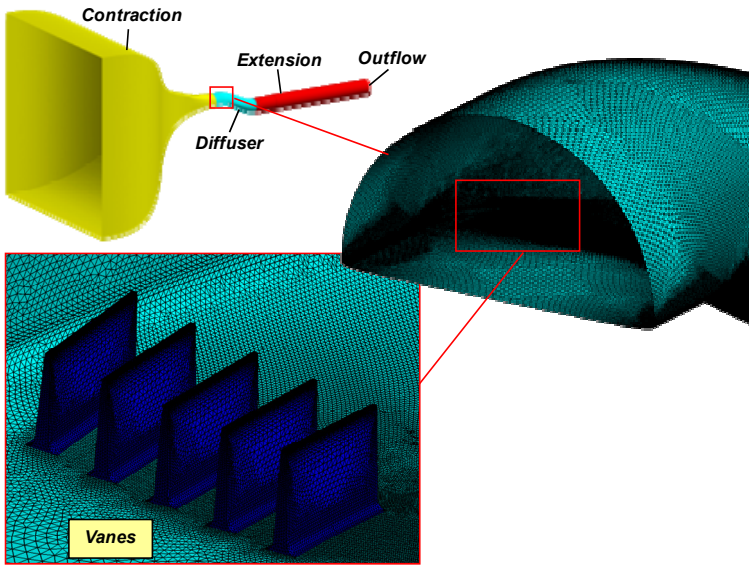

Figure 127. Computational Domain

The simulation was conducted with an AIP Mach number of 0.628, while the experimental AIP Mach number was 0.625. Both correspond to an AIP corrected mass flow rate of 5.46 lbm/sec. The timestep was 6.0 microseconds which corresponds to the characteristic time for the flow to convect across one of the smallest computational elements. A solution was saved every five timesteps, or every 30 microseconds. In total, a dataset of 3350 solutions was accumulated, which is equivalent to just over 0.1 second of simulated time. The simulation was conducted on

248 processors running for 370,000 CPU hours. The duration of the simulated time was substantially shorter than that of the experimental sample time which was on the order of 5 seconds. As mentioned earlier, the time-dependent simulations were done using the SA turbulence model with Detached Eddy Simulation (DES) modeling.

A grid resolution study was conducted. The grid was considered sufficiently refined when the microvane vortices were enveloped by the DES region of the simulation. As an example, the AIP total-pressure contours for the baseline duct with the coarsest and finest grids are shown in Figure 128 and Figure 129, respectively. In both figures, the image on the left indicates the computed total-pressure contours at the AIP, and the image on the right shows an overlay on the contours; the overlay were referred to as an SA mask. The SA mask covers that region for which the SA turbulence model was used. Regions not covered by this mask were computed using the DES model.

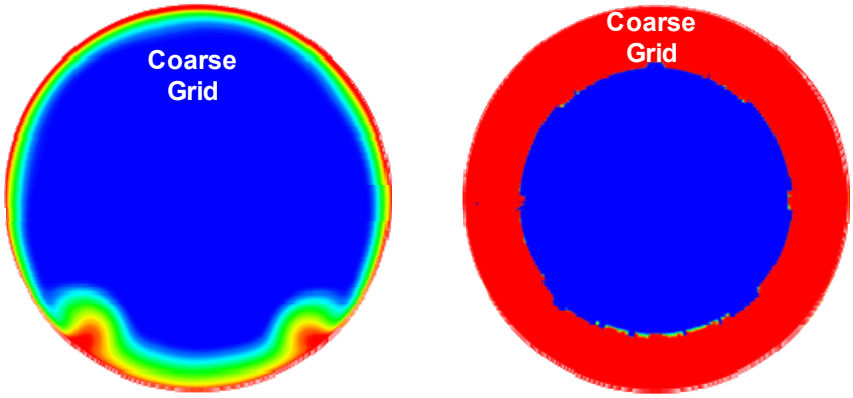

Figure 128. Total-Pressure Contour using the coarse grid (left,) and the same covered by the SA mask (shown in red)

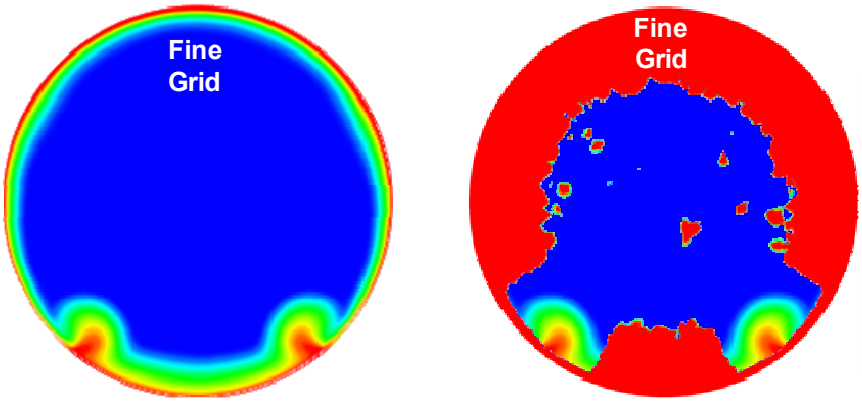

Figure 129. Total-Pressure Contour using the fine grid (left) and same covered by the SA mask (right)

When the coarse grid was used, Figure 128 , the two vortices were completely enveloped in the SA region. The dynamic flow content from these vortices were not sufficiently modeled for a simulation of dynamic distortion. Refining the grid in the regions occupied by the vortices resulted in the AIP contours and mask shape shown in Figure 129. Here the regions in the neighborhood of the vortices were not in the SA region. This indicates that the vortices were modeled with DES.

After the appropriate grid and timestep were determined, the time-dependent simulation was started from a fully-converged RANS simulation. The time histories of the face-averaged total-pressure at the AIP, pfav, is provided in Figure 130. The scan number corresponds to the number of the saved solution in the dataset, therefore each scan number represents a time increment of 30 microseconds. The transition from the steady (RANS) simulation to the unsteady (Detached Eddy Simulation, DES) simulation takes place over approximately the first 500 hundred scans. For this reason, the statistical calculations and comparisons in this Section were performed on the dataset between scans 500 and 3350; that is to say that data in the start-up process was not used. The results presented in the remainder of this Section used this truncated dataset, consisting of 2851 scans, and is referred to as the *statistical dataset*.

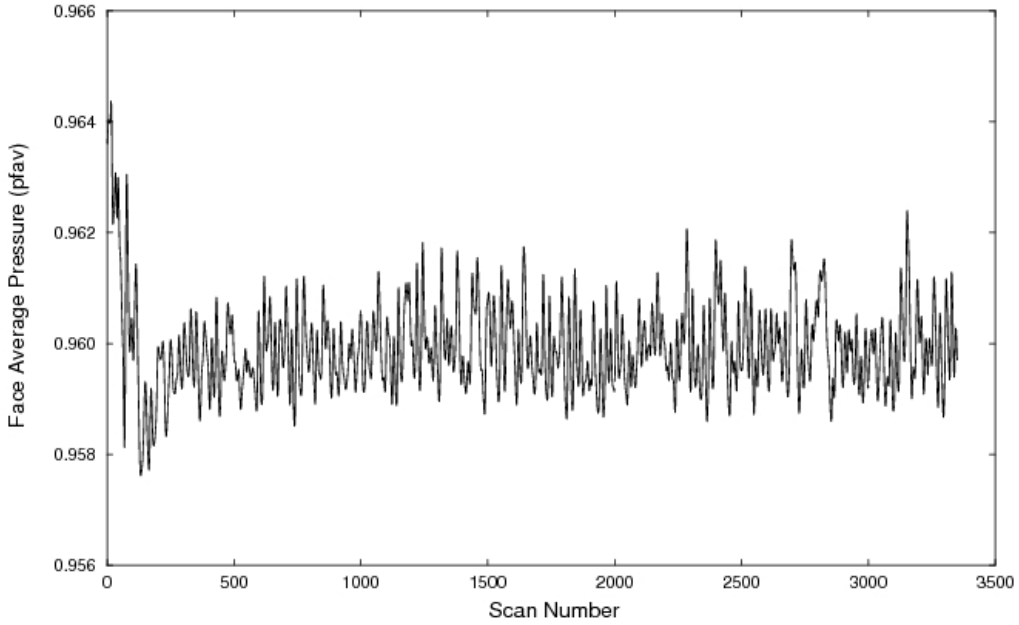

Figure 130. Time history of face-averaged total-pressure at the AIP

The mean properties of the inlet aerodynamic performance, determined from this statistical dataset, were seen to be in reasonable agreement with those measured in experiment. Figure 131 shows the steady-state total-pressure recovery contours at the AIP, and the corresponding distortion indices, from both CFD and experiment. The overall pattern characteristics are seen to be similar. Both patterns exhibit vortices about 90° and 270° which originate with the microvanes. Both exhibit the pressure losses of the naturally occurring secondary flow at 180°. The primary differences between the two is that CFD predicted a larger pressure loss than found in experimental. Despite this, the distortion indices, provided in the table of Figure 131, as well as the recovery show reasonable agreement. It appears that the mean spatial-averaged aerodynamic properties of the inlet flow are being captured by the time-dependent CFD.

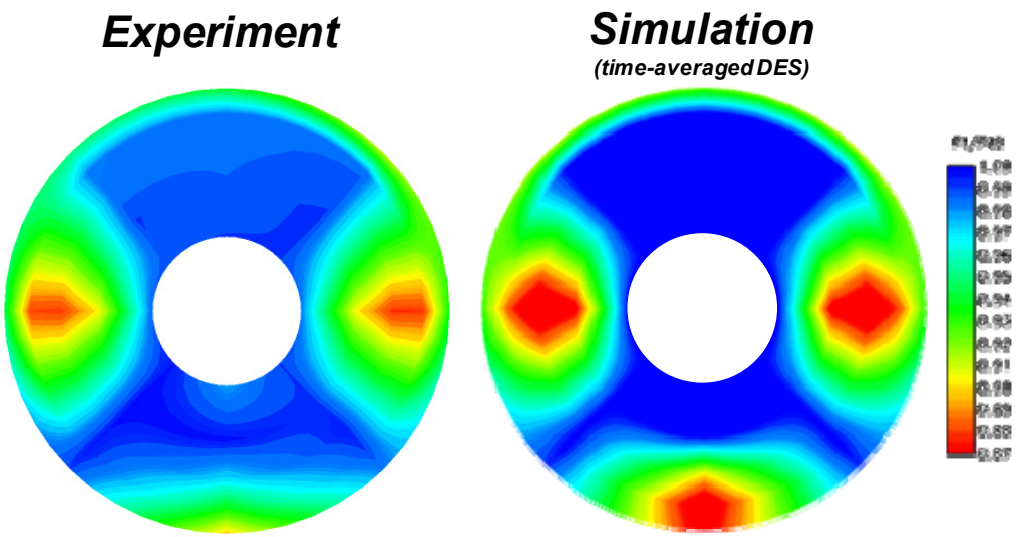

DPCPave	0.028
DPCPh	0.019
DPCPt	0.028
DPRPh	0.000
DPRPt	0.020
Recovery	0.964

DPCPave	0.032
DPCPh	0.026
DPCPt	0.028
DPRPh	0.000
DPRPt	0.029
Recovery	0.960

Figure 131. Comparison of steady-state recovery and distortion between experiment and CFD

Examination of the root-mean-squared (RMS) of the total-pressure fluctuation provides another viewpoint of the CFD process used here. This is quantified in Figure 132, which shows contours of the RMS of $(P_{Ti} - P_{Tss})/ P_{T0}$, the fluctuating component of the total pressure recovery. The vortices from the microvanes are indicated by the increase in pressure RMS in the regions about 90° and 270° of the experimental data. The largest pressure RMS of the experimental data is seen to be located about 180° where the secondary flow passes through the AIP. The pressure RMS contours for the CFD dataset is shown in Figure 132 as well. Suppression of the pressure fluctuations is evident in an annulus around the duct outer radius. And the pressure RMS from the CFD data is larger than found in experiment near the inner edge of the secondary flow region located about 180°. These differences point to the need for improvements in the implementation of the DES model as used here.

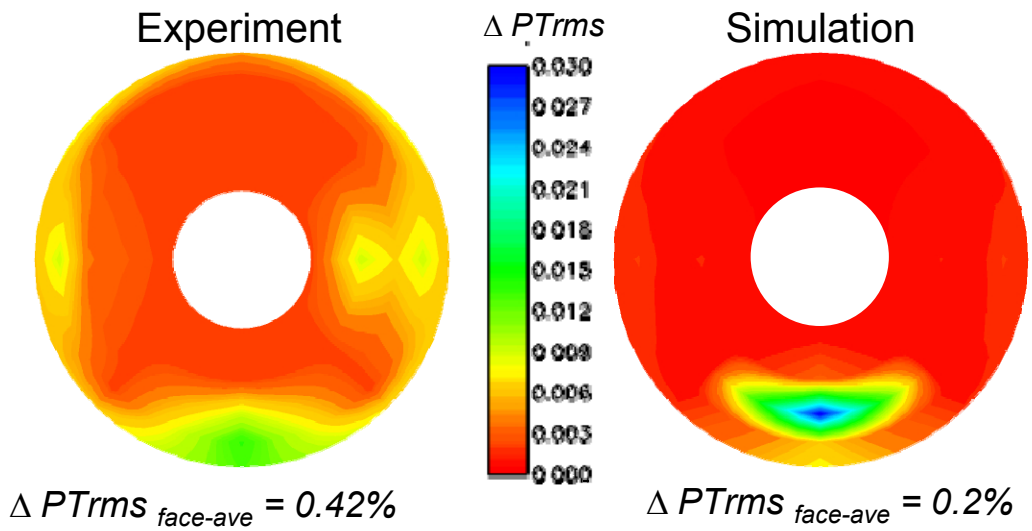

Figure 132. Comparison of the RMS of recovery fluctuations between experiment and simulation

In addition to the assessing steady-state performance, the data and patterns associated with the peaks (maximum value) of the distortion indices were obtained. The peak $DPCP_{ave}$ pattern occurred at scan number 2839 of the simulation. Figure 133 shows that the total pressure contours and peak $DPCP_{ave}$ value for both simulation and experiment are in reasonable agreement.

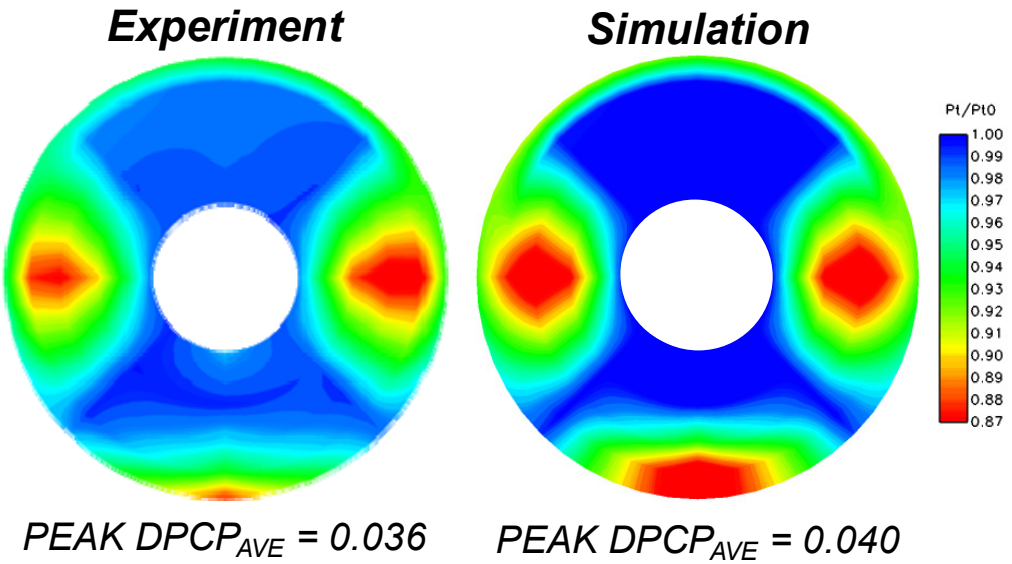

Figure 133. Comparison of peak $DPCP_{ave}$ between experiment and simulation

The peak value of circumferential hub distortion, $DPCP_H$, occurred at a scan number of 1761. The total pressure contours, as well as the peak value, are shown in Figure 134. There is good agreement between simulation and experiment.

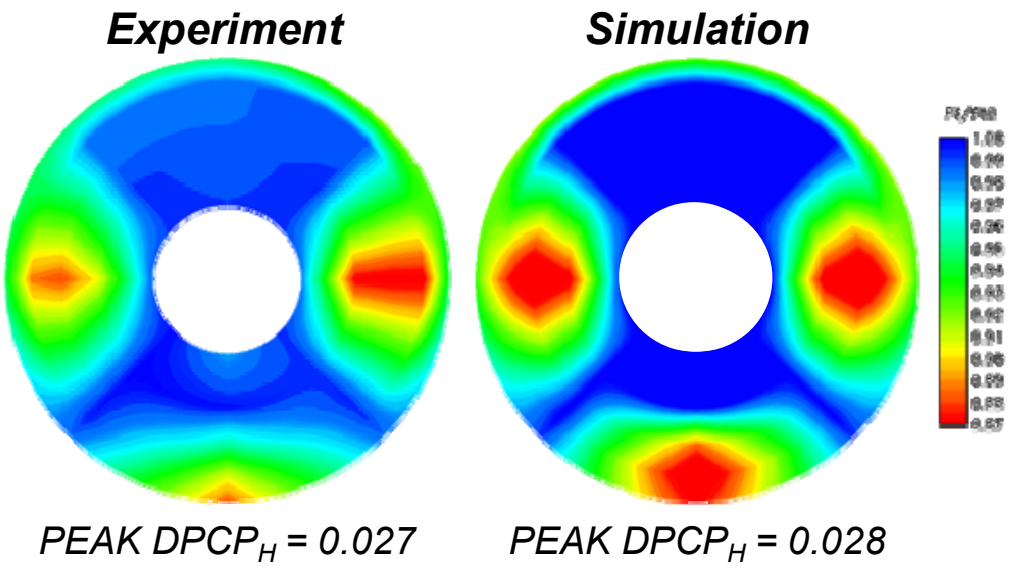

Figure 134. Comparison of peak DPCP$_H$ between experiment and simulation

The peak value of circumferential tip distortion, DPCP$_T$, occurred at the same scan number as the peak DPCP$_{AVE}$. This indicates that the circumferential distortion is more dominate at the tip than the hub. The total pressure contours, as well as the peak values, are shown in Figure 135. Again there appears to be good agreement between simulation and experiment.

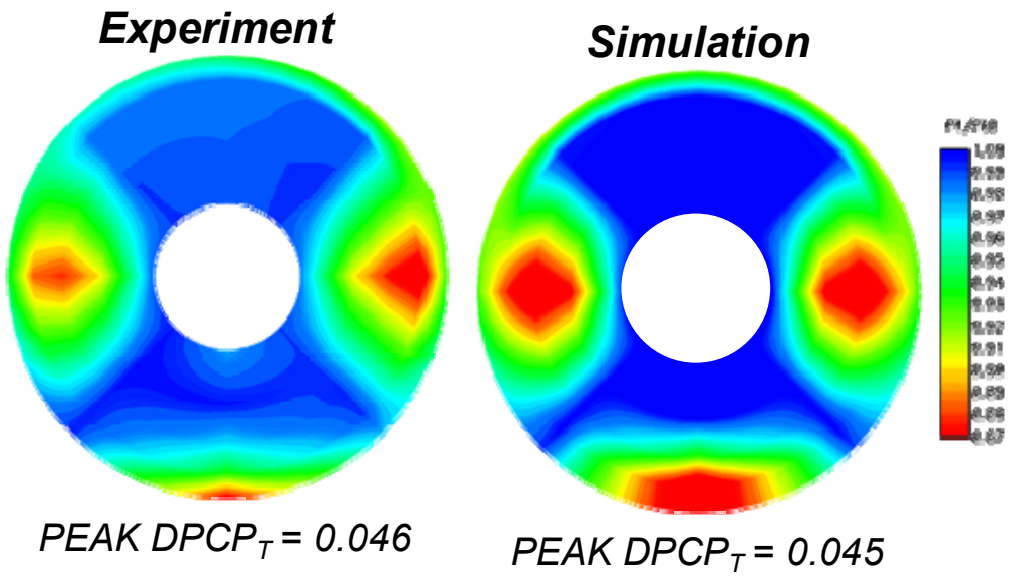

Figure 135. Comparison of peak DPCP$_T$ between experiment and simulation

The peak radial hub distortion, DPRP$_H$, along with the total pressure patterns are shown in Figure 136. They agree reasonably well between simulation and experiment.

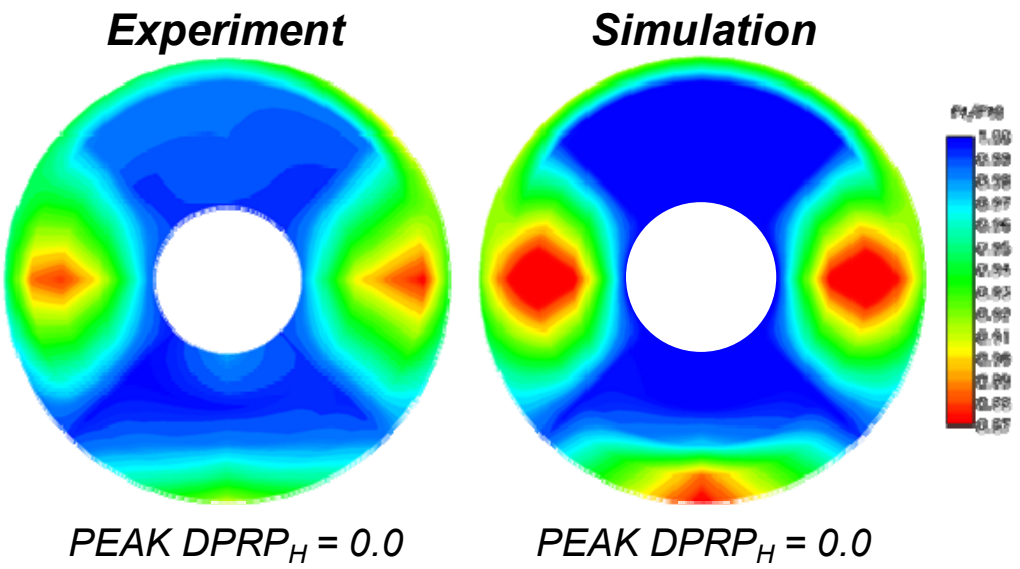

Figure 136. Comparison of peak DPRP$_H$ between experiment and simulation

The peak radial tip distortion, DPRP$_T$, occurred at a scan number of 2825. As seen in Figure 137, the total pressure patterns appear similar between simulation and experiment. However, the value of the peak DPRP$_T$ found from the CFD data is substantially larger than found in experiment.

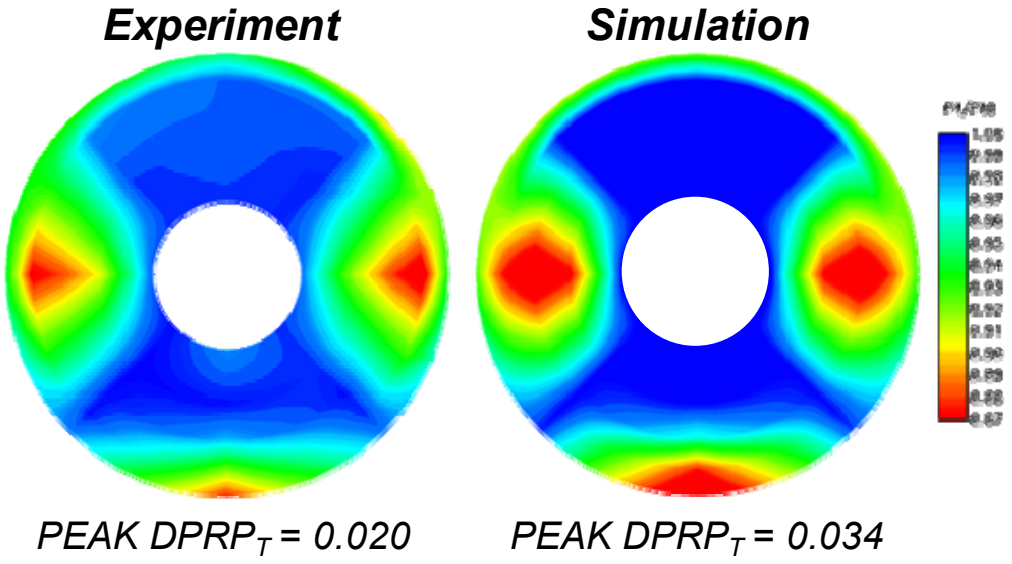

Figure 137. Comparison of peak DPRP$_T$ between experiment and simulation

While deficiencies in the results have been found due to implementation used here, the results from the CFD simulations have shown promise when used for estimating dynamic pressure distortion. This type of simulation certainly is not yet a common practice. Continued development of DES and LES CFD processes is warranted because of the anticipated need to correlate inlet data from wind tunnel to flight conditions for BLI inlet systems.

System-Level Assessments

A system-level assessment was performed of the hybrid flow-control system with steady and synthetic jets. This assessment was done to show system-level payoffs and penalties. The approach compared system-level payoffs and penalties of steady jets with synthetic jets both in a hybrid configuration. The sensitivity on range was compared between the two configurations. The payoffs and penalties on range were computed for weight, performance (total pressure recovery), power extraction (synthetic jets), and engine bleed (steady jets) using existing information. The baseline vehicle used in this study was the N2A-EXTE which is the configuration that meets the N+2 goals for noise and fuel efficiency. Figure 138 shows an image of the baseline vehicle used for this study and gives basic vehicle information. The 6000 nautical mile range is the baseline for which the sensitivities were compared. The propulsion system used on the baseline vehicle included podded flush nacelles with engine bypass ratio of 10. Figure 139 shows the engine used on the baseline vehicle for this study along with basic engine information. The engine was a NASA Glenn Research Center study engine with a fan pressure ratio of 1.6. This engine was used in the performance (SFC) sensitivity on range with existing information.

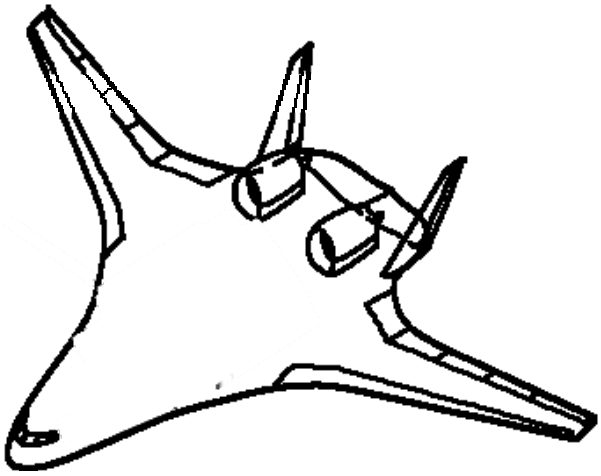

N2A-EXTE Baseline Vehicle
Range = 6000 nm
TOGW = 471,648 lb
OWE = 155,106 lb
Flush Nacelle

Figure 138. Baseline Vehicle used for System-Level Assessment

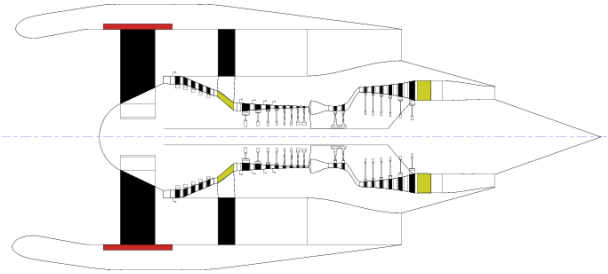

NASA GRC Study Engine
Total Engine Weight = 14044 lb
Engine Length = 185.6 in
Fan Diameter = 106.8 in
BPR = 10, FPR = 1.6

Figure 139. Baseline Engine used for System Level Assessment

The sensitivity to range was computed by using the weight, performance (total pressure recovery) and engine bleed for the hybrid configuration with a steady jet. The change in total pressure recovery from the baseline vehicle affects the engine performance (SFC) which in turn will have an effect on range of the vehicle. Bleeding air from the inlet to use for the steady jet

also has an effect on the engine performance and therefore the range of the vehicle. Finally an increase or decrease in weight from the bleed system for the steady jets will also have an effect on the range. A Taylor series equation was created to compute these sensitivities, Equation 12. A similar approach was taken for the hybrid configuration with synthetic jets. The synthetic jets are a zero net mass system, as described in previous sections, so the bleed air of the engine is not required. However, the synthetic jets will require power and therefore power extraction from the engine. This will affect the engine performance and the range of the vehicle. A Taylor series equation for the synthetic jet was also created for use with the system study, Equation 13. Equation 12 and Equation 13 are virtually identical with changes only in the last term.

$$\Delta R = \left(\frac{\partial R}{\partial OWE}\right)\Delta OWE + \left(\frac{\partial R}{\partial SFC}\right)\left(\frac{\partial SFC}{\partial \frac{P_{T2}}{P_{T0}}}\right)\Delta\frac{P_{T2}}{P_{T0}} + \left(\frac{\partial R}{\partial \dot{m}_{bleed}}\right)\Delta\dot{m}_{bleed}$$

Equation 12

$$\Delta R = \left(\frac{\partial R}{\partial OWE}\right)\Delta OWE + \left(\frac{\partial R}{\partial SFC}\right)\left(\frac{\partial SFC}{\partial \frac{P_{T2}}{P_{T0}}}\right)\Delta\frac{P_{T2}}{P_{T0}} + \left(\frac{\partial R}{\partial HP_{EXT}}\right)\left(\frac{\partial HP_{EXT}}{\partial kW}\right)\Delta kW$$

Equation 13

Test results show the inlet total pressure recovery of the inlet with the steady jet system and the synthetic jet system were nearly identical and less than 0.1% different. This means the sensitivity of the range to performance between the two systems was nearly identical as well. Figure 140 shows the engine SFC sensitivity to total pressure recovery, engine bleed and horse power extraction. These sensitivities were taken at top-of-climb condition with a Mach number of 0.81 and 31,000 foot altitude. The data show the total pressure recovery has the largest effect on the engine SFC, but there is very little difference in recovery from passive and active systems. The sensitivities also show that engine bleed has a much larger impact on engine SFC compared with horse power extraction. Figure 141 shows the range sensitivity with changes to the engine SFC and the vehicle operational weight.

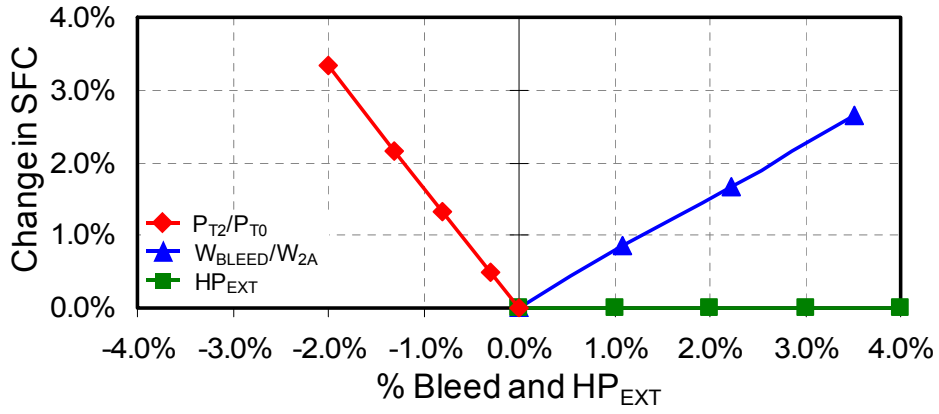

Figure 140. Baseline Engine Sensitivities to Bleed, Horse Power Extraction and Total Pressure Recovery

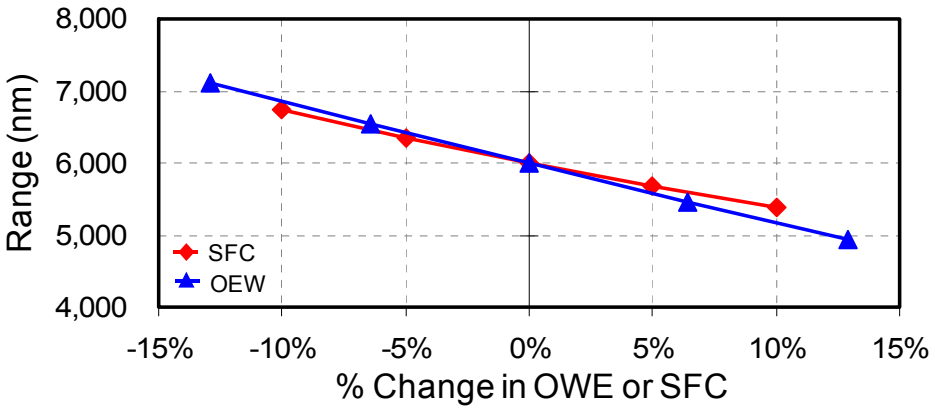

Figure 141. Baseline Vehicle Range Sensitivities to Engine SFC and Vehicle Empty Weight

The baseline configuration assumes the engine is utilizing no engine bleed and power extraction of 100 HP. This system study was done as a comparison of hybrid flow-control system with steady and synthetic jets. Therefore, the baseline assumes an inlet total pressure recovery with passive flow control. As stated previously, the inlet total pressure recovery is nearly identical between passive and hybrid flow-control systems. The weight of a bleed system for a steady jet system was estimated at 200 pounds. The weight of a synthetic jet system was estimated by scaling up an array of actuators. The weight of the synthetic jet system was estimated at 220 pounds. Figure 142 shows the effects of increasing engine bleed or increasing power extraction on the range of the baseline vehicle. The results show a much larger impact on range of the bleed rate of the steady jets compared with the power extraction of the synthetic jets.

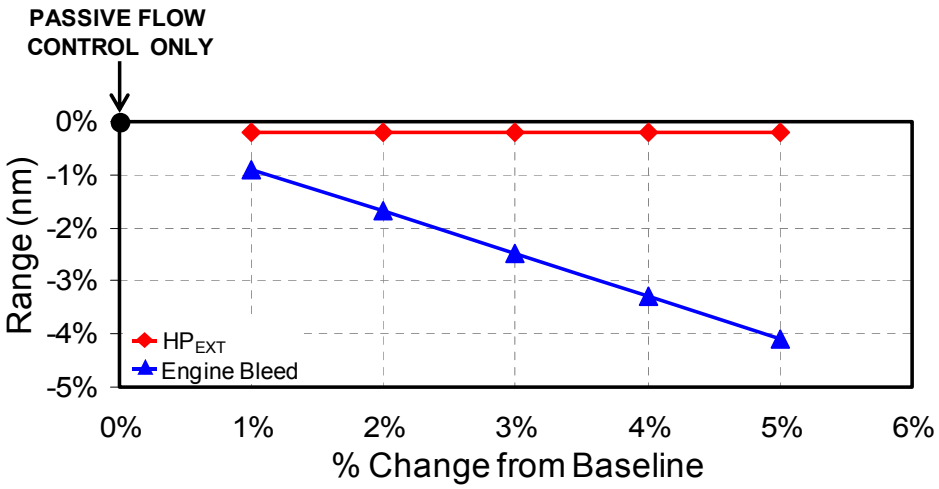

Figure 142. Sensitivity of Hybrid Flow-control systems on Range

Conclusions and Recommendations

This section contains both conclusions reached because of the information gathered during this study along with recommendations for further study. Conclusions are presented first followed by recommendations.

Conclusions

Through this program, significant advances have been achieved in advanced inlet flow-control technology development, modeling, and test techniques. Flow-control technologies and validated prediction tools for controlling inlet total-pressure distortion have been developed that will be applicable across a broad range of aircraft to enable future, subsonic, HWB vehicles to meet and even exceed N+2 program goals. Specifically, flow-control technologies, including 2nd generation hybrid devices, made up of microvanes and synthetic jets, were designed using robust statistical methods and evaluated as a means to control BLI-inlet distortion, and system-level benefits of employing this 2nd generation hybrid flow control system were assessed. In addition, advanced, inlet-distortion prediction methods, based on integrated CFD and testing, were improved and validated against the experimental database developed under this program.

The flow-control technology development accomplished in this program demonstrated that 2nd Generation, hybrid, flow-control devices produce favorable mean-flow structures that lower steady-state distortion in BLI inlets without adversely influencing total-pressure recovery. The 2nd Gen HFC system implemented here produced only a small reduction in dynamic distortion over the steady-state value due to the operating frequency. However, results indicated that operating the synthetic jets with a cycle time of approximately 1/revolution of the engine fan would reduce dynamic distortion. This cycle time would scale with Strouhal number between subscale and full-scale synthetic jets. In addition, because of redundancy, synthetic jets operating alone may provide sufficient operability margin to provide a fail-safe flow-control solution in the absence of passive devices.

In addition to performance at the inlet-system level, the benefits of a 2nd generation, HFC system were quantified at a vehicle level. The vehicle-level trade study conducted in this program indicated that a 2nd Gen HFC system, which uses synthetic jets in lieu of microjets, and therefore, requires no bleed-air extractions, will provide increased mission range over a 1st Gen HFC system.

In addition to advances in flow-control technology, new test techniques for evaluating BLI-inlet flow-control technologies were also developed through this program. The ability to generate a BLI-like inlet-entrance flow in a direct-connect, wind-tunnel facility was developed and successfully demonstrated. The flow was created using a fence consisting of screens and honeycomb structures to produce a boundary-layer-like flow with significant secondary-flow motion. In addition, the use of D-optimal, statistically designed experiments was successfully demonstrated in this research, and enabled interpretation and implementation of the results. The use of response surface methodology allowed geometric and aerodynamic factors to be identified which had statistical significance in influencing the AIP aerodynamic performance, and subsequently allowed design guidelines to be formulated. Because replicates were included as part of the designed experiments, error assessments were straightforward.

Not only were advances in experimental test techniques accomplished during this program, but numerical tools were also improved and validated. Reynolds-Averaged Navier-Stokes CFD, as implemented here using BCFD, was successful in simulating the steady-state flow physics

produced, including the basic flow in the diffuser, as well as, that created by the flow-control devices. This success also included the ability to simulate the flow created by the fence. A mathematical model representing the flow exiting a synthetic-jet was formulated using experimental data obtained through statistically designed experiments. The model was implemented as a wall boundary condition for CFD. Finally, numerical methods were employed in a ground-breaking attempt to directly simulate dynamic distortion. However, shortfalls were found with the ability of Direct-Eddy Simulation CFD to simulate the turbulent flow structure responsible for producing dynamic distortion. Specifically, total pressure fluctuations computed by the DES CFD were suppressed when compared to test measurements of the fluctuations.

This program had two key objectives. The first was to develop fail-safe, flow-control technologies for highly-integrated offset inlets to move towards "N+2" project goals. The second was to develop and improve novel test methods and validate tools for predicting active hybrid flow-control effectiveness in managing inlet pressure distortion. Through results from this program, validated computational tools are available to improve system trades for advanced inlet concepts. The prediction capabilities are applicable to a range of subsonic, fixed-wing aircraft, and validated for advanced HWB vehicles. The tools enable improved accuracy in predicting active hybrid flow-control-system effectiveness in controlling BLI-inlet total-pressure distortion at flight conditions. The advances in inlet technologies and prediction tools accomplished in this program will help to obtain high-speed cruise efficiency and low-noise signature and fuel burn while reducing field lengths for future HWB aircraft.

Recommendations

After considering the results and conclusions, a number of recommendations for future study are offered. Experimental and computational research should be continued using subscale models to mature a 2nd-generation HFC system in a BLI S-duct. A focus should be on developing and using synthetic jets with increased operating frequencies (on the order of 1-2kHz) and jet momentum of about 1-2% of the inlet-throat momentum. Designed experiments should be used to provide broad-based design guidelines leading to optimization of the HFC system. Development of large-scale, flight-like synthetic-jet actuators should be initiated. Here the operating frequencies should be on the order of 100 – 200 Hz, and jet momentum of about 1-2% of the inlet throat momentum. A 2nd Gen HFC system should be tested in a large-scale diffuser rig with large-scale, flight-like actuators. In addition to the AIP aero performance, the focus should be on the "scalability" of the actuator technology, and the durability of the large-scale actuators.

Ultimately, consideration should be given to flight-testing a BLI inlet, with 2nd-generation HFC, on a hybrid wing body aircraft. The focus should be to verify the accuracy of CFD predictions of Reynolds number effects that will be present with a BLI inlet. While full-scale Reynolds numbers are desirable, those reached by the X-48 vehicle would provide insight into the ability of CFD to predict accurately the Reynolds number effects on the aerodynamic performance of a BLI inlet. A flow-through BLI with an instrumented AIP would provide the needed database.

In terms of numerical analysis tools, DES CFD technologies should be further matured. The ability to simulate large-scale turbulent flow structure in a BLI inlet is needed to improve affordably the noise / emissions / performance of hybrid wing-body vehicles, reduce the risks, and shorten the development cycles of hybrid wing-body vehicles. Here the focus should be on improving turbulence models and their integration with the gridding approach.

New Technology

During the course of this research, the following reportable new technology items that may be non-patentable, patentable, or having secondary applications were made:

Non-patentable Discoveries

Improvements:

Inlet aerodynamic performance may be improved by using 2nd Gen HFC systems in BLI inlets.

Innovations:

The development of a mathematical model representing the exit flow conditions of a synthetic jet.

The development of a fence to reproduce a BLI-like flow at the entrance to a diffuser in direct-connect wind tunnels.

Computer Codes:

a) No non-patentable computer codes discoveries were made.

Patentable Inventions

None.

Secondary Applications

It is believed that beneficial effects may be found for applications in which 2nd Gen HFC systems may mitigate adverse flows arising inlet systems in general, not solely BLI inlets. The benefits would arise from reduced fuel burn since no engine bleed air is needed to power flow-control jets.

References

Allan, B, Owens, L, & Lin, J. (2006). Optimal Design of Passive Flow Control for a Boundary-Layer-Ingesting Offset Inlet Using Design-of-Experiments. AIAA 2006-1049.

Amitay, M., Pitt, D., & Glezer, A. (2002). Separation Control in Duct Flows. *Journal of Aircraft , 39*, 616-620.

Amitay, M., Smith, B., & Glezer, A. (1998). Aerodynamic flow control using synthetic jet technology. AIAA Paper 98-0208.

Anabtawi, A.J., Blackwelder, R.F., Lissaman, B.S.P, Liebeck, R.H. (1999). An Experimental Investigation of Boundary Layer ingestion in a Diffusing S-Duct With and Without Passive Flow Control. AIAA Paper 99-0739.

Anderson, B.H., Mace, J.L., Mani, M. (2009). Active “Fail Safe” Micro-Array Flow Control For Advanced Embedded Propulsion Systems. AIAA Paper 2009-741.

Anderson, B.H., Miller, D.N., Addington, G.A., Agrell, J. (2004). Optimal Micro-Jet Flow Control for Compact Air Vehicle Inlets. NASA/TM. 2004-212937.

Anderson, B., Tinapple, J., & Surber, L. (2006). Optimal Control of Shock Wave Turbulent Boundary Layer Interactions Using Micro-Array Actuation. AIAA Paper 2006-3197b.

Anderson, B., Tinapple, J., & Surber, L. (2006, June). Optimal Control of Shock Wave Turbulent Boundary Layer Interactions Using Micro-Array Actuation. San Francisco, CA: AIAA-2006-3197.

Berrier, Bobby L., Allen, Brian G. “Experimental and Computational Evaluation of Flush-Mounted, S-Duct Inlets” AIAA 2004-764

Bruce, E.P. “Design and evaluation of screens to produce multi-cycle 20% amplitude sinusoidal velocity profiles.” AIAA Paper, 74-623.

Compton, D. A. and Johnston, J. P. (1992). Streamwise vortex production by pitched and skewed jets in a turbulent boundary layer. *AIAA J* 30, 640-647.

Kim, W., & Menon, S. (1999). An Unsteady Incompressible Navier-Stokes Solver for Large Eddy Simulation of Turbulent Flows. *International Journal for Numerical Methods in Fluids , 31*, 983-1017.

Lin, J.C. (2002). Review of research on low-profile vortex generators to control boundary-layer separation. *Progress in Aerospace Sciences*, 38, 389-420.

Mani, M. (2004, January-February). Hybrid Turbulence Models for Unsteady Flow Simulations. *Journal of Aircraft , 41* (1).

Mani, M., Cary, A., & Ramakrishnan, S. (2005, July-August). A General Purpose Euler and Navier-Stokes Solver for Structured and Unstructured Grids. *42* (4).

Mani, M., Winkler, C., Fisher, M., & Mackie, S. (2007). A post Processing Approach for CFD Error Associated with Grid Resolution. *45th AIAA Aerospace Sciences Meeting.* Reno, NV: AIAA-2007-66809.

Menter, F. (1993). Zonal Two Equation k- Turbulence Models for Aerodynamic Flows. *24th Fluid Dynamics Conference.* Orlando, FL: AIAA 93-2906.

Owens, L., Allan, B., & Gorton, S. (2006) Boundary-Layer-Ingesting Inlet Flow Control. AIAA Paper 2006-839.

Peake, D.J., Henry, F.S., and Pearcey, H.H. (1999), Viscous Flow Control with Air-Jet Vortex Generators. AIAA Paper 1999-3175.

SAE ARP1420B, "Gas Turbine Engine Inlet Flow Distortion Guidelines," Society of Automotive Engineers, Inc., March 2002, Revision B.

Shin, A., Vanka, S., Mani, M., Dorgan, A., & Michal, T. (2007). Application of BCFD unstructured Grid to Simulation of Microramp Control of Shock / Boundary Layer Interaction. *AIAA CFD Conference.* Miami, FL.

Smith, B., & Glezer, A. (1998). The Formation and Evolution of Synthetic Jets. *Physics of Fluids, 10* (9).

Spalart, P. R. & Allmaras, S. R. (1992). A one-equation turbulence model for aerodynamic flows. AIAA 1992-439.

Spalart, P.R., Jou, W.-H., Strelets, M., Allmaras, S.R.: Comments on the feas1ibility of LES for wings, and on a hybrid RANS/LES approach. In: Proceedings of first AFOSR international conference on DNS/LES, Ruston, Louisiana. Greyden Press, 4–8 Aug (1997)

Shur,M., Spalart, P.R., Strelets,M., Travin,A.: Detached-eddy simulation of an airfoil at high angle of attack. In: proceedings of 4th international symposium on engineering turbulence modeling and measurements,Corsica. Elsevier, 24–26May (1999)

Travin, A., Shur, M., Strelets, M., Spalart, P.: Detached-eddy simulations past a circular cylinder. Flow Turb Comb 63, 293 (2000)

Appendix A – Offset Diffuser Model Instrumentation and Model Drawings

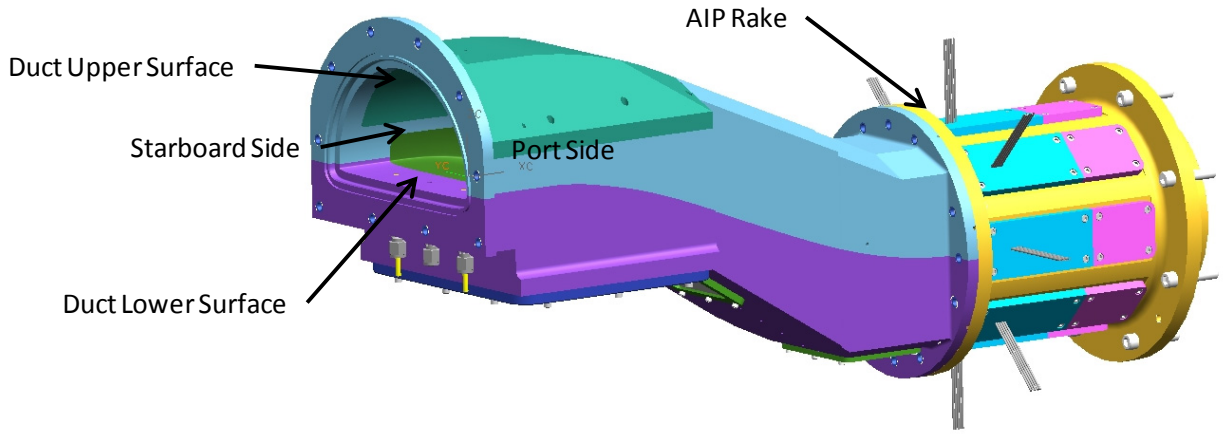

Figure A1 Diffuser Model

DAS Label	x	y	z	Tap	Description
PS(1,1)	-5.875	0.000	-0.218	3	Adapter lower surface static pressure
PS(1,2)	0.000	0.000	0.000	9	Lower surface insert static pressure
PS(1,3)	3.375	0.000	-0.978	10	Lower surface insert static pressure
PS(1,4)	4.000	0.000	-1.291	11	Lower surface insert static pressure
PS(1,5)	4.625	0.000	-1.628	12	Lower surface insert static pressure
PS(1,6)	5.375	0.000	-2.059	13	Lower surface insert static pressure
PS(1,7)	6.325	0.000	-2.621	14	Diffuser lower surface static pressure
PS(1,8)	9.000	0.000	-4.156	15	Diffuser lower surface static pressure
PS(1,9)	9.750	0.000	-4.542	16	Diffuser lower surface static pressure
PS(1,10)	10.500	0.000	-4.901	17	Diffuser lower surface static pressure
PS(1,11)	11.250	0.000	-5.227	18	Diffuser lower surface static pressure
PS(1,12)	12.000	0.000	-5.514	19	Diffuser lower surface static pressure
PS(2,1)	-5.875	0.000	3.604	1	Adapter upper surface static pressure
PS(2,2)	-3.750	0.000	3.511	2	Adapter upper surface static pressure at hot-wire probe
PS(2,3)	0.000	0.000	3.484	4	Diffuser upper surface static pressure
PS(2,4)	3.375	0.000	2.944	5	Diffuser upper surface static pressure
PS(2,5)	6.325	0.000	1.900	6	Diffuser upper surface static pressure
PS(2,6)	9.000	0.000	0.667	7	Diffuser upper surface static pressure
PS(2,7)	12.000	0.000	-0.617	8	Diffuser upper surface static pressure
PS(3,1)	12.000	-2.590	-3.066	20	Diffuser sidewall surface static pressure

PS(3,2)	12.000	2.590	-3.066	21	Diffuser sidewall surface static pressure

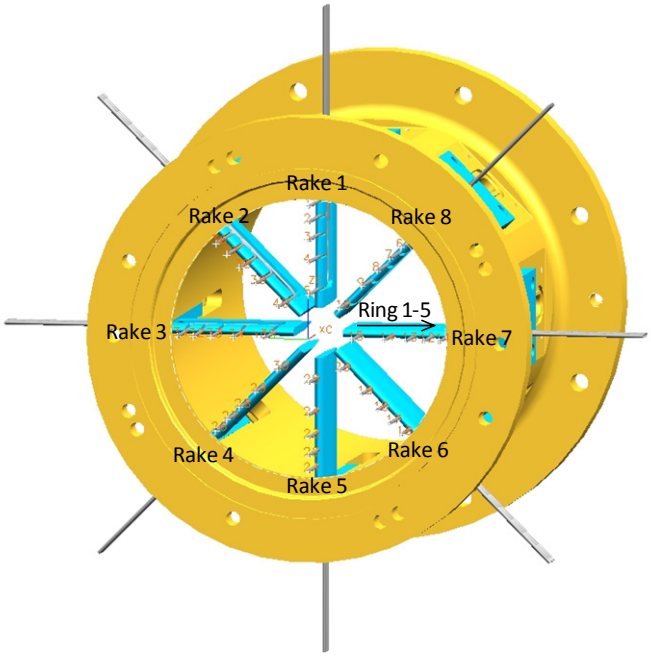

Figure A2 AIP Rake (Forward Looking Aft)

DAS Label	x	y	z	Tap	Description
PS2(1)	15.399	0.000	-1.208	22	Rake 1 (TDC) base static pressure
PS2(2)	15.399	-1.768	-1.940	23	Rake 2 (45 deg) base static pressure
PS2(3)	15.399	-2.500	-3.708	24	Rake 3 (90 deg) base static pressure
PS2(4)	15.399	-1.768	-5.476	25	Rake 4 (135 deg) base static pressure
PS2(5)	15.399	0.000	-6.208	26	Rake 5 (180 deg)base static pressure
PS2(6)	15.399	1.768	-5.476	27	Rake 6 (225 deg) base static pressure
PS2(7)	15.399	2.500	-3.708	28	Rake 7 (270 deg) base static pressure
PS2(8)	15.399	1.768	-1.940	29	Rake 8 (315 deg) base static pressure

DAS Label	x	y	z	Tap	Description
PT2(1,1)	0.001	0.000	0.791	POINT 5	Steady AIP total pressure, ring 1 (hub), rake 1
PT2(2,1)	0.001	0.000	1.369	POINT 4	Steady AIP total pressure, ring 2, rake 1
PT2(3,1)	0.001	0.000	1.768	POINT 3	Steady AIP total pressure, ring 3, rake 1

PT2(4,1)	0.001	0.000	2.092	POINT 2	Steady AIP total pressure, ring 4, rake 1
PT2(5,1)	0.001	0.000	2.372	POINT 1	Steady AIP total pressure, ring 5 (tip), rake 1
PT2(1,2)	0.001	0.559	0.559	POINT 40	Steady AIP total pressure, ring 1 (hub), rake 2
PT2(2,2)	0.001	0.968	0.968	POINT 39	Steady AIP total pressure, ring 2, rake 2
PT2(3,2)	0.001	1.250	1.250	POINT 38	Steady AIP total pressure, ring 3, rake 2
PT2(4,2)	0.001	1.479	1.479	POINT 37	Steady AIP total pressure, ring 4, rake 2
PT2(5,2)	0.001	1.677	1.677	POINT 36	Steady AIP total pressure, ring 5 (tip), rake 2
PT2(1,3)	0.001	0.791	0.000	POINT 35	Steady AIP total pressure, ring 1 (hub), rake 3
PT2(2,3)	0.001	1.369	0.000	POINT 34	Steady AIP total pressure, ring 2, rake 3
PT2(3,3)	0.001	1.768	0.000	POINT 33	Steady AIP total pressure, ring 3, rake 3
PT2(4,3)	0.001	2.092	0.000	POINT 32	Steady AIP total pressure, ring 4, rake 3
PT2(5,3)	0.001	2.372	0.000	POINT 31	Steady AIP total pressure, ring 5 (tip), rake 3
PT2(1,4)	0.001	0.559	-0.559	POINT 30	Steady AIP total pressure, ring 1 (hub), rake 4
PT2(2,4)	0.001	0.968	-0.968	POINT 29	Steady AIP total pressure, ring 2, rake 4
PT2(3,4)	0.001	1.250	-1.250	POINT 28	Steady AIP total pressure, ring 3, rake 4
PT2(4,4)	0.001	1.479	-1.479	POINT 27	Steady AIP total pressure, ring 4, rake 4
PT2(5,4)	0.001	1.677	-1.677	POINT 26	Steady AIP total pressure, ring 5 (tip), rake 4
PT2(1,5)	0.001	0.000	-0.791	POINT 25	Steady AIP total pressure, ring 1 (hub), rake 5
PT2(2,5)	0.001	0.000	-1.369	POINT 24	Steady AIP total pressure, ring 2, rake 5
PT2(3,5)	0.001	0.000	-1.768	POINT 23	Steady AIP total pressure, ring 3, rake 5
PT2(4,5)	0.001	0.000	-2.092	POINT 22	Steady AIP total pressure, ring 4, rake 5
PT2(5,5)	0.001	0.000	-2.372	POINT 21	Steady AIP total pressure, ring 5 (tip), rake 5
PT2(1,6)	0.001	-0.559	-0.559	POINT 20	Steady AIP total pressure, ring 1 (hub), rake 6
PT2(2,6)	0.001	-0.968	-0.968	POINT 19	Steady AIP total pressure, ring 2, rake 6
PT2(3,6)	0.001	-1.250	-1.250	POINT 18	Steady AIP total pressure, ring 3, rake 6
PT2(4,6)	0.001	-1.479	-1.479	POINT 17	Steady AIP total pressure, ring 4, rake 6

PT2(5,6)	0.001	-1.677	-1.677	POINT	16	Steady AIP total pressure, ring 5 (tip), rake 6
PT2(1,7)	0.001	-0.791	0.000	POINT	15	Steady AIP total pressure, ring 1 (hub), rake 7
PT2(2,7)	0.001	-1.369	0.000	POINT	14	Steady AIP total pressure, ring 2, rake 7
PT2(3,7)	0.001	-1.768	0.000	POINT	13	Steady AIP total pressure, ring 3, rake 7
PT2(4,7)	0.001	-2.092	0.000	POINT	12	Steady AIP total pressure, ring 4, rake 7
PT2(5,7)	0.001	-2.372	0.000	POINT	11	Steady AIP total pressure, ring 5 (tip), rake 7
PT2(1,8)	0.001	-0.559	0.559	POINT	10	Steady AIP total pressure, ring 1 (hub), rake 8
PT2(2,8)	0.001	-0.968	0.968	POINT	9	Steady AIP total pressure, ring 2, rake 8
PT2(3,8)	0.001	-1.250	1.250	POINT	8	Steady AIP total pressure, ring 3, rake 8
PT2(4,8)	0.001	-1.479	1.479	POINT	7	Steady AIP total pressure, ring 4, rake 8
PT2(5,8)	0.001	-1.677	1.677	POINT	6	Steady AIP total pressure, ring 5 (tip), rake 8

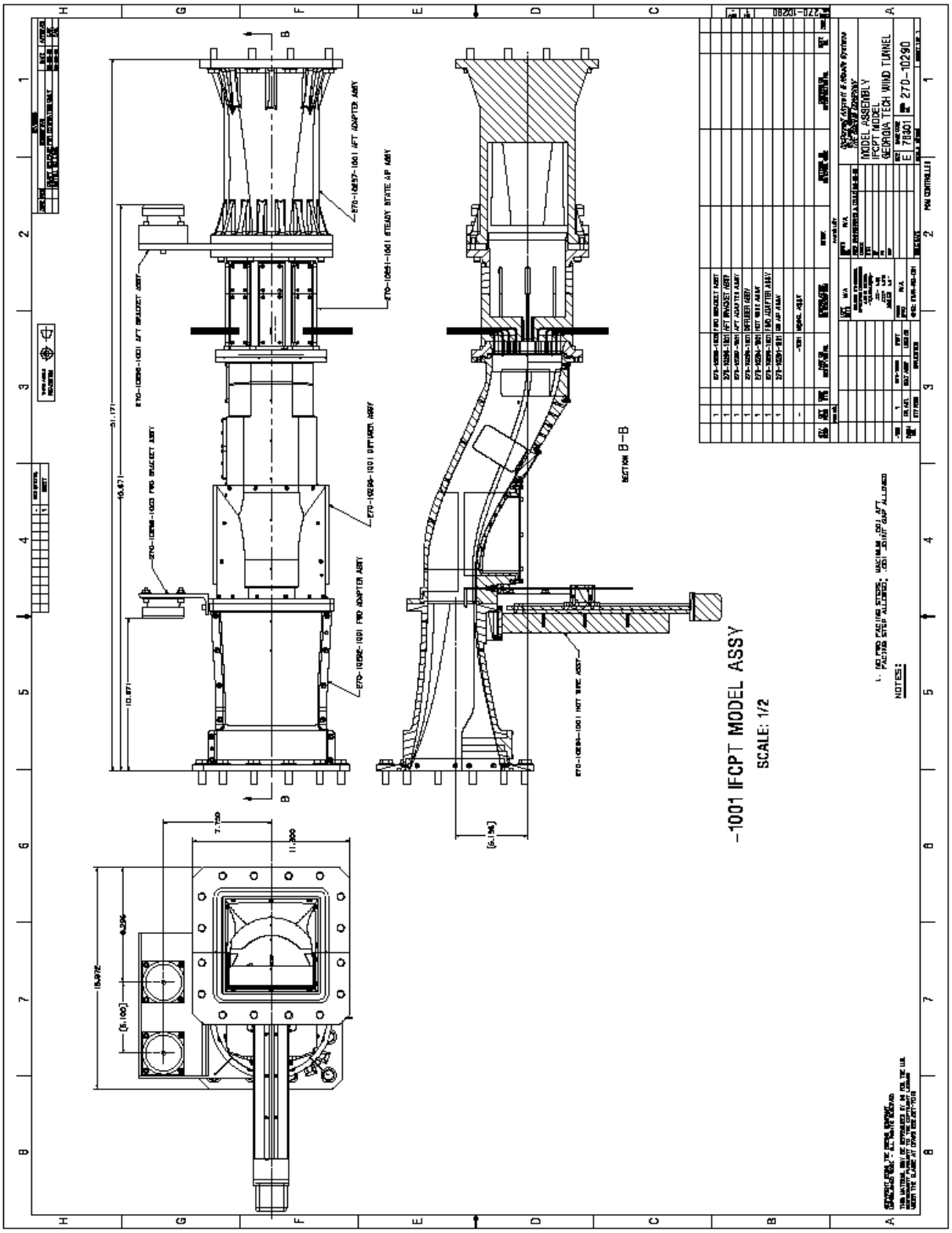

Figure A3 BLI Inlet Assembly

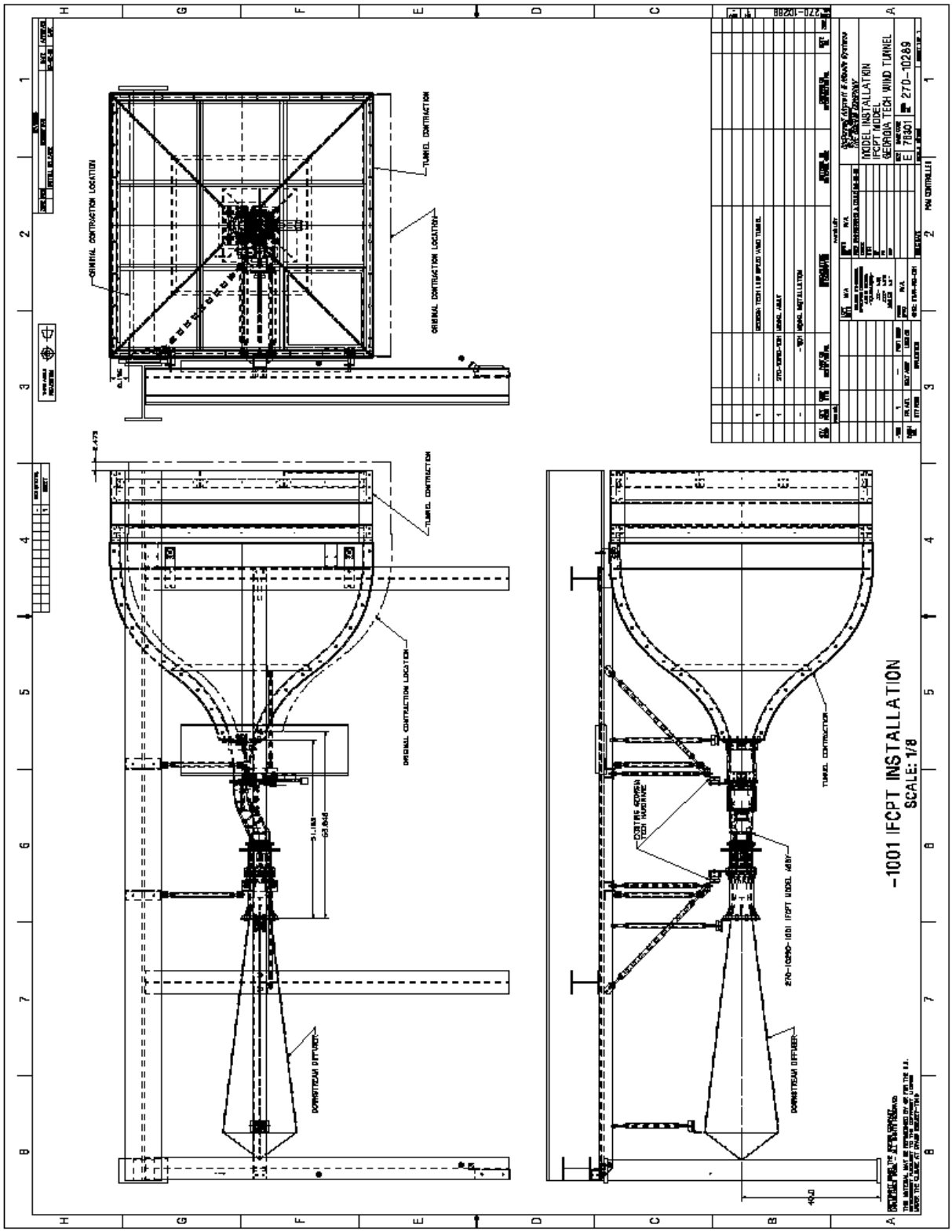

Figure A4 BLI Inlet Installation in Georgia Tech Wind Tunnel

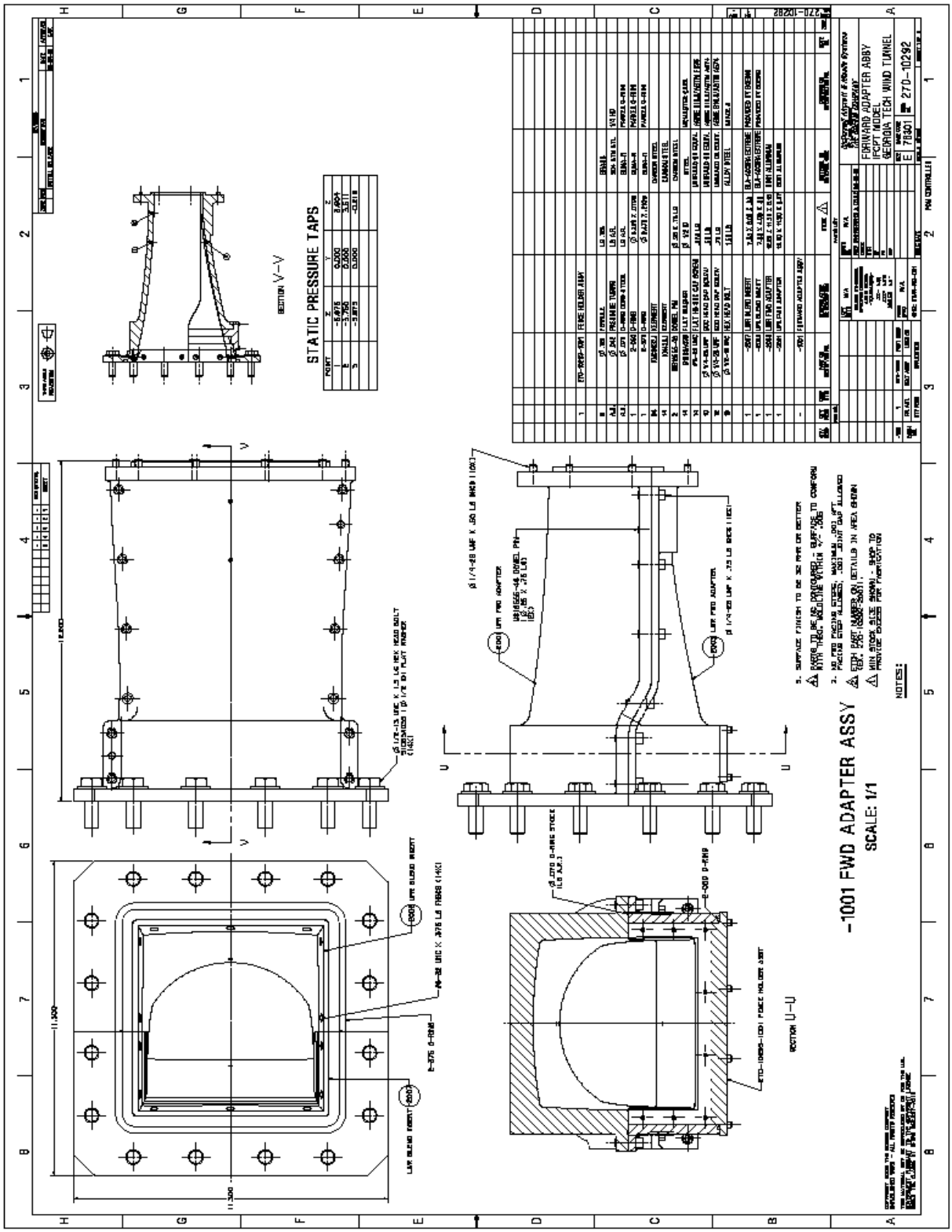

Figure A5 Forward Adapter Assembly

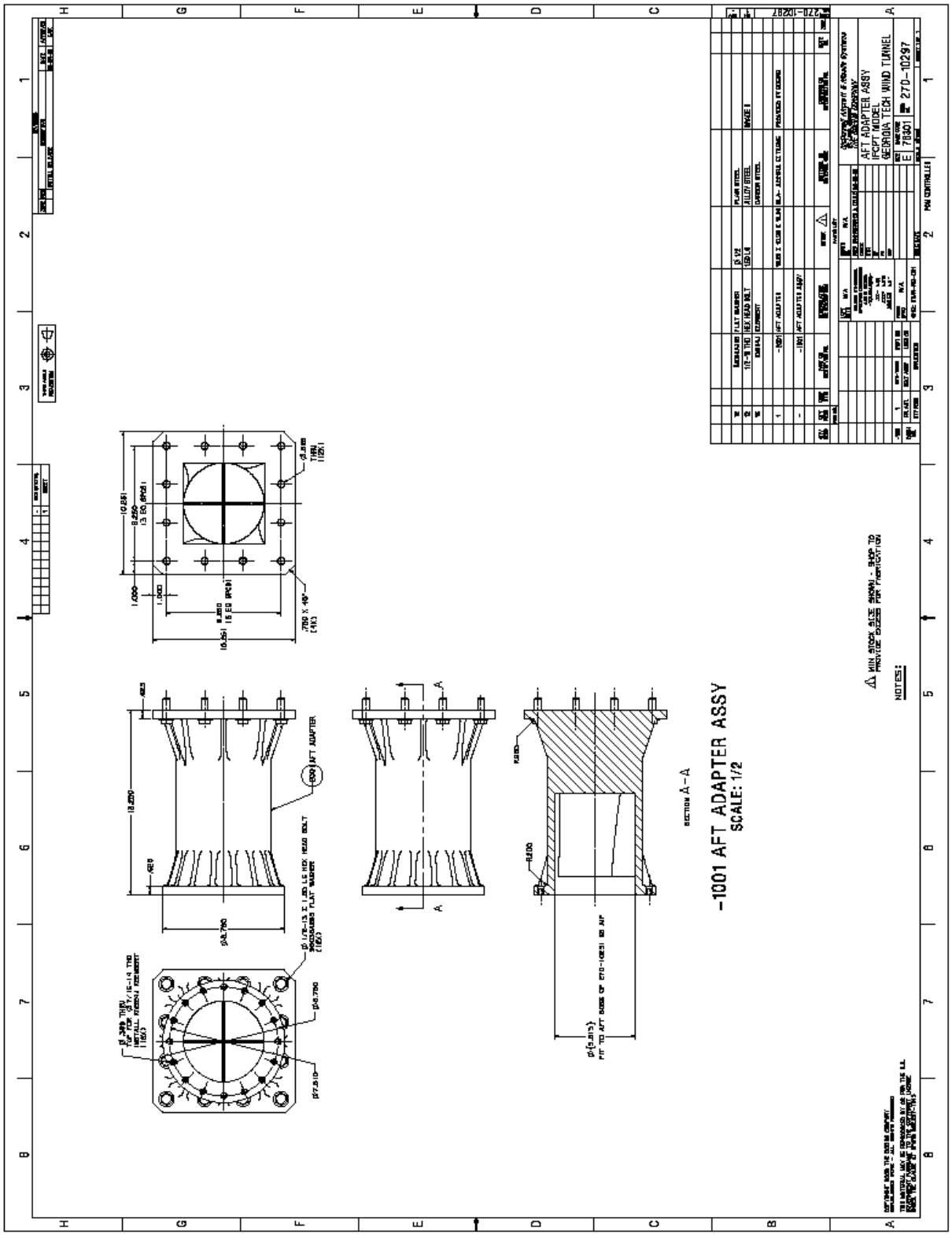

Figure A6 Aft Adapter Assembly

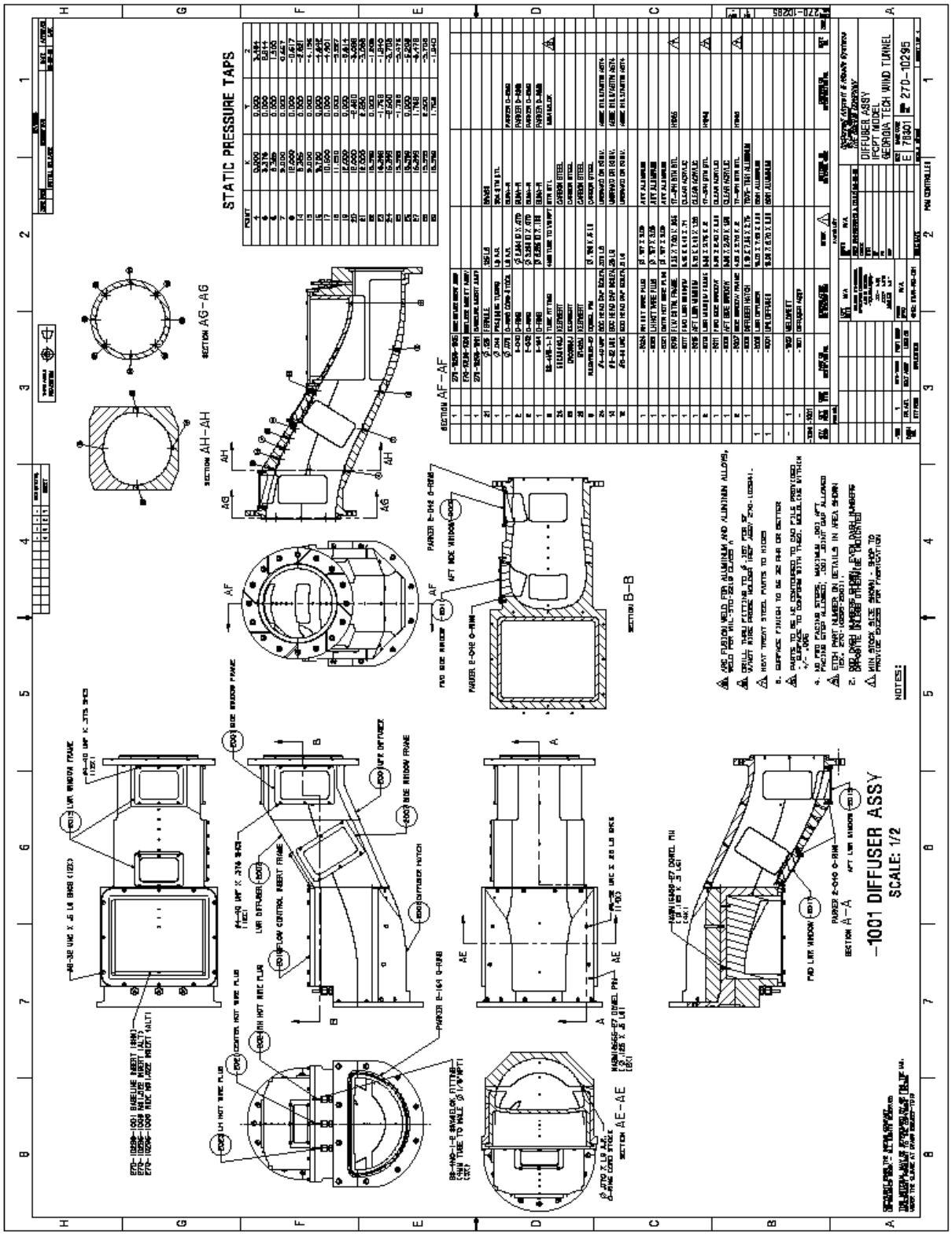

Figure A7 Diffuser Assembly

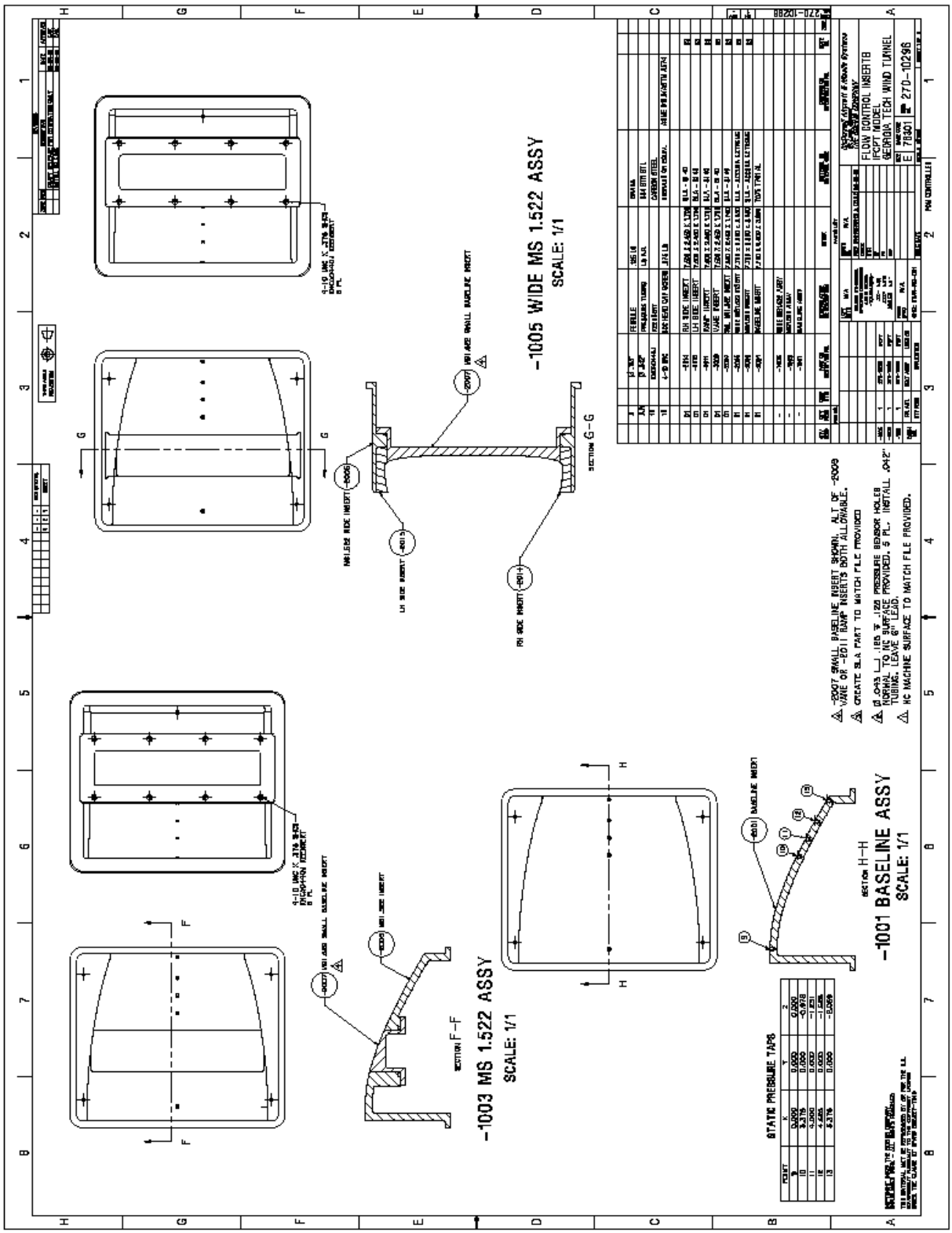

Figure A8 Flow Control Insert Assembly

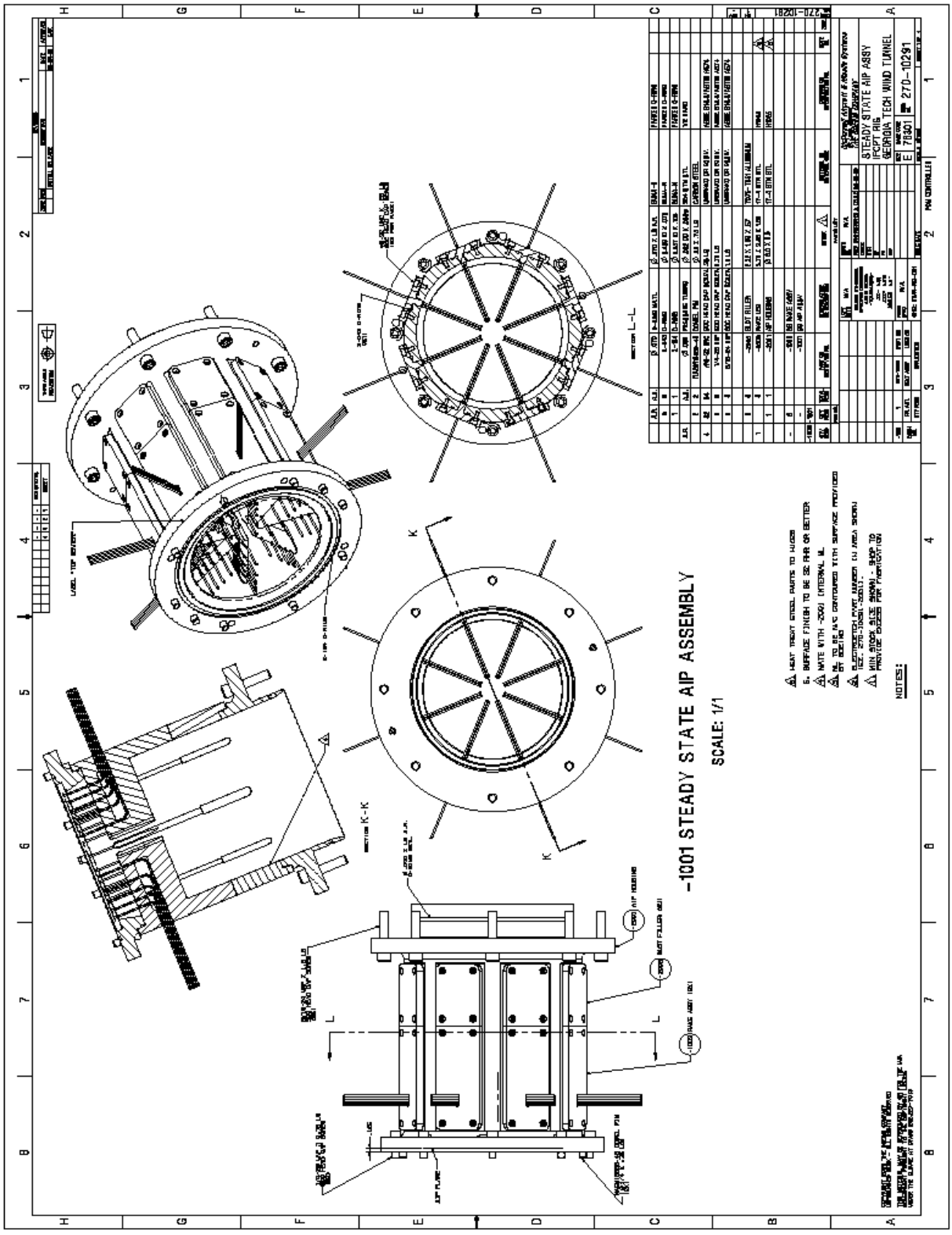

Figure A9 Steady State AIP Assembly

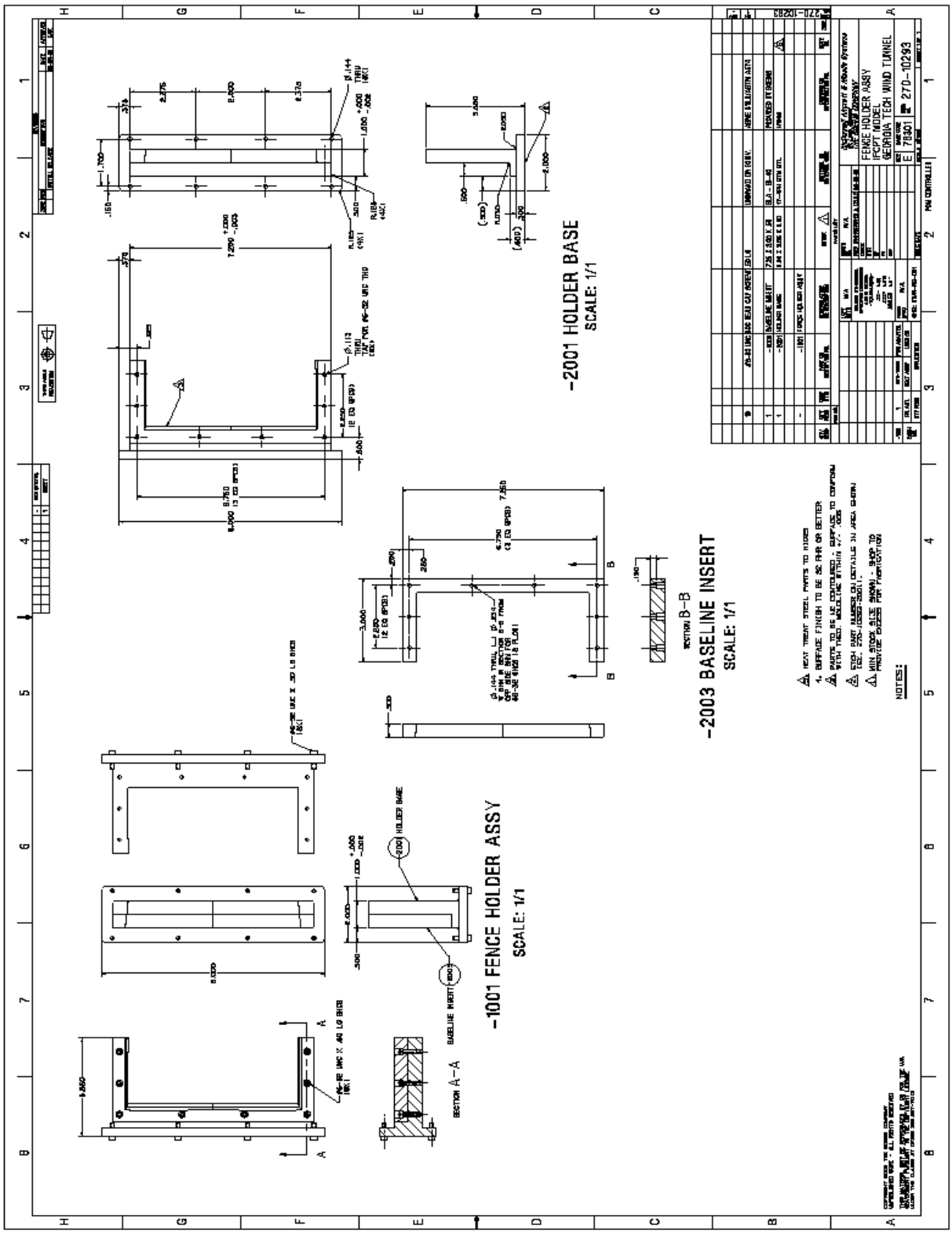

Figure A10 Fence Holder Assembly

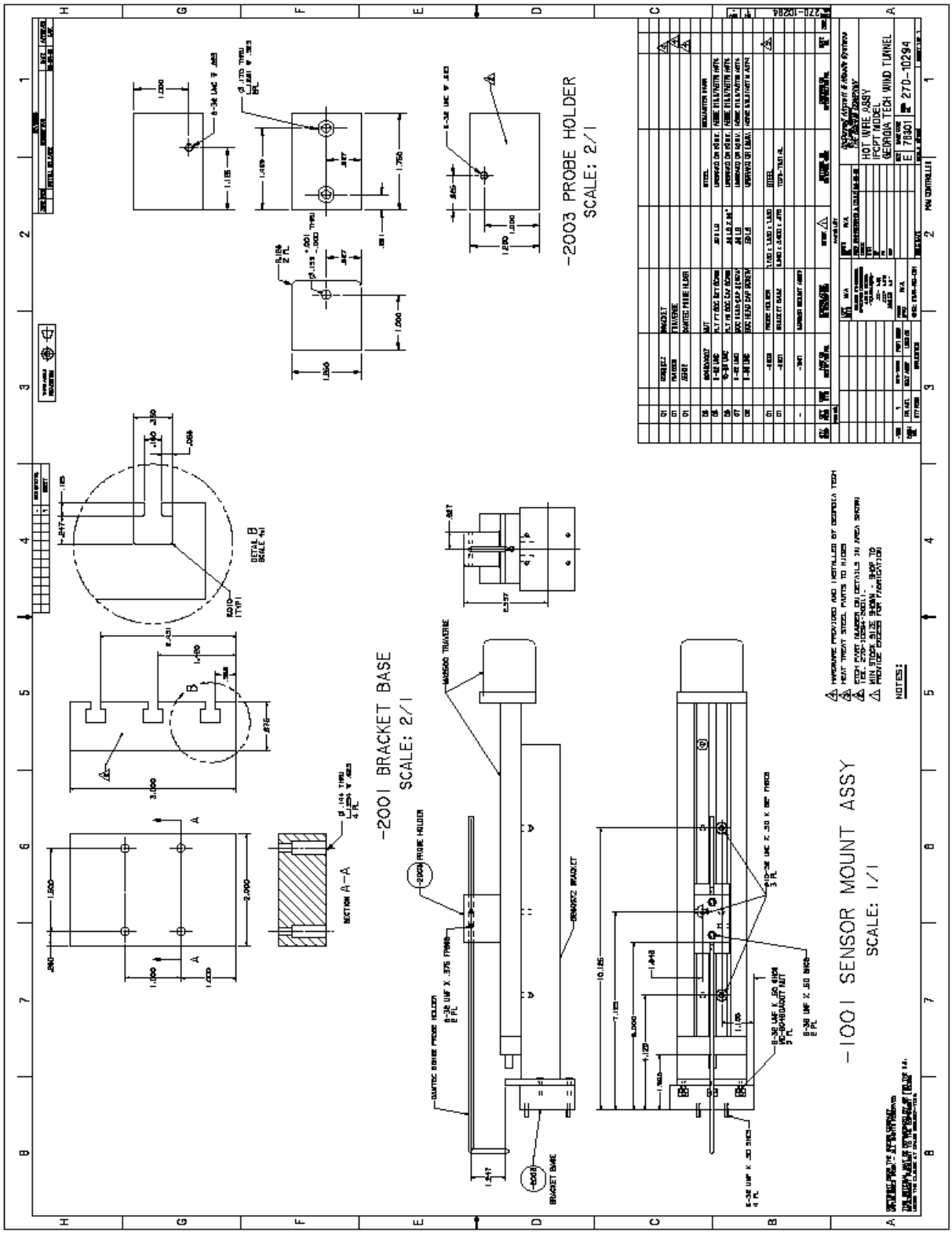

Figure A11 Hot Wire Assembly

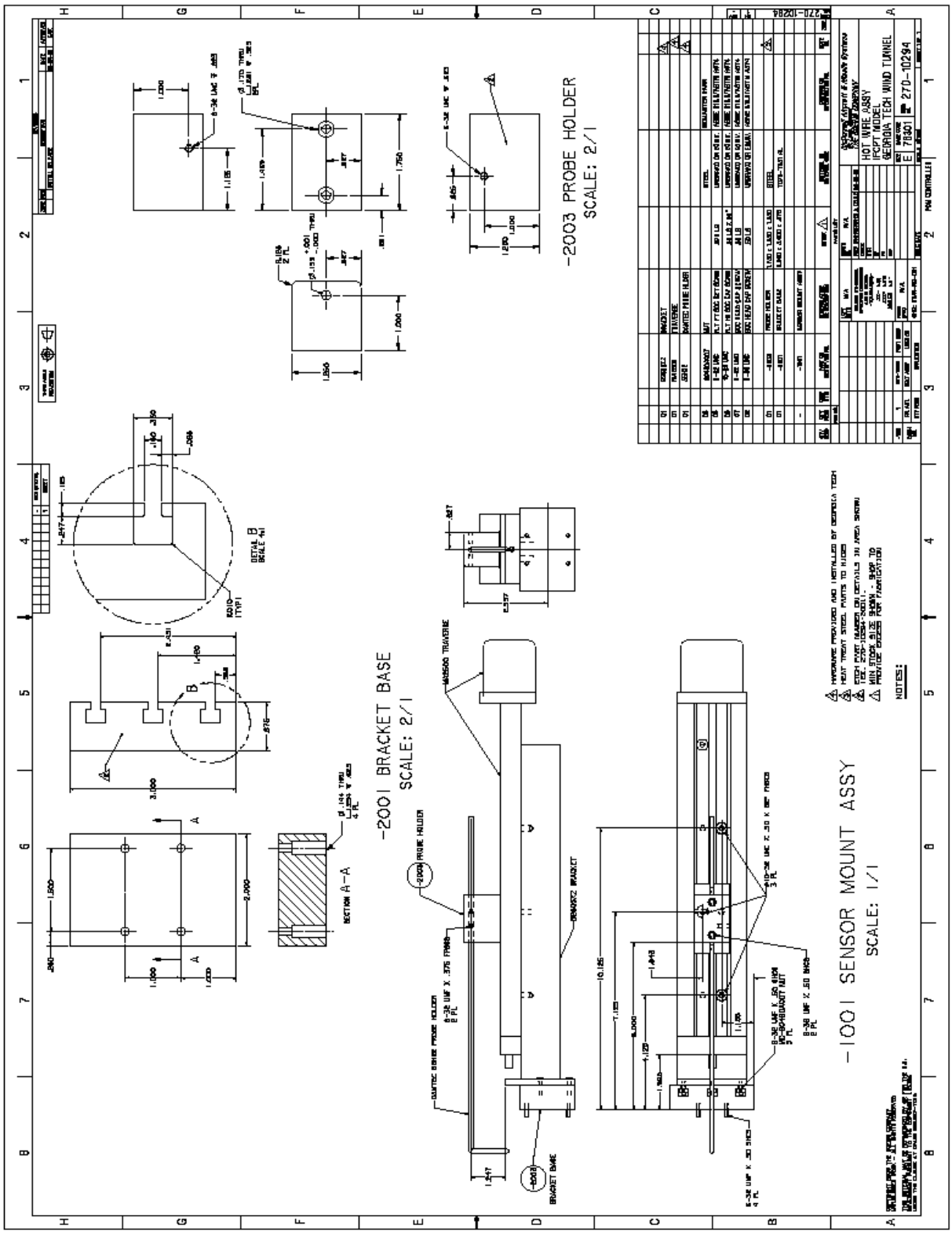

Figure A12 Support Bracket Assembly

Appendix B. Dynamic Data Reduction Process

This appendix contains definition of dynamic distortion data reduction used. It contains definitions of distortion parameters that were calculated for the AIP data. These are SAE standard spatial distortion descriptor elements and indices (SAE ARP1420B).

Circumferential Distortion Descriptors (DPCP)

Circumferential distortion is described on a ring-by-ring basis in terms of intensity, extent function, and multiple-per-revolution elements. The intensity or level of distortion is a numerical indication of the magnitude of the pressure distortion. The extent function element is a numerical indication of the circumferential size of the low-pressure region. The multiple-per-revolution element is a numerical indication of the equivalent number of circumferential regions of low pressure.

One-per-rev Patterns - The “intensity” and “extent” elements of circumferential distortion are obtained by linear interpolation of the pressures in a given instrumentation ring. A typical pressures one-per-revolution pattern contains one pressure defect in 360 degrees at the AIP. Theta minus, q-i, is the circumferential extent of the low-pressure region. It is defined by the intersection between the ring average pressure and the linear interpolation that subtends the low-pressure region.

Multiple-per-rev patterns - The circumferential distortion intensity and extent elements for multiple-per-revolution distortion patterns are also determined by a linear interpolation procedure. A typical multiple-per-revolution pattern contains two low-pressure regions separated by two high-pressure regions of extents θ+i1 and θ+i2.

Patterns with θ+ik < θ+min - If the pattern has low-pressure regions circumferential separated by high-pressure regions with extents less than or equal to θ+min, it is considered as an equivalent one-per-revolution low-pressure region. θ+min is specified by the descriptor system developer. A value of θ+min of 40 degrees was used for this test.

Patterns with θ+ik > θ+min - If the pattern has low-pressure regions circumferentially separated by high-pressure regions with extents greater than θ+ min, then the multiple-per-revolution element is greater than one.

The multiple-per-revolution term is defined as the number of equivalent low-pressure regions, the equivalence being based on the ratio of the total integrated area beneath (PAV)i to the largest single area beneath (PAV)i. This is given by the equations

$$DPCP_i = Intensity_i \times (Extent_i/150) \times (1/MPR_i), \quad i = 1 \text{ thru } 5$$

Equation B1

$$DPCP_H = (DPCP_i + DPCP_{i+1})/2, \quad i = 1$$

Equation B2

$$DPCP_T = (DPCP_i + DPCP_{i+1})/2, \quad i = 4$$

Equation B3

$$DPCP_{ave} = (DPCP_1 + DPCP_2 + DPCP_3 + DPCP_4 + DPCP_5)/5$$

Equation B4

Radial Distortion Descriptors (DPRP)

The radial distortion intensity of a ring is defined as the difference between the face-average pressure and the ring-average pressure, divided by the face-average pressure. Both positive and negative values of radial intensity are considered: positive values reflect a ring average pressure that is below the face average. For the general ring, i, the radial intensity is as follows:

$$DPRP_i = (Pfav - Pave_i)/Pfav, \text{ for } i = 1 \text{ through } 5$$

Equation B5

where

$Pave_i$ = area-averaged pressure of ring i

Pfav = area-averaged pressure at the AIP

$$DPCP_H = DPRP_i, \ i = 1$$

Equation B6

$$DPCP_T = DPRP_i, \ i = 5$$

Equation B7

Turbulence Descriptors

Calculate turbulence ($TURB_i$) for each dynamic pressure probe

$$TUR_{Bi} = PT_{2\,i\,rms} / PT_{2ave}$$

Equation B8

where

$PT_{2\,i\,rms}$ = true rms of an individual dynamic pressure signal

PT_{2ave} = steady state face average total pressure

Appendix C. Experimental Run Matrix

Note	Run	N2 [rpm]	M2	Microvane Configuration	Jet Configuration	Synthetic Jet rpm	Steady Jet Flow Rate [lpm]	Synthetic Jet Diameter [mm]
Baseline Fence and Microvanes	101	2325	0.556	CFG6	NA	NA	NA	NA
Synthetic Jets	102	2325	0.549	CFG6	SYNTHETIC	8000	NA	1.5
	103	2325	0.549	CFG6	NA	NA	NA	NA
	104	2325	0.549	CFG6	NA	NA	NA	NA
	105	2325	0.549	CFG6	NA	NA	NA	NA
	106	2325	0.549	CFG6	SYNTHETIC	8000	NA	1.5
	107	2325	0.549	CFG6	SYNTHETIC	8000	NA	1.5
	108	2325	0.549	CFG6	SYNTHETIC	8000	NA	1.5
	109	1000	0.227	CFG6	NA	NA	NA	NA
	110	1000	0.227	CFG6	SYNTHETIC	8000	NA	1.5
	111	1500	0.352	CFG6	NA	NA	NA	NA
	112	1500	0.352	CFG6	SYNTHETIC	8000	NA	1.5
	113	2000	0.475	CFG6	NA	NA	NA	NA
	114	2000	0.475	CFG6	SYNTHETIC	8000	NA	1.5
	115	2000	0.471	CFG6	SYNTHETIC	2000	NA	1.5
	116	2000	0.471	CFG6	SYNTHETIC	4000	NA	1.5
	117	2000	0.471	CFG6	SYNTHETIC	6000	NA	1.5
	118	2140	0.52	NA	NA	NA	NA	NA
	119	2140	0.523	NA	SYNTHETIC	8000	NA	1.5
Replaced Dynamic with Steady State Rake	120	2140	0.549	NA	NA	NA	NA	NA
	121	2140	0.553	NA	SYNTHETIC	8000	NA	1.5
Sampled the Phase Reference Signal	122	2325	0.555	CFG6	NA	NA	NA	NA
	123	2325	0.551	CFG6	SYNTHETIC	8000	NA	1.5
	124	2325	0.547	CFG6	NA	NA	NA	NA

Note	Run	N2 [rpm]	M2	Microvane Configuration	Jet Configuration	Synthetic Jet rpm	Steady Jet Flow Rate [lpm]	Synthetic Jet Diameter [mm]
	125	2325	0.54	CFG6	SYNTHETIC	8000	NA	1.5
	126	2325	0.547	CFG6	NA	NA	NA	NA
	127	2325	0.54	CFG6	SYNTHETIC	8000	NA	1.5
	142	2030	0.482	CFG6	NA	NA	NA	NA
	143	2030	0.467	CFG6	SYNTHETIC	8000	NA	1.83
	144	2030	0.479	CFG6	NA	NA	NA	NA
	145	2045	0.484	CFG6	NA	NA	NA	NA
	146	2045	0.47	CFG6	SYNTHETIC	8000	NA	1.83
	147	2085	0.484	CFG6	SYNTHETIC	8000	NA	1.83
	148	2290	0.546	CFG6	NA	NA	NA	NA
	149	2290	0.532	CFG6	SYNTHETIC	8000	NA	1.83
	150	2350	0.546	CFG6	SYNTHETIC	8000	NA	1.83
Dynamic Rake	151	2350	0.553	CFG6	SYNTHETIC	8000	NA	1.83
	152	2290	0.547	CFG6	NA	NA	NA	NA
	153	2000	0.475	CFG6	NA	NA	NA	NA
	154	2000	0.466	CFG6	SYNTHETIC	2000	NA	1.83
	155	2000	0.47	CFG6	SYNTHETIC	4000	NA	1.83
	156	2000	0.471	CFG6	SYNTHETIC	6000	NA	1.83
	157	2000	0.47	CFG6	SYNTHETIC	8000	NA	1.83
	170	1000	0.228	CFG6	NA	NA	NA	NA
	171	1000	0.225	CFG6	SYNTHETIC	8000	NA	1.83
	172	1500	0.352	CFG6	NA	NA	NA	NA
	173	1500	0.351	CFG6	SYNTHETIC	8000	NA	1.83
	174	2000	0.476	CFG6	NA	NA	NA	NA
	175	2000	0.47	CFG6	SYNTHETIC	8000	NA	1.83
	176	2020	0.476	CFG6	SYNTHETIC	8000	NA	1.83
	177	2325	0.558	CFG6	NA	NA	NA	NA
	178	2325	0.551	CFG6	SYNTHETIC	8000	NA	1.83
	179	2345	0.556	CFG6	SYNTHETIC	8000	NA	1.83
	216	1000	0.228	NONE	NA	NA	NA	NA
	217	1000	0.235	NONE	SYNTHETIC	8000	NA	1.83
	218	980	0.229	NONE	SYNTHETIC	8000	NA	1.83

Note	Run	N2 [rpm]	M2	Microvane Configuration	Jet Configuration	Synthetic Jet rpm	Steady Jet Flow Rate [lpm]	Synthetic Jet Diameter [mm]
	219	1500	0.354	NONE	NA	NA	NA	NA
	220	1500	0.361	NONE	SYNTHETIC	8000	NA	1.83
	221	1480	0.356	NONE	SYNTHETIC	8000	NA	1.83
	222	2000	0.486	NONE	NA	NA	NA	NA
	223	2000	0.492	NONE	SYNTHETIC	8000	NA	1.83
	224	1980	0.487	NONE	SYNTHETIC	8000	NA	1.83
	225	2240	0.55	NONE	NA	NA	NA	NA
	226	2240	0.556	NONE	SYNTHETIC	8000	NA	1.83
Removed Fence	227	2280	0.629	NONE	NA	NA	NA	NA
	228	1970	0.554	NONE	NA	NA	NA	NA
	229	1670	0.47	NONE	NA	NA	NA	NA
	230	1300	0.358	NONE	NA	NA	NA	NA
	231	850	0.228	NONE	NA	NA	NA	NA
Micro-Vane Configuration for CFD Comparisons	232	2545	0.627	CFG4	NA	NA	NA	NA
	233	2240	0.553	CFG4	NA	NA	NA	NA
	234	1910	0.473	CFG4	NA	NA	NA	NA
	235	1480	0.364	CFG4	NA	NA	NA	NA
	236	950	0.229	CFG4	NA	NA	NA	NA
Steady Jets and Baseline Micro-Vane Configuration	237	2340	0.556	CFG6	NA	NA	NA	1.5
	238	2350	0.557	CFG6	STEADY	NA	100	1.5
	239	2360	0.556	CFG6	STEADY	NA	200	1.5
	240	2380	0.555	CFG6	STEADY	NA	300	1.5
	241	2400	0.555	CFG6	STEADY	NA	400	1.5
	242	2410	0.554	CFG6	STEADY	NA	500	1.5
	243	2010	0.475	CFG6	NA	NA	NA	1.5
	244	2020	0.476	CFG6	STEADY	NA	100	1.5
	245	2030	0.476	CFG6	STEADY	NA	200	1.5
	246	2040	0.473	CFG6	STEADY	NA	300	1.5
	247	2060	0.473	CFG6	STEADY	NA	400	1.5
	248	2080	0.474	CFG6	STEADY	NA	500	1.5
Increased Synthetic Jet Diameter	249	1000	0.227	CFG6	NA	NA	NA	NA

Note	Run	N2 [rpm]	M2	Microvane Configuration	Jet Configuration	Synthetic Jet rpm	Steady Jet Flow Rate [lpm]	Synthetic Jet Diameter [mm]
	250	1000	0.224	CFG6	SYNTHETIC	8000	NA	2.1
	251	1500	0.352	CFG6	NA	NA	NA	NA
	252	1500	0.349	CFG6	SYNTHETIC	8000	NA	2.1
	253	2000	0.474	CFG6	NA	NA	NA	NA
	254	2000	0.466	CFG6	SYNTHETIC	8000	NA	2.1
	255	2325	0.557	CFG6	NA	NA	NA	NA
	256	2325	0.546	CFG6	SYNTHETIC	8000	NA	2.1
	257	1000	0.225	NONE	NA	NA	NA	NA
	258	980	0.225	NONE	SYNTHETIC	8000	NA	2.1
	259	1500	0.353	NONE	NA	NA	NA	NA
	260	1480	0.355	NONE	SYNTHETIC	8000	NA	2.1
	261	2000	0.483	NONE	NA	NA	NA	NA
	262	1980	0.484	NONE	SYNTHETIC	8000	NA	2.1
	263	2240	0.548	NONE	NA	NA	NA	NA
	264	2240	0.555	NONE	SYNTHETIC	8000	NA	2.1

Appendix D. Experimental Database

TEST	NRUN	PT0 [psi]	TT0 [°R]	Pref [psi]	N2 [rpm]	PT2AVG	M2	W2 [pps]	W2C [pps]	DPCPAVG.SS	DPCPH.SS	DPCPT.SS	DPRPH.SS	DPRPT.SS	DPCPAVG.PK	DPCPH.PK	DPCPT.PK	DPRPH.PK	DPRPT.PK
106	101	14.37	528.4	14.37	2325	0.9561	0.55	4.99	5.38	0.0206	0.0240	0.0167	0.0000	0.0335	0.0300	0.0395	0.0289	0.0000	0.0450
106	102	14.37	530.0	14.37	2325	0.9575	0.55	4.95	5.34	0.0176	0.0172	0.0165	0.0000	0.0338	0.0300	0.0384	0.0348	0.0000	0.0490
106	103	14.42	530.0	14.42	2325	0.9559	0.55	5.00	5.38	0.0209	0.0238	0.0172	0.0000	0.0328	0.0302	0.0399	0.0297	0.0000	0.0463
106	104	14.42	530.1	14.42	2325	0.9560	0.55	4.99	5.37	0.0207	0.0236	0.0170	0.0000	0.0328	0.0327	0.0410	0.0315	0.0000	0.0458
106	105	14.42	529.7	14.42	2325	0.9559	0.55	4.99	5.37	0.0206	0.0235	0.0169	0.0000	0.0330	0.0308	0.0432	0.0312	0.0000	0.0450
106	106	14.42	530.3	14.42	2325	0.9572	0.55	4.96	5.34	0.0192	0.0204	0.0170	0.0000	0.0336	0.0299	0.0392	0.0342	0.0000	0.0502
106	107	14.42	530.1	14.42	2325	0.9572	0.55	4.96	5.33	0.0191	0.0203	0.0169	0.0000	0.0339	0.0294	0.0380	0.0332	0.0000	0.0541
106	108	14.42	530.3	14.42	2325	0.9571	0.55	4.97	5.34	0.0192	0.0204	0.0169	0.0000	0.0340	0.0301	0.0375	0.0355	0.0000	0.0527
106	109	14.42	531.5	14.42	1000	0.9909	0.23	2.45	2.54	0.0042	0.0049	0.0036	0.0000	0.0060	0.0064	0.0087	0.0067	0.0000	0.0090
106	110	14.42	530.1	14.42	1000	0.9905	0.22	2.44	2.54	0.0024	0.0024	0.0025	0.0000	0.0068	0.0081	0.0098	0.0083	0.0005	0.0111
106	111	14.42	529.2	14.42	1500	0.9797	0.35	3.61	3.79	0.0096	0.0111	0.0081	0.0000	0.0139	0.0142	0.0196	0.0146	0.0000	0.0198
106	112	14.42	530.3	14.42	1500	0.9800	0.35	3.60	3.78	0.0074	0.0071	0.0071	0.0000	0.0146	0.0155	0.0173	0.0205	0.0000	0.0241
106	113	14.42	529.8	14.42	2000	0.9656	0.47	4.53	4.82	0.0161	0.0188	0.0131	0.0000	0.0251	0.0245	0.0326	0.0236	0.0000	0.0346
106	114	14.42	529.4	14.42	2000	0.9668	0.47	4.49	4.78	0.0145	0.0160	0.0124	0.0000	0.0257	0.0226	0.0288	0.0258	0.0000	0.0396
106	115	14.42	530.0	14.42	2000	0.9667	0.47	4.50	4.79	0.0155	0.0170	0.0136	0.0000	0.0248	0.0234	0.0313	0.0242	0.0000	0.0374
106	116	14.42	530.1	14.42	2000	0.9668	0.47	4.50	4.79	0.0149	0.0166	0.0129	0.0000	0.0255	0.0234	0.0320	0.0252	0.0000	0.0404
106	117	14.42	530.3	14.42	2000	0.9668	0.47	4.50	4.79	0.0147	0.0163	0.0126	0.0000	0.0257	0.0240	0.0303	0.0254	0.0000	0.0408
106	118	14.42	531.5	14.42	2140	0.9625	0.52	4.80	5.14	0.0265	0.0283	0.0213	0.0000	0.0224	0.0397	0.0449	0.0451	0.0000	0.0347
106	119	14.42	530.9	14.42	2140	0.9623	0.52	4.83	5.17	0.0218	0.0250	0.0157	0.0000	0.0270	0.0401	0.0415	0.0419	0.0000	0.0460
106	120	14.42	530.9	14.42	2140	0.9646	0.55	5.02	5.36	0.0258	0.0328	0.0197	0.0000	0.0339	NA	NA	NA	NA	NA
106	121	14.42	530.9	14.42	2140	0.9647	0.55	5.04	5.38	0.0217	0.0275	0.0168	0.0000	0.0396	NA	NA	NA	NA	NA
106	122	14.42	530.9	14.42	2325	0.9610	0.56	5.03	5.40	0.0210	0.0244	0.0161	0.0000	0.0431	NA	NA	NA	NA	NA
106	123	14.42	530.9	14.42	2325	0.9622	0.55	5.02	5.37	0.0188	0.0214	0.0148	0.0000	0.0439	NA	NA	NA	NA	NA
106	124	14.42	530.9	14.42	2325	0.9612	0.55	4.99	5.34	0.0208	0.0244	0.0158	0.0000	0.0429	NA	NA	NA	NA	NA
106	125	14.42	530.9	14.42	2325	0.9629	0.54	4.95	5.30	0.0180	0.0207	0.0136	0.0000	0.0429	NA	NA	NA	NA	NA
106	126	14.42	530.9	14.42	2325	0.9617	0.55	4.99	5.34	0.0204	0.0239	0.0155	0.0000	0.0423	NA	NA	NA	NA	NA
106	127	14.42	530.9	14.42	2325	0.9633	0.54	4.96	5.30	0.0181	0.0204	0.0144	0.0000	0.0428	NA	NA	NA	NA	NA
106	142	14.42	530.9	14.42	2030	0.9690	0.48	4.60	4.89	0.0166	0.0198	0.0123	0.0000	0.0338	NA	NA	NA	NA	NA
106	143	14.42	530.9	14.42	2030	0.9712	0.47	4.51	4.78	0.0127	0.0149	0.0095	0.0000	0.0332	NA	NA	NA	NA	NA
106	151	14.44	530.6	14.44	2350	0.9563	0.55	4.99	5.37	0.0171	0.0161	0.0160	0.0000	0.0342	0.0297	0.0383	0.0384	0.0000	0.0505
106	152	14.44	529.8	14.44	2290	0.9562	0.54	4.96	5.33	0.0201	0.0232	0.0161	0.0000	0.0325	0.0317	0.0404	0.0292	0.0000	0.0434

TEST	NRUN	PT0 [psi]	TT0 [°R]	Pref [psi]	N2 [rpm]	PT2AVG	M2	W2 [pps]	W2C [pps]	DPCPAVG.SS	DPCPH.SS	DPCPT.SS	DPRPH.SS	DPRPT.SS	DPCPAVG.PK	DPCPH.PK	DPCPT.PK	DPRPH.PK	DPRPT.PK
106	153	14.44	529.8	14.44	2000	0.9653	0.47	4.53	4.82	0.0159	0.0186	0.0127	0.0000	0.0252	0.0244	0.0338	0.0230	0.0000	0.0348
106	154	14.44	529.5	14.44	2000	0.9664	0.46	4.47	4.76	0.0154	0.0172	0.0132	0.0000	0.0245	0.0240	0.0299	0.0244	0.0000	0.0354
106	155	14.44	529.7	14.44	2000	0.9665	0.47	4.50	4.78	0.0134	0.0131	0.0125	0.0000	0.0252	0.0235	0.0293	0.0255	0.0000	0.0380
106	156	14.44	529.6	14.44	2000	0.9665	0.47	4.51	4.79	0.0127	0.0124	0.0116	0.0000	0.0254	0.0226	0.0291	0.0304	0.0000	0.0398
106	157	14.44	529.7	14.44	2000	0.9663	0.47	4.50	4.79	0.0122	0.0120	0.0112	0.0000	0.0256	0.0239	0.0289	0.0342	0.0000	0.0395
106	170	14.44	530.7	14.44	1000	0.9909	0.23	2.46	2.55	0.0038	0.0041	0.0035	0.0000	0.0065	0.0066	0.0089	0.0068	0.0000	0.0095
106	171	14.44	530.1	14.44	1000	0.9909	0.22	2.43	2.52	0.0027	0.0023	0.0024	0.0000	0.0064	0.0091	0.0121	0.0090	0.0019	0.0114
106	172	14.44	530.1	14.44	1500	0.9800	0.35	3.61	3.78	0.0086	0.0088	0.0080	0.0000	0.0148	0.0147	0.0206	0.0141	0.0000	0.0210
106	173	14.44	529.9	14.44	1500	0.9799	0.35	3.59	3.77	0.0065	0.0065	0.0061	0.0000	0.0155	0.0189	0.0187	0.0219	0.0017	0.0245
106	174	14.44	529.8	14.44	2000	0.9662	0.47	4.53	4.82	0.0163	0.0188	0.0138	0.0000	0.0267	0.0250	0.0317	0.0244	0.0000	0.0356
106	175	14.44	529.8	14.44	2000	0.9673	0.47	4.49	4.78	0.0126	0.0122	0.0120	0.0000	0.0272	0.0250	0.0286	0.0327	0.0000	0.0412
106	176	14.44	530.0	14.44	2020	0.9668	0.47	4.53	4.82	0.0129	0.0125	0.0124	0.0000	0.0278	0.0244	0.0297	0.0331	0.0000	0.0415
106	177	14.44	530.3	14.44	2325	0.9564	0.55	5.01	5.39	0.0214	0.0241	0.0184	0.0000	0.0355	0.0320	0.0407	0.0323	0.0000	0.0475
106	178	14.44	530.1	14.44	2325	0.9580	0.55	4.98	5.35	0.0172	0.0160	0.0169	0.0000	0.0359	0.0297	0.0371	0.0386	0.0000	0.0520
106	179	14.44	530.0	14.44	2345	0.9575	0.55	5.01	5.38	0.0175	0.0163	0.0172	0.0000	0.0363	0.0304	0.0371	0.0404	0.0000	0.0537
106	216	14.40	530.6	14.40	1000	0.9913	0.23	2.45	2.55	0.0053	0.0061	0.0040	0.0000	0.0050	0.0082	0.0100	0.0089	0.0005	0.0081
106	217	14.40	530.4	14.40	1000	0.9905	0.23	2.52	2.63	0.0037	0.0038	0.0028	0.0000	0.0067	0.0094	0.0103	0.0116	0.0014	0.0122
106	218	14.40	530.0	14.40	980	0.9909	0.23	2.47	2.57	0.0035	0.0035	0.0026	0.0000	0.0064	0.0090	0.0098	0.0097	0.0008	0.0116
106	219	14.40	530.3	14.40	1500	0.9808	0.35	3.61	3.80	0.0123	0.0141	0.0089	0.0000	0.0114	0.0198	0.0222	0.0207	0.0012	0.0177
106	220	14.40	530.1	14.40	1500	0.9800	0.36	3.68	3.87	0.0085	0.0105	0.0070	0.0000	0.0147	0.0183	0.0208	0.0193	0.0004	0.0263
106	221	14.40	530.6	14.40	1480	0.9805	0.35	3.63	3.82	0.0083	0.0103	0.0067	0.0000	0.0144	0.0173	0.0201	0.0196	0.0000	0.0260
106	222	14.40	530.6	14.40	2000	0.9670	0.48	4.59	4.90	0.0224	0.0255	0.0161	0.0000	0.0206	0.0341	0.0381	0.0366	0.0007	0.0305
106	223	14.40	530.6	14.40	2000	0.9663	0.49	4.63	4.95	0.0177	0.0211	0.0137	0.0000	0.0257	0.0356	0.0372	0.0344	0.0000	0.0405
106	224	14.40	530.3	14.40	1980	0.9669	0.48	4.60	4.91	0.0172	0.0206	0.0134	0.0000	0.0253	0.0311	0.0351	0.0318	0.0000	0.0410
106	225	14.40	530.6	14.40	2240	0.9597	0.55	4.97	5.34	0.0286	0.0322	0.0205	0.0000	0.0259	0.0444	0.0489	0.0480	0.0000	0.0377
106	226	14.40	530.5	14.40	2240	0.9591	0.55	5.00	5.38	0.0230	0.0267	0.0175	0.0000	0.0324	0.0413	0.0448	0.0445	0.0000	0.0498
106	227	14.40	529.1	14.40	2280	0.9784	0.63	5.53	5.82	0.0098	0.0036	0.0193	0.0000	0.0344	0.0155	0.0039	0.0332	0.0000	0.0449
106	228	14.40	528.8	14.40	1970	0.9827	0.55	5.14	5.39	0.0064	0.0029	0.0116	0.0000	0.0259	0.0127	0.0032	0.0274	0.0000	0.0336
106	229	14.40	528.3	14.40	1670	0.9869	0.47	4.61	4.80	0.0047	0.0022	0.0084	0.0000	0.0185	0.0096	0.0025	0.0189	0.0000	0.0248
106	230	14.40	528.3	14.40	1300	0.9914	0.36	3.72	3.86	0.0032	0.0014	0.0059	0.0000	0.0113	0.0067	0.0016	0.0129	0.0000	0.0154
106	231	14.40	528.1	14.40	850	0.9960	0.23	2.49	2.57	0.0014	0.0006	0.0026	0.0000	0.0052	0.0034	0.0011	0.0057	0.0000	0.0075
106	232	14.40	528.0	14.40	2545	0.9638	0.62	5.43	5.80	0.0277	0.0194	0.0284	0.0000	0.0196	0.0363	0.0273	0.0457	0.0000	0.0301
106	233	14.40	528.4	14.40	2240	0.9718	0.55	5.07	5.37	0.0213	0.0150	0.0220	0.0000	0.0162	0.0286	0.0215	0.0349	0.0000	0.0252
106	234	14.40	528.5	14.40	2240	0.9793	0.47	4.58	4.81	0.0163	0.0112	0.0177	0.0000	0.0114	0.0207	0.0162	0.0257	0.0000	0.0176
106	235	14.40	528.0	14.40	1480	0.9874	0.36	3.75	3.91	0.0094	0.0069	0.0095	0.0000	0.0068	0.0128	0.0103	0.0153	0.0002	0.0109

TEST	NRUN	PT0 [psi]	TT0 [°R]	Pref [psi]	N2 [rpm]	PT2AVG	M2	W2 [pps]	W2C [pps]	DPCPAVG.SS	DPCPH.SS	DPCPT.SS	DPRPH.SS	DPRPT.SS	DPCPAVG.PK	DPCPH.PK	DPCPT.PK	DPRPH.PK	DPRPT.PK
106	236	14.40	527.6	14.40	950	0.9948	0.23	2.49	2.57	0.0036	0.0027	0.0038	0.0000	0.0028	0.0053	0.0042	0.0063	0.0001	0.0048
106	237	14.40	528.9	14.40	2340	0.9575	0.55	5.00	5.38	0.0204	0.0231	0.0172	0.0000	0.0341	0.0313	0.0396	0.0312	0.0000	0.0460
106	238	14.40	528.9	14.40	2340	0.9573	0.55	5.01	5.39	0.0187	0.0179	0.0179	0.0000	0.0344	0.0317	0.0402	0.0320	0.0000	0.0467
106	239	14.40	528.6	14.40	2340	0.9576	0.55	5.01	5.38	0.0186	0.0163	0.0193	0.0000	0.0338	0.0311	0.0392	0.0333	0.0000	0.0463
106	240	14.40	528.6	14.40	2380	0.9588	0.55	5.00	5.37	0.0180	0.0147	0.0202	0.0000	0.0342	0.0310	0.0326	0.0340	0.0000	0.0482
106	241	14.40	528.0	14.40	2400	0.9595	0.55	5.01	5.37	0.0159	0.0117	0.0186	0.0000	0.0356	0.0274	0.0308	0.0319	0.0000	0.0485
106	242	14.40	528.3	14.40	2400	0.9602	0.55	5.01	5.37	0.0146	0.0108	0.0169	0.0000	0.0373	0.0263	0.0277	0.0329	0.0000	0.0508
106	243	14.40	528.2	14.40	2000	0.9671	0.47	4.53	4.82	0.0141	0.0142	0.0129	0.0000	0.0259	0.0243	0.0305	0.0233	0.0000	0.0371
106	244	14.40	528.2	14.40	2020	0.9669	0.47	4.53	4.82	0.0143	0.0138	0.0137	0.0000	0.0260	0.0251	0.0313	0.0241	0.0000	0.0358
106	245	14.40	528.0	14.40	2030	0.9672	0.47	4.53	4.82	0.0143	0.0128	0.0148	0.0000	0.0258	0.0251	0.0269	0.0250	0.0000	0.0354
106	246	14.40	527.9	14.40	2040	0.9681	0.47	4.52	4.80	0.0137	0.0116	0.0150	0.0000	0.0259	0.0223	0.0253	0.0250	0.0000	0.0355
106	247	14.40	527.3	14.40	2060	0.9689	0.47	4.52	4.80	0.0116	0.0089	0.0132	0.0000	0.0274	0.0211	0.0237	0.0242	0.0000	0.0376
106	248	14.40	527.9	14.40	2080	0.9690	0.47	4.53	4.81	0.0105	0.0082	0.0118	0.0000	0.0294	0.0227	0.0220	0.0281	0.0000	0.0405
106	249	14.40	530.2	14.40	1000	0.9910	0.23	2.44	2.54	0.0041	0.0048	0.0034	0.0000	0.0066	0.0066	0.0085	0.0068	0.0000	0.0094
106	250	14.40	529.7	14.40	1000	0.9910	0.22	2.41	2.51	0.0024	0.0020	0.0021	0.0000	0.0063	0.0094	0.0132	0.0094	0.0013	0.0107
106	251	14.40	529.6	14.40	1500	0.9801	0.35	3.59	3.78	0.0084	0.0086	0.0078	0.0000	0.0146	0.0141	0.0194	0.0149	0.0000	0.0203
106	252	14.40	529.5	14.40	1500	0.9799	0.35	3.57	3.76	0.0061	0.0059	0.0059	0.0000	0.0154	0.0186	0.0189	0.0204	0.0012	0.0238
106	253	14.40	529.6	14.40	2000	0.9665	0.47	4.51	4.81	0.0144	0.0144	0.0134	0.0000	0.0261	0.0238	0.0313	0.0251	0.0000	0.0364
106	254	14.40	529.4	14.40	2000	0.9677	0.46	4.46	4.74	0.0120	0.0112	0.0117	0.0000	0.0268	0.0246	0.0299	0.0324	0.0000	0.0408
106	255	14.40	529.5	14.40	2325	0.9567	0.55	5.00	5.38	0.0209	0.0232	0.0181	0.0000	0.0350	0.0329	0.0399	0.0306	0.0000	0.0467
106	256	14.40	529.5	14.40	2325	0.9582	0.54	4.94	5.32	0.0167	0.0150	0.0166	0.0000	0.0354	0.0303	0.0362	0.0382	0.0000	0.0557
106	257	14.40	530.3	14.40	1000	0.9914	0.22	2.42	2.52	0.0052	0.0060	0.0038	0.0000	0.0052	0.0083	0.0100	0.0086	0.0009	0.0081
106	258	14.40	530.5	14.40	980	0.9912	0.22	2.42	2.52	0.0030	0.0027	0.0024	0.0000	0.0062	0.0088	0.0102	0.0093	0.0010	0.0107
106	259	14.40	530.7	14.40	1500	0.9810	0.35	3.60	3.79	0.0122	0.0140	0.0089	0.0000	0.0110	0.0189	0.0228	0.0203	0.0005	0.0173
106	260	14.40	530.4	14.40	1480	0.9805	0.35	3.62	3.81	0.0082	0.0095	0.0065	0.0000	0.0145	0.0168	0.0197	0.0198	0.0003	0.0257
106	261	14.40	530.3	14.40	2000	0.9672	0.48	4.57	4.88	0.0221	0.0252	0.0159	0.0000	0.0204	0.0337	0.0389	0.0376	0.0016	0.0315
106	262	14.40	530.0	14.40	1980	0.9671	0.48	4.58	4.88	0.0166	0.0196	0.0131	0.0000	0.0256	0.0299	0.0342	0.0324	0.0000	0.0409
106	263	14.40	530.0	14.40	2240	0.9599	0.54	4.96	5.33	0.0280	0.0317	0.0202	0.0000	0.0258	0.0439	0.0498	0.0479	0.0000	0.0387
106	264	14.40	530.4	14.40	2240	0.9592	0.55	5.00	5.37	0.0220	0.0257	0.0173	0.0000	0.0332	0.0419	0.0448	0.0428	0.0000	0.0520

Appendix E. Low-Order Synthetic-Jet Actuator Computational Model

Response surface methods were employed to generate a low-order model to predict the key performance metrics of the synthetic jet necessary to simulate the actuator as a CFD boundary condition, thereby eliminating the need to computationally model the full actuator cavity and diaphragm motion. However, a design-independent, actuator-model-development approach is more useful to future systems than a particular actuator model tailored to one specific design, due to the fact that actuators will continue to evolve to reach new performance and efficiency goals, as well as to accommodate various size and power restrictions dictated by their applications and integrations. Response surface methodology lends itself well to this application.

The response surface method developed and applied during the first year of this program to simulate synthetic jet operation in a rectangular duct employed statistically designed experiments based on the selection of key actuator design variables (factors) and actuator performance metrics. The actuator employed in this effort is described in the Approach section of the report. Actuator performance was controlled through two factors: the input voltage and frequency. Performance was characterized in terms of four response variables: cavity total pressure, ΔP_{Tjet}, jet velocity, U_{jet}, average cavity temperature, ΔT, and a phase lag between pressure and velocity. (Pressure and temperature were reported as changes relative to the ambient conditions.)

The actuator has a periodic output such that the pressure and jet velocity may be accurately represented in terms of a sine wave that is a function of the peak pressure or jet velocity and the input frequency, Figure E1 and Figure E2. The velocity measurements, Figure E2, were obtained using hot wire anemometry. The data was rectified in that hot wire anemometry cannot discern alternating flow directions. In addition, the resolution of the hot wire data was not adequate to capture the point in the cycle where the velocity was identically 0 ft/s. Nevertheless, the sinusoidal wave function did accurately reproduce the measured velocity at alternating peaks, where the jet flow is exiting the actuator cavity. Comparison of the measured pressure and velocity time histories showed that the signals were not in phase, Figure E3. Furthermore, the phase lag between pressure and velocity was not consistent for a given frequency or voltage. As a result, a pressure/velocity phase lag, $\Delta\Theta$, was defined to represent accurately the actuator output. These parameters are adequate to characterize the physics of the jet flow and can be accurately measured.

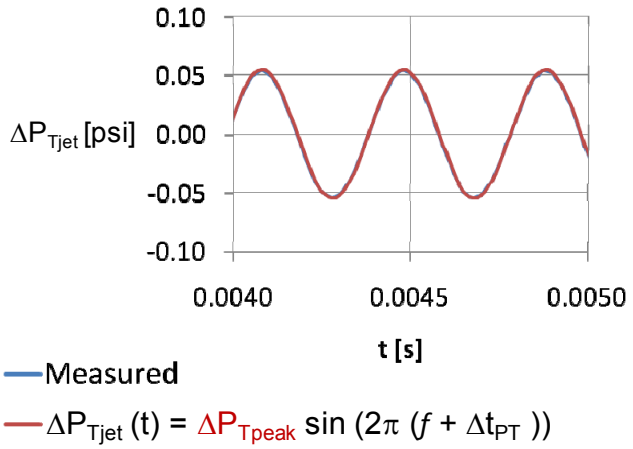

Figure E1. Synthetic-jet actuator Measured and Simulated Cavity Total Pressure Change

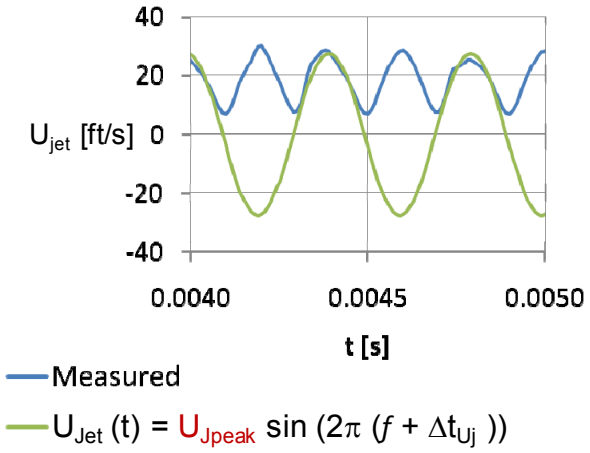

Figure E2. Synthetic-jet actuator Measured and Simulated Jet Velocity

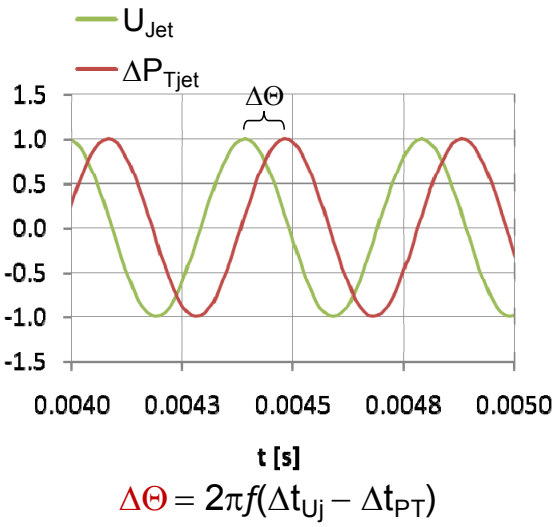

Figure E3. Actuator Jet Velocity / Pressure Phase Lag

The temporal aspect of the synthetic jet may be accurately simulated using a sinusoidal wave function, Figure E1 through Figure E3. However, the amplitude of the signal, which varies as a function of input voltage and frequency, must also be specified to simulate the jet. A response surface approach combined with a statistically designed test matrix was employed to generate the actuator peak pressure, jet velocity, phase difference, and temperature.

The DOE strategy applied to develop the actuator response surfaces was an 11-run, rotatable, central composite design (CCD). This design allows for efficient and accurate estimation of quadratic terms in a regression model. A CC-D comprises three types of points: factorial points, axial points, and center points, Figure E4. Since there were only two design variables in this study, the full factorial was embedded in the DOE, meaning that all combinations of the design factors minimum and maximum values were tested. This resulted in 2^2 or four of the DOE points. The four axial points were selected at values that resulted in a rotatable design, which ensures constant prediction variance at all points equidistant from the design center and thus improves the quality of prediction. Finally, three replicates of the design center point were obtained to quantify experimental error.

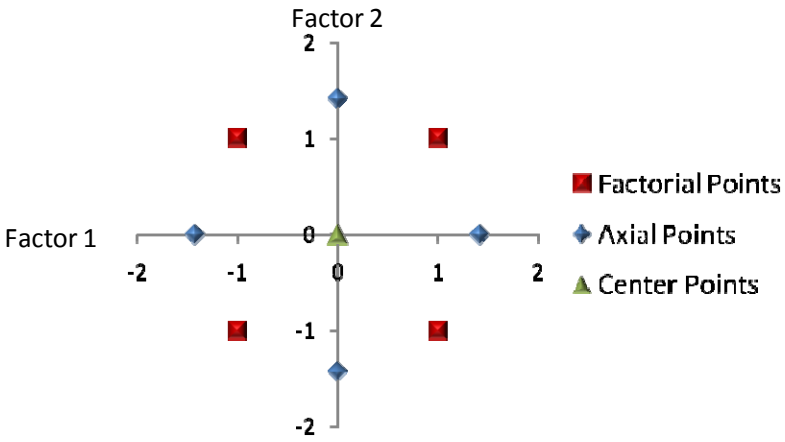

Figure E4. Rotational Central Composite Design

The CC-D was centered around the actuator operating point of 2200 Hz, 60 V, Figure E5, thus ensuring that the model would be most accurate in the frequency and voltage range where the actuator was most likely to be operating. The CC-D selected required five levels of each of the two factors to be measured and a total of 11 runs.

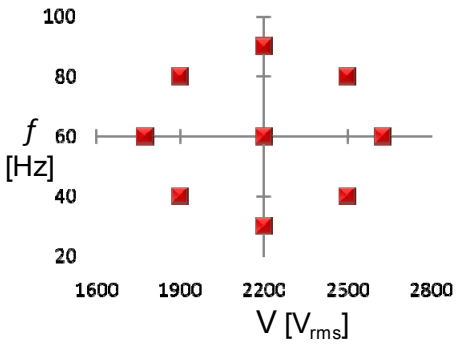

Figure E5. Synthetic-jet actuator DOE matrix

Data for the points defined by the CC-D DOE matrix were obtained experimentally using the actuator-calibration-test setup described in the report. The resulting database is tabulated in Table E1. Through the course of the actuator calibration test, an instability was identified at frequencies above 2500 Hz, which brought the data at those frequencies into question. The data point defined in the DOE matrix at 2625 Hz, 60 V was run at 2500 Hz, 60 V in order to avoid the instability. In addition to those data collected from the DOE trials, previously acquired data from actuator calibration experiments was included in the response surface analysis, Table E2.

Table E1. Synthetic-Jet Actuator DOE Database

Freq [Hz]	V [Vrms]	ΔP_{Tpeak} [Psi]	$U_{j\,peak}$ [ft/s]	$\Delta\Theta_U$ [rad]	ΔT [R]
1775	60	0.117	123.9	1.75	18.9
1900	40	0.085	79.9	1.59	12.2
1900	80	0.202	186.8	2.07	20.7
2200	30	0.130	104.2	1.59	12.4
2200	60	0.233	184.6	1.97	17.6
2200	60	0.232	181.9	1.98	17.6
2200	60	0.229	181.3	2.00	22.0
2200	90	0.261	229.1	2.16	18.0
2500	40	0.055	27.6	1.43	16.7
2500	80	0.138	81.6	4.60	0.0
~~2625~~ 2500	60	0.085	56.6	1.47	7.0

Table E2. Additional Actuator Data Included in the Response Surface Analysis

Freq [Hz]	V [Vrms]	ΔP_{Tpeak} [Psi]	$U_{j\,peak}$ [ft/s]	$\Delta\Theta_U$ [rad]	ΔT [R]
2000	10	0.025	15.71	4.40	16.4
2000	60	0.163	148.67	1.79	15.3
2300	95	0.265	205.89	5.21	7.7
2300	25	0.108	82.17	1.52	7.4
1800	60	0.114	117.91	1.77	6.3

In total, 16 runs were included in the response surface analysis, 11 based on the DOE matrix described above and five additional trials. This provided enough data to estimate all the terms in a cubic response surface model. Initially, models were evaluated based on their adjusted and predicted multiple correlation coefficients, adj-R^2 and pred-R^2, respectively. The pred-R^2 gives a measure of how well the model predicts the response values, where the adj-R^2 gives an assessment of the amount of variation about the mean explained by the model. In addition, p-values and F-values were used to select the individual terms included in the response surface models based on statistical significance criteria. The analysis yielded modified quadratic equations based on voltage and frequency terms for the peak pressure change and jet velocity, Equation E1 and Equation E2, respectively. However, the phase shift between the pressure and velocity was determined to be only a function of the input voltage, Equation E3. Finally, results of the analysis for temperature indicated that the total temperature variation in the cavity was best approximated as an average of the measurements obtained, as no combination of terms resulted in a statistically significant model.

$$\Delta P_{T\,peak}\,[\text{psi}] = -4.295 + 4.006\text{E-}3\,(f) + 4.847\text{E-}3\,(V) - 9.331\text{E-}7\,(f^2) - 2.080\text{E-}5\,(V^2)$$

Equation E1

$$U_{J\,peak}\,[\text{ft/s}] = -3.492\text{E}3 + 3.165\,(\boldsymbol{f}) + 9.188\,(\mathbf{V}) - 3.191\text{E-}3\,(\boldsymbol{f})(\mathbf{V}) - 7.093\text{E-}4\,(\boldsymbol{f}^2)$$

Equation E2

$$\Delta\Theta\,[\text{rad}] = 6.359 - 0.225\,(\mathbf{V}) + 2.499\text{E-}3\,(\mathbf{V}^2)$$

Equation E3

Results from the response surface analysis are represented graphically for pressure, velocity, and phase lag, Figure E6, Figure E7, and Figure E8, respectively. At 60 Vrms, the majority of the measured pressure and velocity data points fall within the 95% confidence intervals of the response surface models, Figure E9 and Figure E10. The 95% confidence intervals for the phase lag response surface are extremely tight with most data points touching the prediction line, Figure E11.

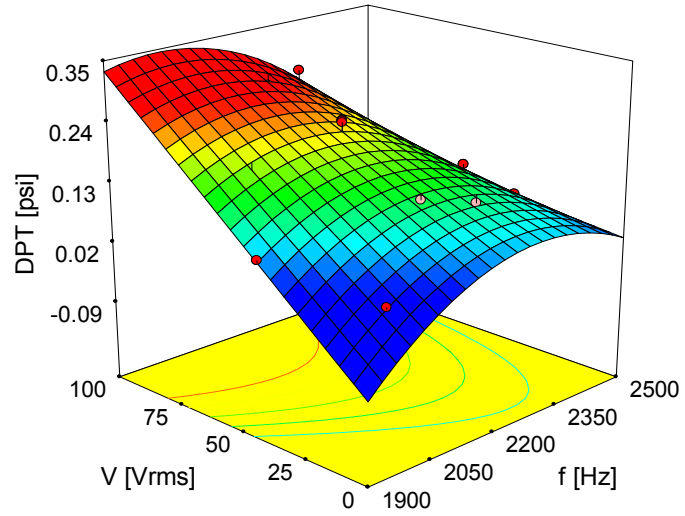

Figure E6. Cavity Peak Total Pressure Change Response Surface

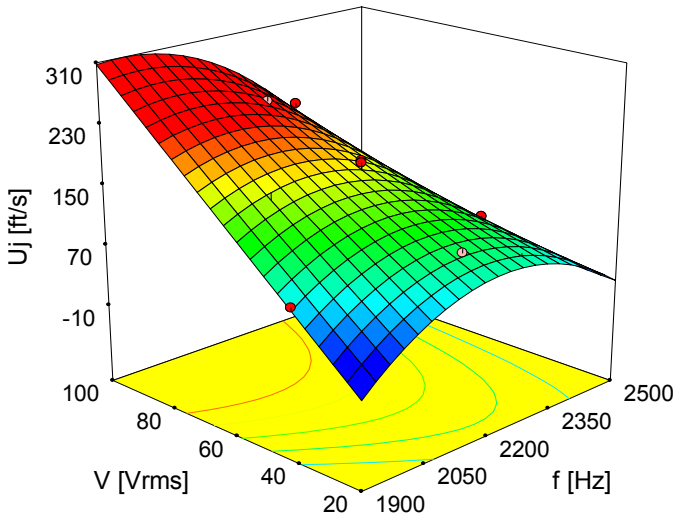

Figure E7. Peak Jet Velocity Response Surface

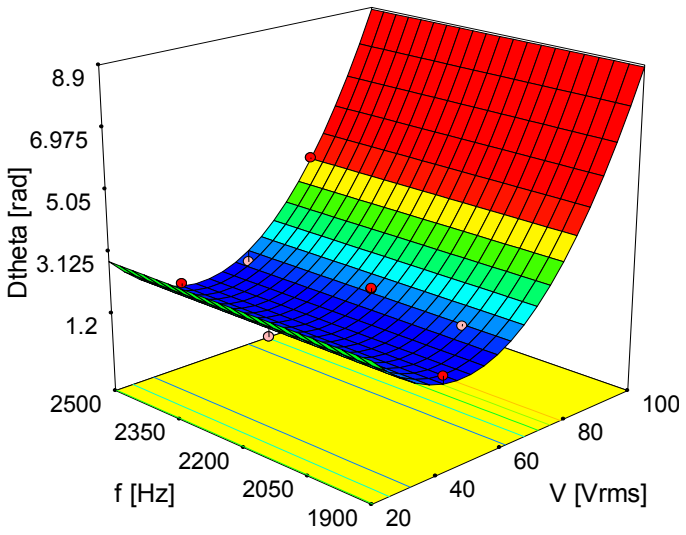

Figure E8. Pressure - Velocity Phase Lag Response Surface

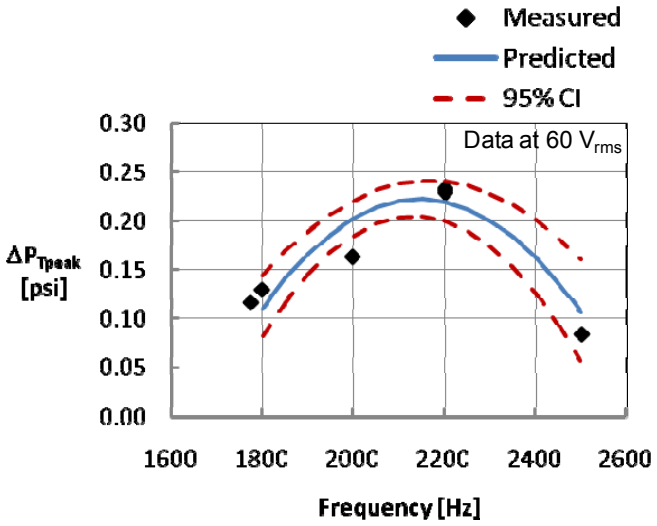

Figure E9. Pressure Response Surface Confidence Interval

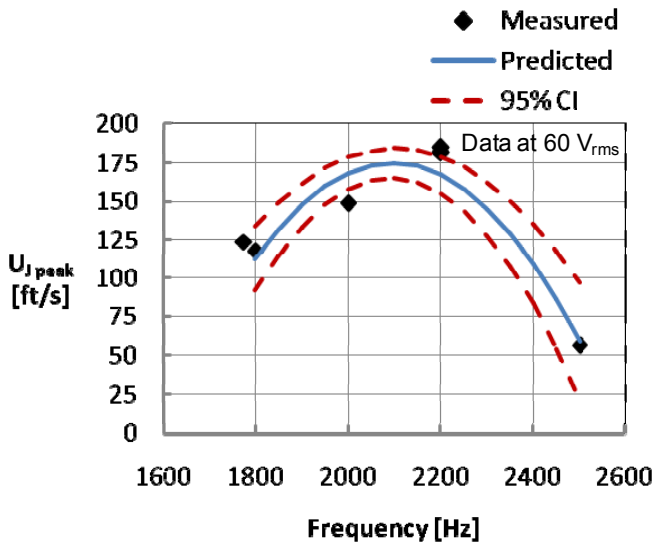

Figure E10. Jet Velocity Response Surface Confidence Interval

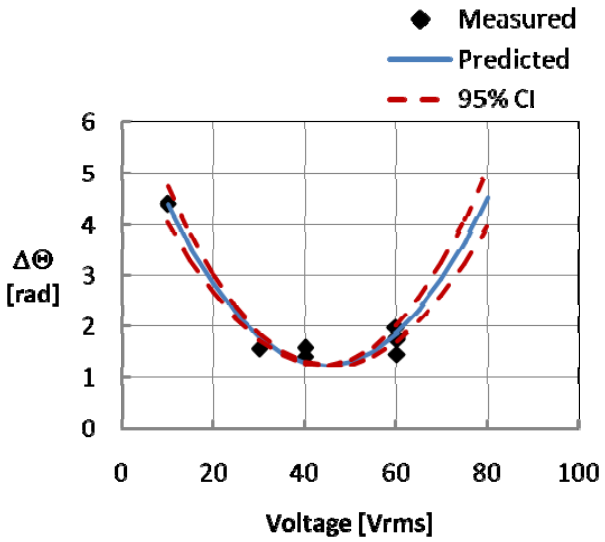

Figure E11. Phase Lag Response Surface Confidence Interval

DOE methods were applied to characterize peak cavity total pressure change, average cavity total temperature change, and peak jet velocity of a synthetic-jet actuator. Response surface models were developed to predict peak cavity total pressure change, jet velocity, and phase lag between them. This approach was successfully applied to generate models of two slightly different synthetic-jet actuators with equally favorable outcomes. Results of these analyses were successfully implemented into the Boeing BCFD flow solver as sinusoidal boundary conditions to simulate the effects of the synthetic jet portion of a closely-coupled (2nd generation) hybrid flow-control system. Those results are detailed in subsequent sections of this report. The model was delivered on 28 April 2010 to the NPARC Alliance for implementation into WIND-US code and is expected to be part of the beta 3.0 release.

Model Validation

A validation study of the low order synthetic jet actuator model was conducted to establish confidence in the model as well as the simulation tool. The approach for validation was to use BCFD in obtaining time dependent simulation data of a streamwise oriented slot synthetic jet mounted upstream of a ramp vortex generator, Figure E12, and compare this to experimental data provided by Georgia Tech. A baseline was established with the synthetic jet turned off. When the synthetic jet was on, it was operated at 2200Hz and 60V_{RMS} which, based on the model, resulted in a peak jet-fluid speed of approximately 172 ft/s.

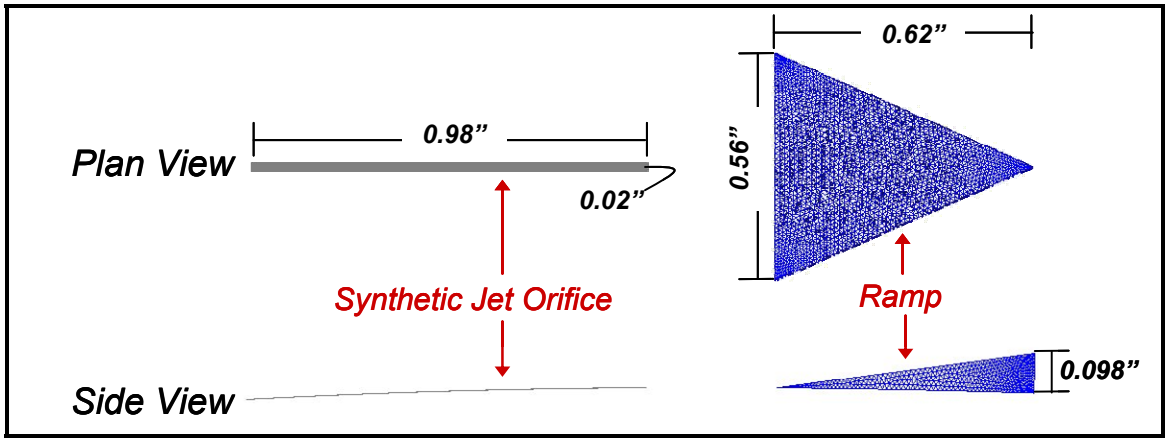

Figure E12. The hybrid flow control device used for validation of the low order synthetic jet model

The device in Figure E12 was mounted near the throat of a converging/diverging section in an approximately rectangular duct having an approach flow with Mach number 0.5. This geometry modeled the experimental setup of the wind tunnel test section at Georgia Tech, and is shown in Figure E13.

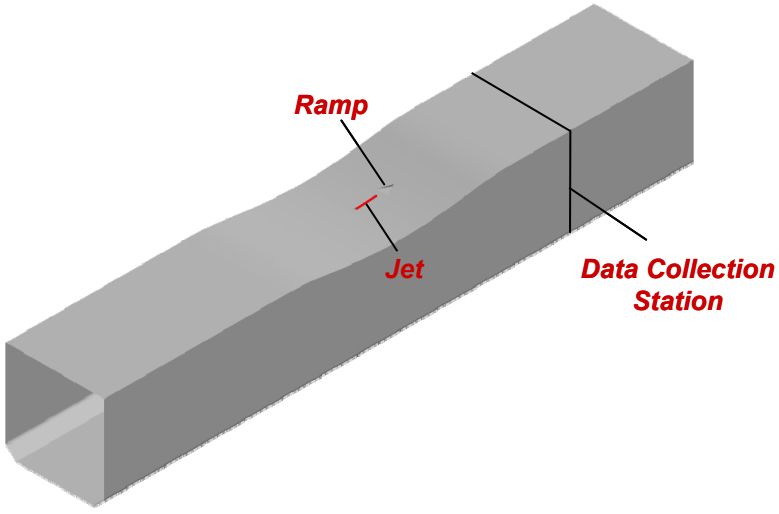

Figure E13. Key components of the computational domain used to validate the synthetic jet model

The data collection station depicted in Figure E13 was located 7.38” downstream of the geometric throat, and it was the location at which flow information was collected for comparison in both the simulation and experiment. The dataset used for comparison consisted of

streamwise and crossflow (wall normal) mean and fluctuating velocity components. All data was phase-locked averaged at 90 degree increments in the synthetic jet's cycle, and was taken at the centerline and a spanwise location 0.24" off centerline.

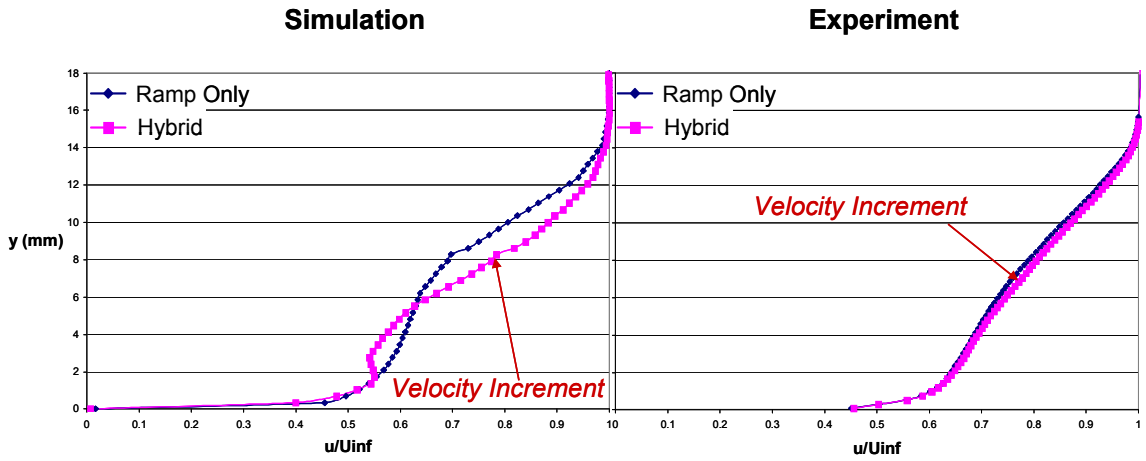

Figure E14. Streamwise velocity comparison for ramp only and hybrid configurations

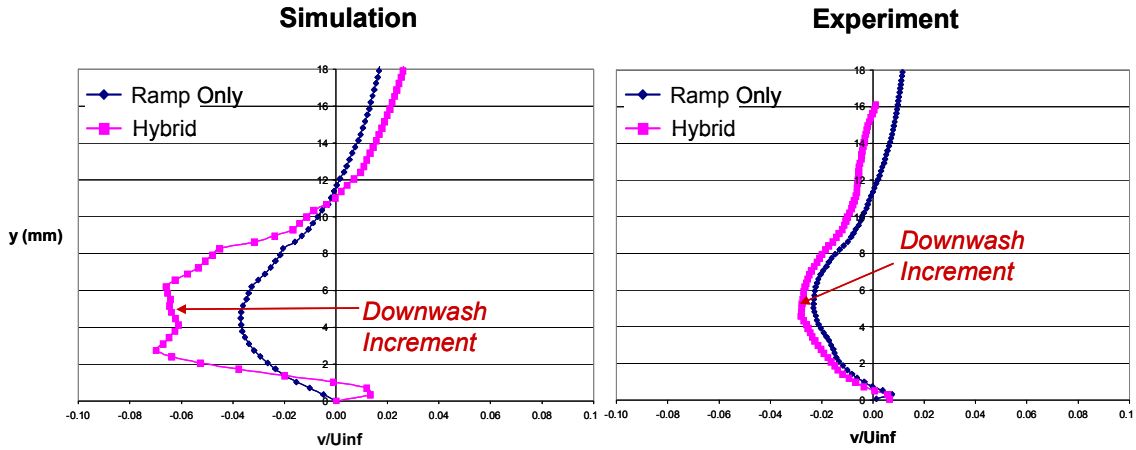

Figure E15. Crossflow velocity comparison for ramp only and hybrid configurations

Mean centerline velocity profiles for the streamwise, Figure E14, and crossflow, Figure E15, components are shown for both simulation and experiment. The two cases depicted by the blue and pink curves are ramp only (synthetic jet turned off), and hybrid (synthetic jet turned on). In the comparison of the streamwise component of velocity, both the simulation and experiment agree that the effect of turning the jet on is to increase the velocity in the boundary layer. Similarly, the simulation and experiment agree that activating the jet creates a downwash increment in the crossflow velocity component.

The increment in velocity introduced by the synthetic jet is due to the vortex pair that the jet creates. The production of these vortices is realized in the simulation of the synthetic jet actuator model. Qualitatively, the simulation is in agreement with the experiment, and validates the actuator model as well as the simulation tool and technique. The quantitative agreement is

somewhat less conclusive, and understandably so for the following reasons. The actuator model is a low order model and so neglects the fine details of the flow physics involved with the synthetic jet. In addition, the high frequency of the synthetic jet requires long simulation durations to capture its effects with any fidelity. This makes acquiring a dataset which has a statistically meaningful duration difficult if not impossible with today's available computing resources. For the comparisons in Figure E14 and Figure E15, the simulation data were the result of an average over only five complete cycles of the synthetic jet, while the experimental results were averaged over thousands of cycles. Despite the aforementioned restrictions, the key flow features (and their affect on the flow field) produced by the synthetic jet are accurately captured by the low order synthetic jet actuator model. This was demonstrated using the BCFD flow solver as the simulation tool.

REPORT DOCUMENTATION PAGE			Form Approved OMB No. 0704-0188

1. REPORT DATE *(DD-MM-YYYY)*	2. REPORT TYPE	3. DATES COVERED *(From - To)*
01-12-2011	Final Contractor Report	

4. TITLE AND SUBTITLE
Inlet Flow Control and Prediction Technologies for Embedded Propulsion Systems
Program Summary Report

5a. CONTRACT NUMBER
NNC07CB76C

5b. GRANT NUMBER

5c. PROGRAM ELEMENT NUMBER

6. AUTHOR(S)
McMillan, Michelle, L.; Mackie, Scott, A.; Gissen, Abe; Vukasinovic, Bojan; Lakebrink, Matthew, T.; Glezer, Ari; Mani, Mori; Mace, James, L.

5d. PROJECT NUMBER

5e. TASK NUMBER

5f. WORK UNIT NUMBER
WBS 561581.02.08.03.21.06

7. PERFORMING ORGANIZATION NAME(S) AND ADDRESS(ES)
SynGenics Corporation
5190 Olentangy River Road
Delaware, Ohio 43015

8. PERFORMING ORGANIZATION REPORT NUMBER
E-17993

9. SPONSORING/MONITORING AGENCY NAME(S) AND ADDRESS(ES)
National Aeronautics and Space Administration
Washington, DC 20546-0001

10. SPONSORING/MONITOR'S ACRONYM(S)
NASA

11. SPONSORING/MONITORING REPORT NUMBER
NASA/CR-2011-217237

12. DISTRIBUTION/AVAILABILITY STATEMENT
Unclassified-Unlimited
Subject Categories: 01, 02, 07, 05, 34, and 64
Available electronically at http://www.sti.nasa.gov
This publication is available from the NASA Center for AeroSpace Information, 443-757-5802

13. SUPPLEMENTARY NOTES

14. ABSTRACT
Fail-safe, hybrid, flow control (HFC) is a promising technology for meeting high-speed cruise efficiency, low-noise signature, and reduced fuel-burn goals for future, Hybrid-Wing-Body (HWB) aircraft with embedded engines. This report details the development of HFC technology that enables improved inlet performance in HWB vehicles with highly integrated inlets and embedded engines without adversely affecting vehicle performance. In addition, new test techniques for evaluating Boundary-Layer-Ingesting (BLI)-inlet flow-control technologies developed and demonstrated through this program are documented, including the ability to generate a BLI-like inlet-entrance flow in a direct-connect, wind-tunnel facility, as well as, the use of D-optimal, statistically designed experiments to optimize test efficiency and enable interpretation of results. Validated improvements in numerical analysis tools and methods accomplished through this program are also documented, including Reynolds-Averaged Navier-Stokes CFD simulations of steady-state flow physics for baseline, BLI-inlet diffuser flow, as well as, that created by flow-control devices. Finally, numerical methods were employed in a ground-breaking attempt to directly simulate dynamic distortion. The advances in inlet technologies and prediction tools will help to meet and exceed "N+2" project goals for future HWB aircraft.

15. SUBJECT TERMS
Aerodynamics; Boundary layer control; Turbulent boundary layer; Jet control; Vortex generators; Computational fluid dynamics; Turbulence models

16. SECURITY CLASSIFICATION OF:			17. LIMITATION OF ABSTRACT	18. NUMBER OF PAGES	19a. NAME OF RESPONSIBLE PERSON
a. REPORT	b. ABSTRACT	c. THIS PAGE			STI Help Desk (email:help@sti.nasa.gov)
U	U	U	UU	161	19b. TELEPHONE NUMBER *(include area code)* 443-757-5802